KYOTO UNIVERSITY

DOCTORAL THESIS

Diagnostics for Physical Processes of X-ray Plasma in Supernova Remnants

Author:
Yuki AMANO

A thesis submitted in fulfillment of the requirements for the degree of Doctor of Philosophy

in the

Cosmic ray Group
Department of Physics

April 20, 2023

KYOTO UNIVERSITY

Abstract

Faculty Name
Department of Physics

Doctor of Philosophy

Diagnostics for Physical Processes of X-ray Plasma in Supernova Remnants

by Yuki AMANO

X-ray imaging spectroscopy of Supernova remnants (SNRs) enables us to estimate the abundances and spatial distribution of heavy elements synthesized by the progenitors. This information provide us with many insights into the evolution process and explosion mechanism of the progenitors. Improvement of the performance of X-ray detectors have revealed that the formation process, ionization state, and X-ray emission process of SNRs are more complex than that expected by the conventional picture. For example, recent studies point out the importance of charge exchange (CX) and resonance scattering (RS) in SNRs. Since signs of the RS or CX are expected to be found in intensity ratios of multiplet lines (e.g., OVII Heα), which cannot be resolved with widely-used detectors such as CCDs, it is difficult to obtain the observational evidence for CX or RS. If we can quantify the effects of these processes, we can measure several important information such as microturbulence velocities and 3D structure of SNRs.

We performed a high-resolution X-ray spectroscopy of N49, J0453.6−6829 with the RGS onboard XMM-Newton to obtain the observational evidence of CX and RS. The RGS spectrum of N49 shows a high G-ratio of OVII Heα lines as well as OVIII Lyβ/α and FeXVII (3s–2p)/(3d–2p) ratios, which cannot be explained by the emission from an optically thin thermal plasma. These line ratios can be well explained by the effect of RS. In the case of the J0453.6−6829, we find a high f/r ratio of OVII Heα lines and OVIII Lyβ/α ratio. The spectrum is fairly explained by taking into account a CX emission in addition to the thermal component. Analyzing archival ATCA & Parkes radio data, we also reveal that H I cloud is possibly interacting with J0453.6−6829. These results support the presence of CX in J0453.6−6829, as the origin of the obtained high f/r ratio. Although a contribution of the RS cannot be ruled out at this time, we conclude that CX seems more likely than RS considering the relatively symmetric morphology of this remnant.

We present a method to constrain the 3D structure of SNRs by measuring their line-of-sight length through the effects of RS. Additionally, we apply this methodology to one of the brightest extra-Galactic SNRs, 1E 0102−72.9 (hereafter E0102), whose 3D structure is currently a controversial. Previous studies have proposed various structures for 1E 0102.2−7219, such as barrel-like and cylindrical structure. These structures require strong scattering effect, which is inconsistent with our results. Therefore, we have proposed a double-ring structure and a cylindrical structure with the expansion velocity as structures that are consistent with both our observations and previous studies. This method can be applied to many celestial objects using the future satellite XRISM.

The RGS spectra of N49 and J0453.6−6829 show the excess around 16 Å, which cannot be explained by the effect of CX and RS. We attribute these discrepancies to uncertainties in the atomic data related to Fe-L emission lines. To solve these problems, it is necessary to experimentally measure atomic data. Ground experiments, such as EBIT are indispensable for the future development of X-ray astronomy.

Acknowledgements

I would like to express my gratitude to Prof. Takeshi Tsuru, Ass. Prof. Hiroyuki Uchida and Assoc. Prof. Takaaki Tanaka for guiding me throughout the five years at Kyoto university. I am very grateful to my collaborators, Dr. Liyi Gu, Dr. Hidetoshi Sano, Dr. Hiroya Yamaguchi and Mr. Yosuke Koshiba I would like to thank Dr. Hidetoshi Sano for providing us with the ATCA & Parke data. Mr. Yosuke Koshiba played the most important role in the research of J0453. I appreciate the supports and encouragements of all the people in the Cosmic ray group and JAXA/ISAS. Finally, I thank my family for their support.

Contents

List of Figures

List of Tables

Chapter 1

Introduction

A supernova (SN) is an explosion at the end of a star's life. Heavy elements synthesized in the interior of a star are released into interstellar space by an SN explosion. Ejected material from an SN collides with surrounding gases and forms a high-temperature plasma called supernova remnant (SNR). Since SNR plasmas are often optically thin in the X-ray band, X-ray imaging spectroscopy enables us to directly estimate the abundances and spatial distribution of heavy elements. This information provide us with many insights into the evolution process and explosion mechanism of the progenitors (e.g., Sato et al., 2021).

Recent studies pointed out that the formation process and X-ray emission process of SNRs are more complex than those expected in the conventional picture assuming spherically symmetric explosions in uniform environments (e.g., Okon et al., 2020; Yamaguchi et al., 2018; Uchida et al., 2019). Such diversity in the physics of SNRs has been revealed by improvements in the performance of X-ray detectors. Figure 1.1 show the improvement history of energy resolution of X-ray instruments and important findings, which resulted from the spectral study. CCD detectors, which are widely used in X-ray astronomy, can separate the major K-shell emission lines from heavy elements with different ionization states. On the other hand, X-ray grating spectrometers and future available X-ray calorimeters have an energy resolution one order of magnitude better than CCDs. Such energy resolution enables us to measure the kinetic velocities of gases and the abundances of rare elements, as well as to investigate physical processes such as charge exchange (CX) due to collisions between ions and neutral atoms, and scattering of line photons by ions (resonance scattering: RS).

In this thesis, we perform diagnostics for physical processes such as CX and RS in SNRs with the grating spectrometer. Although these processes are predicted to occur in SNRs by previous calculations (e.g., Lallement, 2004; Kaastra and Mewe, 1995), established observational evidence is still limited. This is because it is difficult to apply the grating spectrometer to diffuse objects such as SNRs. Since the effect of these processes apparently reduce or enhance intensities of some lines, ignoring their contribution can sometimes lead to, for example, biases in elemental abundance measurements. On the other hand, quantifying their contribution will allow us to obtain several important information such as microturbulence velocities, absolute abundances and 3D structure of SNRs.

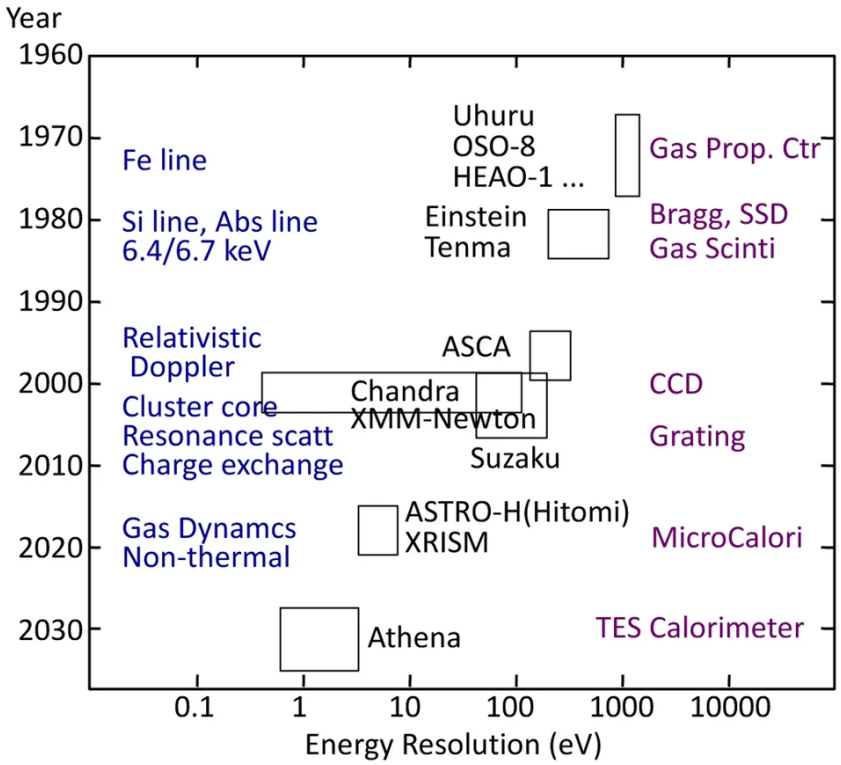

FIGURE 1.1: History of energy resolution of X-ray spectrometers in X-ray astronomy (Ezoe et al., 2021). The energy resolution is FWHM in energy for 6 keV X-rays.

In Chapter 2, we describe the reviews of SN and SNR, respectively. The basic characteristics of the instruments aboard XMM-Newton which we used in this study are summarized in Chapter 4. Chapter 5 provide the results of the high resolution X-ray spectroscopy of SNRs located in Large Magellanic Cloud (LMC): N49 and J0453−6829. In Chapter 6, we introduce a method to constrain the 3D structure of SNR plasmas using the effect of RS. Combining all the works, we develop the discussions in Chapter 7, and we finally describe the summary and conclusion of this thesis in Chapter 8.

Chapter 2

Supernova and Supernova Remnant

A supernova (SN) is an explosion at the end of a star's life. It is one of the most dramatic explosion phenomena in the universe, with a brightness comparable to that of a single galaxy and a released kinetic energy of $\sim 10^{51}$ erg. SN explosions are the final stage of stellar evolution and the origin of compact objects such as black holes and neutron stars. In addition, heavy elements synthesized in the interior of stars during their evolution and explosions are released into interstellar space by SN explosions. This diversity makes SNs one of the most interesting phenomena in the universe. In this chapter, we explain the evolutionary process leading up to the explosion of a star, the classification and explosion mechanism of SN, and the supernova remnant (SNR).

2.1 Stellar Evolution of the Progenitor

2.1.1 Stellar Evolution

Stars are classified according to the observed temperature (spectrum type) and luminosity. Figure 2.1 shows an HR diagram showing the types of stars. Stars produce energy by nuclear fusion reactions in their cores, creating enough pressure to support their self-gravity. Nuclear fusion reactions inside stars begin with nuclear reactions of hydrogen, gradually synthesizing heavier elements. A star in the early stages of stellar evolution that is burning hydrogen is called a main sequence star (for example, the B-type star indicated by the red circle in Figure 2.1). The temperature and brightness of main sequence stars depend primarily on their mass. When a star exhausts the hydrogen in its core, hydrogen nuclear reactions begin in a shell outside the core, then the radius of the star expands and the surface temperature drops. As the radius expands and the surface temperature drops, the star moves to the right on the HR diagram and becomes a giant star such as a red supergiant (RSG). A Star with an initial mass of less than 25 $M_{\odot}$ are considered to be an SN explosion in the giant star phase. Massive stars with initial mass exceeds 25 $M_{\odot}$ move to the left again in the HR diagram due to their large amount of mass loss. Such Massive stars considered to explode after becoming a Wolf-Rayet star (WR star).

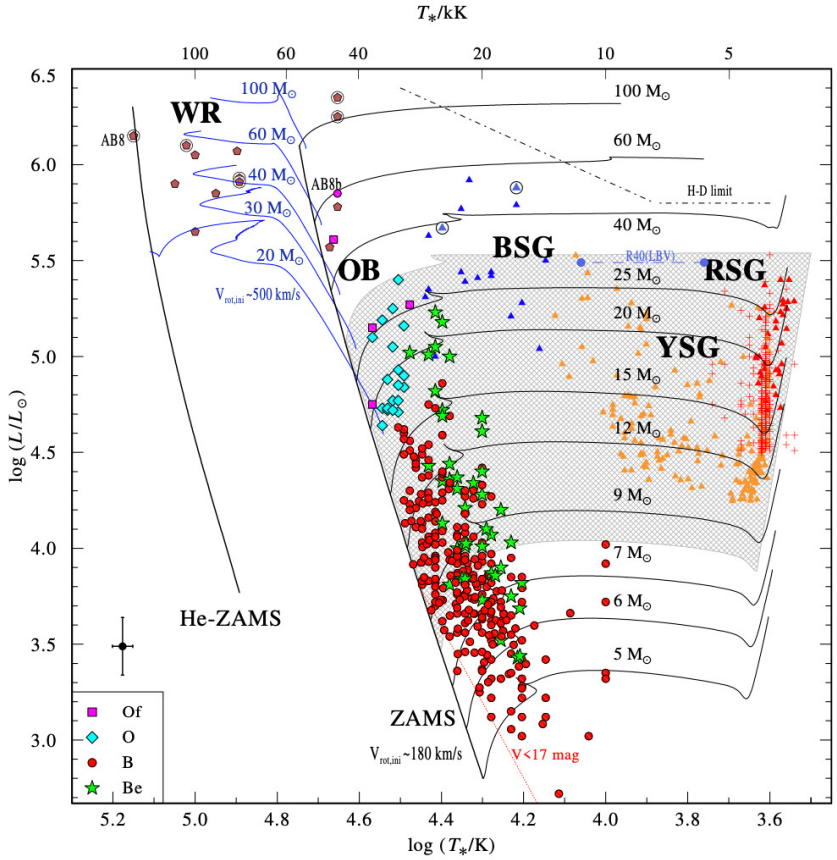

FIGURE 2.1: Hertzsprung Russell diagram for massive stars in the SMC (Millette, 2021) based on the observation of Ramachandran et al. (2019). The brown pentagons represent WR stars (encircled if in a binary system), yellow symbols represent yellow supergiant (YSG) stars, blue triangles for blue supergiant stars (BSG), and red triangles for red supergiant (RSG). Black tracks show standard stellar evolutionary paths, while the blue tracks show the paths of WR stars.

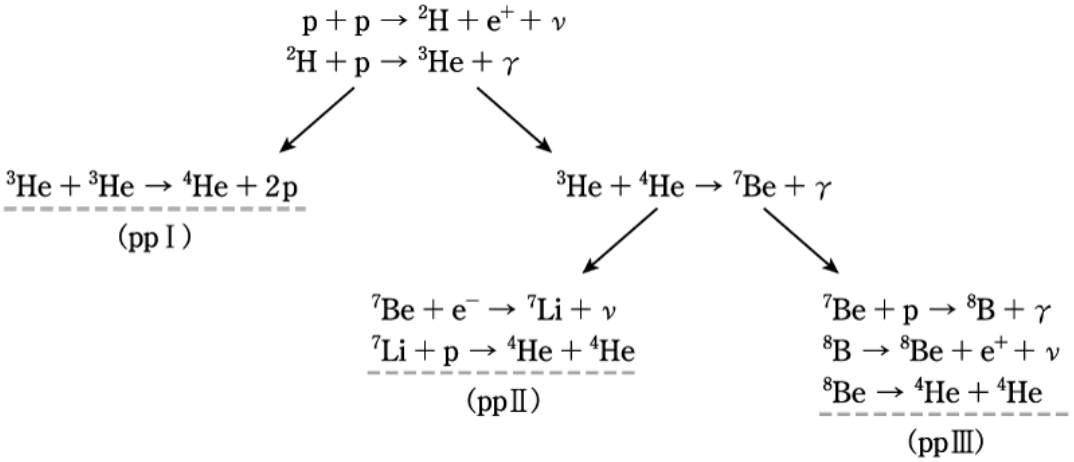

FIGURE 2.2: p–p chain reaction (taken from astronomical dictionary)

2.1.2 Stellar Nucleosynthesis

The stars contract quasi-statically due to self-gravity while maintaining the balance between the pressure gradient force and gravity. Part of the released gravitational energy is released as photons and the rest becomes internal energy. Gradually, the interior of the star becomes hot and dense, and the nuclear fusion reaction of hydrogen begins.

Hydrogen Burning The phenomenon of synthesizing helium nuclei from four hydrogen nuclei (protons) is called hydrogen burning. Hydrogen burning occurs in the core of main-sequence stars with temperatures of $\sim 10^7$ K. Hydrogen burning includes the p–p chain reaction, which is dominant in main-sequence stars of solar mass or less, and the CNO cycle, which is dominant in stars that are more than 1.3 times as massive as the Sun.

In the p–p chain reaction, two protons first become deuterium, and the deuterium reacts with a proton to be ^{3}He. This reaction can be described as

$$\mathrm{p} + \mathrm{p} \rightarrow {}^2\mathrm{H} + \mathrm{e}^+ + \nu \tag{2.1}$$
$$^2\mathrm{H} + \mathrm{p} \rightarrow {}^3\mathrm{He} + \gamma. \tag{2.2}$$

The p–p chain reaction is classified into ppI, ppII and ppIII depending on the subsequent reactions. A summery of these reactions is shown in Figure 2.2.

In the CNO cycle, protons are successively captured by carbon, nitrogen, and oxygen nuclei and become helium nuclei. The series of reactions shown in the following Equations (2.3), (2.4), (2.5), (2.6), (2.7) and (2.8) is the main reaction of the CNO cycle called the CN cycle, and CNO are used as catalysts here.

$$^{12}\mathrm{C} + \mathrm{p} \rightarrow {}^{13}\mathrm{N} \tag{2.3}$$
$$^{13}\mathrm{N} \rightarrow {}^{13}\mathrm{C} + \mathrm{e}^+ + \gamma \tag{2.4}$$

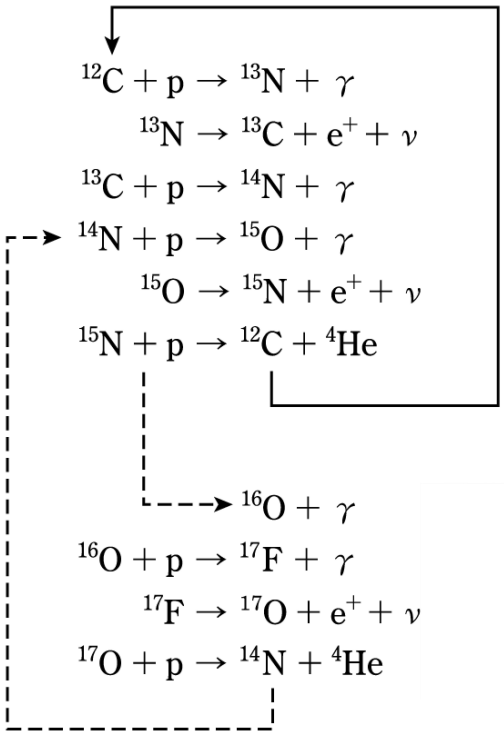

FIGURE 2.3: CNO cycle (taken from astronomical dictionary)

$$^{13}C + p \rightarrow {}^{14}N + \gamma \tag{2.5}$$
$$^{14}N + p \rightarrow {}^{15}O + \gamma \tag{2.6}$$
$$^{15}O \rightarrow {}^{15}N + e^+ + \nu \tag{2.7}$$
$$^{15}N + p \rightarrow {}^{12}C + {}^4He \tag{2.8}$$

The reaction of Equation (2.6) has the following branching reaction.

$$^{15}N + p \rightarrow {}^{15}O + \gamma \tag{2.9}$$

This reaction occurs at a rate of 10^{-4}. In the CNO cycle, there is also reactions called the NO cycle that starts from this reaction. Figure 2.3 summarizes these reactions.

Helium Burning and Fusion of Heavier elements When the central temperature reaches $\sim 10^8$ K, helium is ignited via the triple-alpha process. In the triple-alpha process, three helium nuclei (α particles) fuse to be a carbon nucleus. This process occurs through the two-step reaction shown in Equations (2.10) and (2.11) below.

$$^4He + {}^4He \rightleftharpoons {}^8Be \tag{2.10}$$
$$^8Be + {}^4He \rightarrow {}^{12}C + \gamma \tag{2.11}$$

Since ^{8}Be is unstable, it decays to ^{4}He in $\sim 10^{-16}$ seconds. Therefore, the reaction described as Equation (2.10) is in an equilibrium state, and ^{12}C is

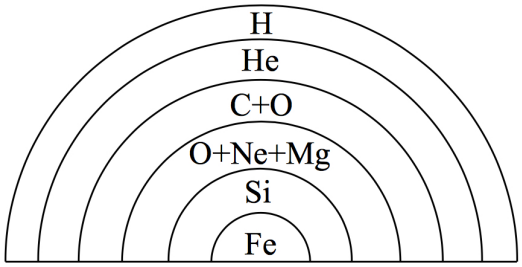

FIGURE 2.4: Onion-like structure in massive stars. (The scale is not exact.)

synthesized from the fusion of ^{4}He with a small amount of ^{8}Be. The ^{12}C produced here reacts with helium to produce ^{16}O.

$$^{12}\mathrm{C} + {}^{4}\mathrm{He} \rightarrow {}^{16}\mathrm{O} + \gamma \tag{2.12}$$

For stars with a mass of $\leq 8\ \mathrm{M}_{\odot}$, the nuclear fusion reaction does not proceed any further and eventually evolves into a white dwarf with a core of carbon and oxygen.

Inside stars with a mass of $\geq 8\ \mathrm{M}_{\odot}$, nuclear fusion reactions of heavier elements take place. When the central temperature reaches $\sim 6 \times 10^{8}$ K, carbon burning occurs, and the carbon nuclei become mainly oxygen, neon, and magnesium. For stars with a mass of $\geq 10\ \mathrm{M}_{\odot}$, oxygen burning subsequently takes place at a central temperature above $\sim 2 \times 10^{9}$ K, producing Si, S, and Ca. At temperatures above $\sim 3 \times 10^{9}$ K, high-energy photons break silicon nuclei, and Fe is synthesized by silicon burning. As a result of these reactions, the star has an onion-like structure as shown in Figure 2.4, at the final stage of its evolution.

2.1.3 Mass Loss of Massive Stars and Their Environment

Massive stars lose a large amount of their mass before their explosion as SNe. Mass loss from massive stars modifies the surrounding medium, forming a dense and inhomogeneous circumstellar medium (CSM). The resulting CSM subsequently affects the evolution of SNRs. Here, for single stars and binary stars, we describe the environmental structure resulting from the mass loss of massive stars during their evolutionary process.

Single Massive Stars

Since massive stars have high luminosity, their envelope is removed as a stellar wind due to high radiation pressure. The mass loss rate and the velocity of a stellar wind differ depending on their evolutionary stage. Here, we explain the evolutionary process of stars and the surrounding environment created by stellar winds of each evolutionary stage. Main sequence stars evolve into various stars, such as red supergiants or Wolf-Rayet stars, depending on their initial mass and metallicity (Figure 2.1), where metallicity is the abundance ratio of heavy elements to hydrogen. Figure 2.5 shows the mass loss rate and

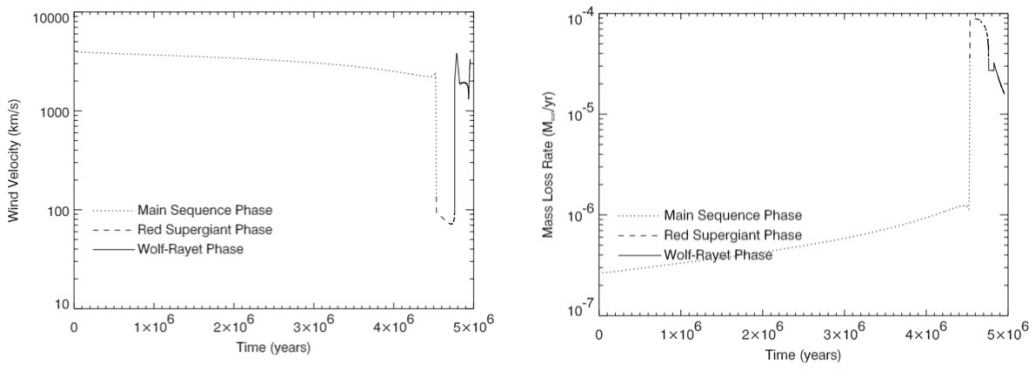

FIGURE 2.5: Evolution of the velocity (left) and mass-loss rate (right) of the wind from the star with time (Dwarkadas et al., 2007).

stellar wind velocity at each evolutionary stage of a star with an initial mass of 35 $M_{\odot}$. This star follows a sequence of evolution from a main sequence star to a red supergiant and finally to a Wolf-Rayet star. Main sequence stars have high stellar wind velocity and low mass loss rate. The stellar wind of a main sequence star expands while sweeping up the surrounding ISM, and forms an ISM shell and main sequence wind bubble. At the RSG phase, contrary to the main sequence star phase, stellar wind velocity is low and the mass loss rate is high. Therefore, the RSG stellar wind forms a dense region inside the main-sequence wind bubble. On the other hand, a WR star has high stellar wind velocity and a high mass loss rate. Consequently, the WR star wind creates a cavity wall inside the CSM produced by the RSG wind. As a result, the final stage of a single massive star's evolution results in an ambient medium with a radially non-uniform density profile, as demonstrated in Figure 2.6.

Binary Stars

Another important mass loss mechanism is "binary interaction". About half of the stars are found in binary systems in which two or more stars revolve around each other. When two stars evolve in a binary system that is close to each other, they mutually change their masses and orbits by exchanging mass and momentum. This process is called "binary interaction". Since it has been reported that almost all O-type stars in the main sequence stage are in binary systems (Sana et al., 2014), binary interaction is an important process for massive stars.

In a binary star system consisting of two stars, the heavier star is called the primary star, and the lighter one is called the companion star. Figure 2.7 (a) shows the gravitational potential created by a binary star in a coordinate system that revolves with the binary star. Figure 2.7 (b)–(d) show a cross sectional view of the potential when the axis passing through the two stars is taken as the x-axis. As stars evolve, there are stages in which the stellar radius expands significantly (such as a RSG). At this time, when the volume

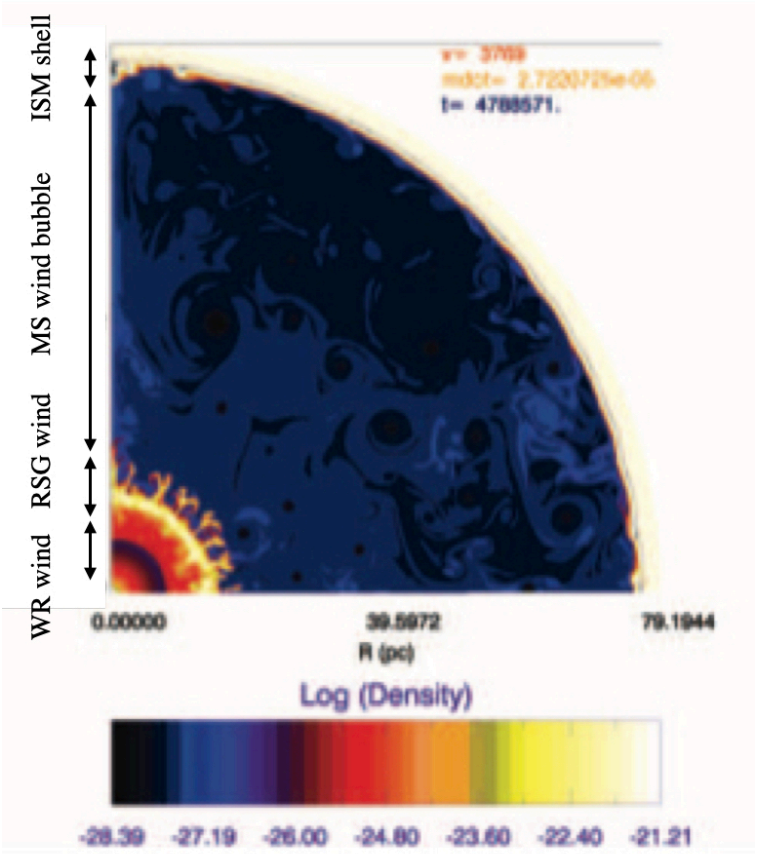

FIGURE 2.6: Density plots of the 2D evolution of the bubble during the WR phase (Dwarkadas et al., 2007).

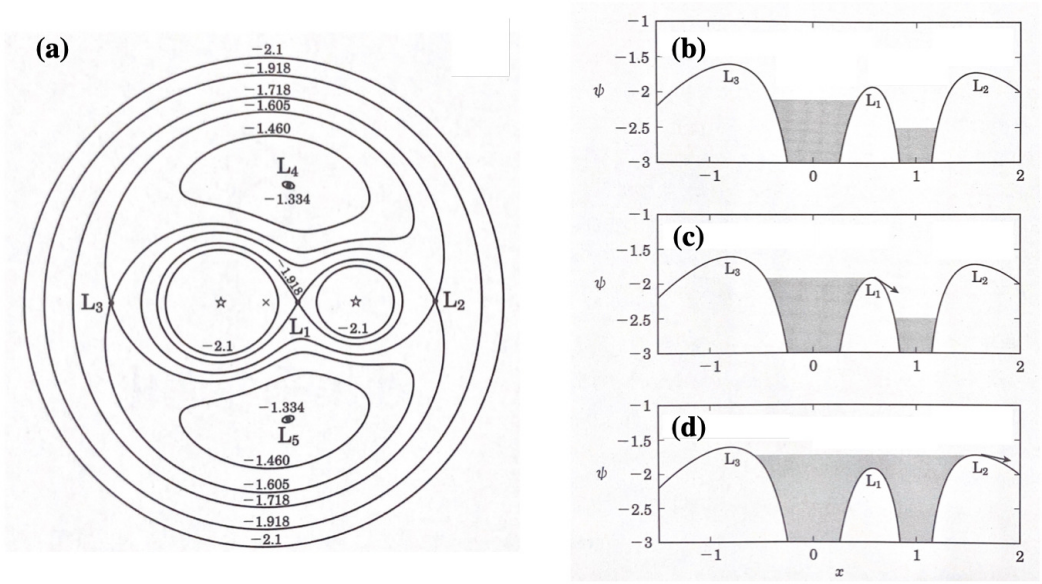

FIGURE 2.7: left: (a) Dimensionless Roche potential contours on the plane of orbit in a binary system with a mass ratio of 2. right: Roche potential and Roche lobe overflow (RLOF) diagrams with the x-axis passing through the two stars on the orbital plane. (b) Neither of the two stars exceeds their own gravitational potential, and no mass transfer occurs. (c) Mass transfer from L1 to the companion star (stable RLOF) as the heavier star expands and exceeds its own gravitational potential. (d) Binary systems have a common envelope.

of the primary star expands beyond its own gravitational potential, its envelope is transferred to the companion star through the L1 point in Figure 2.7 (a). When the mass transfer is relatively slow and the envelope is stably transferred to the companion star, it is called a stable Roche-Lobe overflow (left panel of Figure 2.8). On the other hand, when the mass transfer is fast, the companion star also exceeds its own gravitational potential as shown in Figure 2.7 (d). At this time, the companion star is incorporated into the primary star's envelope, which is called the common envelope. Binaries that form a common envelope undergo mass loss due to stellar winds in the envelope which has a structure extending in the equatorial direction, as shown in the right panel of Figure 2.8. A supernova explosion in such a structure may form a peculiarly shaped SNR, such as that seen in 1987A (see Subsection 2.3.2).

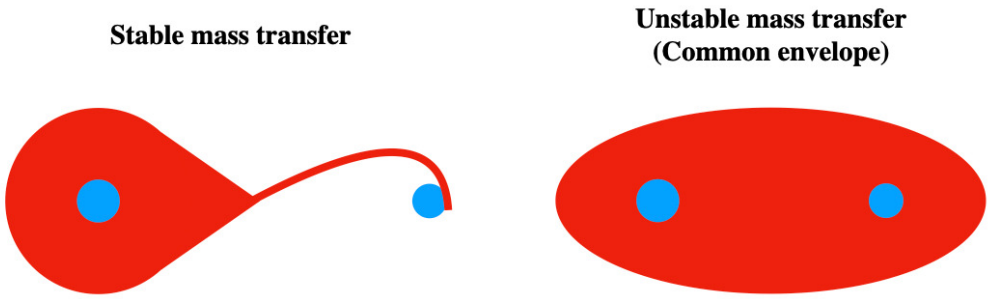

FIGURE 2.8: Schematic view of mass transfer in binary stars

2.2 Supernova

2.2.1 Explosive Nucleosynthesis

Neucleo fusion take place not only in a stellar evolution stage but also in an SN due to explosive burning by the shock wave. The elements synthesized by explosive nuclear fusion depend on the temperature and density. The relation between dominant nucleosynthesis processes and temperature are summarized in table 2.1.

TABLE 2.1: Explosive nucleosynthesis (Thielemann et al., 1996)

Burning Site	Main Products	Ignition temperature [10^9 K]
C/Ne burning	O, Mg, Si, Ne	2.1
O burning	O, Si, S, Ar, Ca	3.3
Incomplete Si burning	Si, S, Fe, Ar, Ca	4
Complete Si burning	Fe, He	5

2.2.2 Classification of Supernova

SNs are classified into several types based on the optical spectra near maximum light. SNs with absorption lines of hydrogen Balmer series in their spectra are classified as type II SNs and ones that do not are called type I SNs. Type I SN is further divided based on the presence or absence of silicon (Si) and helium (He) in their spectra. Type Ia SN contain a Si absorption at 6150 Å, Type Ib has no Si but shows He as an emission signature, and Type Ic has neither. Type II SNs are classified into IIP and IIL types by the shape of their light curves. The main feature of IIP SNs is their plateau-like light curves, while the light curve of SNe IIL is a nearly linear decline. Figure 2.10 shows the optical spectra of type Ia, Ib, Ic, and type II SNs, and Figure 2.11 shows the SN classification. The above classification is not based on the explosion mechanism of SN. SNs are classified into Type Ia SN (Thermonuclear supernova) and Core-Collapse SN based on their explosion mechanism.

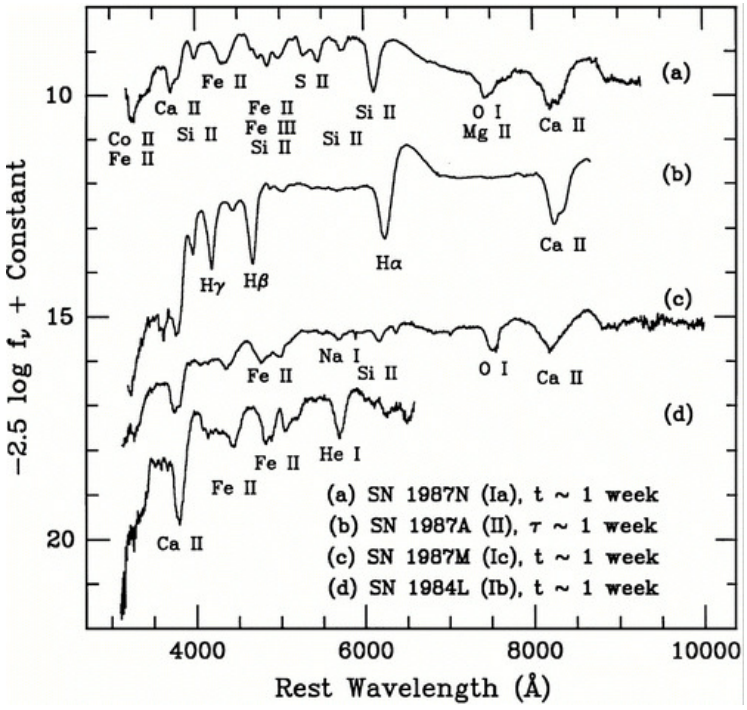

FIGURE 2.9: Optical spectra of SN (Filippenko, 1997).

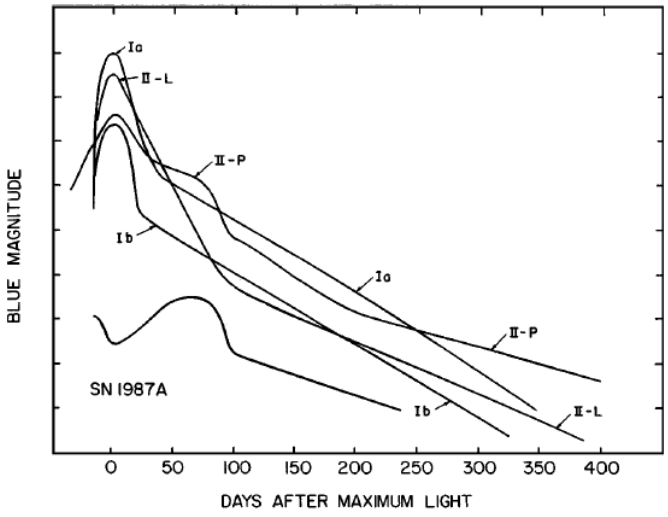

FIGURE 2.10: Light curves of Type Ia, Ib, II-P, and II-L supernovae (Filippenko, 1997).

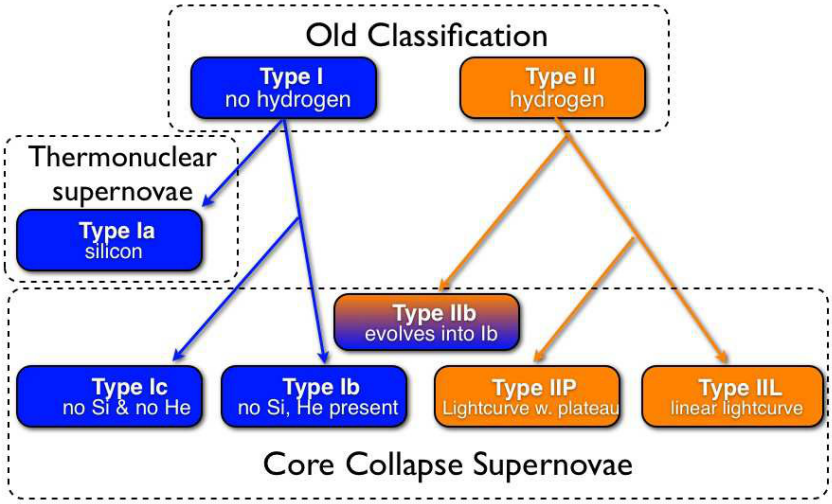

FIGURE 2.11: Classification of SNs (Vink, 2012).

2.2.3 Type Ia SNe

Type Ia supernovae are characterized by no hydrogen absorption lines, and exponentially decaying light curves, and found in old galaxies such as elliptical galaxies. Based on these features, Type Ia SN is thought to be the result of the explosion of a carbon-oxygen white dwarf (e.g., Nomoto, 1982). When a white dwarf reaches Chandrasekhar mass ($\sim 1.4\ M_{\odot}$), it cannot support its own gravity by the degeneracy pressure of electrons. As a result, the white dwarf contracts, the density and temperature of the core increase, and the carbon burning is ignited at the core. These fusion reactions proceed explosively and the white dwarf explodes with the energy of the nuclear reaction released. Since the progenitor is completely distructed by the explosion, no compact objects such as neutron stars or black holes are left at the center. Two scenarios have been proposed for how white dwarfs reach Chandrasekhar mass. One is the accretion of mass from a companion star to a white dwarf in a binary system with a main sequence or a red giant (Single Degenerate model). The other is the merger of two white dwarfs in a binary star system (Double Degenerate model). Recent study suggests that both scenarios are required to explain the elemental abundance of iron peak elements the Perseus cluster (Collaboration, 2017).

2.2.4 Core-collapse SNe

Explosion Mechanism As described in Subsection 2.1.1, massive stars have a Fe core at the final stage of their evolution. Since Fe is a quite stable element, the core can no longer generate nuclear energy. Therefore, the density and temperature increase due to the subsequent contraction. When the temperature of the core exceeds $\sim 3 \times 10^9$ K photo-disintegration of Fe nuclei

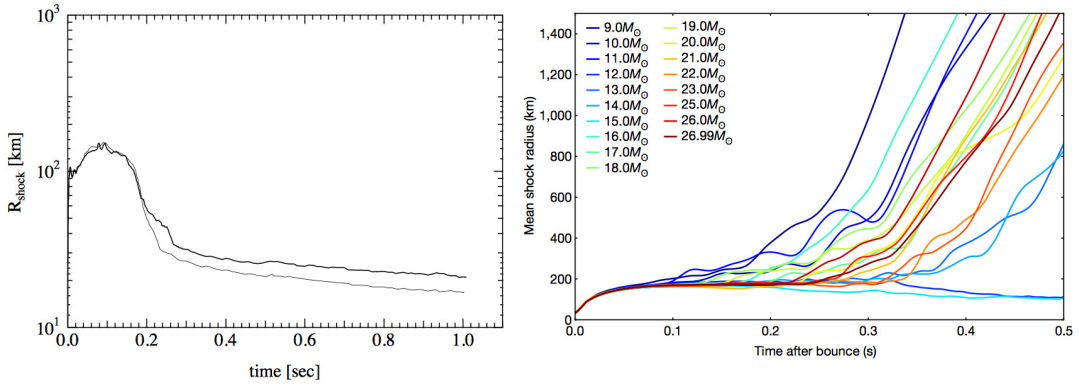

FIGURE 2.12: (left) Radial positions of shock waves as a function of time after bounce by one-dimentional simulation (Sumiyoshi et al., 2005). (right) Mean shock radii of 2D models (Burrows and Vartanyan, 2021). The different colors of the lines represent the mass of the progenitor.

takes place:

$$^{56}\mathrm{Fe} \rightarrow 13\,^{4}\mathrm{He} + 4\mathrm{n} - 124.4\ \mathrm{MeV} \tag{2.13}$$

$$^{4}\mathrm{He} \rightarrow 2\mathrm{p} + 2\mathrm{n} - 28.3\ \mathrm{MeV}. \tag{2.14}$$

Since these processes are endothermic reaction, the pressure of the core decreases and collapses gravitationally. Electron capture takes place in the dense core, and a proto-neutron star is formed.

$$\mathrm{p}^{+} + e^{-} \rightarrow \mathrm{n} + \nu_e \tag{2.15}$$

Falling material bounces at the surface of the proto-neutron star, forming an outward shock wave. This shock wave is called "bounce shock". When the bounce shock reaches the surface of the star, it is observed as an SN.

The bounce shock generally does not reach the surface of the star since the shock stalls by the falling outer material. To revive bounce shocks, an additional mechanism to heat the shock wave is required. A promising process is neutrino heating, but stars in most mas range do not explode in spherically symmetric (one-dimensional) simulation (the left panel of Figure 2.12). Multi-dimensional effects are also the key of the explosion mechanism.

Neutrinos generated in the center of SN heat the inner part of the SN efficiently. The resulting temperature gradient (more precisely, the entropy gradient) creates convection inside the shock wave. Such convection may efficiently carry the energy due to neutrino heating to the location just behind the shock, and the pressure from the vortices generated by the convection also revives the shock wave (e.g., Kifonidis et al., 2003). Meanwhile, convection is not the only promising hydrodynamical instability to revive the shock wave. The standing accretion shock has been recognized to be generically unstable to non-radial deformation. In the stagnant shock front, the perturbation is amplified by the back and forth of sound waves and vortices

between the protoneutron star and the shock wave. This causes the shock wave to distort and vibrate. As a result, the shock wave becomes stronger in the vibrating direction, and the shock wave revives in that direction (e.g., Hanke et al., 2013). Magnetic fields and rotation are also believed to be important asymmetric effects. The magnetic field of the PNS is amplified in the polar direction by the fast rotation (e.g., Takiwaki and Kotake, 2011). This effect causes a jet-like explosion (e.g., Khokhlov et al., 1999). It is promising as a hypernova explosion mechanism because it reproduces high explosion energy reaching 10^{52} erg.

Nucleosysthesis The maximum temperature due to shock wave heating can be estimated as follows. We assume that the inside of the shock wave is filled with uniform radiation and that its energy accounts for most of the explosion energy. At this time, the relationship between the temperature ($T_{\rm max}$) and the radius of the shock wave ($r_{\rm sh}$) is described as:

$$aT_{\rm max}^4 \left(\frac{4\pi}{3} r_{\rm sh}^3\right) = E_{\rm exp}, \tag{2.16}$$

where $E_{\rm exp}$ is the explosion energy, $a = 7.57 \times 10^{-15}$ergs cm^{-3} K^{-4}. Therefore, $T_{\rm max}$ is

$$T_{\rm max} = 1.33 \times 10^{10}{\rm K} \left(\frac{E_{\rm exp}}{10^{51}\ {\rm erg}}\right)^{1/4} \left(\frac{r_{\rm sh}}{10^8\ {\rm cm}}\right)^{-3/4}. \tag{2.17}$$

Therefore, the maximum temperature, which decides the synthesized elements, is lower for the outer layer. Outside the radius of 13000 km, the maximum temperature is below $T \sim 2 \times 10^9$ K, so explosive nucleosynthesis does not occur.

The abundances of the ejected material from SN consists of the elements synthesized by the explosive and stellar nucleosynthesis. The yields of these elements depend sensitively on physical parameter of the progenitor and the details of the explosion mechanism, such as the progenitor mass. Overall the yields of core collapse supernovae are dominated by carbon, oxygen, neon and magnesium, which are products of the various stellar burning phases. The yields of these elements reflect the physical parameter of the progenitor, such as mass and metallicity (Figure 2.13).

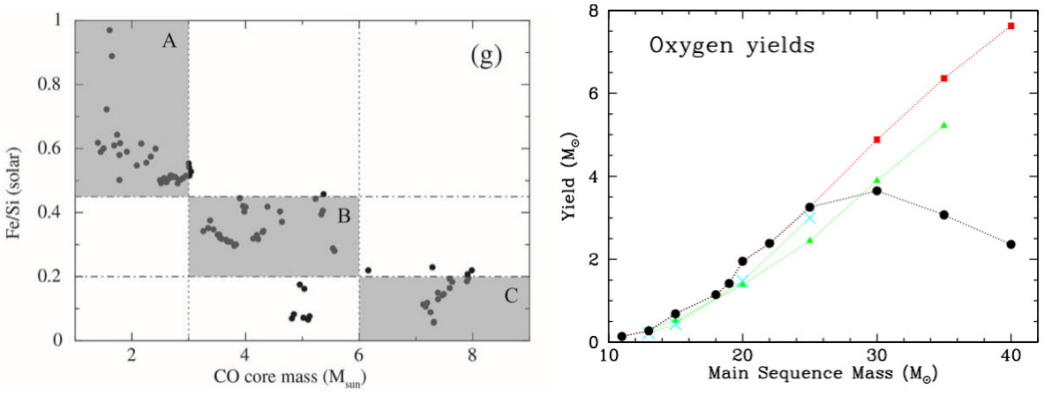

FIGURE 2.13: Relationship between the progenitor mass and abundance. Left: Abundance ratios (Fe/Si) as a function of the CO core mass (Katsuda et al., 2018), based on the nucleosynthesis models by Sukhbold et al., 2016. The abundances are relative to the solar values (Anders and Grevesse, 1989). Right: Oxygen yield of core collapse supernovae as a function of main sequence mass (Vink, 2012). The circles and squares are the predictions of Woosley and Weaver, 1995, the triangles are predictions of Chieffi and Limongi, 2004, and the crosses of Thielemann et al., 1996. In general the oxygen yields obtained by the various groups are very similar, but above 30 $M_{\odot}$ one sees that certain models predict a diminishing oxygen yield. The reason is that above30 $M_{\odot}$ stellar cores may collapse into black holes, and part of the oxygen falls onto the black hole. The amount of fall-back is governed by the explosion energy and the amount of pre-supernova mass loss, but it is also sensitive to the numerical treatment of the explosion.

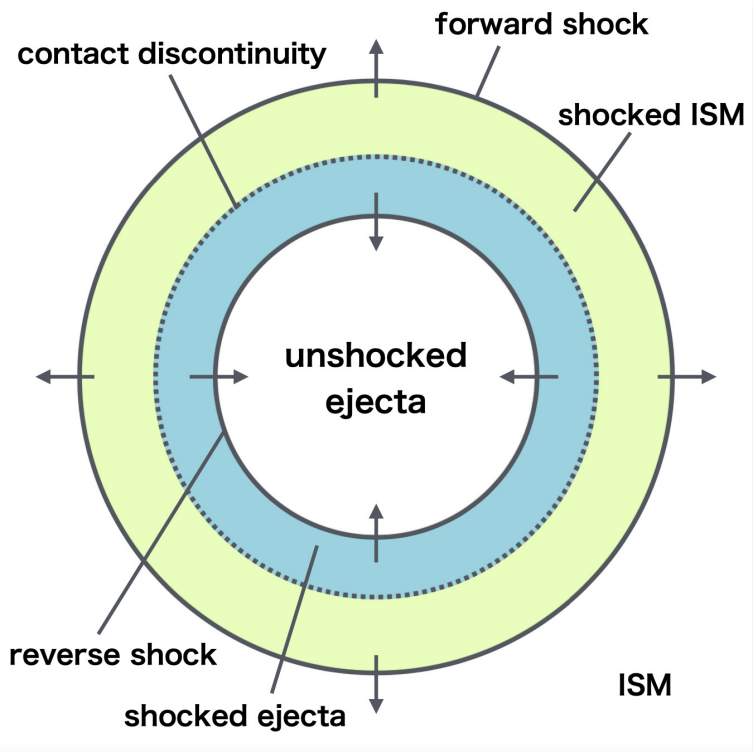

FIGURE 2.14: Schematic image of an SNR.

2.3 Supernova remnant

A supernova remnant (SNR) is an object resulting from a supernova. The SN ejecta expands in the interstellar medium (ISM). The expansion velocity ($\sim 10^4$ km s^{-1}) is much larger than the sound speed in the ISM (~ 10 km s^{-1}), and hence shock wave (blast wave) is generated. The blast wave sweep-ups the surrounding ISM and ionizes them. As the mass of the swept-up ISM increases, the decelerated outer-layer ejecta collides with the inner-layer ejecta, forming an inward shock wave called the reverse shock. As a result, the SNR have the structure shown in Figure 2.14. In this chapter, we explain the overview of physics concerning SNRs: the heating process performed by their shock wave, the macroscopic evolution of SNRs.

2.3.1 Basic Physics of Supernova Remnants

Shock Wave Heating

The relationships between the properties of the upstream and downstream fluids are derived by the conservations of some fluid quantities across the shock. We take a coordinate to be the rest frame of the shock, and define upstream and downstream, as shown in Figure 2.15. The conservations of the mass, momentum, and energy (per unit mass) across the shock are expressed as:

$$\rho_u v_u = \rho_d v_d \tag{2.18}$$

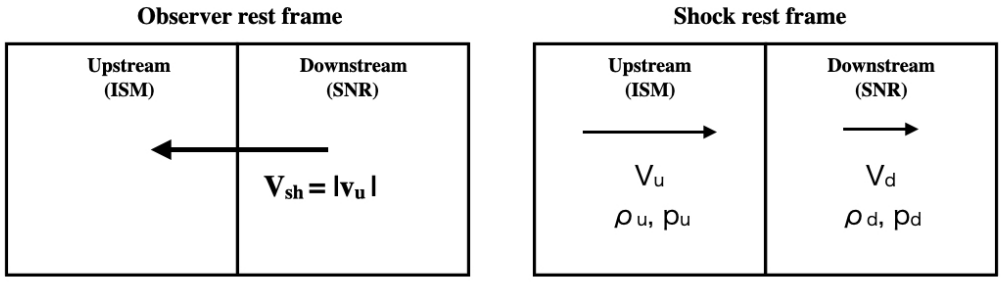

FIGURE 2.15: Schematic view of the shock front in observer rest frame (left) and shock rest frame (right). ρ, v, and P are the density, velocity, and pressure, respectively.

$$\rho_u v_u^2 + P_u = \rho_d v_d^2 + P_u \tag{2.19}$$

$$\frac{1}{2}v_u^2 + \frac{\gamma}{1-\gamma}\frac{P_u}{\rho_u} = \frac{1}{2}v_d^2 + \frac{\gamma}{1-\gamma}\frac{P_d}{\rho_d}, \tag{2.20}$$

where ρ, v, P, are the density, velocity, and pressure of upstream (subscript u) and downstream (subscript d), γ is the specific heat ratio ($\gamma = C_p/C_v$).

The Rankine-Hugoniot equations are obtained as:

$$\frac{P_u}{P_d} = \frac{(\gamma+1)\rho_d - (\gamma-1)\rho_u}{(\gamma+1)\rho_u - (\gamma-1)\rho_d} \tag{2.21}$$

$$\chi \equiv \frac{\rho_d}{\rho_u} = \frac{v_u}{v_d} = \frac{(\gamma-1)P_u + (\gamma+1)P_d}{(\gamma+1)P_u - (\gamma-1)P_d}, \tag{2.22}$$

where χ is the compression ratio. Here we introduce the Mach number of the upstream fluid ($M_u = v_u/c_{su}$), where c_{su} is the sound speed in the upstream fluid. Equations (2.21) and (2.22) can also be expressed as:

$$\frac{P_u}{P_d} = \frac{2\gamma M_u^2 - \gamma + 1}{\gamma + 1} \tag{2.23}$$

$$\chi = \frac{\rho_d}{\rho_u} = \frac{v_u}{v_d} = \frac{(\gamma+1)M_u^2}{(\gamma-1)M_u^2 + 2}. \tag{2.24}$$

For monoatomic gas ($\gamma = 5/3$), assuming the strong shock ($\rho_d/\rho_u \gg 1$),the compression ratio χ is 4. Combining Equations (2.21) and (2.22) with the ideal gas law, we obtain the downstream temperature to be

$$kT_d = \frac{2(\gamma-1)}{(\gamma+1)^2}\mu m_p v_u^2 = \frac{3}{16}\mu m_p v_u^2, \tag{2.25}$$

which corresponds to $\sim$ 1.2 keV ($\sim$ 1.4×10^7 K) for a shock velocity of 1000 km s^{-1} and the solar composition ISM ($\mu \approx 0.6$). We can see in Equation (2.25), the shock heating can be understood as a process that converts a certain fraction of the kinetic energy to internal (thermal) energy.

Evolution of Supernova Remnant

The evolution phase of SNRs can be classified into the following four stages based on the relationship between the mass of the ejecta, $M_{\rm ejecta}$, and the mass of the swept-up ISM, $M_{\rm ISM}$.

1. Free expansion phase
2. Adiabatic (Sedov) phase
3. Radiative cooling phase
4. Disappearance phase

Free expansion phase At the early stage of SNRs evolution, $M_{\rm ISM}$ is much smaller than $M_{\rm ejecta}$. Therefore, the ejecta expands freely. Most of the kinetic energy of the explosion (E) becomes the kinetic energy of the ejecta ($E_{\rm ejecta}$). The velocity ($v_{\rm s}$) and the radius ($R_{\rm s}$) of the blast wave are described as:

$$v_{\rm s} = \sqrt{\frac{2E}{M_{\rm ejecta}}} = 1.0 \times 10^9 \left(\frac{E}{10^{51}\ {\rm erg}}\right)^{1/2} \left(\frac{M_{\rm ejecta}}{M_\odot}\right)^{1/2} \ [{\rm cm\ s^{-1}}] \quad (2.26)$$

$$R_{\rm s} = v_s t, \quad (2.27)$$

where t is the elapsed time since explosion. $M_{\rm ISM}$ become

$$M_{\rm ISM} = \frac{4}{3}\pi R_s^3 \mu m_H n_0, \quad (2.28)$$

where n_0 is hydrogen number density of the ISM. From Equations (2.26), (2.27) and (2.28), the timescale for $M_{\rm ISM} \sim M_{\rm ejecta}$ is

$$t \sim 1.9 \times 10^2 \left(\frac{E}{10^{51}\ {\rm erg}}\right)^{-1/2} \left(\frac{E_{\rm ejecta}}{M_\odot}\right)^{5/6} \left(\frac{\mu}{1.4}\right)^{-1/3} \left(\frac{n_0}{1\ {\rm cm^{-3}}}\right)^{-1/3} \ [{\rm yr}] \quad (2.29)$$

Therefore, this phase typically continues for a few hundred years.

Adiabatic (Sedov) phase When $M_{\rm ISM} \geq M_{\rm ejecta}$, the eject is decelerated by the swept ISM. The SNR expands adiabatically since the energy loss due to radiation is negligible. The Adiabatic stage is also called the Sedov stage, since the exact solution for spherically symmetric shock waves is known as the Sedov-Taylar solution. The shock wave radius ($R_{\rm s}$), velocity ($v_{\rm s}$), and temperature downstream of the shock wave ($T_{\rm s}$) are

$$R_{\rm s} = 4 \times 10^{19} \left(\frac{t}{10^4\ {\rm yr}}\right)^{2/5} \left(\frac{E}{10^{51}\ {\rm erg}}\right)^{1/5} \left(\frac{n_0}{1\ {\rm cm^{-3}}}\right)^{-1/5} [{\rm cm}] \quad (2.30)$$

$$v_{\rm s} = 5 \times 10^7 \left(\frac{t}{10^4\ {\rm yr}}\right)^{-3/5} \left(\frac{E}{10^{51}\ {\rm erg}}\right)^{1/5} \left(\frac{n_0}{1\ {\rm cm^{-3}}}\right)^{-1/5} [{\rm cm\ s^{-1}}] \quad (2.31)$$

$$T_{\rm s} = 3 \times 10^6 \left(\frac{t}{10^4\ {\rm yr}}\right)^{-6/5} \left(\frac{E}{10^{51}\ {\rm erg}}\right)^{2/5} \left(\frac{n_0}{1\ {\rm cm}^{-3}}\right)^{-2/5} [{\rm K}]. \quad (2.32)$$

The Sedov phase continues for tens of thousands of years and converts about 70% of the kinetic energy of the explosion into thermal energy (Chevalier, 1974).

Radiative cooling phase At this stage, radiative cooling is non-negligible. The dense shell cools faster, but the inner region is still hot and under high pressure. Therefore, the outer shell is pushed by the internal gas pressure $P \propto V^{-\gamma}$ where V is the volume of the internal gas. This phase is also called "pressure-driven snowplow" phase. Assuming a non-relativistic monatomic gas ($\gamma = 5/3$), the shock wave expands according to

$$R_s \propto t^{2/7}. \quad (2.33)$$

As the temperature decreases further, the internal pressure is also negligible and the shell expands while conserving momentum ($M_s v_s$). The shock wave radius can be described as

$$R_s \propto t^{1/4}. \quad (2.34)$$

This stage is also called "the momentum-conserving snowplow" stage.

Disappearance phase When the shock wave velocity equals the velocity of the proper motion of the ISM (10–20 km s^{-1}), the SNR loses its boundary and vanishes. This stage is reached on a timescale of $\sim 10^5$ years from the explosion.

2.3.2 Observational View of Supernova Remnants

In the previous section, we explained the evolution of SNRs by spherically symmetric explosions in a homogeneous environment. However, as shown in Figure 2.16, many supernova remnants have spherically asymmetrical morphologies. These morphologies may reflect the asymmetric effects of the explosion and the effects of non-uniform interactions with the surrounding environment, as explained in Section 2. Here we explain the information that can be obtained from such morphologies of SNRs.

Lopez et al., 2011 claims that it is possible to distinguish between type Ia SNR and CC SNR based on their X-ray morphologies. Figure 2.17 shows P_2/P_0 versus P_3/P_0 plot for SNRs in the Milky Way and LMC where P_2/P_0 and P_3/P_0 are parameters that characterize the morphologies of SNRs. P_2/P_0 is the quadrupole ratio. SNRs that have high P_2/P_0 are those with elliptical/elongated morphologies or those with off-center centroids because one side is substantially brighter than the other. P_3/P_0 is the octupole ratio. Examples that have high P_3/P_0 are those that have asymmetric or non-uniform

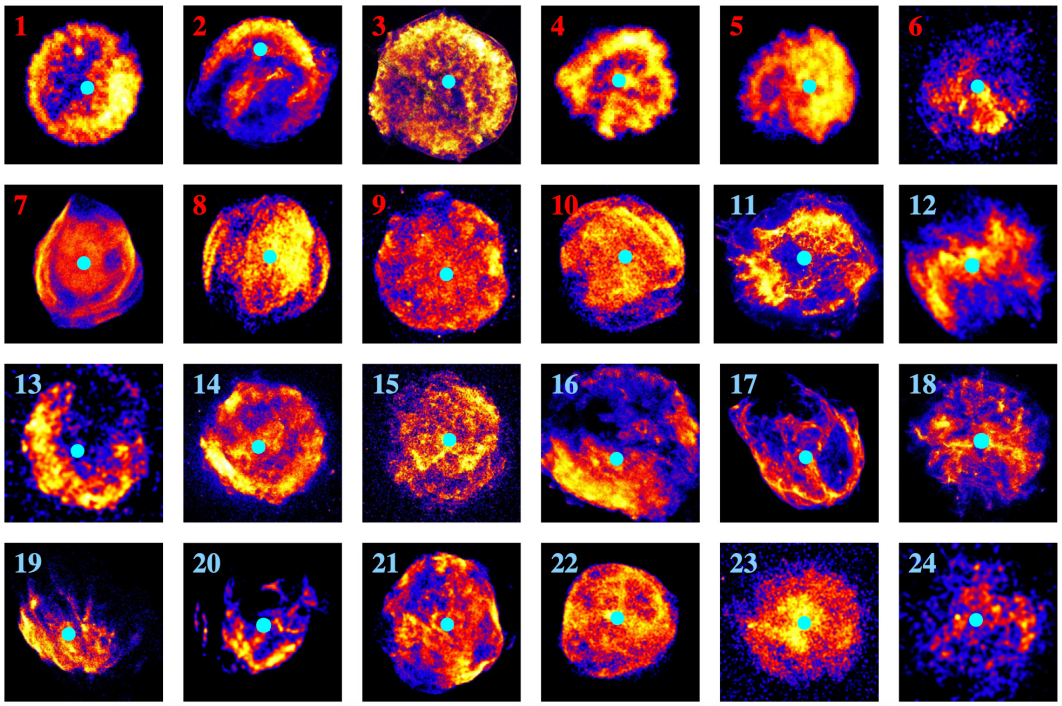

FIGURE 2.16: Chandra X-ray (0.5–2.1 keV) images of the 24 SNRs (Lopez et al., 2011). The cyan circles mark the full-band centroids of each SNR determined by Lopez et al. (2011). Red numbers denote Type Ia SNRs; light blue numbers denote CC SNRs.

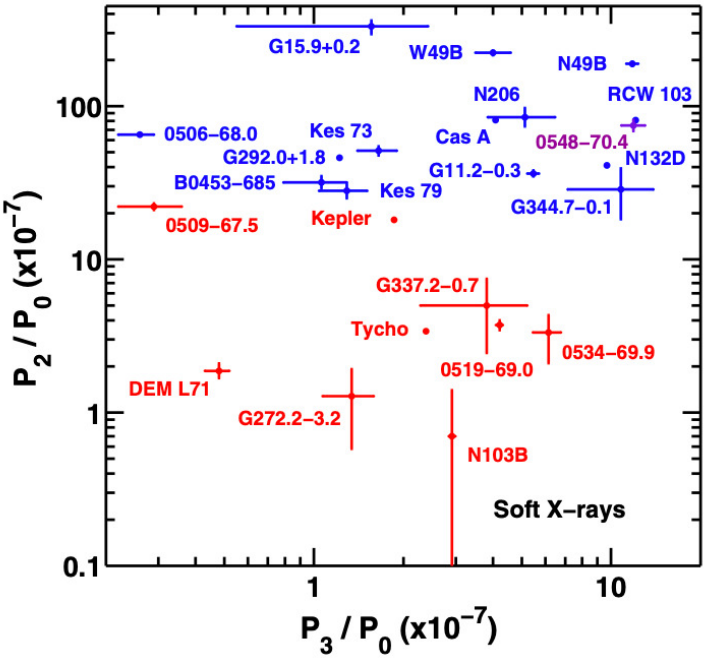

FIGURE 2.17: Power ratios, the quadrupole ratio P_2/P_0 vs. the octupole ratio P_3/P_0, of the soft X-ray band (0.5–2.1 keV) for SNRs in the Milky Way and LMC. Type Ia SNRs are in red, CC SNRs are in blue, and 0548−70.4 is in purple because of its anomalous ejecta properties that make its type uncertain. The quadrupole ratio is a measure of ellipticity/elongation, and the octupole ratio quantifies the mirror asymmetry of the emission.

surface brightness distributions. CC SNRs tend to have a non-spherical symmetry morphologies compared to Type Ia. This is because the progenitor of the CC SNR is a massive star, and non-uniform CSM tends to form around it as we explained in Subsection 2.1.3.

SN 1987A was first detected on February 23, 1987 in the Large Magellanic Cloud. Pre-supernova image shows that the progenitor of SN 1987A is a blue super giant (e.g., White and Malin, 1987). The X-ray emission of SN 1987A has a ring-like structure. The optical observation reveals that there are two rings to the north and south of the X-ray ring. These optical rings are in approximate alignment with the symmetry axis of the inner ring as shown in the right panel of Figure 2.18. The origin of this triple ring nebula is a controversial, but as mentioned in Podsiadlowski, 2017, binary interactions may play an important role. The progenitor of 1987A may be a binary star that evolved in a common envelope. These stars merges to form a blue super giant. The fast blue super giant wind sweep up all the slowly expanding structures that had been ejected previously and produce two dense physical rings at the end of two bipolar caps. This formation scenario for SN1987A is summarized in Figure 2.19.

Convection generated by neutrino heating forms high-entropy bubbles (the left panel of Figure 2.20). Some of the high-entropy bubbles can develop into Rayleigh-Taylor instabilities on a larger scale at late stages of the

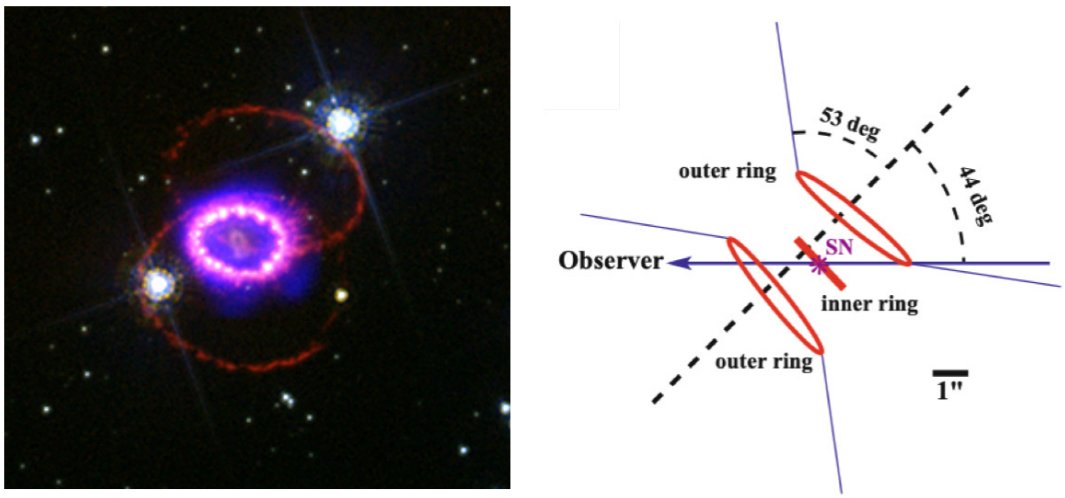

FIGURE 2.18: (right) X-ray and optical image of SN1987A observed with Chandra and HST (taken from Chandra photo album). The purple ring corresponds to X-rays. There are two optical rings to the north and south of the X-ray ring. (left) Schematic view of geometrical model for the triple-ring nebula (Podsiadlowski, 2017).

explosion and penetrate into the hydrogen envelope with large velocities creating iron-dominated plumes. The SNR Cassiopeia A has an Fe-protruding structure that suggests this picture (the right panel of Figure 2.20). Based on the Ti/Fe and Cr/Fe ratio, Sato et al. (2021) revealed that this structure was synthesized in the center of the SN. This result supports the picture of the convective SN explosion mechanism.

As these studies show, the morphology of the SNR has important information about the progenitor and its explosion mechanism. Our objective is to obtain observational evidence for CX and RS from SNRs with high resolution X-ray spectroscopy. This allow us to accurate measure the abundances accurately, as we will discuss later, and also help us to estimate the 3D structure of the SNRs.

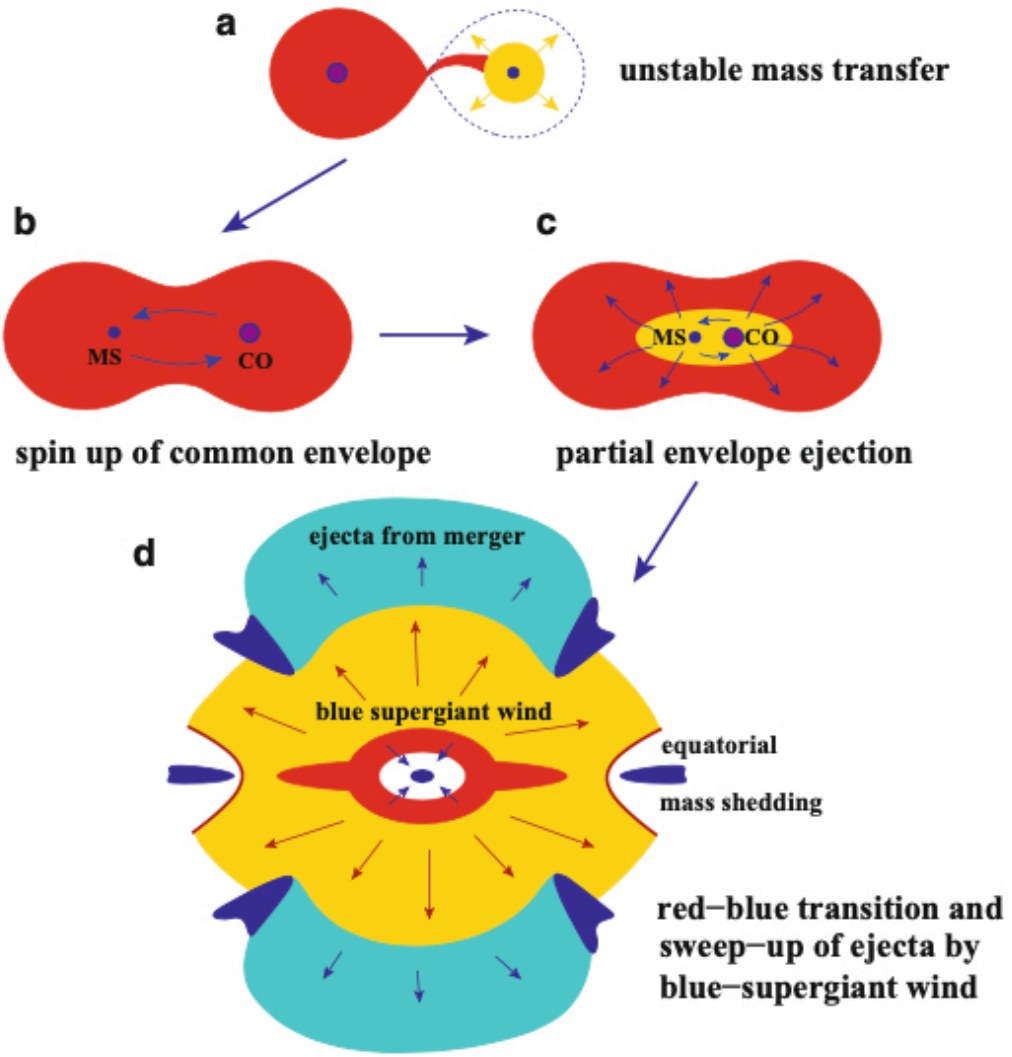

FIGURE 2.19: Schematic image of the formation of the triple-ring nebula (Podsiadlowski, 2017).

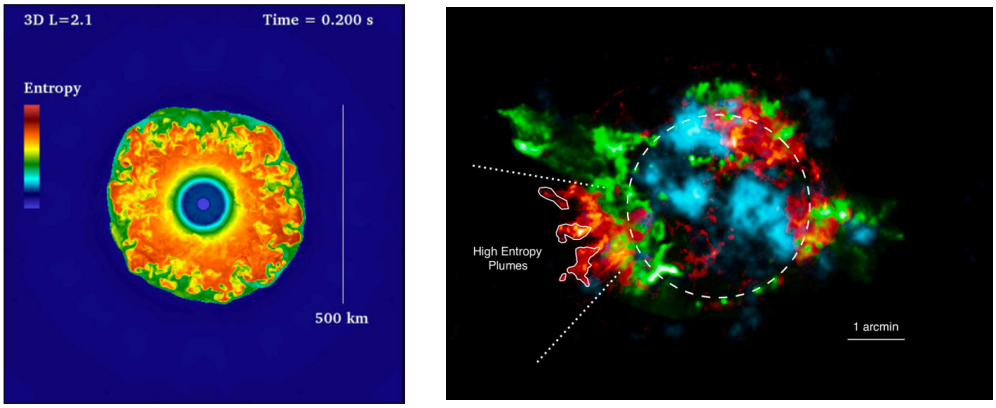

FIGURE 2.20: (left) 3D simulation of SN (Burrows et al., 2012). Convection is induced by neutrino heating. (right) Distribution of heavy elements in Cassiopeia A (Sato et al., 2021). The iron ejecta are shown in red. The Chandra ratio map of the Si/Mg band is shown in green. The ^{44}Ti observed by NuSTAR is shown in blue.

Chapter 3

Plasma Processes and X-ray Radiation in Collisionally Ionized Plasma

3.1 Collisionally Ionized Plasma

As explained in Chapter 2.1, hot gas ($\sim$ 1–5 keV) is produced by the shock wave heating. Free electrons in such hot gases have enough energy to remove electrons bound in inner- or outer-shell of heavy elements in the gases (see Figure 3.1). As a consequence, heavy elements in SNRs are ionized via free electron collision. Such plasma is called Collisionally Ionized Plasma (CIP). The properties of CIP can be investigated through spectral diagnostics of thermal X-ray emission, which is characterized by atomic emission lines and continuum emission components. In this section, we explain the ionization and recombination processes that take place in CIP and introduce the concept of ionization equilibrium. We also summarize X-ray radiation processes of CIP.

3.1.1 Ionization and Recombination

Ionization and Recombination Processes

In the CIP, four distinct ionization processes occur, each of which has a corresponding recombination process (reverse reaction), as summarized below.

$$\begin{aligned}
\text{Collisional ionization} &\rightleftharpoons \text{Three-body recombination} \\
\text{Collisional excitation auto-ionization} &\rightleftharpoons \text{Dielectronic recombination collisional deexcitation} \\
\text{Photo ionization} &\rightleftharpoons \text{Radiative recombination} \\
\text{Photo excitationauto-ionization} &\rightleftharpoons \text{Dielectronic recombination}
\end{aligned}$$

Figure 3.2 shows a schematic image of each process. When the plasma density is enough high, these ionization and recombination processes balance each other. However, SNR plasmas have low density ($\sim 1\ \mathrm{cm}^{-3}$) and are basically optically thin. Therefore these individual reactions are not balanced. While there are exceptions, SNR plasmas generally satisfy the following conditions.

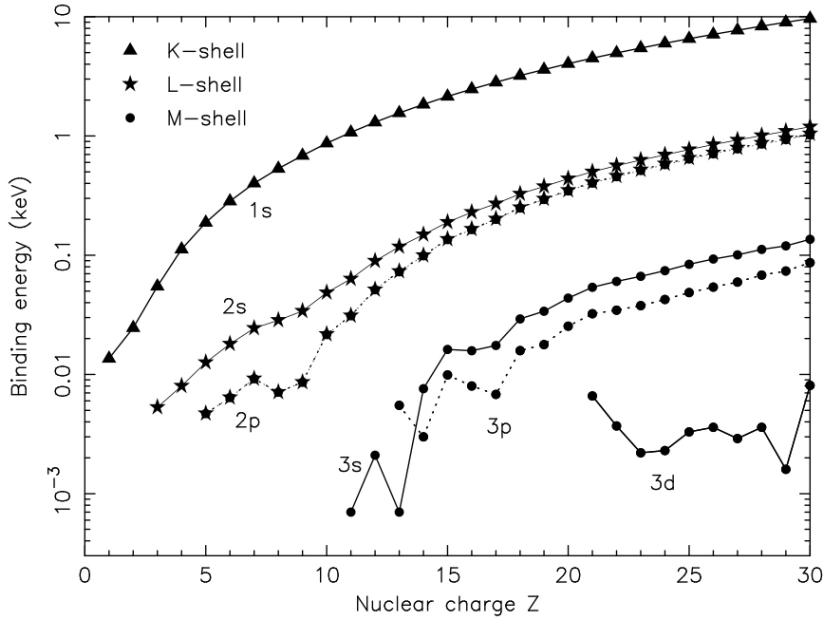

FIGURE 3.1: Binding energy of atomic subshells for neutral atoms (Kaastra et al., 2008).

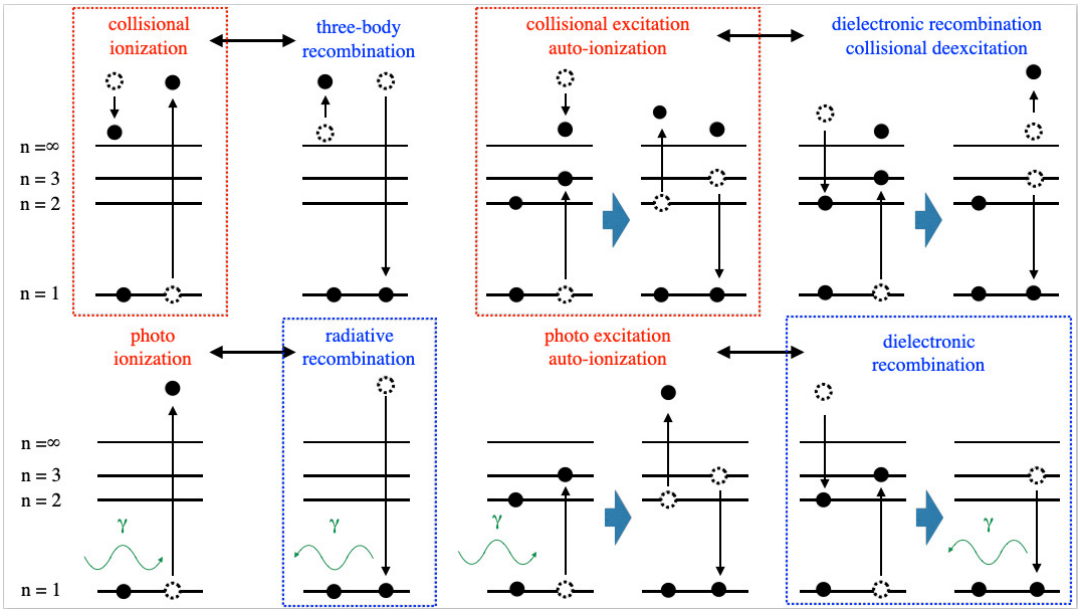

FIGURE 3.2: Ionization and recombination processes in CIP. Horizontal lines represent energy levels, and above $n = \infty$ is the free electron energy region. Ionization processes are shown in red, and recombination processes are shown in blue. The dashed lines indicate processes that are important in plasmas of SNRs.

1. The plasma is optically thin. Therefore, photons emitted by the plasma are not attenuated by self-absorption and do not excite or ionize atoms.
2. Due to the low plasma density, the number of excited-state atoms is negligible compared to that of ground-state atoms.

As a result, photoionization and photoexcitation autoionization are negligible in SNR plasma. Additionally, three-body reactions (such as three-body recombination and Dielectronic recombination collisional deexcitation) are also negligible due to the low density. Below is an overview of the important processes that take place in SNRs.

Collisional ionization Collisional ionization is a process in which free electrons interact with ions through inelastic collisions. When a bombarding free electron has higher kinetic energy than the binding energy of the target electron bound in the ion (A^{+q} in Equation (3.2)), the bound electron can be removed. This process is described as:

$$A^{+q} + e^- \rightarrow A^{+(q+1)} + 2e^-. \tag{3.1}$$

The collisional ionization cross section is described by the equation published by Lotz, 1968:

$$\sigma = 4.5 \times 10^{-20} \frac{N_e \log(E/I)}{EI} \text{ cm}^2, \tag{3.2}$$

where E is a kinetic energy of an electron, I is the binding energy of the atomic shell, and N_e is the total number of electrons bound to the shell. The cross section mainly depends on the energy of the free electron. The cross-section is zero when the kinetic energy of the free electron is lower than the binding energy, but increases as the kinetic energy exceeds the binding energy. It reaches a maximum value when the free electron energy is roughly three to four times the binding energy (e.g., Gillaspy, 2001).

Collisional excitation auto-ionization In the case where $E < I$, ionization can still occur through a collisional excitation auto-ionization. This process can be described as follows. An electron bound to a shell is excited to a higher state by a free electron collision. The electron is then removed from the ion through an Auger transition. The resulting vacancy is then filled by another electron from the outermost shell. In this case, energy conservation requires that the excited electron originated from an inner shell. This process is described as:

$$A^{+q} + e^- \rightarrow A^{+q*} + e^- \rightarrow A^{+(q+1)} + 2e^-, \tag{3.3}$$

where A^{+q} means the excited state of the ion.

Radiative recombination Radiative recombination is a process where a free electron is captured by an ion and a photon is emitted simultaneously. This

process is the inverse process of photo ionization described as:

$$\mathrm{A}^{+(q+1)} + e^- \rightarrow \mathrm{A}^{+q} + h\nu \tag{3.4}$$

The energy of the emitted photon is defined as:

$$E_\gamma = E_{kin} - E_{bind}. \tag{3.5}$$

Radiative recombination is also important process as an X-ray radiation process.

Dielectronic recombination Another recombination process is dielectronic recombination. When an electron with a certain kinetic energy is captured in an ion, part of the kinetic energy of the electron is non-radiatively transfersed to a bound electron, which cause an excitation of the bound electron. This process is described as:

$$\mathrm{A}^{+(q+1)} + e^- \rightarrow \mathrm{A}^{+q**} \rightarrow \mathrm{A}^{+q} + h\nu, \tag{3.6}$$

where A^{+q**} means the doubly excited state of the ion. When the excited ion relaxes to an energetically lower state, a photon is emitted. This process is a resonance process, which tends to take place when the kinetic energy of the free electrons is equal to the energy required to excite a bound electron.

Ionization Distribution

When the electron temperature in the SNR plasma becomes sufficiently high, atoms are gradually ionized through several processes described in Subsubsection 3.1.1.1. Finally, SNR plasmas reach an ionization equilibrium state in which ionization and recombination are balanced. Here, we describe the time evolution of the ionization distribution in CIP and explain the concepts of collisional ionization equilibrium (CIE) and ionization non-equilibrium ionization (NEI). Then, we explain the standard picture of plasma evolution in SNRs and the origin of recombining plasmas, which is an ionized state that challenges this standard picture.

Time evolution of the charge number distribution of ions (ionization distribution) in CIP is given as

$$\frac{1}{n_\mathrm{e}}\frac{dN_{Z,z}}{dt} = N_{Z,z-1}S_{Z,z-1}(T_\mathrm{e}) - N_{Z,z}(S_{Z,z}(T_\mathrm{e}) + \alpha_{Z,z}(T_\mathrm{e})) + N_{Z,z+1}\alpha_{Z,z+1}(T_\mathrm{e}), \tag{3.7}$$

where n_e is the number density of electron, $N_{Z,z}$ is the number density of ions with atomic number Z and charge number $+z$, $S_{Z,z}$ and $\alpha_{Z,z}$ are rate coefficient of ionization and recombination, both of which depend solely on the electron temperature (T_e). Therefore, ionization distribution of CIP is detremined by the electron temperature (T_e), the number density of electron (n_e), and time (t) which corresponds to the elapsed time from shock wave heating in the case of SNRs. From condition 2 in Subsubsection 3.1.1.1, only ions

in the ground state are included when Equation (3.2) is calculated. Therefore, Equation (3.2) is the time-dependent equation of the (Z+1)-dimensional vector.

Collisional Ionization Equilibrium (CIE) The equilibrium state of ionization and recombination in CIP is called Collisional Ionization Equilibrium (CIE). The ionization distribution of each element in CIE plasma can be calculated by giving the following two conditions to Equation (3.7).

$$\frac{1}{n_{\rm e}}\frac{dN_{Z,z}}{dt} = 0 \tag{3.8}$$

$$N_Z = \sum_{z=0}^{z=Z} N_{Z,z} \tag{3.9}$$

N_Z is the number density of atoms with atomic number Z. The ionization distribution of each ion is

$$N_{Z,0} = N_Z[1 + \sum_{k=1}^{Z}\prod_{j=0}^{k-1}(\frac{S_{Z,j}(T_{\rm e})}{\alpha_{Z,j+1}(T_{\rm e})})] \tag{3.10}$$

$$N_{Z,k} = N_{Z,0}\prod_{j=0}^{k-1}(\frac{S_{Z,j}(T_{\rm e})}{\alpha_{Z,j+1}(T_{\rm e})})\ (k \geq 1). \tag{3.11}$$

According to Equation (3.10) and (3.11), the ionization distribution of each ion can be determined by the electron temperature ($T_{\rm e}$). Figure 3.3 shows the relation between the ionization distribution and electron temperature. The electron temperature of a typical SNR is about 0.1 – 2.0 keV. As shown in the upper panel of Figure 3.3, relatively light elements, such as O, exist stably in an ionized state of He-like (i.e., the state with two bound electrons) with a closed K-shell structure in CIE plasma with an electron temperature of 0.1–2.0 keV. On the other hand, heavy elements, such as Fe, remain stably in a Ne-like state (i.e., the state with 10 electrons) with a closed L-shell structure.

Non-Equilibrium Ionization(NEI) The state in which the ionization rate and the recombination rate are not balanced is called non-equilibrium ionization (NEI). Furthermore, the NEI plasma is classified into the following two types of plasma.

- Ionizing Plasma (IP)
  A plasma that is in a lower ionization state (closer to neutral state) than the CIE plasma. The ionization rate is higher than the recombination rate, and ionization progresses toward the CIE state.

- Recombining Plasma (RP)
  Contrary to the IP, plasmas in a higher ionization state than the CIE plasma in which recombination process is dominant.

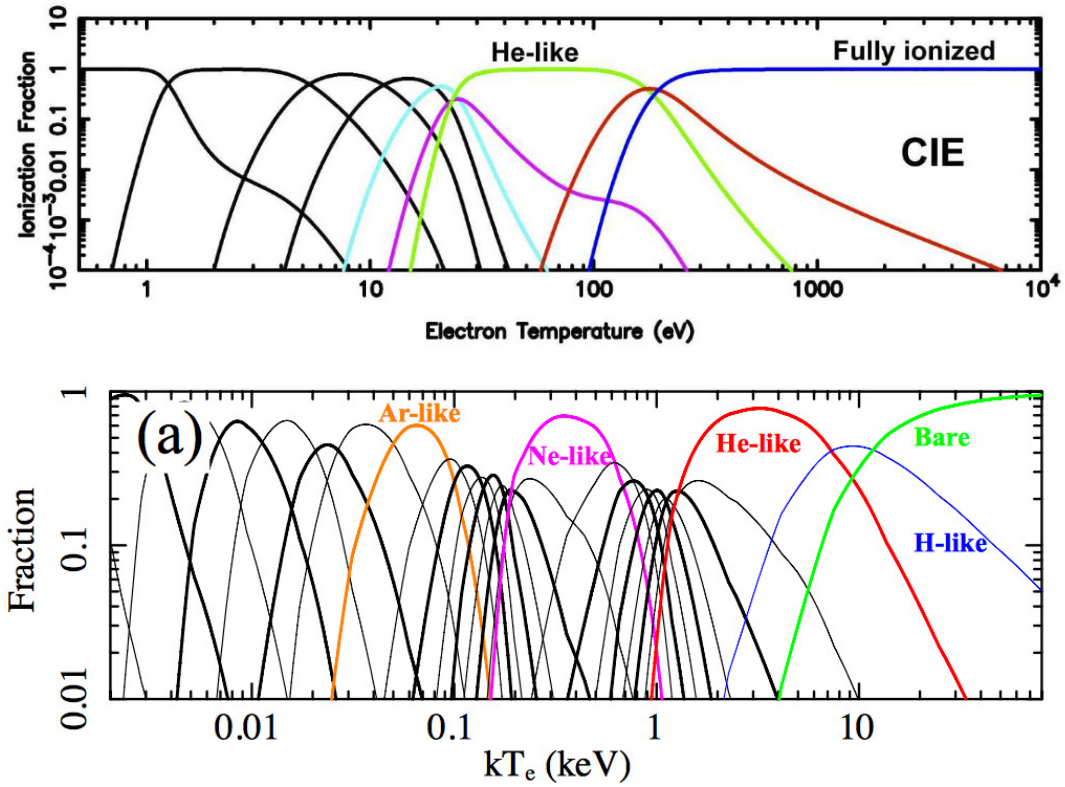

FIGURE 3.3: Ionization distribution of CIE plasma. The horizontal axis corresponds to the electron temperature. The vertical axis corresponds to ion fraction ($N_{Z,z}/N_Z$). The upper panel shows that of oxygen ions (Vink, 2012). Solid lines represent ion fractions of O^{+8} (blue), O^{+7} (brown), O^{+6} (yellow-green), O^{+5} (purple), and O^{+4} (cyan), respectively. The bottom panel shows that of iron ions (ASTRO-H White paper). Colored solid lines represent ion fractions of Fe^{+26} (yellow-green), Fe^{+25} (blue), Fe^{+24} (red), Fe^{+16} (magenta), and Fe^{+8} (orange).

From Equation (3.7), the ion fraction of IP is a function of n_e and t. Masai, 1994 computed the timescale for the plasma to reach the CIE from the neutral state as:

$$n_e t \sim 10^{12}\ \mathrm{cm}^{-3}\ \mathrm{s}. \tag{3.12}$$

Therefore, the t is

$$t \sim 10^{12} \left(\frac{1\ \mathrm{cm}^{-3}}{n_e}\right)\ s \sim 3 \times 10^4 \left(\frac{1\ \mathrm{cm}^{-3}}{n_e}\right)\ \mathrm{yr}. \tag{3.13}$$

SNR plasma is often IP because this timescale is comparable to or longer than SNR ages.

The standard evolution scenario of SNR plasma has been established based on the above theoretical calculation and observational studies. IP is observed in young SNRs such as Cas A and Tycho (e.g., Tsunemi et al., 1986), and CIE is observed in relatively old SNRs (e.g., Sato et al., 2016). Therefore, in the standard scenario of SNR plasma evolution, the SNR plasma is considered to evolve from the initial low ionization state IP to CIE. Therefore, the RP has not been considered in the standard scenario of SNR plasma evolution. However, a recent studies using an X-ray CCD detector revealed that the SNR plasma can be the RP (e.g., Kawasaki et al., 2002). To date, RP have been discovered in more than 10 SNRs, and two theories have been proposed as the origin of RP. One is rapid cooling due to adiabatic expansion of the SNR (Itoh and Masai, 1989), and the other is cooling due to thermal conduction with surrounding dense gas (Kawasaki et al., 2002). A recent study found a clear correlation between the ionization state and electron temperature from W49B (Yamaguchi et al., 2018) and W44 (Okon et al., 2020), confirming that both adiabatic expansion and thermal conduction are the origins of RP. In both cases, RP is caused by rapid plasma cooling due to interaction with the dense inhomogeneous surrounding environment.

3.1.2 Atomic Structure and Radiation Processes

Atomic Structure

As can be seen from Figure 3.3 and 3.4, SNRs include ions with multiple electrons in their orbits. Line emissions from SNRs is due to the orbital transitions of the electrons bound to these ions. Here we describe the atomic structure and the selection rules for electron transitions, that help us derive plasma properties from line emissions.

Energy Level of Single-electron Atoms The energy level of single-electron atoms can be characterized by solving the Schrödinger equation of a single electron in the central field created by an atomic nucleus. The resulting energy level is defined by the principal quantum number (n), the azimuthal quantum number (l), and the magnetic quantum number (m). Here, l and m

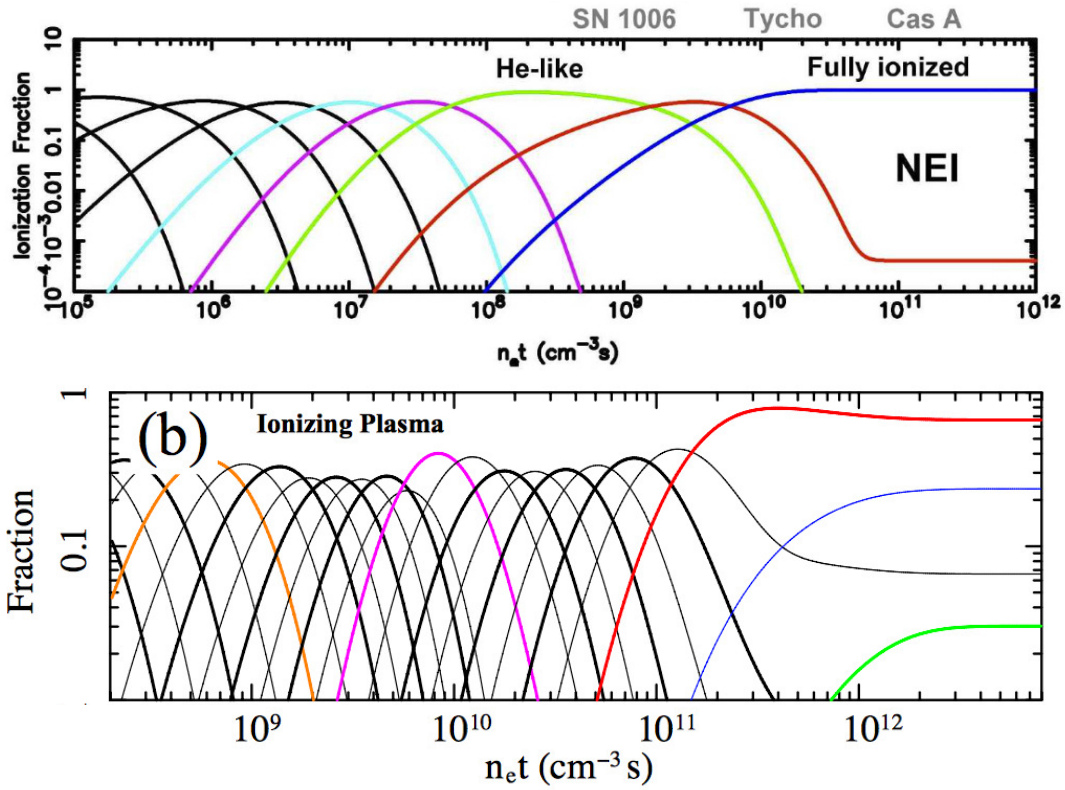

FIGURE 3.4: Ionization distribution of IP. The horizontal axis corresponds to the ionization timescale ($n_e t$). The vertical axis corresponds to ion fraction ($N_{Z,z}/N_Z$). The upper panel shows that of oxygen ions (Vink, 2012). Solid lines represent ion fractions of O^{+8} (blue), O^{+7} (brown), O^{+6} (yellow-green), O^{+5} (purple), and O^{+4} (cyan), respectively. The bottom panel shows that of iron ions (ASTRO-H White paper). Colored solid lines represent ion fractions of Fe^{+26} (yellow-green), Fe^{+25} (blue), Fe^{+24} (red), Fe^{+16} (magenta), and Fe^{+8} (orange).

are the following values.

$$l = 0, 1, 2, \ldots, n-1 \tag{3.14}$$
$$m = -l, -l+1, \ldots, 0, \ldots, l-1, l \tag{3.15}$$

Additionally, the total angular momentum quantum number, j, is introduced, taking into account the interaction between the electron's spin and orbital motion (known as spin-orbit interaction). j is the following value depending on the direction of spin and angular momentum.

$$|l - s| \leq j \leq l + s \tag{3.16}$$

Without a strong external magnetic field, the energy level of the electron is determined by n, l and m. The principal quantum number, n, corresponds to the distance between the atomic nucleus and the electron. Orbitals with $n = 1, 2, 3, \ldots$ are referred to as the K-shell, L-shell, M-shell, and so on. The photon emitted by the electron transition from $n = 2$ to $n = 1$ is called the Kα line, while the transition from $n = 3$ to $n = 1$ is known as the Kβ line. Photons emitted by electron transition from $n > 3$ to $n = 1$ are called Kγ, Kδ, ..., respectively.

Energy Level of Multi-electron Atoms In the case of multi-electron atoms, as with single-electron atoms, the energy levels of individual electrons bound by the central-field created by atomic nuclei are defined by the principal quantum number (n), the orbital quantum number (l), and the total angular momentum quantum number (j) (independent particle approximation). Furthermore, the electron-electron Coulomb interaction has to be considered to determine the energy levels of multi-electron atoms. Therefore, we introduce the total angular momentum **J**, which is the sum of the spins and orbital angular momentum of all electrons.

For atoms with small atomic numbers ($Z < 30$) observed in X-ray astronomy, the spin-orbit interaction is weaker than the Coulomb interaction between electrons. The energy levels of such atoms can be well described under the assumption of LS coupling (Russell-Saunders coupling). In the LS coupling scheme, we first consider the total orbital angular momentum **L** and the total spin angular momentum **S** expressed as Equation (3.17) and (3.18). The **L** and **S** are the sum of orbital angular momentum (**l**) and spin angular momentum (**s**) of all electrons, respectively.

$$\mathbf{L} = \sum_i \mathbf{l_i} \tag{3.17}$$
$$\mathbf{S} = \sum_i \mathbf{s_i} \tag{3.18}$$

Multi-electron atoms have energy levels classified by the **L** and **S**. The total angular momentum **J** is the sum of the total orbital angular momentum **L**

and the total spin angular momentum **S** expressed as:

$$\mathbf{J} = \mathbf{L} + \mathbf{S} \tag{3.19}$$

The energy difference between the energy levels due to the difference in **J** is smaller than that due to **L** and **S** (see Figure 3.9).

In the LS coupling scheme, using the quantum number of **J**, **L**, and **S**, the state of the atom is expressed as:

$$^{2S+1}\mathrm{L}_J, \tag{3.20}$$

where $L = 0, 1, 2, 3, 4, 5, 6, \ldots$ are written as S, P, D, F, G, H, I, ..., respectively.

Selection Rule Under the assumption of LS coupling, selection rules of electric dipole transition are described as below.

$$\Delta S = 0 \tag{3.21}$$
$$\Delta L = 0, \pm 1 \tag{3.22}$$
$$\Delta J = 0, \pm 1 \text{ (except for } J = 0 \rightarrow 0) \tag{3.23}$$

Transitions that satisfy the selection rules are called allowed transitions, and those that do not are called forbidden transitions. Allowed transitions have high transition probabilities, and line emission due to allowed transitions is generally observed prominently in X-ray spectra of astronomical objects.

Radiation Processes

The X-ray spectrum of the thermal plasma in supernova remnants consists of continuum emissions due to scattering and recombination of free electrons, and line emissions due to state transitions of atoms. Photo ionization/excitation processes are negligible since the supernova remnant plasma is optically thin. Due to their low density, atoms in an excited state de-excite through spontaneous emission before the next collision. Therefore, the processes summarized in Figure 3.5 are the main X-ray emission processes in SNRs. Here, we outline each process. In particular, for line emission, we introduce emissivity, which is an important physical quantity that determines the observed flux of line emission.

Line Emission

The emissivity $J^{lk}_{Z,z}$ (pthoton cm^{3}s^{-1}) in a spectral line $k \rightarrow l$ emitted by ions of Z^{+z} in an optically thin plasma can be written as:

$$J^{lk}_{Z,z} = [S^{\mathrm{II}}_{z-1}\,\eta_{z-1} + (S^{E/IE}_z + \alpha^{DRS}_z)\eta_z + (\alpha^{RR}_{z+1} + \alpha^{DR}_{z+1})\eta_{z+1}], \tag{3.24}$$

where S^{II}_{z-1} and $S^{E/IE}_z$ are the rate coefficients (cm^3 s^{-1}) of the innershell ionization (II) of ion $Z^{+(z-1)}$ and excitation (E) or inner shell excitation (IE) of

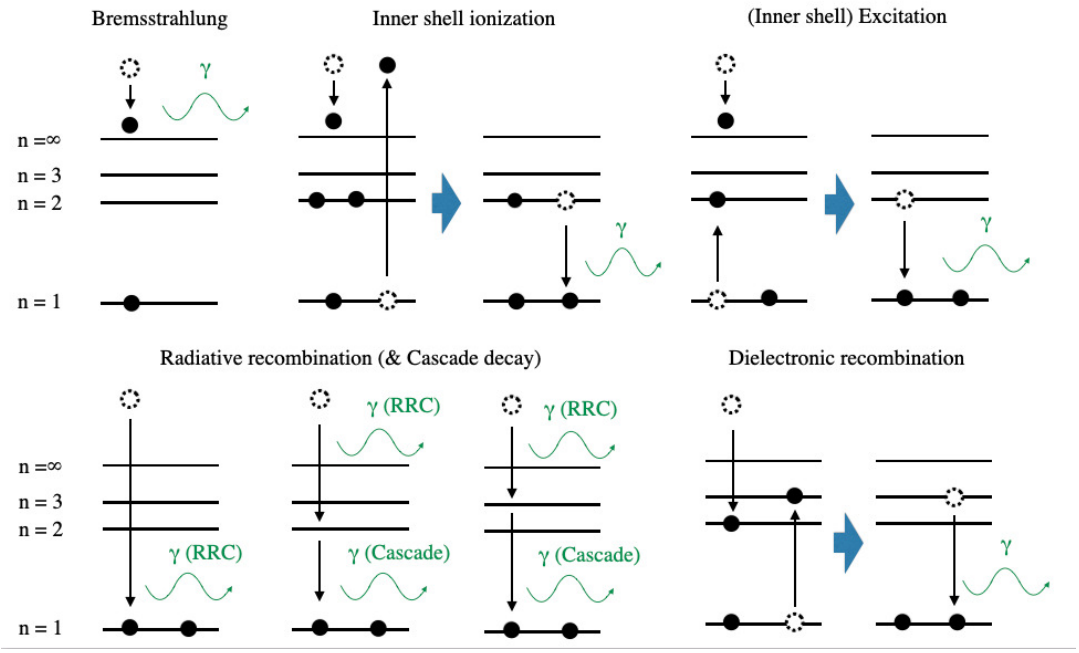

FIGURE 3.5: X-ray Radiation processes in SNRs. Horizontal lines represent energy levels, and above n = ∞ is the free electron energy region.

ion Z^{+z} (Mewe et al., 1981). Furthermore, α^{RR}_{z+1} and α^{DR}_{z+1} are those of the radiative or dielectronic recombination (RR or DR), respectively. η is the ion fraction described as:

$$\eta = \frac{N_{Z,z}}{N_Z}, \tag{3.25}$$

which is calculated from Equation 3.7. As described below, each rate coefficient is a function of electron temperature. Therefore, the emissivities of line emissions are the function of the electron temperature (kT_e) and the ion fraction ($n_e t$).

Inner Shell Ionization In typical SNRs, the relatively light elements such as O are dominated by the He-like and H-like ionization state (Figure 3.3 (a)). On the other hand, high-Z elements, such as Fe, are often less ionized than the He-like state (Figure 3.3 (b)). Therefore, in SNR plasmas, inner K-shell ionization is induced by collision interactions between high-energy free electrons and low-ionized ions. The vacancy left after the inner shell ionization is filled another electron in the outermost shell. Then, Line photons are emitted by this orbital transition of the electron. Using the formula of Lotz, 1968, Mewe et al., 1981 introduces the rate coefficient $S^{\rm II}_{z-1}$ as:

$$S^{\rm II}_{z-1} = 6.49 \times 10^{-4} T_e^{-1/2} C_{II} (\chi^{\rm II}_{z-1})^{-1} \times E_1(\chi^{II}_{z-1}/kT_e), \tag{3.26}$$

where χ_{z-1}^{II} is the ionization energy, and C_{II} is described as:

$$C_{II} = \frac{w_{\rm j}}{\Sigma w_{\rm j}} \frac{A_r}{A_a + \Sigma A_r}, \tag{3.27}$$

where $\Sigma w_{\rm j}$ is the total statistical weight of the configuration to which the level j belongs and, A_a and A_r are transition probabilities for decay by auto-ionization and radiation, where the summation is over all possible radiative transitions from level j. C_{II} is a constant depending on the ion species and the transition as calculated by Mewe et al., 1981.

Collisional Excitation Ions in the ground state are excited by free electron collisions, and subsequent de-excitation induces line emission. The rate coefficient of collisional excitation for this process are calculated as follow. We assume that all excited ions Z^{+z} were in the ground state (of statical weight w_g). After excitation by electron impact to the upper level, the line transition takes place with some branching ratio factor $BR = A_r/(A_a + A_r)$ described as:

$$S_z^{E/IE} = 8.62 \times 10^{-6} (\overline{\Omega}/w_g)\ BR\ C_1\ T_{\rm e}^{-1/2} \exp\left(-\frac{\chi_z^{\rm E/IE}}{kT_{\rm e}}\right), \tag{3.28}$$

where w_g is the statistical weight of the ground state, $\chi_z^{\rm E/IE}$ is the photon energy, C_1 is the correction factor that is a constant depending on the ion species and the transition. $\overline{\Omega}$ is the collision strength averaged over the Maxwellian electron energy distribution (given in Mewe et al., 1978) and described as:

$$\overline{\Omega}/w_g = (8\pi/\sqrt{3})(\chi_{\rm H}/\chi_z^{\rm E/IE}) f \overline{g}, \tag{3.29}$$

where f is the absorption oscillator strength of the considered line, $\overline{g}$ is the average of the Gaunt factor, which can be regarded as a constant depending on the electron temperature.

As shown in Equations (3.28) and (3.29), the rate coefficient of collisional excitation includes the absorption oscillator strength, which will be described in detail in Subsection 3.3.3. Collisional excitation is the most general X-ray line emission process in SNR plasmas. Therefore, the line emissions with large oscillator strength, such as a resonance line of He-like ion, have high intensity. Therefore, line emissions with large oscillator strength, such as a resonance line of He-like ion, are observed prominently in X-ray spectra of SNRs.

Radiative Recombination When the electron is bound to an excited level by radiative recombination, a line photon is emitted by spontaneous de-excitation (cascade decay: bottom left of Figure 3.5). The contribution to a

certain line in ion Z^{+z} due to radiative recombination of ion $Z^{+(z+1)}$ is written as:

$$\alpha_{z+1}^{RR} = 10^{-11}\ BR\ C_{RR}(z+1)^{2\eta+1}T_e^{-\eta}, \tag{3.30}$$

where η and C_{RR} is a constant that differs for each ion species, and η has a value of about 0.6 to 0.8 (see Table 1 in Aldrovandi et al., 1973).

Dielectronic Recombination The rate coefficient of dielectronic recombination of ion $Z^{+(z+1)}$ of a line emission by ion Z^{+z} is given by

$$\alpha_{z+1}^{DR} = 2.07 \times 10^{-16} T_e^{-3/2} B_s \exp\left(-\frac{\chi_s}{kT_e}\right), \tag{3.31}$$

where

$$B_s = \frac{w_s A_a A_r}{w_1(A_a + \Sigma A_r)}. \tag{3.32}$$

χ_s is the energy difference between the upper level s of the satellite line (with statistical weight w_s) in ion Z^{+z} and the ground state (with statistical weight w_1) of the recombining ion $Z^{+(z+1)}$.

Continuum Emission

Bremsstrahlung A charged particle emits a photon when it is scattered by an electric field created by another charged particle (top left of Figure 3.5). This process is called bremsstrahlung. Since a electron has a smaller mass than an ion, bremsstrahlung emitted in plasma is mainly from electrons scattered by the electric field of ions.

$$f(v_e) \;=\; 4\pi v_e^2 \left(\frac{m_e}{2\pi k T_e}\right)^{3/2} \exp\left(-\frac{m_e v_e^2}{2kT_e}\right) \tag{3.33}$$

When the electrons follow the Maxwell-Boltzmann distribution described as the equation (3.33), the intensity per unit time, unit volume, and unit frequency is

$$\frac{dW}{dV dt d\nu} \propto T_e^{-1/2} Z^2 n_e n_i \exp\left(-\frac{h\nu}{kT_e}\right) \overline{g_{ff}}, \tag{3.34}$$

where v_e, m_e, T_e, n_e are the velocity, mass, temperature, number density of electrons respectively, Z and n_i are atomic number and number density of the scattering ion, k is the Boltzmann constant, h is the Planck constant. $\overline{g_{ff}}$ is velocity averaged Gaunt Factor. In X-ray emitting plasmas,

$$\overline{g_{ff}} = \left(\frac{3kT_e}{\pi h\nu}\right). \tag{3.35}$$

From Equations (3.34) and (3.35), the spectrum bremsstrahlung becomes a continuum spectrum with a cutoff at $h\nu \sim kT_e$, so the electron temperature can be determined by the cut-off energy.

Radiative Recombination Continuum Radiative Recombination Continuum (RRC) is electromagnetic radiation emitted when free electrons are captured by ions. As shown in the bottom left of Figure 3.5, a photon is emitted with an energy corresponding to the sum of the binding energy of the electron and the kinetic energy of the free electron. The intensity per unit time, unit volume, and unit frequency of the RRC of electrons following the Maxwell-Boltzmann distribution is

$$\frac{dW}{dVdtdv} \propto \begin{cases} \exp\left(-\frac{E-E_{\rm edge}}{kT_e}\right) (E \geq E_{\rm edge}) \\ 0 (E < E_{\rm edge}), \end{cases} \tag{3.36}$$

where $E_{\rm edge}$ is the binding energy of the electron. The spectrum of RRC has an energy edge with an energy corresponding to the binding energy of electron.

3.2 Interaction between Collisionally Ionized Plasma and Neutral Gas

When an ion collide with a neutral atom, various reactions occur such as ionization and excitation of an ion or a neutral atom, and charge transfer from a neutral atom to an ion (Charge eXchange: CX). Since SNRs is systems in which neutral atoms and ions interact in the shock wave, these processes cannot be ignored in some cases. CX is a particularly important process when the collision velocity between ions and neutral atoms is lower than the orbital velocity of electrons in the classical hydrogen atom ($\sim$ 2000 km/s). CX may be important because shock wave velocities of SNRs range from several hundred to 2000 km/s. Here we describe the basic physics of CX. Detailed spectral features of CX are summarized in Subsection 3.4.2.

3.2.1 Charge Exchange

When a neutral atom collides with an ion, the potential barrier between them become lower, and an electron bound to the neutral atom can be transfered to the energy level of the ion (see Figure 3.6). This interaction is described as:

$$X^{q+} + Y \rightarrow X^{*(q-1)+} + Y^{+}, \tag{3.37}$$

where X is the ion, $q+$ is its charge number, Y is the neutral atom, and the star superscript denotes an excited state. If the neutral atom is not hydrogen, multiple electrons can be transferred, leading to a multiply excited ion. However the cross section for multiple transfer is much smaller than that for a single transfer (Wargelin et al., 2008). Therefore, we consider CX between

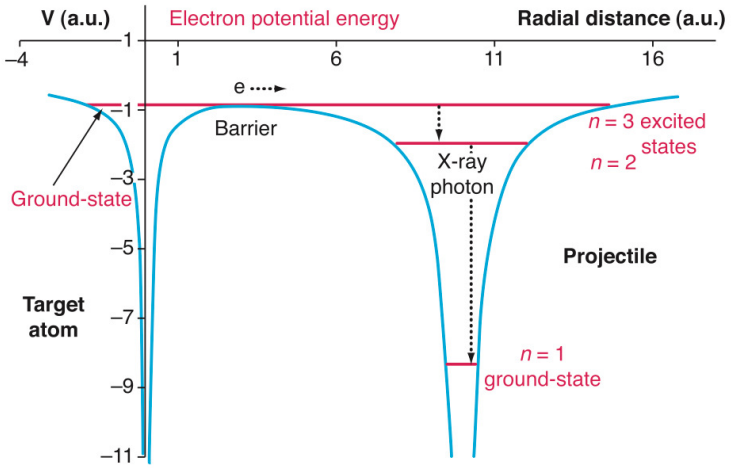

FIGURE 3.6: A Diagram of CX (Cravens, 2002). The vertical axis corresponds to the potential depth. The solid cyan lines represent potential barriers and the solid red lines represent energy levels.

ions and neutral hydrogen. Since the potential of hydrogen is shallower than that of ions, the electron first is captured the excited level. Then, CX produces a X-ray line emission due to subsequent de-excitation. The most probable energy level to which an electron is transferred from neutral hydrogen is given by:

$$n_p \sim \left(1 + \frac{q-1}{\sqrt{2q}}\right)^{-1/2} \sim q^{3/4}, \tag{3.38}$$

where, q is the charge number of the ion (Janev and Winter, 1985). Therefore, for example, in the case of the reaction described as Equation (3.39), electrons are likely to be trapped to $n \sim 4$.

$$O^{7+} + H \rightarrow O^{*6+} + H^{+} \tag{3.39}$$

Besides this n-selectivity, the electron transfer process exhibits also selective properties with respect to the electron orbital angular momentum (l-selectivity). Contrary to the case of n-selectivity, l selective property no underlying physical criteria have been establish. However, the l-selectivity considered to be related to the collision velocity between the neutral hydrogen and an ion (e.g., Janev and Winter, 1985). In the low velocity regime, the peak l shell is $l = 1$ or 2. On the other hands, in the high velocity regime, the l-selectivity follows the statistical weight (e.g., Gu et al., 2016).

3.3 Radiative Transfer

3.3.1 Optical Depth

When radiation passes through a material of optical depth τ, its intensity becomes $e^{-\tau}$. The optical depth τ is defined as

$$\tau = \alpha L = \kappa \rho L = N\sigma, \tag{3.40}$$

where α (cm^{-1}) is the absorption coefficient, L (cm) is the thickness of the material, κ (cm^2/g) is the mass absorption coefficient, N (cm^{-2}) is the column density, σ (cm^2) is the cross section. The column density is obtained by integrating the number density n (cm^{-3}) along the line of sight.

$$N = \int_0^L n(s) ds \tag{3.41}$$

In general, these values depend on photon energy.

The mean free path of photons is defined as the average distance a photon travels through an absorbing material without being absorbed. The probability that a photon travels through the material with τ is $e^{-\tau}$. The mean optical depth traveled is equal to unity.

$$\langle \tau \rangle = \int_0^\infty \tau e^{-\tau} d\tau = 1 \tag{3.42}$$

The mean free path l in a homogeneous medium is determined by

$$\langle \tau \rangle = \alpha l = 1 \tag{3.43}$$

From Equations (3.43) and (3.40), the relation between the mean free path l and the thickness of the material L (cm) is

$$l = L/\tau. \tag{3.44}$$

A medium with a low optical depth ($\tau < 1$) is described as optically thin, whereas one with a high optical depth is optically thick. According to the equation (3.44), in an optically thick medium, the mean free path l is smaller than the thickness of the material L, and most photons are absorbed. On the other hand, most photons pass through an optically thin medium without being absorbed.

3.3.2 Radiative Transfer

The source function S_ν is defined as the ratio of the emissivity j_ν [$\mathrm{erg/s/cm^3/Hz/str}$] to the absorption coefficient α_ν [cm^{-1}]:

$$S_\nu \equiv \frac{j_\nu}{\alpha_\nu}. \tag{3.45}$$

Using the source function, the radiative transfer equation can be written,

$$\frac{dI_\nu}{d\tau_\nu} = -I_\nu + S_\nu, \tag{3.46}$$

where I_ν is the specific intensity. Considering only absorption and radiation (without considering scattering), we can solve the radiative transfer equation if S_ν is independent of τ.

$$I_\nu(\tau) = S_\nu(1 - e^{-\tau}) + I_\nu(0)e^{-\tau} \tag{3.47}$$

In the optically thin case ($\tau \ll 1$), the specific intensity described as

$$I_\nu(\tau) = I_\nu(0) + \tau_\nu S_\nu. \tag{3.48}$$

$I_\nu(\tau)$ is proportional to the optical depth. Therefore, in three dimensions, the brightness of an optically thin object is proportional to its volume. Emission from the background of an astronomical object ($I_\nu(0)$) is also observed.

In the optically thick case ($\tau \gg 1$), the specific intensity described as

$$I_\nu(\tau) = S_\nu. \tag{3.49}$$

The background emission ($I_\nu(0)$) cannot be observed. $I_\nu(\tau)$ is independent of τ. Therefore, the brightness of an optically thick object is proportional to its surface area.

It is known that SNR plasmas are optically thin for continuum radiation. For example, the optical depth of Thomson scattering ($\tau_{\rm T}$) can be calculated as:

$$\tau_{\rm T} = 2.1 \times 10^{-5} \left(\frac{L}{10\,{\rm pc}}\right) \left(\frac{n_e}{1\,{\rm cm}^{-3}}\right), \tag{3.50}$$

where the typical electron number density and the diameter of SNR are 1–10 cm^{-3} and the diameter is 10 pc. Thus, the X-ray emission from SNRs is optically thin in most energy bands, so self-absorption is negligible.

3.3.3 Resonance Scattering

Resonance Scattering (RS) is an apparent scattering phenomena due to an absorption and re-emission of line photons by ions. When a photon with energy equal to the energy difference between an excited state and the ground state of an ion is incident on the ion, the ion absorbs the photon and excited. The ion then emits a photon of energy equal to the incident photon due to de-excitation. This makes the photon appear to be scattered without changing its energy.

The optical depth τ of RS is expressed as:

$$\tau = N_{\rm ion}\sigma, \tag{3.51}$$

where $N_{\rm ion}$ is the column density of ions that cause RS, for example, the column density of He-like O when considering the RS of the O VII Heα line. Using elemental abundance ($n_{\rm z}/n_{\rm H}$) and ion fraction, τ can be described as:

$$\tau = N_{\rm H}\left(\frac{n_{\rm z}}{n_{\rm H}}\right)\left(\frac{n_{\rm i}}{n_{\rm z}}\right)\sigma. \tag{3.52}$$

The cross section of RS at a line center is

$$\sigma = \frac{\sqrt{\pi}e^2}{mc}\frac{f}{\nu}\left(\frac{\rm v}{c}\right)^{-1}\ {\rm cm}^2, \tag{3.53}$$

where f is the oscillator strength, ν is the frequency, m is the electron mass, v is the root-mean-square kinetic velocity of the ion described as:

$${\rm v}^2 = \frac{2kT_{\rm i}}{m_{\rm i}} + {\rm v}_{\rm tur}^2. \tag{3.54}$$

The $kT_{\rm i}$ is the ion temperature in keV, $m_{\rm i}$ is the ion mass, and $\rm v_{tur}$ is the root-mean-square turbulent velocity due to motions other than thermal one. From Equations (3.52), (3.53) and (3.54), Kaastra and Mewe, 1995 calculate the τ to be:

$$\tau = \frac{4.24\times10^6 f N_{\rm H}\left(\frac{n_{\rm i}}{n_{\rm z}}\right)\left(\frac{n_{\rm z}}{n_{\rm H}}\right)\left(\frac{M}{T_{\rm keV}}\right)^{1/2}}{E_{\rm eV}\left(1+\frac{0.0522Mv_{100}^2}{T_{\rm keV}}\right)^{1/2}}, \tag{3.55}$$

where f is the oscillator strength of the line, $E_{\rm eV}$ is the line centroid energy in eV, $N_{\rm H}$ is the hydrogen column density in cm^{-2}, $n_{\rm i}$ is the number density of the ion, $n_{\rm Z}$ is the number density of the element, M is the atomic weight of the ion, $T_{\rm keV}$ is the ion temperature in keV, and v_{100} is the micro-turbulence velocity in units of 100 km s^{-1}. From Equation (3.55), it can be seen that an optical depth of RS is proportional to an oscillator strength f. An oscillator strength f_{lu} for a transition from an energy level l to u is expressed as:

$$f_{lu} = \frac{m_e c}{4\pi^2 e^2} h\nu_{lu} B_{lu}, \tag{3.56}$$

where B_{lu} is Einstein absorption coefficient. Therefore, it is a dimensionless quantity that reflects the probability of electronic transitions between energy levels, which are induced by the absorption of photons. Table 3.1 summarizes the oscillator strengths of the O VII (He-like oxygen) Kα lines.

It can be seen that the oscillator strength differs by many orders of magnitude from line to line. Transitions that satisfy the selection rule introduced in Subsubsection 3.1.2.1 have large oscillator strengths. Using Equation (3.55), optical depths of Resonance line and Forbidden line listed in Table 3.1 are calculated as:

$$\tau_{\rm r} \;=\; 1.06\left(\frac{L}{10\ {\rm pc}}\right)\left(\frac{n_e}{1\ {\rm cm}^{-3}}\right) \tag{3.57}$$

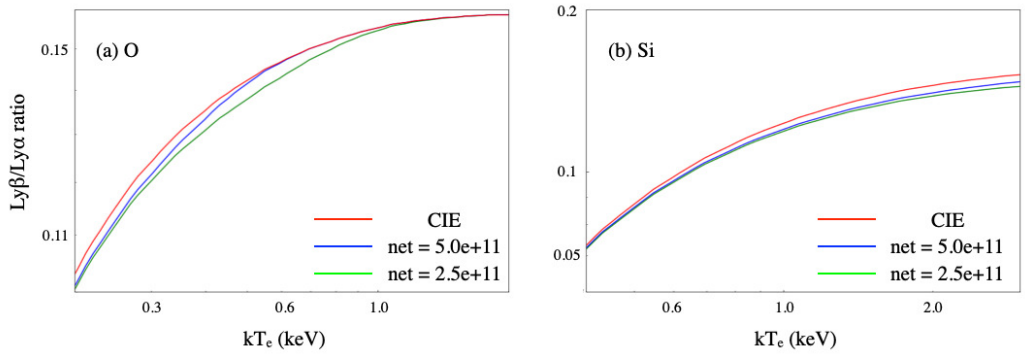

FIGURE 3.7: Line intensity ratios expected for CIE or NEI (ionizing) plasma. (calculated with pyatomdb) (a) Lyβ/α ratio of O as a function of electron temperature. (b) Same as panel (a), but for Si.

$$\tau_{\rm f} \;=\; 2.95\times10^{-10}\left(\frac{L}{10\ {\rm pc}}\right)\left(\frac{n_e}{1\ {\rm cm}^{-3}}\right) \tag{3.58}$$

where we assume the plasma is in the CIE state with an electron temperature of 0.2 keV whose abundance of oxygen is solar value (Anders and Grevesse, 1989). Thus some resonance lines have an optical depth of approximately 1 in a typical SNR plasma, and the effect of RS may not be negligible.

3.4 Plasma Diagnostic

3.4.1 Electron Temperture & Charge Distribution (Ionization timescale)

As mentioned in 3.1.1.2, the electron temperature and ionization timescale ($n_{\rm e}t$) are important parameters that characterize the physical condition of SNR plasmas. In this subsection, we introduce how to constrain these parameters based on the line ratios of the X-ray spectrum.

Electron Temperture

To derive the electron temperature, it is useful to measure the line intensity ratio between atomic transitions involving different quantum levels of identical ions. This is because collisional excitation to higher quantum levels requires a larger kinetic energy (i.e., higher temperature) of free electrons. Figure 3.7 shows Lyβ/Lyα ratios of H-like O and Si as a function of $kT_{\rm e}$. It can be seen that this line ratios are sensitive to the electron temperature, while the difference due to $n_{\rm e}t$ is relatively small. The electron temperature can also be measured by the shape of the continuum (bremsstrahlung and RRC). However, when the continuum is dominated by non-thermal components, or when multiple plasmas with different temperatures are observed, electron temperature measurements based on line ratios are particularly useful.

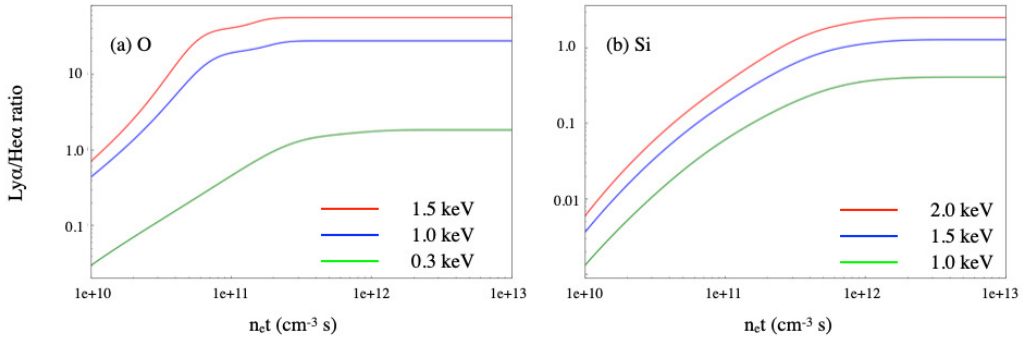

FIGURE 3.8: (a) Lyα/Heα ratios of O as a function of $n_e t$ (calculated with pyatomdb). (b) Same as panel (a), but for Si.

Charge Distribution (Ionization timescale)

By investigating the ion population together with the electron temperature, we can determine whether the plasma has reached ionization equilibrium. For example, the line ratio of Lyα and Heα reflects the population of H-like and He-like ions, which can be used to constrain the ionization timescale $n_e t$. Figure 3.8 show the line ratio of Lyα and Heα of O as a function of $n_e t$ In typical SNRs, the heavy elements lighter than Ca ($Z \leq 20$) are dominated by the He-like and H-like ions, and thus this diagnostic can be applied.

3.4.2 Diagnostic Using Heα Line ratio

Since He-like ions are closed-shell structures, they exist under a wide range of physical conditions (temperature, density, plasma ionization state, etc.). Therefore, the line flux ratio of He-like ions is useful for probing a wide range of physical quantities. Here, we describe the basics of the line structure of the Kα lines (Heα line) of He-like ions, and explain the diagnostic method of physical quantities and physical processes of plasma using the Heα Line ratio.

Under the assumption of LS coupling, the energy levels of He-like ions can be expressed as shown in the Figure 3.9. The Heα line emitted by the transition indicated by **w** and **z** in the left panel of Figure 3.9 is called the resonance (r) and forbidden (f) line, respectively. The Heα lines indicated by both **x** and **y** are called intercombination (i) line. Basic information for O VII and Fe XXV Heα lines are summarized in Table 3.1. According to selection rule (Subsubsection 3.1.2.1), the transition **w** is allowed transition. On the other hand, **x**, **y**, and **z** are forbidden transition. This is the reason why resonance line has several orders of magnitude larger oscillator strength than the other lines. The energy level shown in red in the right panel of Figure 3.9 is called a singlet where the two electrons have opposite spin directions. The energy level in blue is called triplet with electrons with spins in the same direction. **x**, **y**, and **z** are triplets, which have a lower oscillator strength than **w**, but have a higher statistical weight. Therefore, electrons are more likely to be trapped in the excited levels of **x**, **y**, and **z** due to recombination. Table 3.1

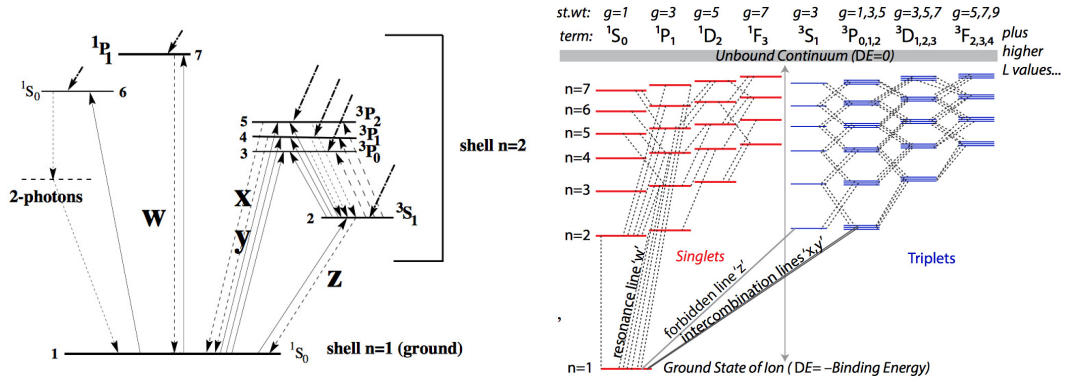

FIGURE 3.9: (left) Schematic Grotrian diagram for a He-like ion (Porquet et al., 2001). Energy levels up to n = 2 are shown, considering the case where only one electron is excited. w (or r), x, y (or i), and z (or f): resonance, intercombination, and forbidden lines, respectively. Full upward arrows: collisional excitation transitions, broken arrows: radiative transitions, and thick skew arrows: recombination (radiative and dielectronic) and cascade processes. (right) Same as left panel, but including the energy level of $n > 3$ (Smith et al., 2014). g corresponds to statistical weigh.

shows the centroid energy of Heα lines of O and Fe. These transitions can be resolved only by high-resolution spectrometers, such as the Reflective Grating Spectrometer on board XMM–Newton and the X-ray microcalorimeter Resolve on board XRISM.

TABLE 3.1: Basic information for O VII and Fe XXV Heα lines (taken from Atomdb)

Element	Line Name	Upper State	Oscillator Strength	Centroid Energy
O	Resonance Line (**w**)	$^1P_1$	7.20×10^{-1}	574 eV
	Intercombination Line (**x**)	$^3P_2$	1.14×10^{-7}	569 eV
	Intercombination Line (**y**)	$^3P_1$	8.19×10^{-5}	569 eV
	Forbidden Line (**z**)	$^3S_1$	2.00×10^{-10}	561 eV
Fe	Resonance Line (**w**)	$^1P_1$	7.20×10^{-1}	6700 eV
	Intercombination Line (**x**)	$^3P_2$	1.14×10^{-7}	6680 eV
	Intercombination Line (**y**)	$^3P_1$	8.19×10^{-5}	6670 eV
	Forbidden Line (**z**)	$^3S_1$	2.00×10^{-10}	6640 eV

R-ratio

The intensity ratio (f/i) is called R-ratio. According to the selection rule, the transition between $^3S_1$ and $^3P_{2,1,0}$ is an allowed transition. In low density plasmas such as in SNRs, the transition of ions in the excited state to the ground state by spontaneous emission takes place faster than the next collision. Therefore, the excitation from $^3S_1$ to $^3P_{2,1,0}$ is negligible. However, as

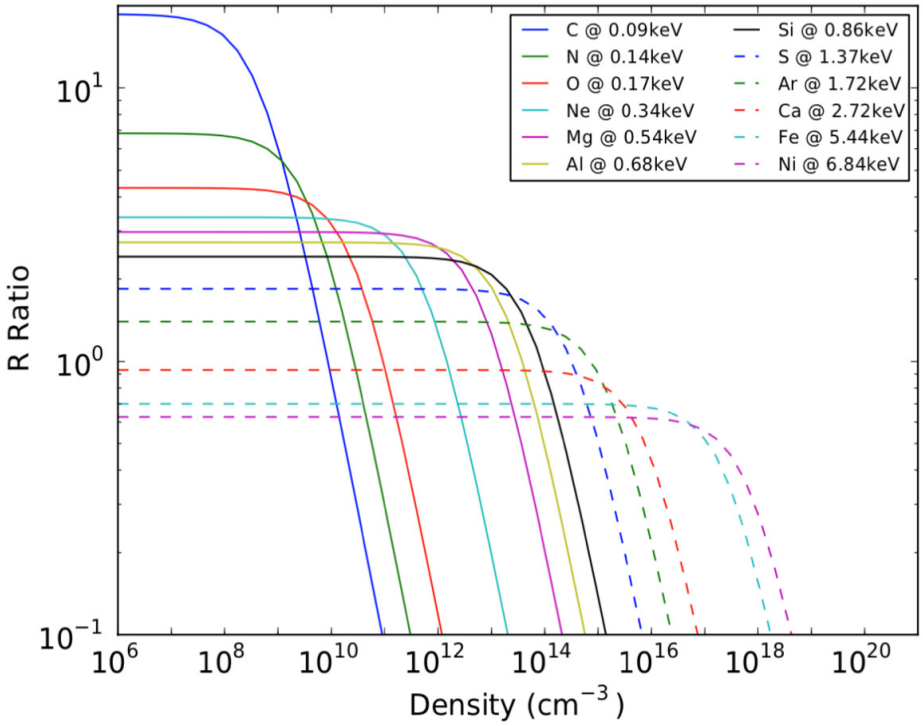

FIGURE 3.10: R-ratio as a function of electron density.

the plasma density increases, the collisional excitation from $^3S_1$ to $^3P_{2,1,0}$ cannot be ignored, and the R-ratio increases. Figure 3.10 shows the R-ratio as a function of density. Each element is sensitive to different density regions.

G-ratio

The G-ratio, defined as the ratio of $(f+i)/r$, can be used to probe the electron temperature. As mentioned above, the flux ratio between i and f depends on the electron density of the plasma. Therefore, $(f+i)/r$ can be used to constrain the electron temperature independent of electron density. Since collisional excitation is the dominant radiation process of Heα lines in IP and CIE, which are commonly seen in SNR, the value of G-ratio is generally small. For example, the G-ratio of the O VII Heα lines is generally smaller than unity in CIE and IP (Figure 3.11). On the other hand, RP, inner-shell ionization, charge exchange, and resonance scattering, which are described below, are characterized by a high G-ratio. Therefore, as explained below, G-ratio can be used to probe these physical processes and ionization states.

RP RP is the plasma in a higher ionization state than the CIE plasma in which recombination process is dominant. Therefore, its X-ray spectrum is characterized by relatively strong radiation components due to recombination, such as RRC and line emission from cascade decay appear. When free electrons are trapped by H-like ions, electrons tend to enter spin triplet energy levels (the energy levels shown in blue in the right panel of Figure 3.9)

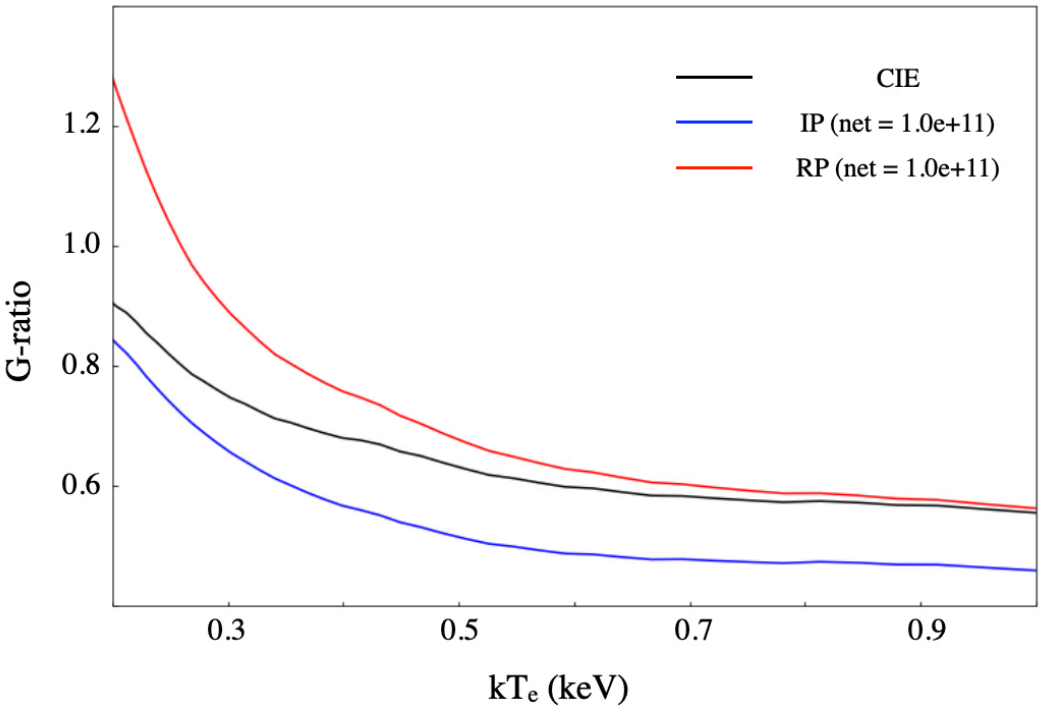

FIGURE 3.11: G-ratio of O VII Heα lines as a function of electron temperature.

because the selectivity of angular momentum l and spin s of captured electrons follows statistical weights. Moreover, electrons captured into the spin triplet energy level always goes through the $n = 2$ levels to the ground state due to the selection rule. Therefore, the final de-excitation of the electrons emits either f or i, resulting in a large G-ratio (Figure 3.11). In addition to the high G-ratio, the Kβ and Kγ, ... lines due to the de-excitation of electrons captured into $n > 3$ spin siglet energy levels to the ground state and the RRC due to radiative recombination are also enhanced in the RP.

Inner-shell Ionization The electron configuration of Li-like ions in ground state is $1s^2 2s$. There are two excited states, $^1S_0$, and $^3S_1$, induced by the inner-shell ionization of the electron in the $1s$ orbit of the Li-like ion. Therefore, the two-photon decay emission due to the $1s2s\ (^1S_0) \rightarrow 1s^2\ (^1S_0)$ transition and the forbidden line due to the $1s2s\ (^3S_1) \rightarrow 1s^2\ (^1S_0)$ transition can be emitted by inner-shell ionization, which enhance the observed G-ratio.

CX Since CX is a recombination process, the G-ratio is enhanced for the same reason as RP. On the other hand, CX is a non-radiative recombination process, RRC is not enhanced. The bottom panel of Figure 3.12 shows the experimental CX spectra where the w line is relatively weaker than z line.

RS As explained in Subsection 2.3.3, a cross section of RS is proportional to the oscillator strength. Table 3.1 summarize the oscillator strengths of Heα lines of O and Fe. Resonance lines have oscillator strengths several orders of

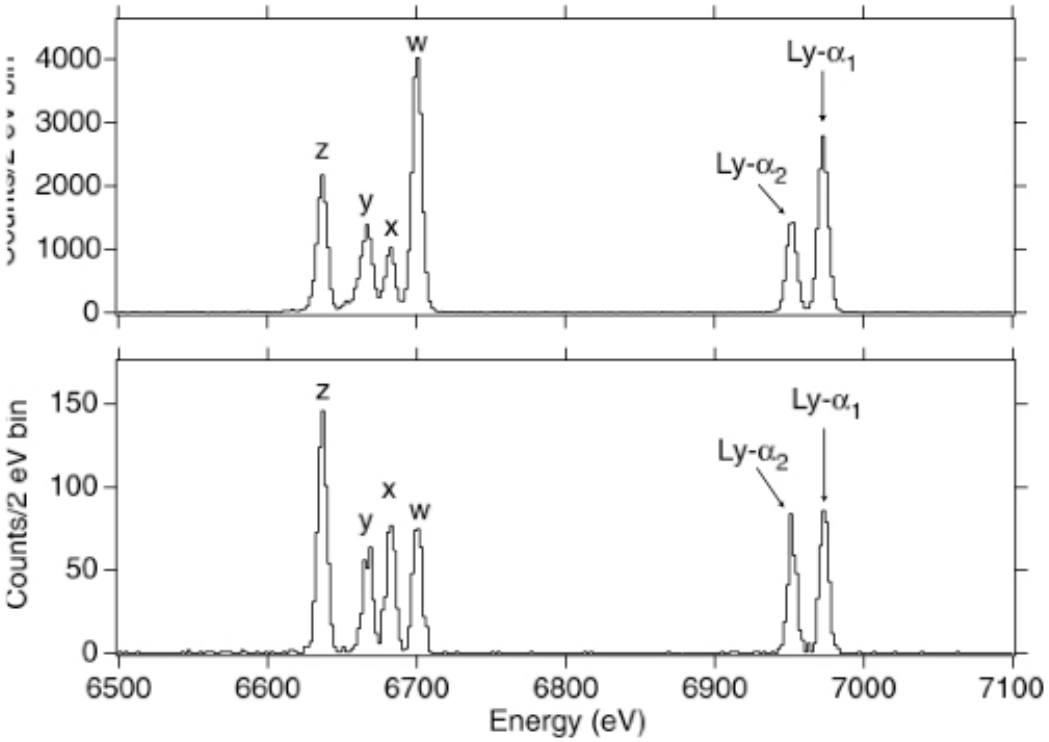

FIGURE 3.12: Experimental He-like and H-like Fe spectra from collisional excitation by monochromatic electron as 15 keV (top) and from CX with N_2 (bottom) (Wargelin et al., 2008). Both spectra are observed with the X-ray microcalorimeter.

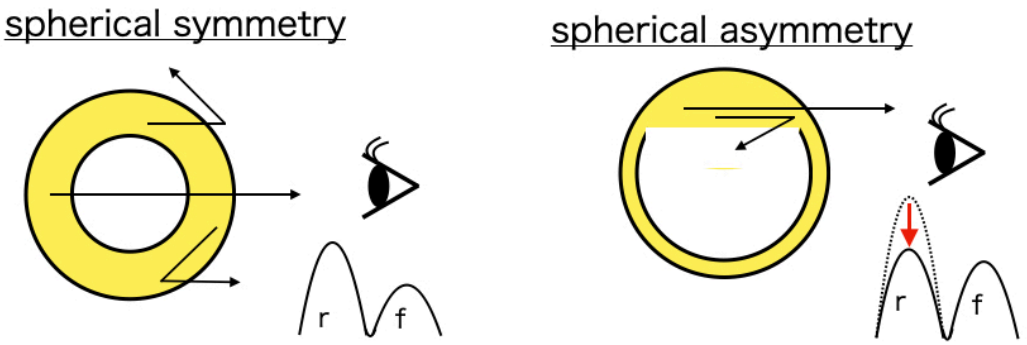

FIGURE 3.13: Schematic image of the RS in SNRs. (left) In the case of spherical symmetric SNRs. The RS effect is cancelled out and an enhancement of f/r is not observed 3.1. (right) In the case of spherical asymmetric SNRs. The intensity reduction of resonance line would be observed.

magnitude larger than those of forbidden lines and intercombination lines, and are particularly susceptible to the effects of RS. Therefore, the G-ratio can be enhanced by the intensity reduction of resonance line due to RS.

The observed RS effect depends on the structure of the object. If an object has an ideal spherical symmetric structure, the RS effect is cancelled out and an enhancement of f/r is not observed (the left panel in Figure **??**). On the other hand, when observing an object with a long structure in the line-of-sight direction, only the resonance lines are scattered outside the line-of-sight direction, resulting in a high G-ratio.

3.5 Observational Evidence for Charge Exchange and Resonance Scattering in Astrophysical Plasma

3.5.1 CX

CX is a possible X-ray emission process in any system where ionized gas interact with a neutral gas. CX X-ray emission from an astrophysical object was first observed from the comet Hyakutake with ROSAT in 1996 (Lisse et al., 1996). Since then, CX X-ray emission has been detected from other astronomical object, such as stars (e.g., Pollock, 2012), star forming regions (e.g., Liu et al., 2012), active galactic nuclei (e.g., Gu et al., 2022), and clusters of galaxies (e.g., Conselice et al., 2001).

Lallement, 2004 calculate the contribution of X-ray emission from CX in shock front of an SNR. Based on their estimation, the X-ray emitting region would be the outer edge of the shock front (a few percent of the shock radius: Figure 3.14). The observational evidence is obtained from the Cygnus Loop (Uchida et al., 2019), Puppis A (Katsuda et al., 2012), and G296.1−0.5 (Tanaka et al., 2022). The elemental abundances in some of the outermost rim regions of the Cygnus Loop are anomalously enhanced ($\sim$ 1 solar), whereas

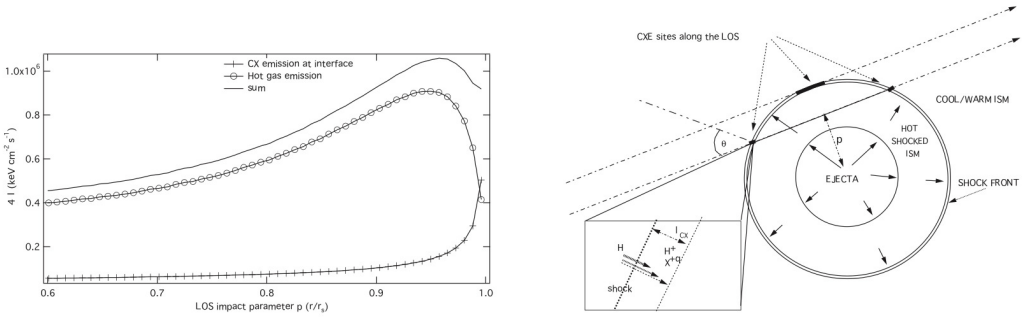

FIGURE 3.14: (left) Contribution of X-ray emission from thermal plasma and CX as functions of the impact parameter p defined as showan in the right panel (Lallement, 2004). The CX exceeds the thermal emission at $p \sim 0.99$. (right) Schematic image of CX in the outer layer of SNR.

the abundances are typically $\sim$ 0.2 solar for most of the rim (e.g., Katsuda et al., 2008). Based on CCD observation, Katsuda et al., 2011 found the possible CX X-ray emission from these abundance enhanced regions where a strong line emission is detected at $\sim$ 0.7 keV, which is likely cascade lines of He-like oxygen (O He$\gamma + \delta + \epsilon$). They pointed out that the excess at $\sim$ 0.7 keV due to CX emission causes an apparent abundance enhancement if an X-ray spectrum is fitted with a CIP model without the CX component. RGS observation of the Southwestern knot region of the Cygnus Loop where elemental abundances are enhanced show high O VII Heα F/R ratiom that cannot be reproduced by emission from CIP (Uchida et al., 2019), which provides strong evidence for CX X-ray emission.

3.5.2 RS

Since RS has large cross sections, it may be observed even in objects that are generally assumed to be optically thin, such as SNR and galaxy clusters. At the center of the Perseus cluster, Hitomi Collaboration, 2018 observed a larger F/R ratio than expected from an optically thin CIP, which is well explained by the RS effect (Figure 3.15).

Kaastra and Mewe, 1995 predicted that RS of X-ray photons can occur in a plasma with a large depth along the line of sight such as a rim of SNRs. Several observational signatures of RS have been reported such as a high forbidden-to-resonance ratio of O VII Heα obtained from grating spectra of DEM L71 (van der Heyden et al., 2003) and N23 (Broersen et al., 2011). A difference in surface brightness between forbidden and resonance lines also supports the presence of RS (e.g., van der Heyden et al., 2003). Based on a observation of the Cygnus Loop with Suzaku satellite, Miyata et al., 2008 claimed that a depleted abundance of O may be partially explained by RS. A recent grating observation of the Loop also hints at a possibility of RS

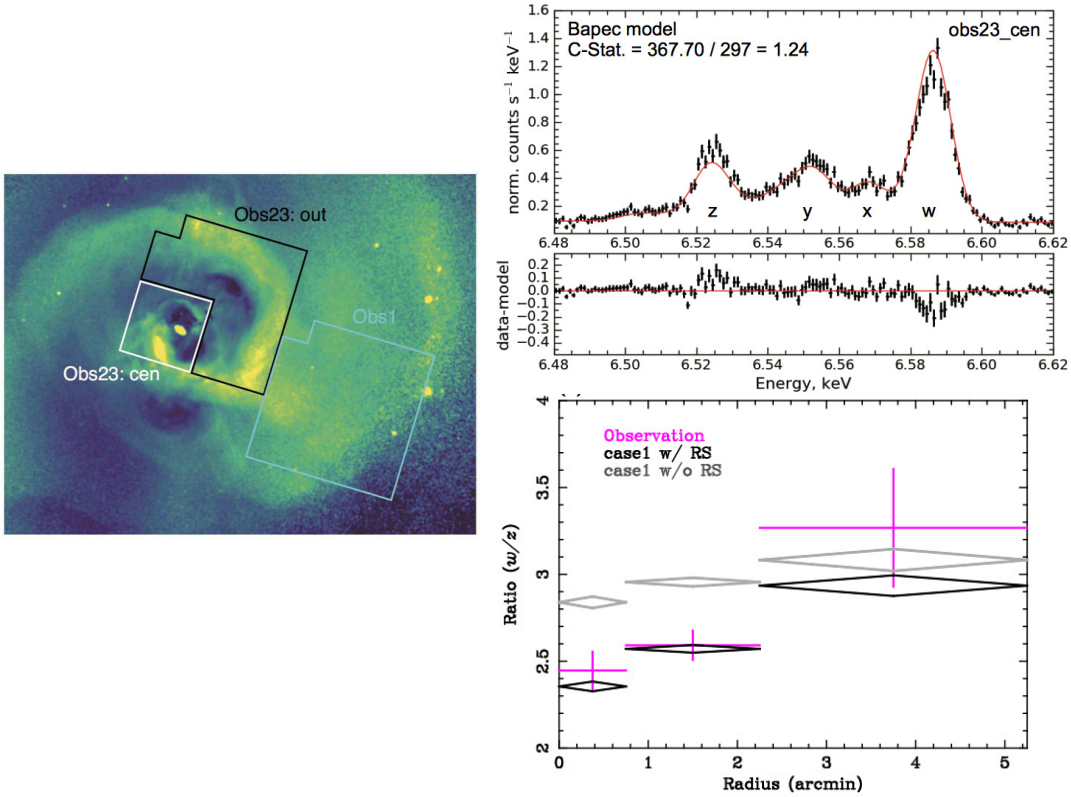

FIGURE 3.15: (left) The Hitomi SXS observation regions overlaid on the Chandra X- ray image of the Perseus Cluster in the 1.8–9.0 keV band (Collaboration, 2017). (top right) Flux suppression in the strongest line of He-like Fe XXV (w) in the center region of the Perseus Cluster. The red lines show the best-fitting models. (bottom right) Comparisons of the observed and predicted ratios of the Fe Heα resonance (w), Heα forbidden (z) lines. Observations are shown as magenta crosses and the simulations with RS as black diamonds and the same without RS as gray diamonds.

(Uchida et al., 2019). These studies suggest that the RS effect may potentially be significant in SNRs. However, no strong observational evidence has been established so far.

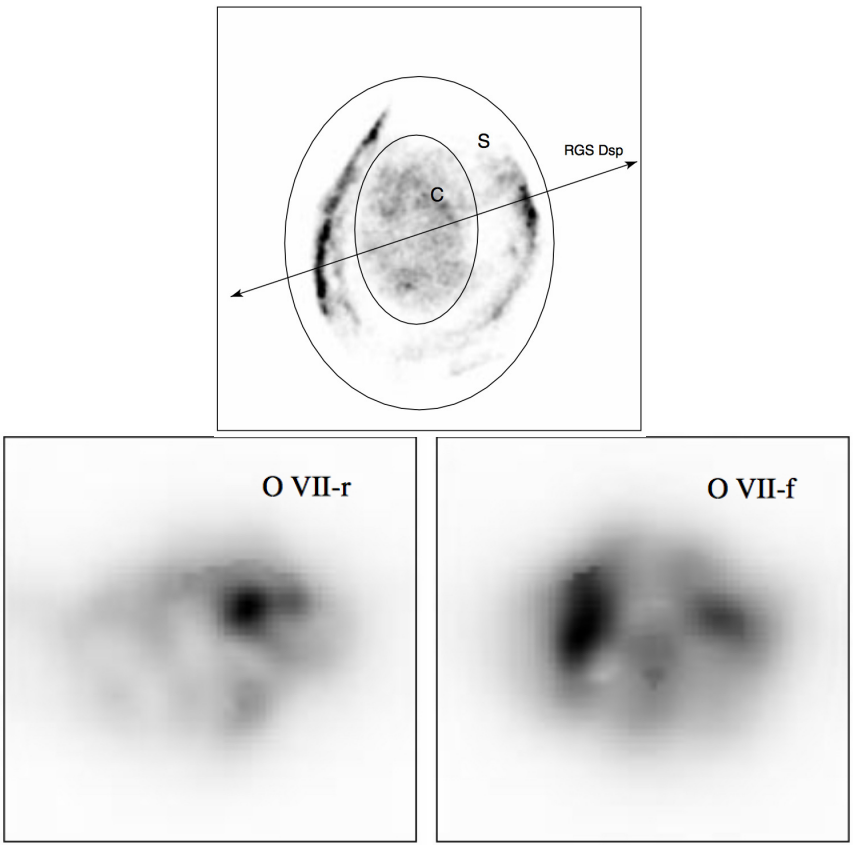

FIGURE 3.16: (top) Chandra X-ray image of DEM L 71 for the energy range 0.7–1.0 keV (van der Heyden et al., 2003). The RGS dispersion axis is also indicated by the black arrow. RGS monochromatic images for O VII resonance (lower left) and O VII forbidden (lower right).

Chapter 4

Instruments

As mentioned in Chapter 3, signs of the RS or CX are expected to be found in intensity ratios of multiplet lines (e.g., OVII Heα), which cannot be resolved with widely-used detectors such as CCDs. In this study, we thus use a grating spectrometer, the RGS onboard the XMM-Newton satellite, which has a much better energy resolution than the CCDs. In this chapter, we briefly summarize the basic properties of the XMM-Newton satellite and its instruments.

4.1 XMM-Newton satelite

The X-ray Multi-Mirror Mission (XMM)-Newton satellite (Jansen et al., 2001) (hereafter XMM-Newton) was launched by the European Space Agency (ESA) in December 1999 and put into an elliptical orbit with a perigee of 5000 km and an apogee of 115000 km. Figure 4.1 and Figure 4.2 show a schematic view of the spacecraft and the orbit of XMM-Newton. XMM-Newton is equipped with two types of telescopes: three X-ray reflecting telescopes with Wolter-I type mirrors and an optical/ultraviolet telescope with an aperture of 30 cm.

As explained below, three CCDs and two grating spectrometer are mounted on the focal plane of the telescopes. The European Photon Imaging Camera (EPIC) is an X-ray imager of CCDs for an energy range of 0.15–12 keV. EPIC consists of two types of charge-coupled devices (CCDs), Metal Oxide Semiconductor (MOS) (Turner et al., 2001) and pn (Strüder et al., 2001). The Reflection Grating Spectrometer is suited for high spectral resolution X-ray spectroscopy in the energy range 5–38 Å(0.33-2.5 keV). The Optical/Ultraviolet Monitor (OM) CCDs for optical/ultraviolet imaging and grism spectroscopy is mounted on the focal plane of the optical/ultraviolet telescope telescopes. In this study, we use the data obtained with MOS and RGS. Therefore, we summarize the design and performance of the X-ray telescope, EPIC-MOS, and RGS in the following section.

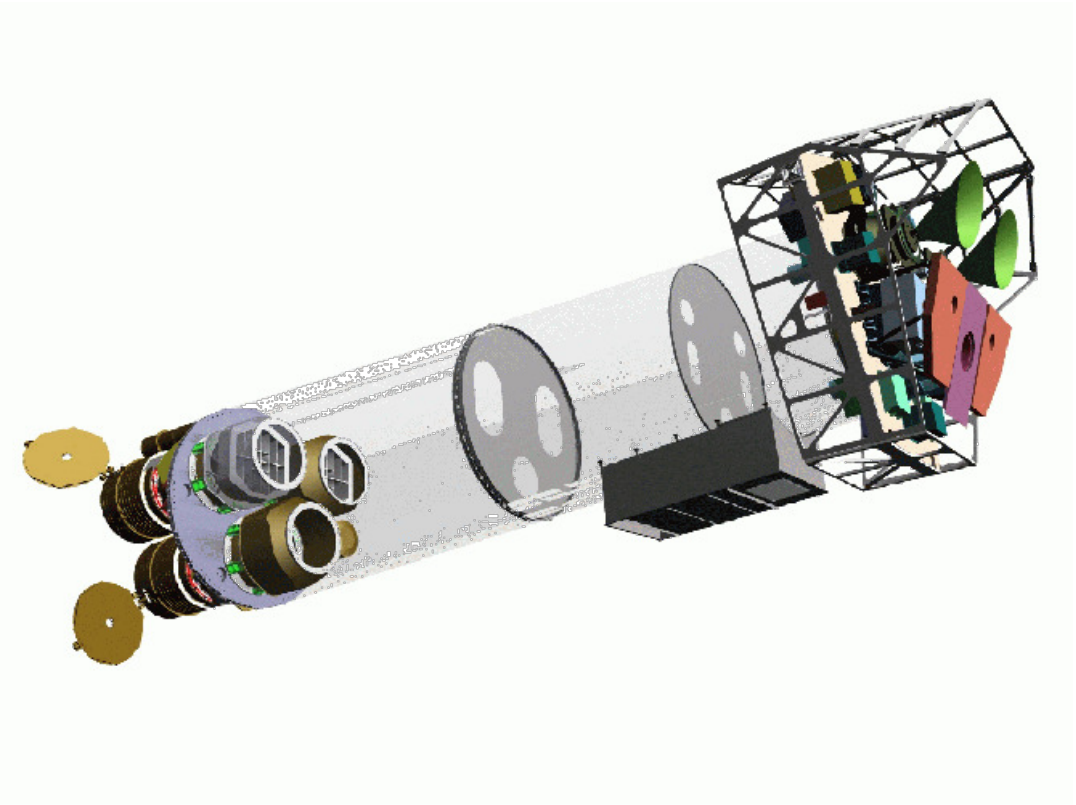

FIGURE 4.1: Sketch of the XMM-Newton satellite (XMM User's Handbook). The mirror modules, two of which are equipped with Reflection Grating Arrays, are visible at the lower left. The right side is the focal plane, where the CCDs are installed. Green, purple, and light blue are radiators for MOS, pn, and RGS, respectively.

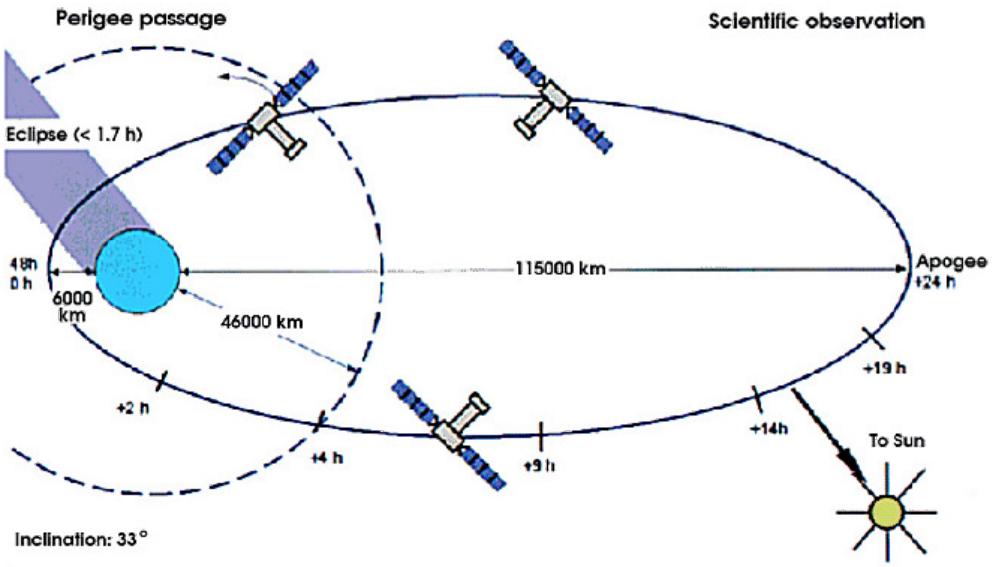

FIGURE 4.2: Orbit of the XMM-Newton satellite (XMM User's Handbook).

4.2 X-ray Telescopes

4.2.1 Overview

Since the refractive index of materials for X-rays is approximately unity, we commonly use a total refection or diffraction to focus X-rays. The X-ray telescopes on board XMM-Newton utilize the Wolter-I type optics which focus the X-ray by total reflection. The Wolter-I type optics employ paraboloidal and hyperboloidal surfaces as primary and secondary mirrors (see Figure 4.3). The X-ray telescopes are comprised of 58 Wolter-I type optics with a 70 cm aperture, a focal length of 7500 mm and a field of view of 30 arcmin.

4.2.2 Performance

Here we describe a performance of the X-ray telescopes, which is mainly characterized by the imaging capability and effective area.

Imaging Performance

The Point Spread Function (PSF) describes the distribution of observed X-rays in the focal plane for point sources. The fractional encircled energy (FEE) is defined as the ratio of the number of X-ray photons obtained by integrating the PSF in the radial direction to total X-ray photons. Figure 4.4 shows FEE as a function of radius from the center of the PSF.

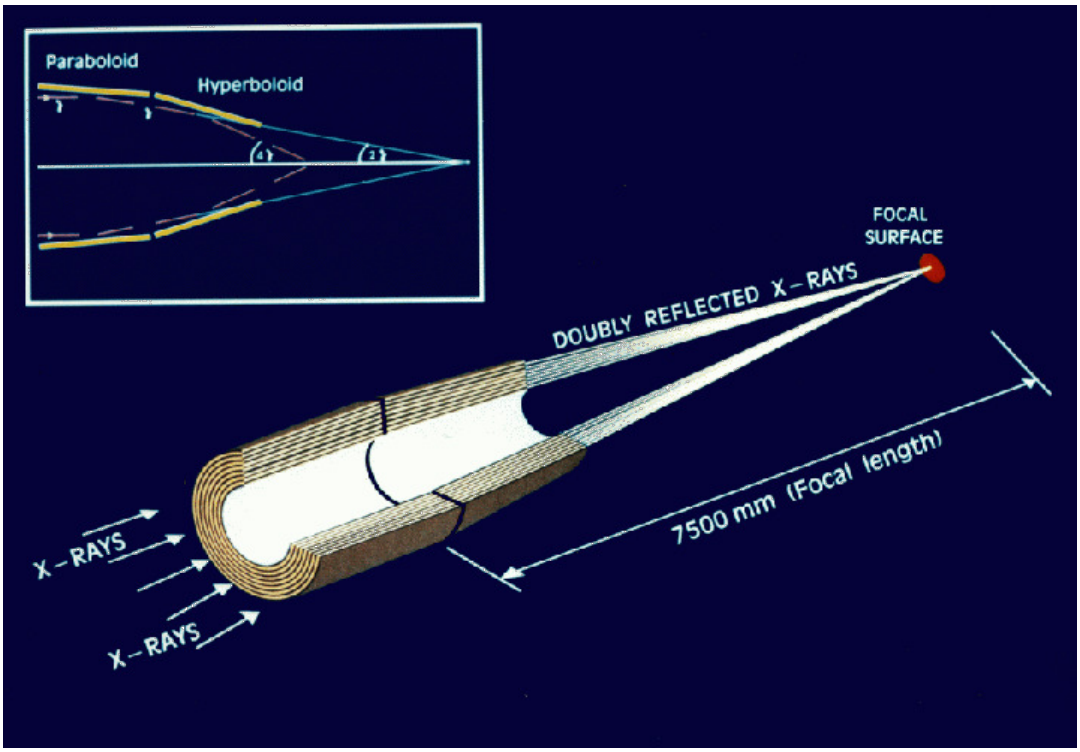

FIGURE 4.3: A schematic view of the Wolter-I type optics of the XMM-Newton (XMM User's Handbook).

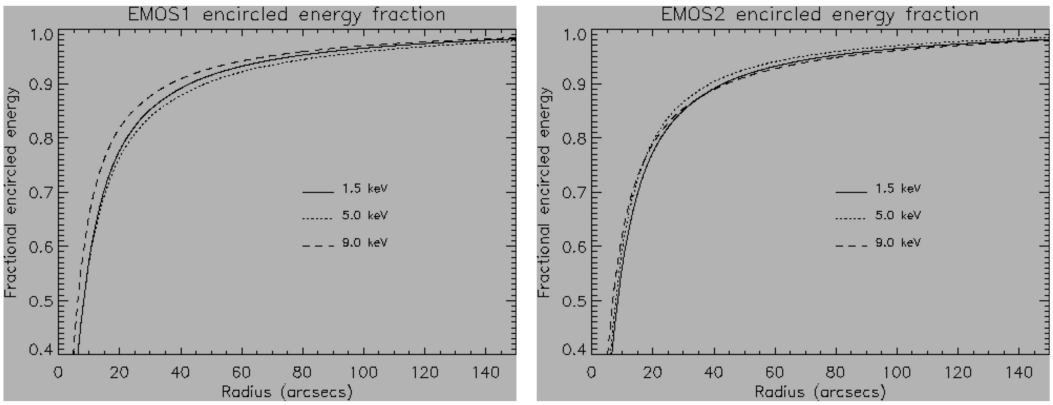

FIGURE 4.4: Fractional encircled energy of the MOS1 (left) and MOS2 (right)(XMM User's Handbook).

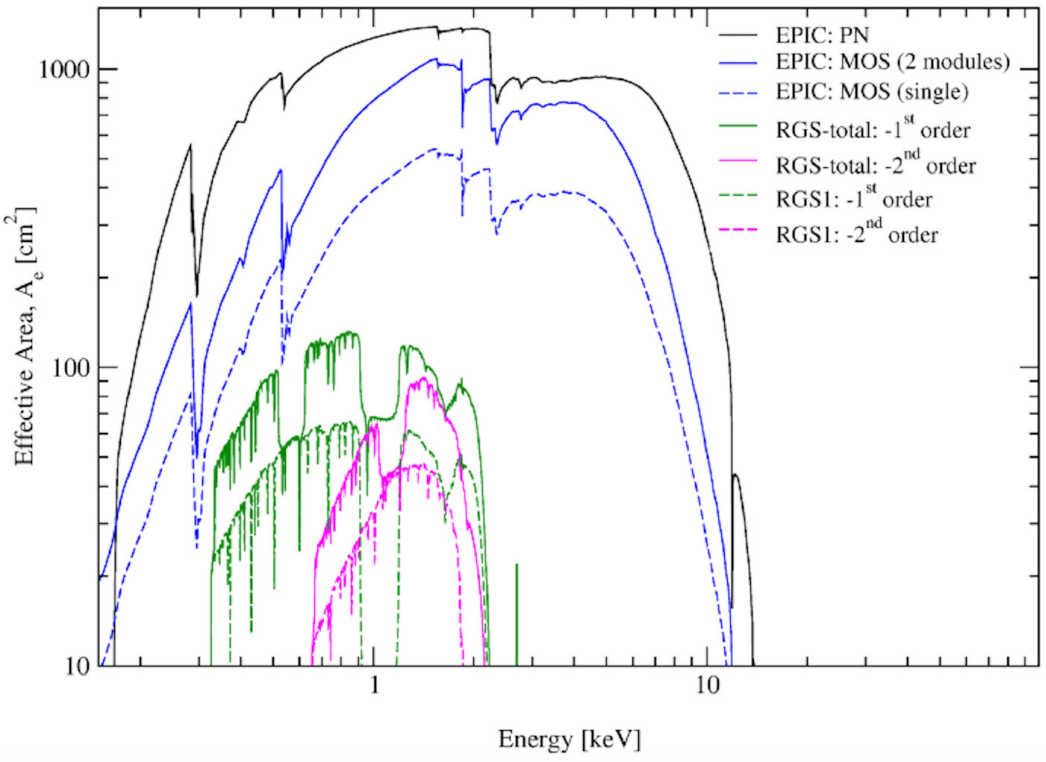

FIGURE 4.5: Effective areas of EPIC cameras and RGS spectrometers (XMM User's Handbook).

Effective Area

The effective area describes the photon collection capability of X-ray telescopes, which depend on an actual aperture size of the telescope and an efficiency of the detector. Figure 4.5 shows the effective area on the optical axis considering the efficiency of each detector. The effective area for off-axis sources is smaller than that for on-axis sources (Figure 4.6). This effect is called "vignetting", and becomes significant in higher energy bands. We corrected the vignetting effect in our image analysis and spectral analysis.

4.3 X-ray CCD Camera (European Photon Imaging Camera: EPIC)

As mentioned above, the XMM-Newton satellite carries two types of CCD detectors called MOS and pn. Among them, we only used the MOS for the following imaging analysis and a wide-band spectroscopy. In this section, we thus focus on a details of the design and performance of the MOS.

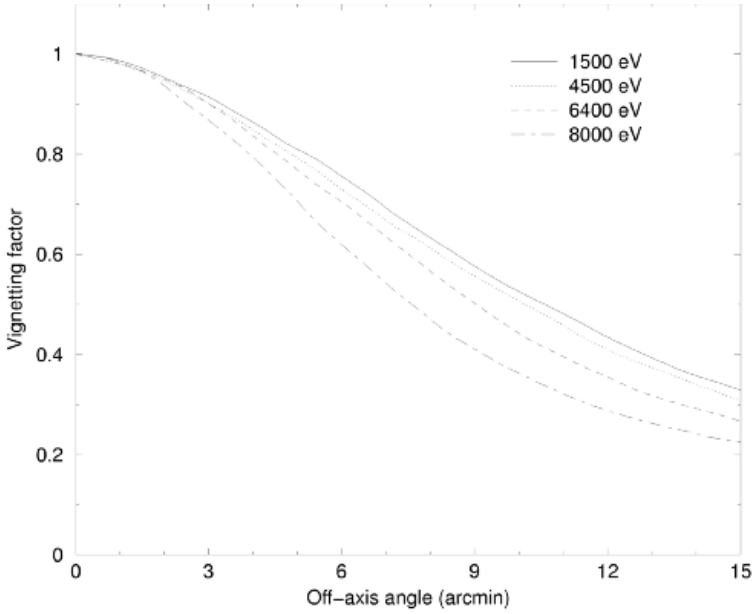

FIGURE 4.6: Vignetting factor defined as the ratio of the effective area against incident angle to that on on-axis (XMM User's Handbook).

4.3.1 Overview and performance of MOS

Photon-counting CCD detectors have a good imaging performance and energy resolution, and are widely used as focal plane detectors of X-ray astronomical satellite. A CCD is an image sensor that consists of two-dimensionally arranged pixels. Photons incidenting on each pixel are absorbed in the depletion layer of the CCDs, and finally charges the number of which is proportional to the energy of the X-ray photons are generated. The number of X-ray photons incident on one pixel is at most one per exposure when observing a general X-ray astronomical object. Therefore, by measuring the number of charges generated at each pixel, the position and energy of the incident X-ray can be determined.

Figure 4.7 represents an example of a schematic of the structure of CCDs used for X-ray astronomy. CCDs are classified into two types, front-illuminated (FI) and back-illuminated (BI) by a direction of photons onto the detector. Since X-rays enter the FI CCDs from the electrode side, some photons are absorbed by the electrodes. For this reason, FI CCDs has a disadvantage that the detection efficiency drops on the low energy side. In addition, since the electrode of the FI CCDs is exposed to debris and micrometeorites, they are more easily to be damaged than BI CCDs. On the other hand, BI CCDs are superior to FI CCDs in these respects, but they have a disadvantage that it is difficult to thicken the depletion layer because it is not easy to provide an electrode on the back side. Figure 4.8 shows schematic views of the field of view (FOV) of the telescope and MOS and pn. The MOS consists of seven FI CCDs with an imaging area of 2.5 cm square.

The energy resolution of the MOS during the early in-orbit phase was about 10 % worse than the ground calibration value before launch. After that,

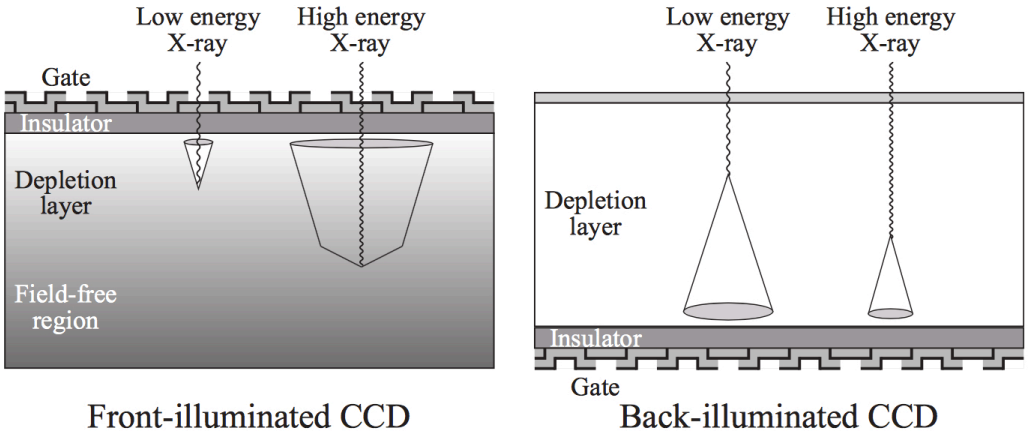

FIGURE 4.7: Cross sectional view of a Front-illuminated CCD (left) and a Back-illuminated CCD (right).

additional cooling was performed to improve the energy resolution, and the current energy resolution is almost stable at the pre-launch value (see Figure 4.9).

TABLE 4.1: design and performance of MOS (XMM User's Handbook)

Energy range	$0.15 - 12$ keV
Pixel size	40 μm
Pixel grid	600×600
Timing resolution	1.5 ms
Energy resolution (FWHM)	$\sim$ 70 eV (@1 keV)

4.3.2 Background of the MOS

The background of the MOS includes X-ray emission from celestial objects and instrumental background. The instrumental background consists of detector noise which is important in the low energy band (< 0.3 keV) and the particles-induced background which is important in the high energy band. The particles-induced background is classified into a time-varying component and a non-time-varying component. The non-time-varying component is observed steadily even outside the exposure time, and has a spectrum consisting of a flat continuum and fluorescence lines as shown in Figure 4.10. These are high-energy charged particles directly incident on the detector from outside the field of view of the telescope, and X-ray fluorescence due to interactions between the detector housing and the high-energy charged particles. The time-varying component is detected within the telescope field of view on the CCD (the shaded area of Figure 4.8) and has a flat-shaped spectrum. It is considered that this component is caused by the direct incidence on the CCD of low-energy protons.

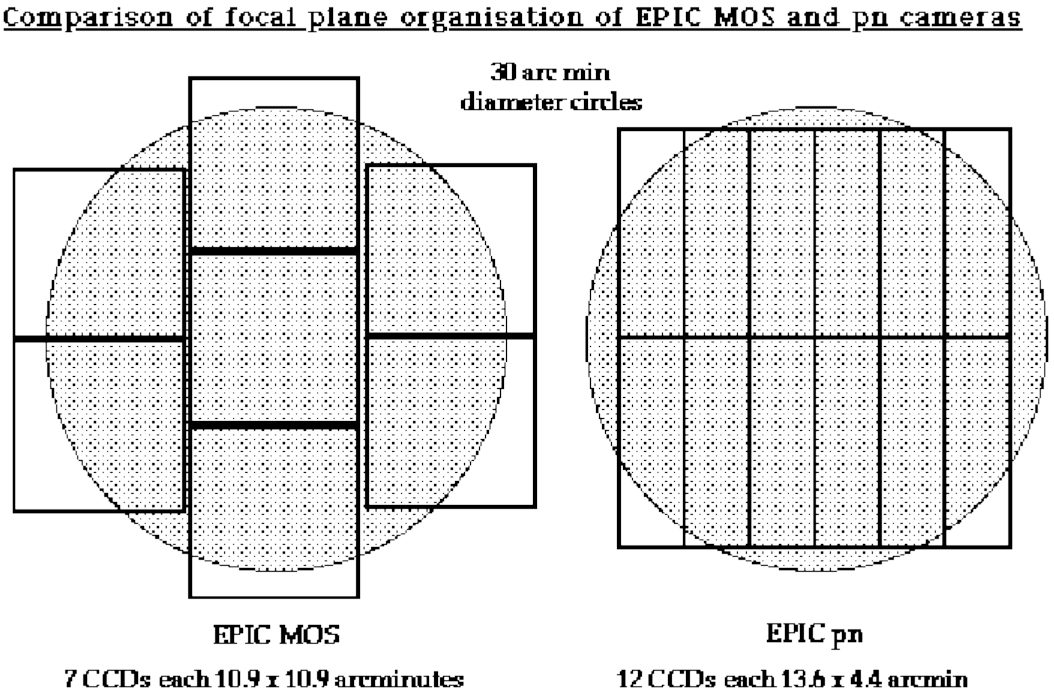

FIGURE 4.8: Schematic view of MOS (left) and pn (right). The shaded circle areas correspond to the field of view with 30 arcmin (XMM User's Handbook).

4.4 Reflection Grating Spectrometer (RGS)

4.4.1 Overview

RGS consists of Reflection Grating Assemblies (RGA) and CCDs (RGS Focal Cameras: RFC) that detect photons dispersed by the RGA. RGS is sensitive to X-rays of 5-38 Å (0.35–2.5 keV) and has an energy resolution of 2.0 eV (@ 1 keV) for point sources. This makes it possible to separate and detect K-shell transition lines containing He-like triplet of C, N, O, Ne, Mg, and Si, and L-shell transition lines of Fe and Ni. Figure 4.11 shows the layout of the telescope, RGA and RFC. Two RGAs are placed between the telescope and MOS1 and 2, respectively. About 44% of photons reflected by the telescope incident the MOS, 40% are dispersed, and the rest are absorbed by the grating. RGS resolves the wavelength of the photon from the X-ray incident position on the RFC by the following diffraction grating equation described as:

$$m\lambda = d\,(\cos\beta - \cos\alpha), \tag{4.1}$$

where m $(= -1, -2, ...)$ is the spectral order, d is the groove spacing, λ is the X-ray wavelength, α is the angle between the incoming ray and the grating plane, and β is the angle between the outgoing ray and the grating plane. As shown in Figure 4.11, RGA, RFC, and MOS are placed on the Rowland circle, which reduces the aberration caused by arranging the gratings. 1st, 2nd, and higher order diffracted photons may be overlapped on the RFC. Since

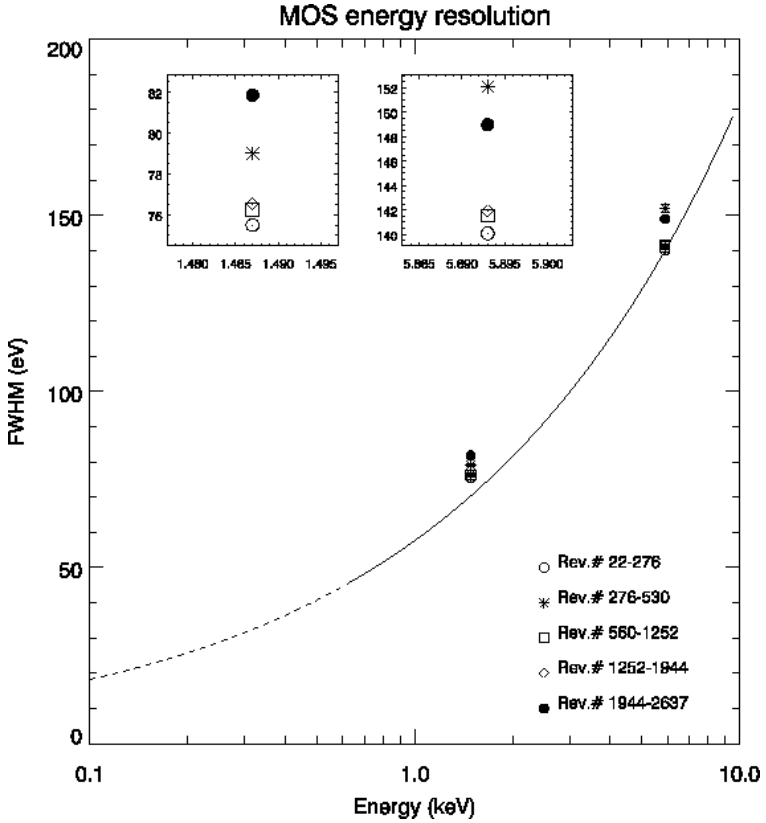

FIGURE 4.9: Energy resolution of MOS (XMM User's Handbook). Solid lines are the results of the ground calibration test and each data point is those of in-orbit calibration. The difference in the shapes of the data points corresponds to the difference in the date on which the data were obtained. Cooling to improve the energy resolution was performed between Rev.#530 and Rev.#560.

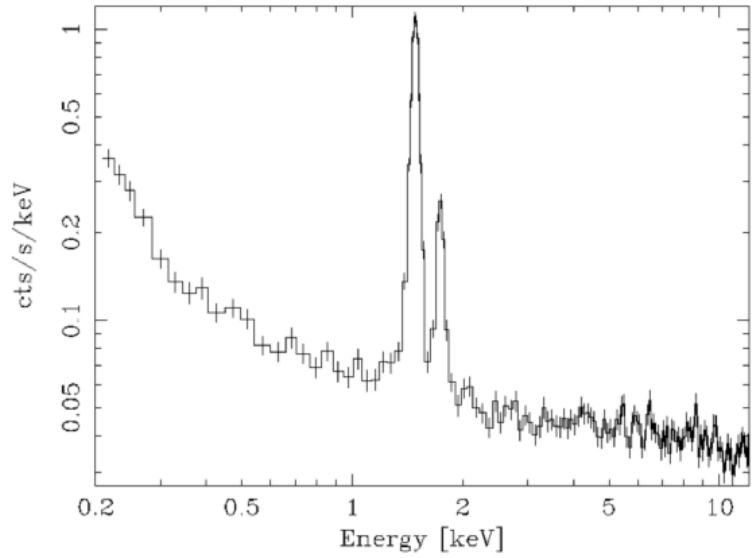

FIGURE 4.10: Background spectrum of the MOS (XMM User's Handbook). The emission lines at 1.5 keV and 1.7 keV are the K-shell emission lines of Al and Si, respectively.

CCDs are used as the X-ray detector, two pieces of information regarding the incident photon energy are obtained: the signal charge amount of the CCD and the incident position on the RFC. From these two pieces of information, we can separate the spectral order as shown in Figure 4.14.

RGA

RGA consists of 182 blazed gratings. As shown in Figure 4.12, blazed gratings have a sawtooth shape, which makes it possible to cause interference between diffracted photons of a specific wavelength and specific order and reflected photons by adjusting the incident angle (α) and the blaze angle. A plane grating maximizes the intensity of the 0 th-order photon, but a blazed grating can maximize the intensity of any order of diffracted photon due to this structure. In the case of RGA, the blaze angle and incident angle (α) are set so that the diffraction efficiency is maximized for the first-order photons of 15 Å. Each grating is a SiC substrate about 10 cm $\times$ 20 cm in size coated with 2000 thick gold. The groove density varies by about 10 % to correct aberrations on the RFC, but is about 646 mm^{-1}.

RFC

The RFC consists of 9 CCDs with almost the same specifications as the EPIC-MOS detector, arranged along the dispersion axis as shown in Figure 4.13. Each CCD is assigned an ID number from 1 to 9 in order from the longer wavelength side. Figure 4.14 shows an X-ray image obtained with RFC and a plot with the dispersion angle on the horizontal axis and the pulse height output from the CCDs on the vertical axis. The first- and second-order spectrum overlap on the RFC. The RFC has an energy resolution of 160 eV (FWHM) for 2 keV X-rays. The spectral orders are resolved by the energy resolution of the RFC (see the bottom panel of Figure 4.14).

4.4.2 Performance

We summarize the basic performance of RGS in Table 4.2. The centroid energies of the resonance and forbidden of OVII Heα lines that we focus on in this study are $\sim$574 eV and $\sim$561 eV, respectively. The RGS has an energy resolution of $\sim$1 eV in the energy band of 500 eV, which allows us to separate the OVII Heα lines.

Although there are X-ray detectors other than the RGS that have better energy resolution than that of CCDs, the RGS is particularly suited for spectroscopy of the O VII Heα lines. The grating spectrometers onboard the Chandra satellite (High Energy Grating: HEG, Medium Energy Grating: MEG, Low-Energy Transmission Grating: LETG) and the calorimeter onboard the Hitomi satellite (Soft X-ray Spectrometer: SXS) also have better energy resolution than that of CCDs. Figure 4.15 shows a comparison of effective area and energy resolution between these detectors and RGS. RGS has better performance than the SXS and the grating spectrometers onboard the

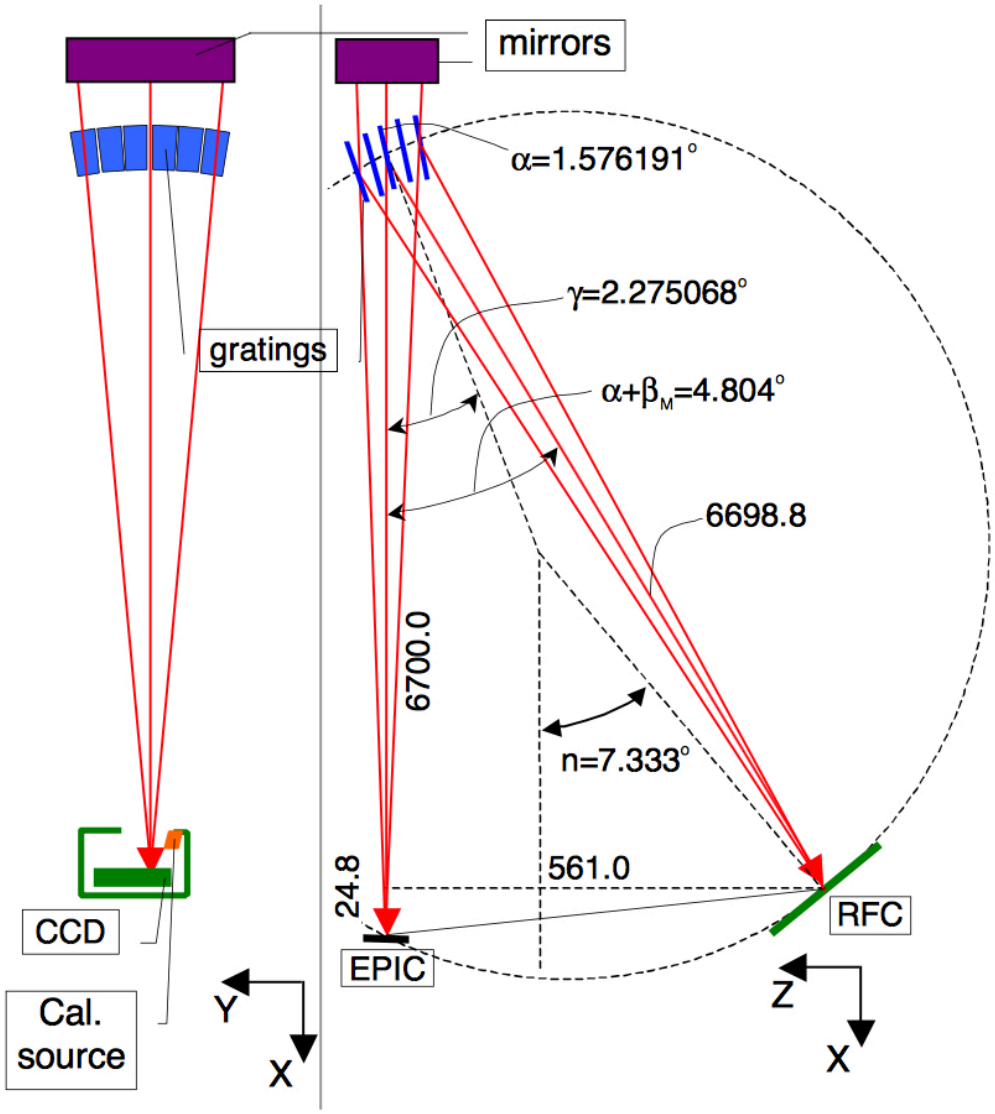

FIGURE 4.11: Schematic view of RGS (taken from XMM Users Handbook). The RGA is shown in blue on the dashed circle. The unit of length is mm. The solid red line corresponds to the optical path of X-rays.

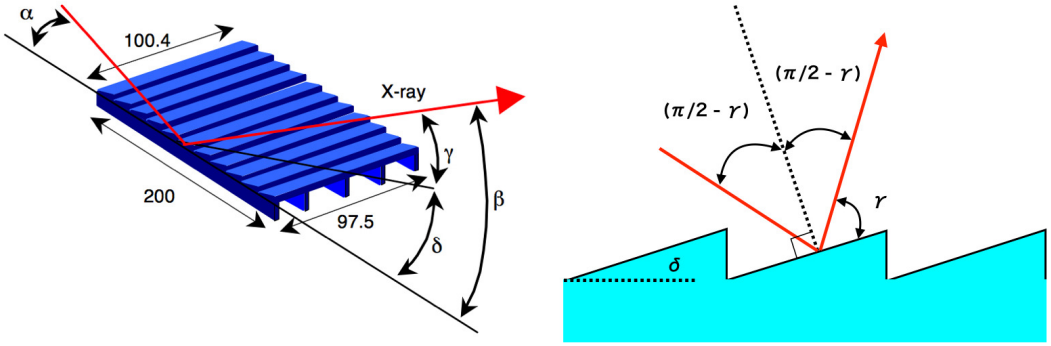

FIGURE 4.12: (left) Schematic view of RGS (taken from XMM Users Handbook). α, β, and σ represent the angle of incidence, the angle of diffraction, and the tilt of the mirror surface, respectively. The unit of length is mm. (right) Schematic view of a blazed grating.

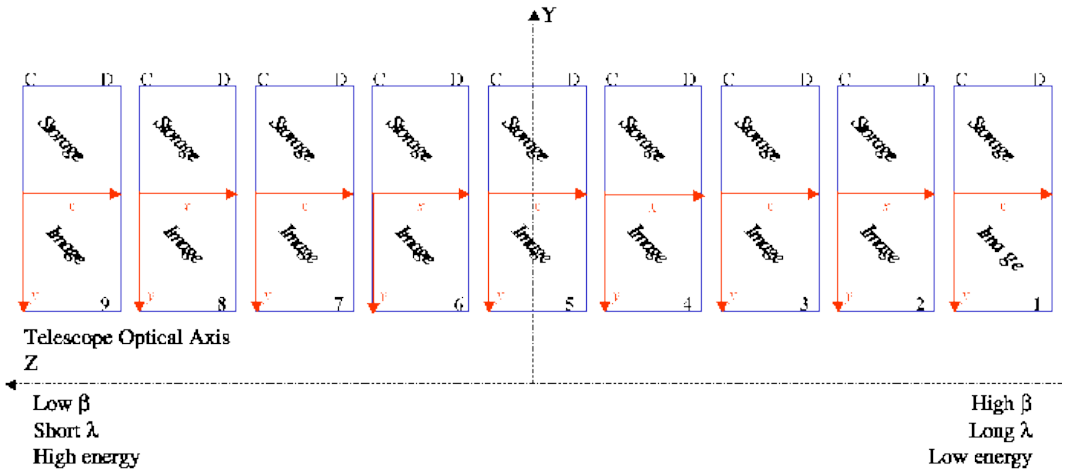

FIGURE 4.13: Sketch of an RFC chip array (XMM User's Handbook). The Z axis is the dispersion axis. The left side corresponds to the short wavelength side (high energy side and the right side corresponds to the long wavelength side (low energy side).

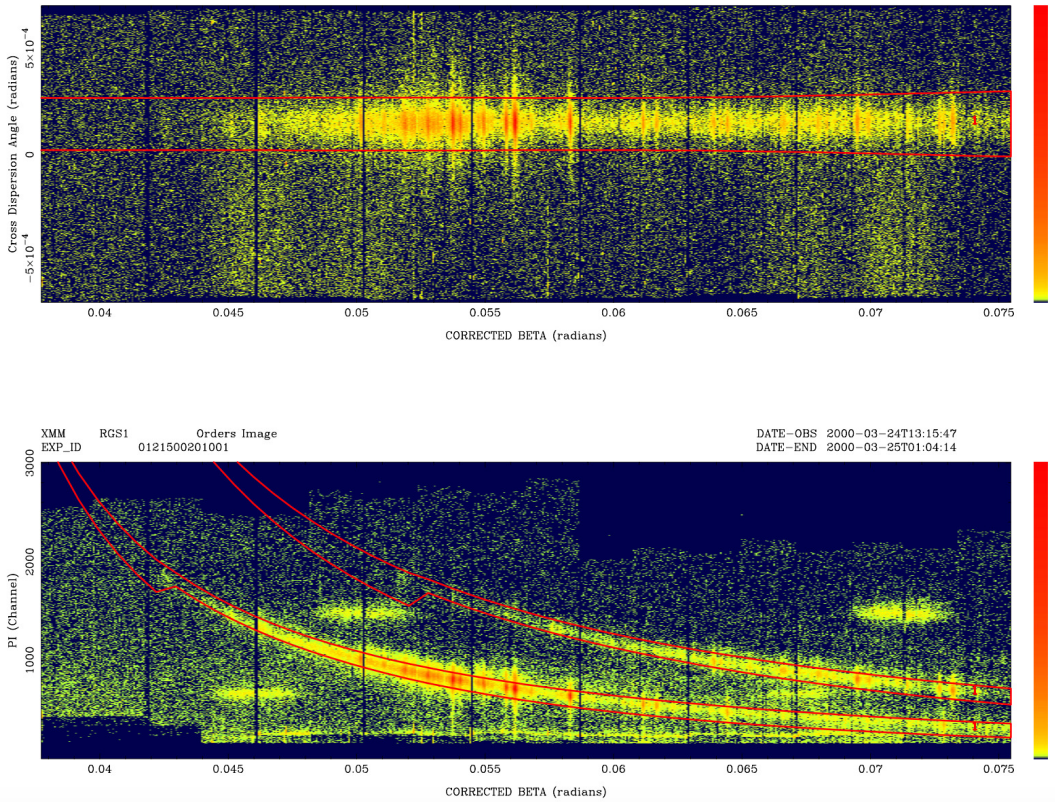

FIGURE 4.14: (Top) X-ray image obtained with RFC. The horizontal axis corresponds to the dispersion angle, and the vertical axis corresponds to the off-axis angle along the vertical direction of the dispersion axis. (Bottom) The X-ray image called "Banana plot". The horizontal axis corresponds to the dispersion angle, and the vertical axis corresponds to the pulse height output from the CCDs. The area enclosed by the solid red line corresponds to the first-order on the bottom and the second-order on the top (XMM Users Handbook).

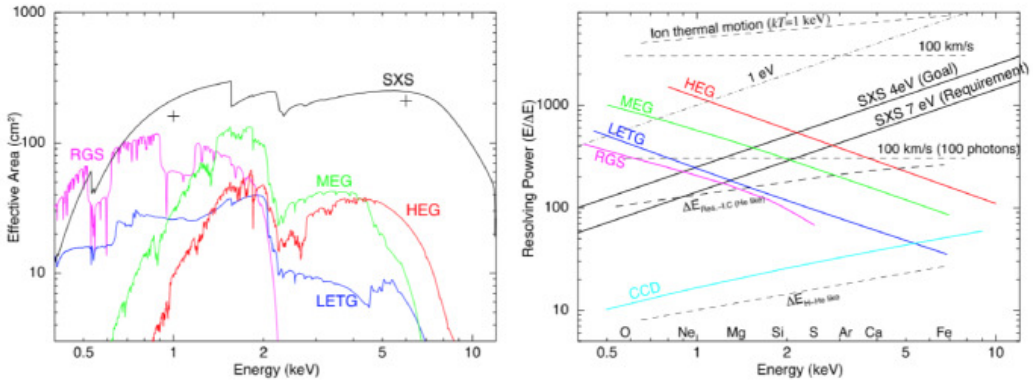

FIGURE 4.15: Performance comparison between RGS and other high-resolution X-ray spectrometers (Mitsuda et al., 2010). The left and right figures show the effective area and energy resolution, respectively.

Chandra satellite in the energy band below 1 keV where the L-shell transition lines of Fe and the K-shell transition lines of C, N, and O are detected.

TABLE 4.2: Performance of the RGS (XMM User's Handbook)

Energy range	0.35–2.5 keV (first-order)
	0.62–2.5 keV (second-order)
Pixel size	27 μm
Energy resolution (FWHM)	$\sim$ 1.0 eV (@0.5 keV)

4.4.3 Background

The RGS background consists of X-ray emissions from other celestial objects (cosmic X-ray background; CXB) and instrumental background, and these backgrounds have to be removed for spectral analysis. Similar to MOS, the instrumental background of the RGS includes detector noise and the particles-induced background. The particles-induced background consists of high-energy charged particles (minimum ionizing particles, protons, ions of heavy elements) incident from outside the telescope field of view and soft protons that incident from the field of view of the telescope. The high-energy charged particles are uniformly incident on the RFC. The RGS has two pieces of information about the energy of the detected event: the position (dispersion angle) and the pulse height of the RFC. The background induced by high-energy charged particles can be removed by extracting the event from the region where the energy obtained from the peak value of the CCD and the energy obtained from the detection position are not inconsistent (region enclosed by the solid red lines in Figure 4.14). Since the other background, which is caused by soft protons, is time-dependent, the flux level is estimated from the light curve of detected photons and can be removed by setting an appropriate threshold.

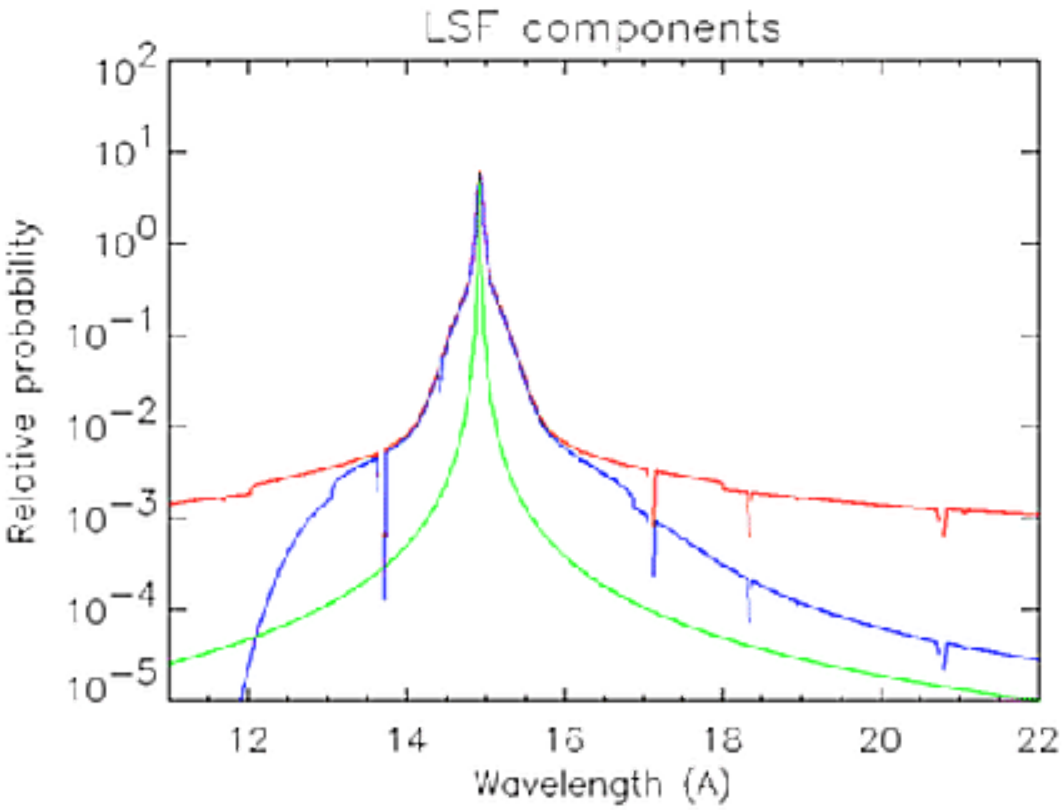

FIGURE 4.16: Line spread function (LSF) of RGS (XMM User's Handbook): the mirror response (green), broadened after folding with the RGA response (red), and after applying the detector energy selections (blue). All components are normalised to their maximum.

4.4.4 Response Function

The RGS response function for a point source consists of the Line Spread Function (LSF) and the effective area. The LSF is the observed X-ray distribution along the dispersion axis when monochromatic X-rays are incident from the optical axis. The LSF is a convolution of the response functions of mirrors and the grating, followed by convolution with the detector response (see Figure 4.16).

Since RGS is not equipped with a slit, the spatial broadening of the source is convolved with the spectrum. In order to perform a high-resolution spectroscopy of a diffuse source with RGS, it is required to generate a response function convolved with the brightness distribution along the dispersion axis of the source. The off-axis angle θ of the incident photon corresponds to the deviation of the wavelength:

$$\Delta\lambda = 0.138 m^{-1} \, (\theta/\mathrm{arcmin}) \, , \tag{4.2}$$

where m is the spectral order. For a diffuse sources, the energy resolution of

the RGS is degraded. The centroid wavelengths of the resonance and forbidden of OVII Heα lines are $\sim$21.60 Å and $\sim$22.10 Å, respectively. A difference of 0.5 Å between the centroid wavelengths of these emission lines corresponds to a source diameter of about 4 arcmin from Equation (4.1). Therefore, in this study, we observe objects with a diameter of less than 4 arcmin for spectroscopy of the O VII Heα lines.

Chapter 5

Evidence for RS and CX in SNRs

5.1 Our Objective and Target Selection

As mentioned in Chapter 3, recent studies pointed out the importance of CX and RS in SNRs. Both of these processes are predicted to occur in SNRs by previous calculations (e.g., Lallement, 2004; Kaastra and Mewe, 1995). However, it is not clear under what physical conditions CX and/or RS efficiently take place, since established observational evidence is limited.

Possible detections of the spectral feature of CX are reported from RGS observations of the Cygnus Loop (Uchida et al., 2019) and Puppis A (Katsuda et al., 2012). If CX takes place in these SNRs, its emitting region would be the outer edge of the shock front (a few percent of the shock radius) in contact with dense clouds (see Chapter 3). However no quantitative constraint on the CX emitting region has been performed. In the case of RS, several observational signatures have been reported such as a high forbidden-to-resonance ratio of O VII Heα lines obtained from RGS spectra of DEM L71 (van der Heyden et al., 2003) and N23 (Broersen et al., 2011). A difference in surface brightness between forbidden and resonance lines also supports the presence of RS (e.g., van der Heyden et al., 2003). However there is no strong observational evidence has been established so far.

We perform a high-resolution X-ray spectroscopy of N49, J0453.6−6829 with the RGS onboard XMM-Newton in order to obtain observational evidence for CX and RS from SNRs based on quantitative measurements. These targets are chosen among the SNRs located in the LMC, since they are relatively compact ($\sim 2'$ in diameter) remnant, which makes it possible to perform high-resolution X-ray spectroscopy with the RGS. Furthermore, both SNRs are located in dense gases. As previous studies pointed out, CX is considered to be induced by collisions between SNRs and surrounding dense gases (e.g., Uchida et al., 2019). Additionally, N49 has a spherically asymmetric structure where the effect of RS is expected to be observed (Kaastra and Mewe, 1995). Therefore, these SNRs are ideal targets for our study.

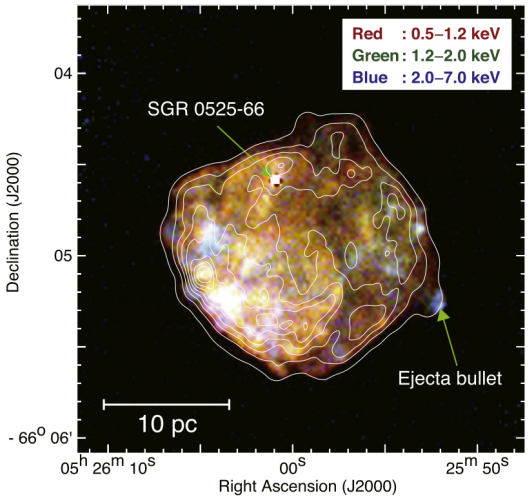

FIGURE 5.1: X-ray image superimposed and the radio continuum contours of N49 (Yamane et al., 2018). The X-ray image was observed with the Chandra satellite (Park et al., 2012). The soft gamma-ray repeater and the "bullet" ejecta are indicated by white arrows.

5.2 N49

5.2.1 Overview of N49

N49 is a middle-aged ($\sim$ 4800 yr; Park et al., 2012) SNR located in the LMC. Its radio emission shows a clear shell structure, while the X-ray emission is bright in the southeastern part of the inner radio shell (Figure 5.1). The western part has a "bullet" like the structure of ejecta (Park et al., 2012). Although the origin of N49 is somewhat controversial, most recent research supports that it originated from a core-collapse explosion based on a possible association with the soft gamma-ray repeater (SGR) 0526–66 (Cline et al., 1981) and the presence of a dense interstellar medium (ISM; e.g., Banas et al., 1997; Yamaguchi et al., 2014). The thermal X-ray emission is explained by a mixture of two components; metal-rich ejecta and a shock-heated ISM (e.g., Uchida et al., 2015). It is also notable that N49 is in an overionized state (Uchida et al., 2015) and is interacting with dense molecular clouds on the eastern side (Banas et al., 1997; Yamane et al., 2018). Due to the interaction with molecular clouds, the thermal X-ray emission of N49 is particularly bright on the southeastern rim. N49 is an attractive object since Kaastra and Mewe (1995) pointed out that the effect of RS can show up if an SNR has such a spherically asymmetric structure.

5.2.2 Observation and Data Reduction

N49 was observed with the XMM-Newton satellite (Jansen et al., 2001) in 2001 (Obs.ID 0113000201) and 2007 (Obs.ID 0505310101). The observation in 2007 was performed with a roll angle which placed N49 and a nearby SNR, N49B, along the dispersion direction of the RGS, making it difficult to

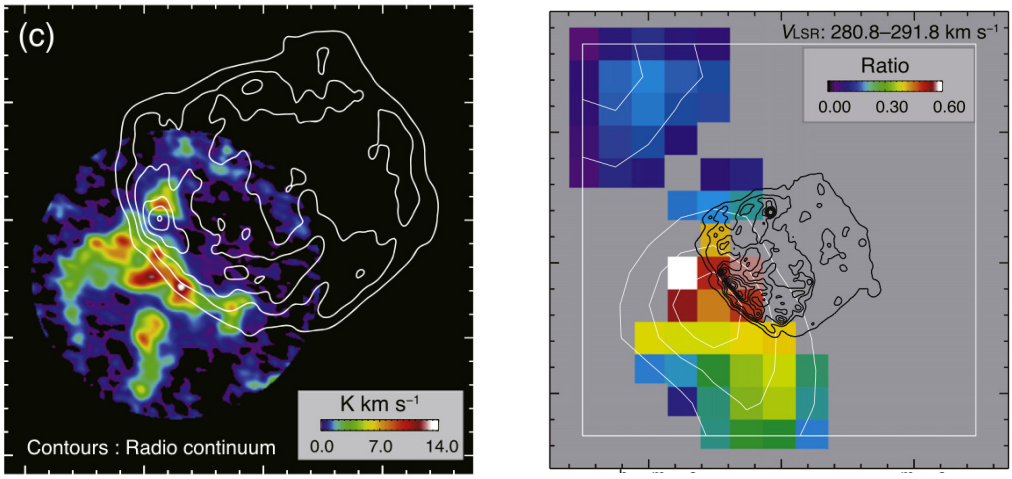

FIGURE 5.2: (left) ^{12}CO($J = 1 - 0$) integrated intensity maps (Yamane et al., 2018). White contours indicate the hard X-rays observed with Chandra. (right) Distribution of the ^{12}CO($J = 3 - 2$)/^{12}CO($J = 1 - 0$) intensity ratio (Yamane et al., 2018). The contours indicate broadband X-rays.

extract the RGS spectra of N49. We thus analyzed only the data obtained in 2001. For our spectral analysis, we used the RGS (Herder et al., 2001) and the EPIC MOS (Turner et al., 2001) data. We reduced the data using XMM Science Analysis Software version 16.1.0. The RGS data were processed with the RGS pipeline tool `rgsproc`. To discard periods of background flares, we applied good time intervals based on the count rate in CCD9 (Figure 5.3), which is the closest to the optical axis of the mirror and most affected by the background flares. The resulting effective exposure time is 11 ks for both RGS1 and RGS2. Since the second-order spectra are of low statistical quality, we analyzed only the first-order spectra.

5.2.3 Analysis

We analyzed the spectra using version 3.04.0 of the SRON SPEX package (Kaastra et al., 1996) with the maximum likelihood C-statistic (Cash, 1979; Kaastra, 2017). The RGS spectra were fitted simultaneously with those of MOS1 and 2. To account for the spatial broadening of the source, we multiplied spectral models with the SPEX model `lpro`, to which we input the MOS1 image of the source. Our models have two absorption models: one for the Milky Way and the other for the LMC. The column density of the former was fixed to 6×10^{20} cm^{-2} (Dickey and Lockman, 1990) whereas that of the latter is left free. The elemental abundances for the LMC absorption were fixed to values found in the literature (~ 0.3 solar; Russell and Dopita, 1992; Schenck et al., 2016).

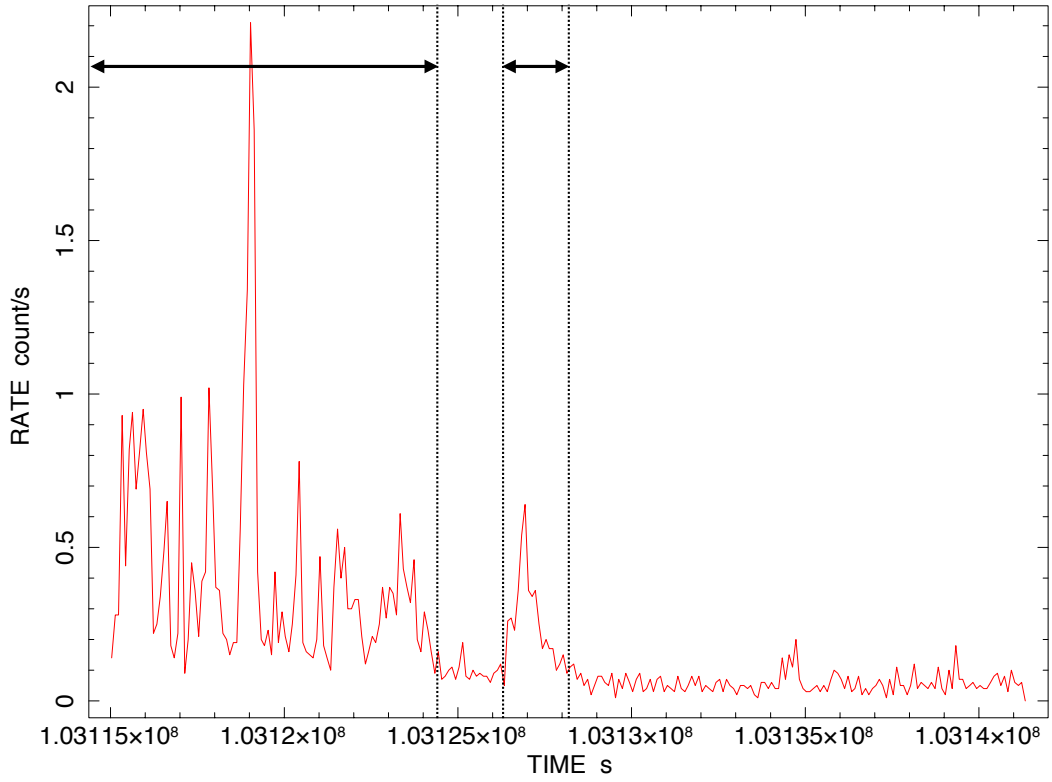

FIGURE 5.3: Light curve of the RGS 1. The areas indicated by the arrows are the periods of background flares.

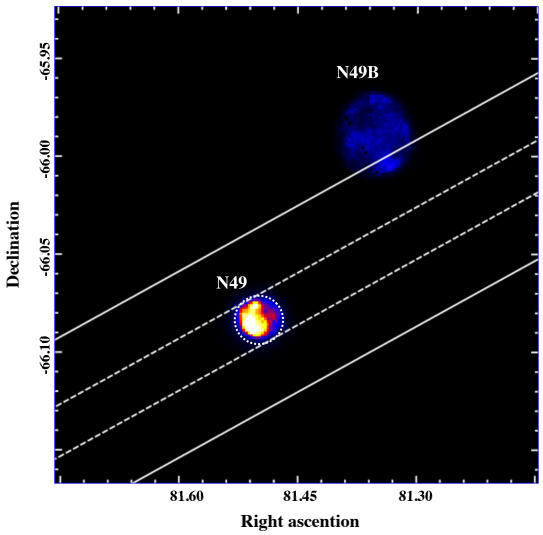

FIGURE 5.4: EPIC-MOS image (0.4–8.0 keV) of N49. The cross-dispersion width of the RGS (5 arcmin) is in between the white solid line. The spectral extraction region is enclosed by the white dashed line. N49B is another SNR near N49.

Spectral Analysis with CIP Model

Figure 5.5 shows MOS1 and combined RGS1+2 spectra of N49. Prominent lines are detected at ∼12 Å (Ne X Lyα), ∼13.5 Å (Ne IX Heα), ∼15 Å (Fe XVII Lα; 3d–2p), ∼16 Å (O VIII Lyβ), ∼17 Å (Fe XVII Lα; 3s–2p), ∼20 Å (O VII Heβ, O VIII Lyα), ∼22 Å (O VII Heα). We first applied a two-component NEI model (`neij`; Kaastra and Jansen, 1993) absorbed by neutral gas to the spectra. The NEI model consists of emissions from the overionized hot ejecta and an ionizing cool component originating from the swept-up ISM (Uchida et al., 2015). Although SGR 0526−66 cannot be spatially resolved with the RGS, according to the result of Uchida et al. (2015), the emission is negligible compared to that from N49 in the energy band covered by the RGS (0.3–2.0 keV). This model is described as:

$$Neutral\ Interstellar\ Abs. \times [NEI\ (ISM) + NEI\ (ejecta)]. \tag{5.1}$$

Free parameters of the NEI components include the electron temperature ($kT_{\rm e}$), ionization time scale ($n_{\rm e}t$, where $n_{\rm e}$ and t are the electron number density and the elapsed time since shock heating or rapid cooling, respectively), and emission measure ($n_{\rm e}n_{\rm H}V$). In addition to these parameters, the abundances of O (=N=C), Ne, Mg, Si, S, Ar, and Fe (=Ni) of the ejecta were set free. The `neij` model has another parameter $kT_{\rm init}$, which represents an initial temperature before a rapid cooling or a shock heating of the plasma. Uchida et al. (2015) determined $kT_{\rm init}$ for the ejecta component mainly from the ionization state of the Fe Kα emission at ∼6.6 keV. Since the line centroid is out of the wavelength band of the RGS data, we fixed the $kT_{\rm init}$ of the ejecta component at 11 keV based on Uchida et al. (2015). On the other hand, the $kT_{\rm init}$ of the ISM component is fixed at ∼ 0 keV.

Figure 5.5 shows the result of the spectral fitting with the two-component NEI model (hereafter, NEI model). The best-fit parameters are listed in Table 5.1. The model well reproduces the overall MOS spectrum; the best-fit parameters of $kT_{\rm e}$ and $n_{\rm e}t$ of the ejecta component are consistent with those obtained by Uchida et al. (2015). Focusing on the RGS spectrum in Figure 5.6, however, we found discrepancies between the model and the data especially around the O VII triplet, O VIII Lyβ, and Fe XVII Lα series.

Plasma Diagnostic Using O VII Heα Line Ratio

We first focus on the O VII Heα line, more specifically on its G-ratio. As mentioned in Chapter 3, the G-ratio is strongly depends on $kT_{\rm e}$ (see Figure 5.7). We assume here that the emitting plasma is in an ionizing state since most of the O VII Heα line emission of N49 is attributed to the shocked ISM (Figure 5.5 (a)). Fitting with four Gaussians, we estimated the G-ratio of the O VII Heα line observed in N49, which is plotted in Figure 5.7. The observed G-ratio obviously requires an unreasonably low $kT_{\rm e}$ (< 0.15 keV) with any reasonable range of $n_{\rm e}t$, indicating necessity of some physical process to enhance the G-ratio.

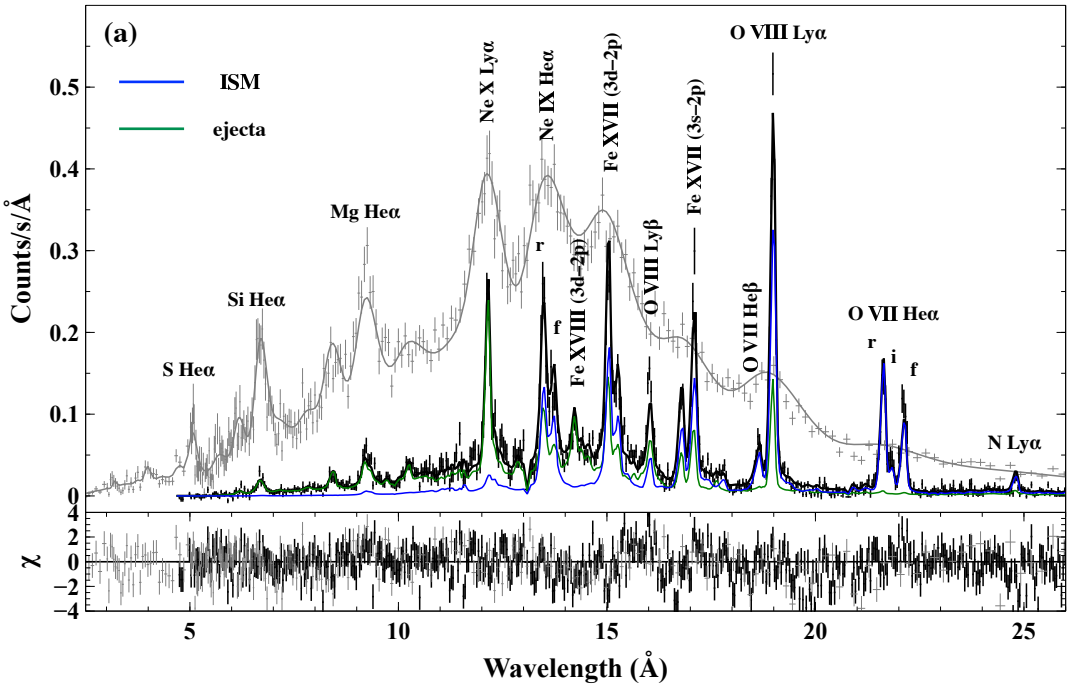

FIGURE 5.5: RGS +2 (black) and MOS1 (gray) spectra of N49. Overlaid is the best-fit "NEI" model.

5.2.4 Discussion

Physical Origin of High G-ratio

Our analysis revealed that the RGS spectrum of N49 shows a high G-ratio. As described in Chapter 3, the G-ratio is enhanced by CX and RS, inner-shell ionization and recombination plasma (RP). Here, we consider the physical processes that explain the high G-ratio of N49.

Inner-Shell Ionization As mentioned in Chapter 3, X-ray fluorescence due to inner-shell ionization of Li-like ions increase the G-ratio. The ion fraction of Li-like O is expected to increase in low-ionized plasma. Therefore, reducing the $n_e t$ is expected to increase the G-ratio (Figure 5.7). A low value of $n_e t < 3 \times 10^9$ cm^{-3} s is required to explain the G-ratio with an electron temperature of 0.2 keV. t corresponds to the elapsed time since the plasma was shock heated. Therefore, in this case, $t < 100\ (1\ \mathrm{cm}^{-3}/n_e)$ yr for a typical interstellar space density of $n_e = 1$. Because N49 is 5000 years old, it is unreasonable that only a few decades have passed since the ISM plasma of N49 was heated. Therefore, we rejected the possibility of the contribution of X-ray fluorescences due to inner-shell ionization of Li-like O.

RP We next examine the possibility that the ISM plasma of N49 is in an over-ionized state (RP). Figure 5.8 shows the temperature dependence of the G-ratio of an over-ionized plasma. In this case, there seems to be a wide

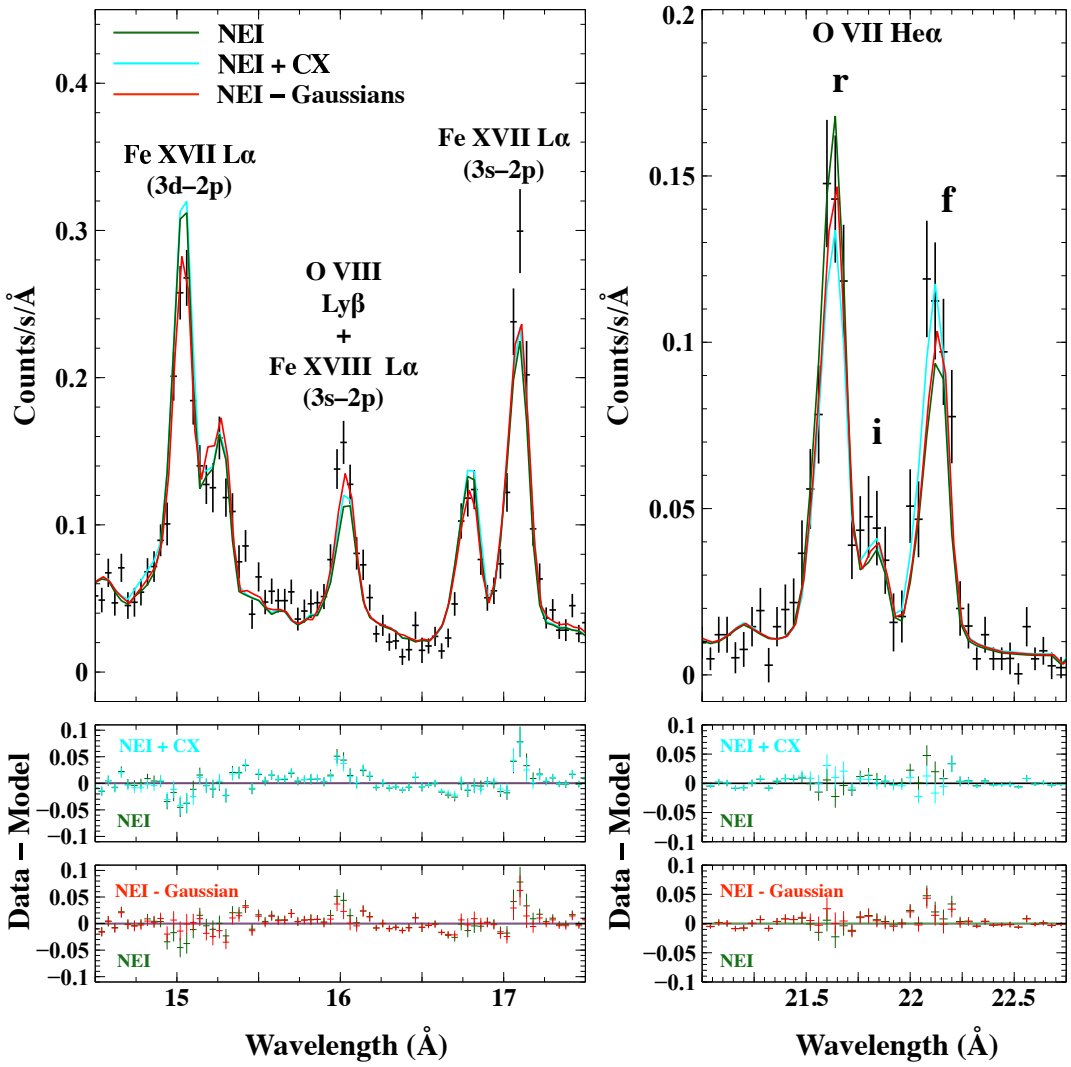

FIGURE 5.6: Close-up views of the RGS spectrum (Figure 5.5) around Fe XVII Lα and O VIII Lyβ (left) and O VII Heα (right). The dark green, cyan, and red solid lines in the top panels represent the best-fit "NEI", "NEI+CX", and "NEI−Gaussians" models, respectively. The middle and bottom panels show residuals from the models with the same color scheme as the top panels.

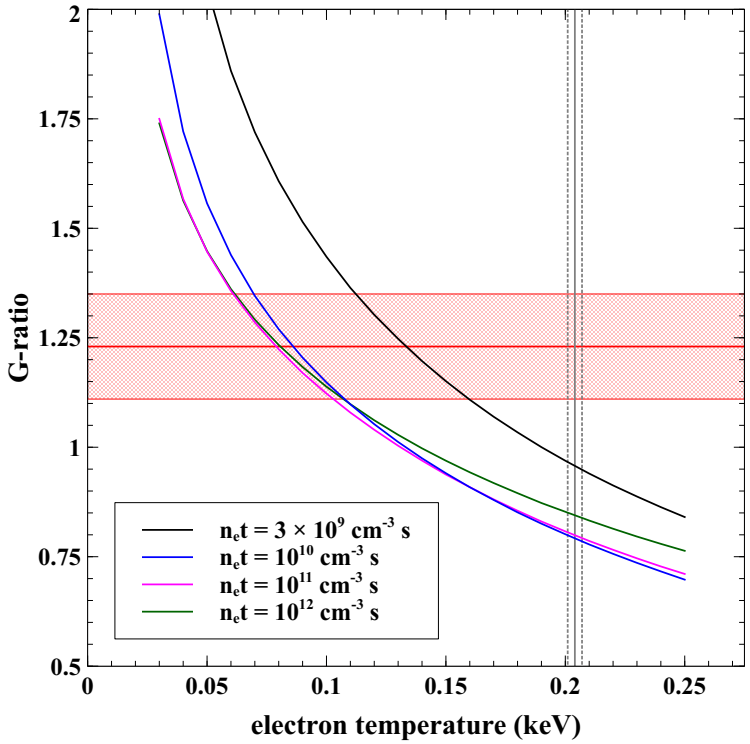

FIGURE 5.7: Relation between kT_e and the G-ratio of OVII Heα. The solid curves represent the G-ratio expected for an ionizing plasma emission predicted by the `neij` model in SPEX. The colors of each line indicate $n_e t$ assumed. The red hatched area denotes the G-ratio derived from the observed line ratio and its statistical error. The gray lines indicate kT_e from the best-fit NEI model.

TABLE 5.1: Best fit parameters of N49

Component	Parameters (unit)	NEI	NEI + CX	NEI - Gaussians
Absorption	$N_{\rm H}(MW)$ (10^{22} cm^{-2})	0.6 (fixed)	0.6 (fixed)	0.6 (fixed)
	$N_{\rm H}(LMC)$ (10^{22} cm^{-2})	3.1 ± 0.1	2.8 ± 0.1	3.3 ± 0.1
ISM	$kT_{\rm e}$ (keV)	0.204 ± 0.003	0.230 ± 0.006	0.205 ± 0.003
	$n_{\rm e}t$ (10^{11} cm^{-3} s)	> 10	> 10	> 10
	EM (10^{56} cm^{-3})	260 ± 20	170^{+20}_{-10}	322^{+23}_{-22}
Ejecta	$kT_{\rm e}$ (keV)	0.61 ± 0.01	0.63 ± 0.01	$0.56^{+0.08}_{-0.01}$
	$kT_{\rm init}$ (keV)	11 (fixed)	11 (fixed)	11 (fixed)
	$n_{\rm e}t$ (10^{11} cm^{-3})	$7.2^{+0.5}_{-0.3}$	$7.2^{+0.4}_{-0.3}$	$6.9^{+1.0}_{-0.4}$
	O(= C = N)	$0.71^{+0.16}_{0.06}$	$0.67^{+0.20}_{-0.14}$	1.3 ± 0.1
	Ne	$0.96^{+0.09}_{-0.07}$	$0.94^{+0.09}_{-0.06}$	$1.0 \pm 0,1$
	Mg	0.75 ± 0.07	$0.72^{+0.07}_{-0.06}$	0.75(fixed)
	Si	$0.87^{+0.08}_{-0.06}$	$0.85^{+0.08}_{-0.06}$	0.87(fixed)
	S	1.2 ± 0.1	1.2 ± 0.1	1.2(fixed)
	Ar	1.8 ± 0.5	$1.8^{+0.4}_{-0.3}$	1.8(fixed)
	Fe	0.32 ± 0.03	$0.29^{+0.03}_{-0.02}$	0.32 ± 0.01
	EM (10^{56} cm^{-3})	58 ± 4	57^{+5}_{-2}	53 ± 0.1
CX	$kT_{\rm e}$ (keV)		(= value of the ISM)	
	abundance		(= abundances of the ISM)	
	$v_{\rm collision}$		270 ± 110	
	EM (10^{56} cm^{-3})		47^{+25}_{-13}	
	C-statistic/d.o.f.	4700/3211	4660/3214	4611/3190

range of parameters ($kT_{\rm e}$ and $n_{\rm e}t$) that reproduce the observed G-ratio. However, as described below, when we also focused on observational spectra in wavelength bands other than the O VII Heα emission line, we found that the possibility that the ISM is the RP can be almost ruled out. As shown in Figure 5.9, the RP model that can explain the G-ratio overestimates the O VIII Lyα intensity. The intensity ratio of O VIII Lyα and O VII Heα reflects the ion fraction of H-like O and He-like O ions. The O VIII Lyα / O VII Heα ratio in the RGS spectrum of N49 does not require the high H-like O / He-like O ratio expected by the RP model. Therefore, we also rejected the possibility that the ISM plasma of N49 is in an over-ionized state.

CX As suggested by Uchida et al. (2019), the CX emission can be enhanced particularly in a region where a shock is interacting with dense gas. CX is therefore promising in the case of N49 since it is interacting with surrounding molecular clouds (Yamane et al., 2018). We thus added a CX model (Gu et al., 2016) to the NEI model. All the abundances and $kT_{\rm e}$ for the CX component were coupled to those of the ISM component. The collision velocity $v_{\rm collision}$ (*i.e.* shock velocity) was allowed to vary. We assumed a multiple collision case in which an ion continuously undergoes CX until it becomes neutral. This model is described as:

$$Neutral\ Interstellar\ Abs. \times [NEI(ISM) + NEI(ejecta) + CX]. \quad (5.2)$$

The best-fit "NEI+CX" model is displayed in Figure 5.10, and the parameters are listed in Table 5.1. Although the addition of the CX component improves the residuals at the O VII triplet, the discrepancies still remain around O VIII

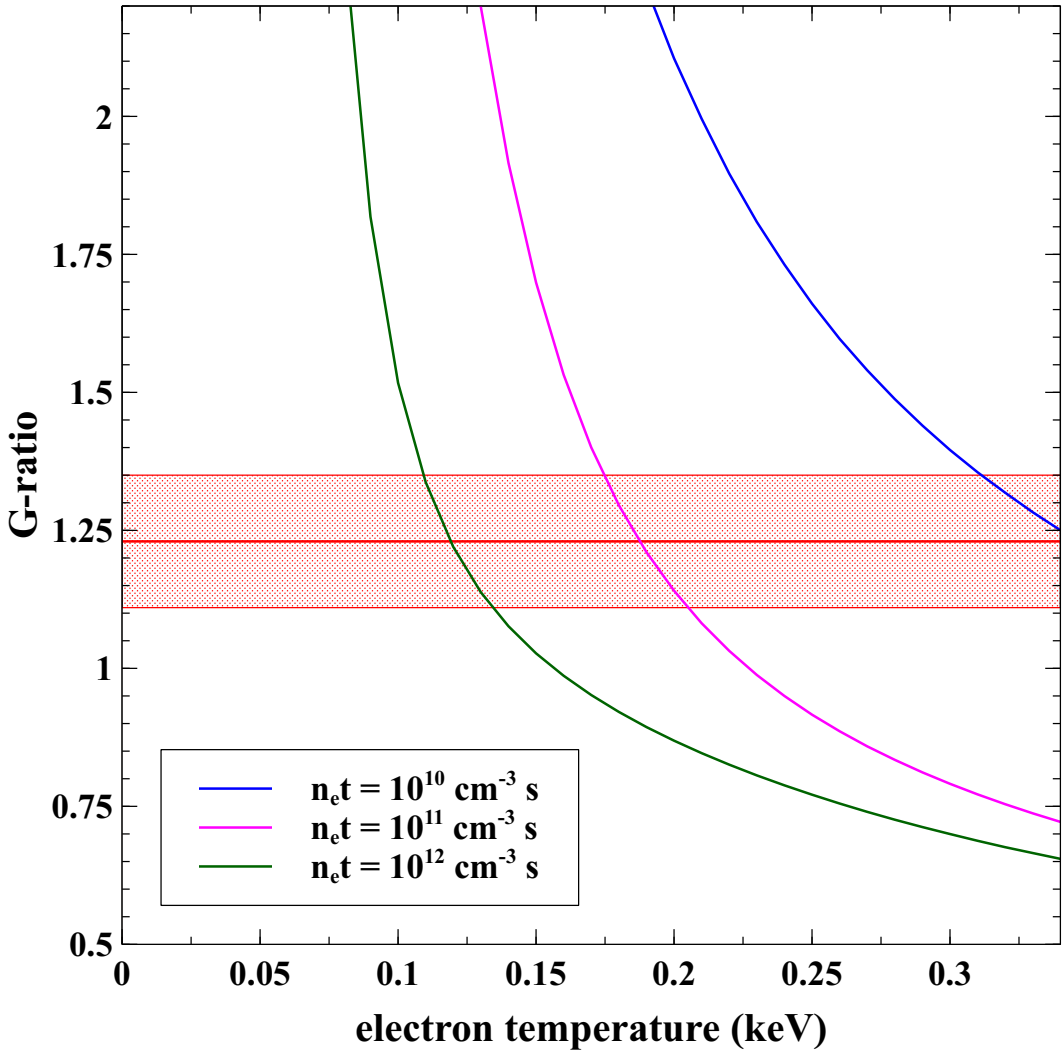

FIGURE 5.8: Same as 5.7 but the G-ratio for RP.

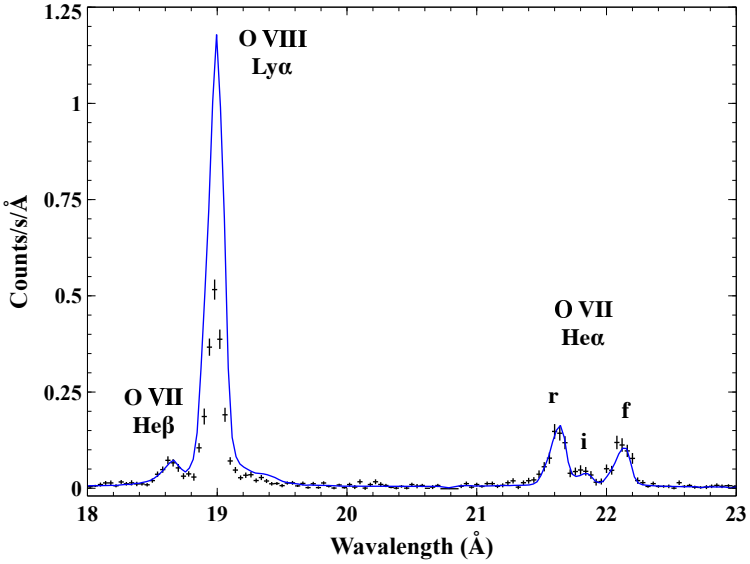

FIGURE 5.9: The fitting result of O VIII Lyα and O VII Heα lines when the ISM plasma of N49 is RP.

Lyβ and Fe XVII Lα series (Figure 5.6). Therefore, we conclude that the NEI + CX model is insufficient to describe the spectrum of N49.

RS RS is other possible process that would be responsible for the enhanced G-ratio. The observed high Fe XVII (3s–2p)/(3d–2p) and O VIII Lyβ/α ratios can also be caused by RS, as pointed out by previous studies (e.g., Xu et al., 2002; Hitomi Collaboration, 2018). To quantify the contribution of the scattering effect, we added negative Gaussians at wavelengths where lines of the ISM component are prominent in the best-fit NEI model: the O VII Heα intercombination, O VII Heα resonance, O VII Heβ, O VIII Lyα, O VIII Lyβ, Fe XVII Lα, and Ne IX Heα resonance lines. Since the oscillator strengths of the O VII and Ne IX forbidden lines are several orders of magnitude smaller than those of the other lines, we assume that the scattering effect is negligible for the forbidden lines. The free parameters of the NEI components are the electron temperature (kT_e), ionization time scale ($n_e t$), and emission measure ($n_e n_H V$). The abundances of O (=N=C), Ne, and Fe (=Ni) of the ejecta were set free and the abundances of Mg, Si, S, and Ar were fixed to the values obtained in the NEI model fit. This model is described as:

$$Neutral\ Interstellar\ Abs. \times [NEI(ISM) + NEI(ejecta) - Gaussians]. \quad (5.3)$$

The best-fit "NEI − Gaussians" model is displayed in Figure 5.11 and the best-fit parameters are listed in Table 5.1.

We compare transmission factors estimated based on the result from the "NEI − Gaussians" model fit with those expected for RS. The transmission factor p is defined as

$$p = \frac{A - \Delta A}{A}, \quad (5.4)$$

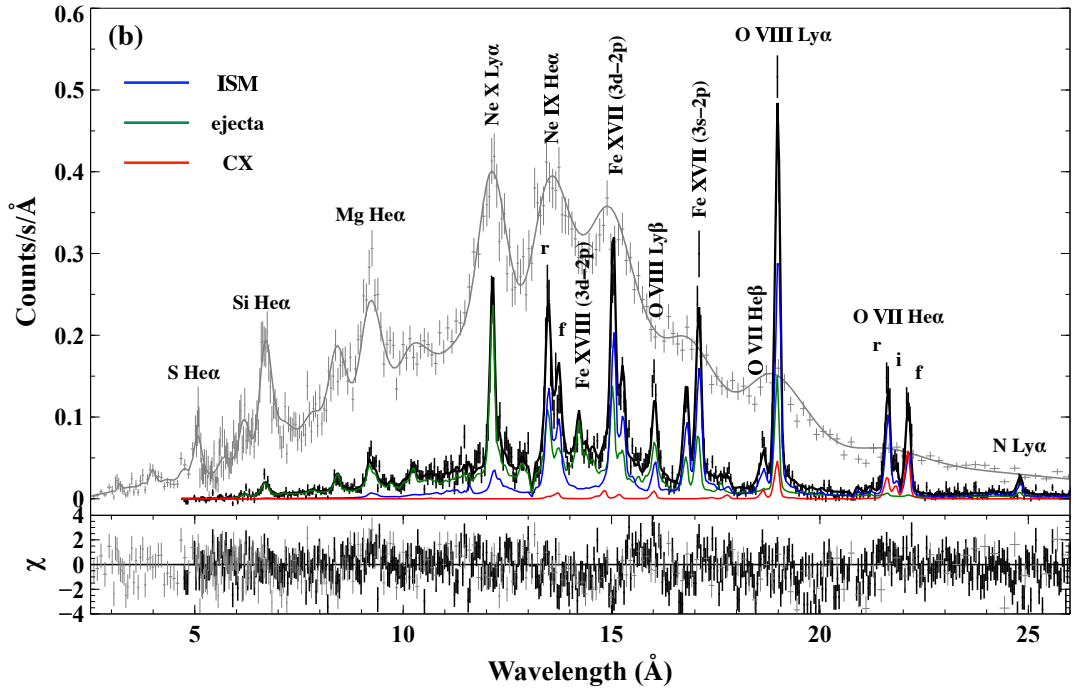

FIGURE 5.10: Same as Figure 5.5 but with the "NEI + CX" model. The red solid line represents the CX model.

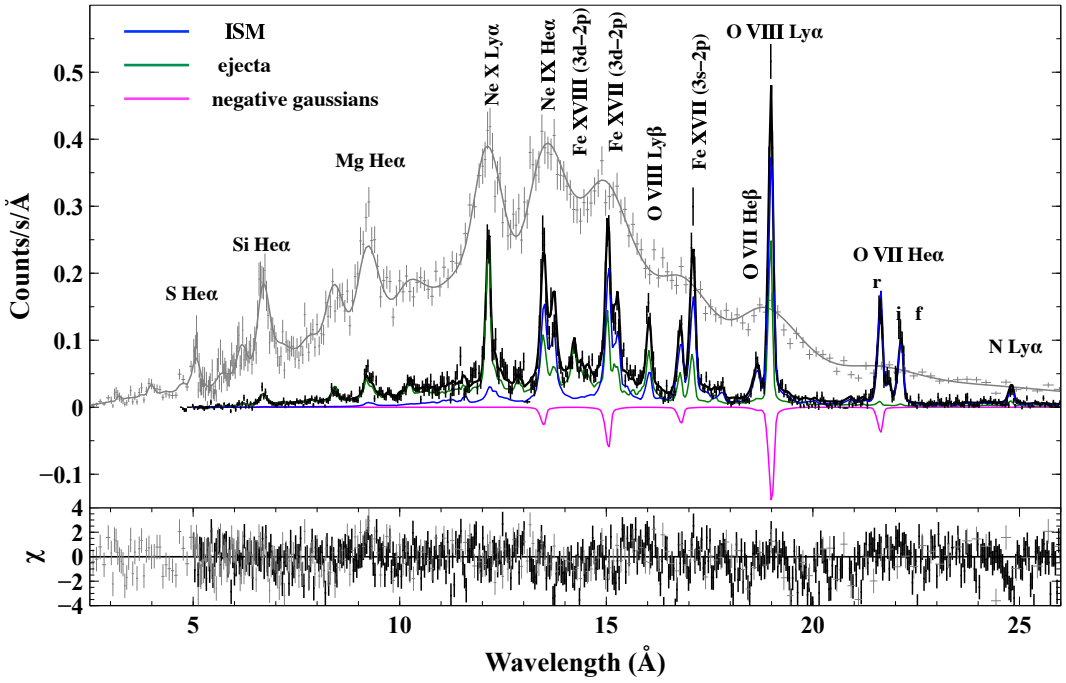

FIGURE 5.11: Same as Figure 5.5 but with the "NEI − Gaussians" model. The magenta solid line represents the negative Gaussians.

where A is the total number of photons emitted by the plasma, and ΔA is the number of photons scattered out of our line of sight. We can derive p for each line from the data, given that the best-fit normalizations of the negative Gaussians and the line intensities of the ISM component correspond to ΔA and A, respectively.

Referring to Kaastra and Mewe (1995), we calculate the transmission factors in a case where RS effectively occurs. Under the slab approximation as a simple geometrical model of the SNR rim, Kaastra and Mewe (1995) used a single-scattering treatment where a photon completely escapes from the line of sight at every scattering event. As shown by Park et al. (2003), the ISM plasma of N49 has a particularly bright emission at the southeastern rim. Assuming that the RS occurs dominantly at the southeastern rim, we adopt the same assumption as Kaastra and Mewe (1995). Then, the transmission factor is written as

$$p = \frac{1}{1 + 0.43\tau}, \tag{5.5}$$

where τ is the optical depth of the ISM plasma (Kastner and Kastner, 1990). The optical depth τ at the line centroid is given as Equation (3.55) in Chapter 3. We assumed a thermal equilibrium between all ions and electrons and neglected the micro-turbulence velocity. The oscillator strengths and ion fractions for each element were taken from SPEX. In our case, the absorption column density ($N_{\rm H}$) is the only free parameter.

In Figure 5.12, we compare the transmission factors estimated from the data and those calculated with Equation (5.5). They are roughly consistent if $N_{\rm H}$ is (3.0–10) $\times$ 10^{19} cm^{-2}, which corresponds to a plasma depth of (10–34)$\times$($n_{\rm H}$/cm^{-3}) pc. Since the plasma depth is comparable to the diameter of N49, $\sim$ 20 pc, the result supports that RS occurs at the rim of N49.

O VIII Lyβ/α ratio

The effect of RS roughly explains the observed line ratios, but as seen in Figure 5.12, OVIII Lyα requires a higher column density than the other lines. A possible explanation would be that RS occurs also in the Galactic Halo (GH), as proposed by Gu et al. (2016). According to Nakashima et al. (2018), GH spectra are represented by a CIE plasma model with $kT_{\rm e}$ $\sim$ 0.26 keV. Since such a plasma has a larger optical depth for the OVIII Lyα line than that of the OVII Heα resonance line, the GH should selectively reduce the intensity of OVIII Lyα. We applied the foreground CIE absorption model, `hot` (Plaa et al., 2004; Steenbrugge et al., 2005), to the NEI $-$ Gaussians model. The electron temperature and Fe abundance of the `hot` model are fixed to 0.26 keV and 0.56 solar, respectively (the other elemental abundances are fixed to the solar values), by referring to Nakashima et al. (2018). We found that the discrepancy cannot be reduced with the model, where the transmission factors of OVIII Lyα and OVII Heα are calculated to be $\sim$ 0.43 and $\sim$ 0.80, respectively.

The cause of the observed high OVIII Lyβ/α ratio (the measured value is 0.18 as an upper limit) is not clear. Uncertainties in the model of the Fe-L lines (e.g., Gu et al., 2019) might partially explain the result since OVIII Lyβ

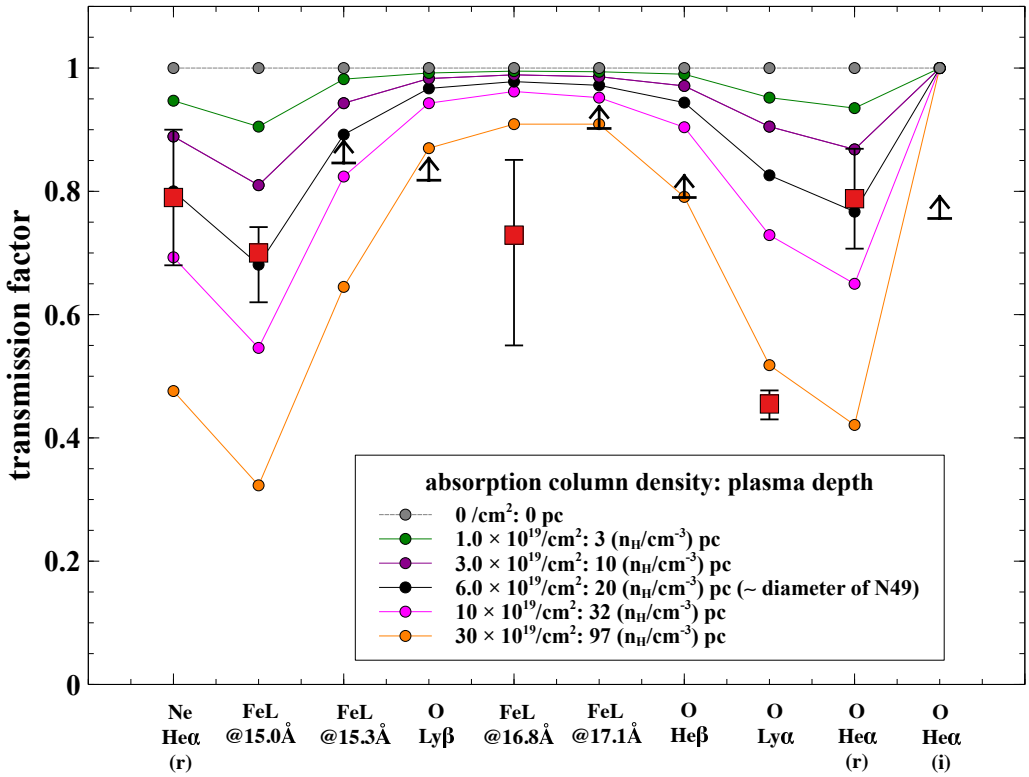

FIGURE 5.12: Transmission factors for each line. The squares and arrows are the values and lower limits derived from the observational data whereas the circles are those expected for RS. The colors indicate $N_{\rm H}$ assumed in the calculation.

overlaps with the FeXVIII Lα line. RS by the ejecta may selectively reduce Lyα, which we did not take into account in our analysis. We will be able to evaluate the ejecta contribution by measuring the intensity ratio of the emission lines in Fe Kα, which originates only from the ejecta (e.g., Yamaguchi et al., 2014; Uchida et al., 2015). Since Fe Kα is out of the wavelength band of the RGS, further observations with X-ray microcalorimeters (e.g., Kelley et al., 2016) are required to clarify this point.

5.2.5 Conclusion of N49

We analyzed a high-resolution X-ray grating spectrum of N49 obtained with the RGS on board XMM-Newton. We found that the G-ratio of OVII Heα in the RGS spectrum of N49 is higher than that expected for a CIP emission. The ratios of FeXVII Lα (3s–2p)/(3d–2p) and OVIII Lyβ/α also show large residuals from the CIP emission model. While an extra CX component well reproduces the G-ratio of the OVII Heα triplet, the residuals around FeXVII Lα and OVIII Lyα still remain. On the other hand, RS can reproduce the RGS spectrum including the G-ratio of the OVII Heα triplet and the ratios of FeXVII Lα (3s–2p)/(3d–2p). We estimated the optical depth for the RS from the intensities of the scattered lines and found that the depth is roughly consistent with the size of N49. Therefore, we conclude that RS is responsible for the high G-ratio of the RGS spectra of N49.

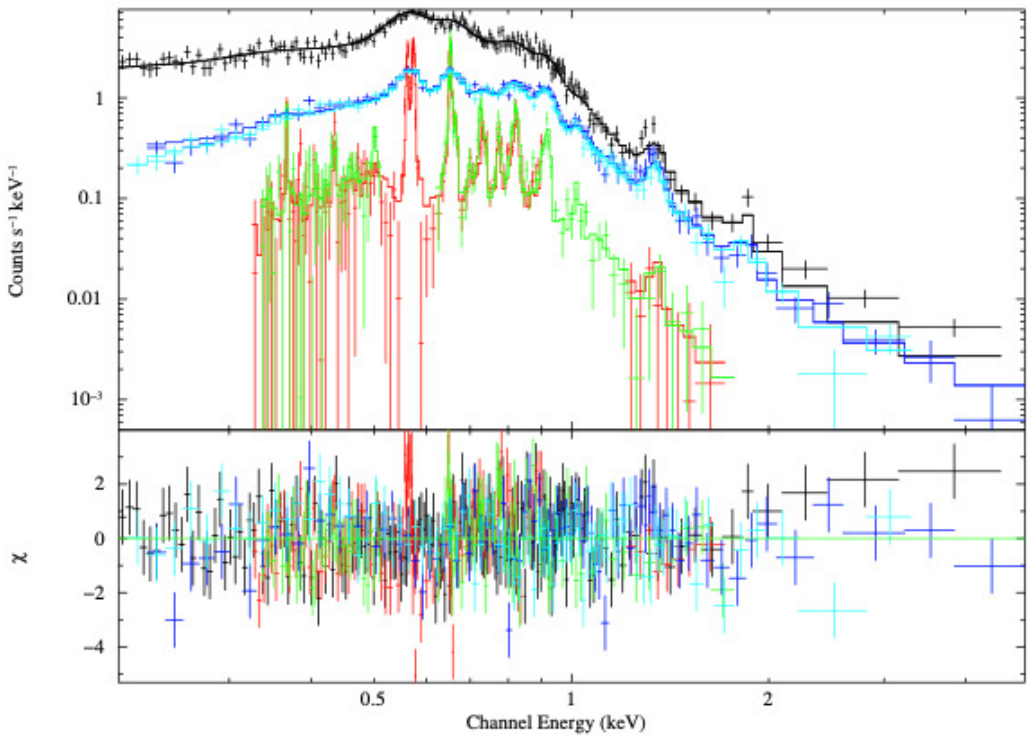

FIGURE 5.13: Fitting results for the EPIC and RGS of SNR J0453.6−6829 (Haberl et al., 2012). The detectors for each color are pn (black), MOS1 (blue), MOS2 (cyan), RGS1 (red), and RGS2 (green). The bottom row shows residuals.

5.3 J0453.6−6829

5.3.1 Overview of J0453.6−6829

J0453.6−6829 is a relatively compact ($\sim 2'$ in diameter) remnant of a core-collapse explosion (Lopez et al., 2009; McEntaffer et al., 2012), containing a pulsar wind nebula (PWN) at the center of the shell (Gaensler et al., 2003). In addition to synchrotron radiation from the PWN, McEntaffer et al. (2012) indicated that the X-ray spectrum of J0453.6−6829 obtained with Chandra is well explained by a shock-heated ISM. A similar conclusion was reached by Haberl et al. (2012), who performed multi-frequency observations of J0453.6−6829, including X-ray band with XMM-Newton. In their spectral fit, the forbidden line of O VII is seemingly higher than a normally expected by CIP model (Figure 5.13). Furthermore, J0453.6−6829 is reported to have a high dust density in the surrounding environment (Williams et al., 2006). We thus revisit the RGS data with particular attention to the He-like lines, in conjunction with an HI observation around the remnant, in order to investigate the relation between the f/r ratio and the surrounding environment of J0453.6−6829.

5.3.2 Observation and Data Reduction

J0453.6−6829 was observed with XMM-Newton on 2001 March 29 (Obs. IDs 0062340101 and 0062340501). Since one of the data sets (Obs. ID 0062340501) was affected by large soft-proton flares, we present results only from Obs. ID 0062340101. The raw data were processed with the XMM Science Analysis Software (SAS) version 18.0.0 and the calibration data files released in 2020 June. In the following spectral analysis, we combine RGS 1 and RGS 2 data with MOS spectra. After discarding periods of background flares, we obtained MOS and RGS data with effective exposure times of $\sim$ 6 ks and $\sim$ 20 ks, respectively. We do not analyze second-order spectra because of their poor statistics.

5.3.3 Analysis

Spectral Analysis with CIP Model

Figure 5.14 shows a background-subtracted three-color image of J0453.6−6829 taken by EPIC (MOS and pn). We extracted RGS spectra by limiting the cross-dispersion width so as to cover the whole of J0453.6−6829. MOS spectra were obtained from the entire region of the remnant. Off-source regions in the field of view (FOV) were used to extract background spectra for each instrument. We simultaneously fitted the unbinned RGS and MOS spectra using SPEX version 3.06.01 (Kaastra et al., 1996), applying a maximum likelihood method, W-stat (Wachter et al., 1979). Throughout this analysis, same as N49, the hydrogen column density ($N_{\rm H}$) of the Galactic absorption was fixed to 6×10^{20} cm^{-2} (Dickey and Lockman, 1990) and that of the LMC was left free. We referred to Russell and Dopita (1992) for the elemental abundances of the LMC.

Figure 5.15 presents the MOS and RGS spectra of J0453.6−6829. McEntaffer et al. (2012) reported that the X-ray spectrum of J0453.6−6829 can be explained by a two-temperature NEI model (`neij`) with a power-law component for the PWN. We first applied this "2-NEI" model, in which photon index Γ and normalization of the power-law component were fixed to 2.0 and 3.5×10^{43} photons s^{-1}keV^{-1}(McEntaffer et al., 2012), respectively. Free parameters for the thermal components include the kT$_{\rm e}$, $n_{\rm e}t$, and emission measure ($n_{\rm e}n_{\rm H}V$. Abundances of C, N, O, Ne, Mg, Si, and Fe were set free and tied between the two components.

The best-fit model of the 2-NEI model is plotted in Figure 5.15, and its parameters are summarized in Table 5.2. We found that whereas the model can reproduce the MOS spectrum, significant residuals remain in the RGS spectrum especially at the O VII Heα and O VIII Lyβ lines. The result implies that some additional considerations are required to better explain the fine structures of the spectrum of J0453.6−6829.

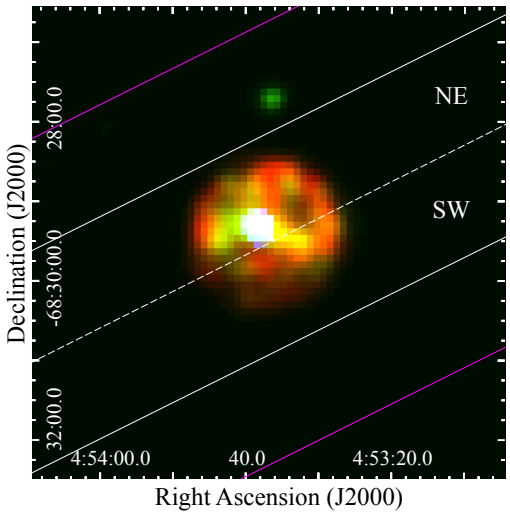

FIGURE 5.14: Three-color image of J0453.6−6829 obtained with EPIC (MOS and pn). Red, green, and blue correspond to the energy bands of 0.3–1.2 keV (soft), 1.2–2.0 keV (medium), and 2.0–8.0 keV (hard), respectively. The magenta lines indicate the cross dispersion width of the RGS (5′). The spectra and background are extracted from the region sandwiched by the white lines and the region above the source region sandwiched by the magenta and white lines, respectively. The dashed line shows how the source region is divided for a spatially-resolved analysis.

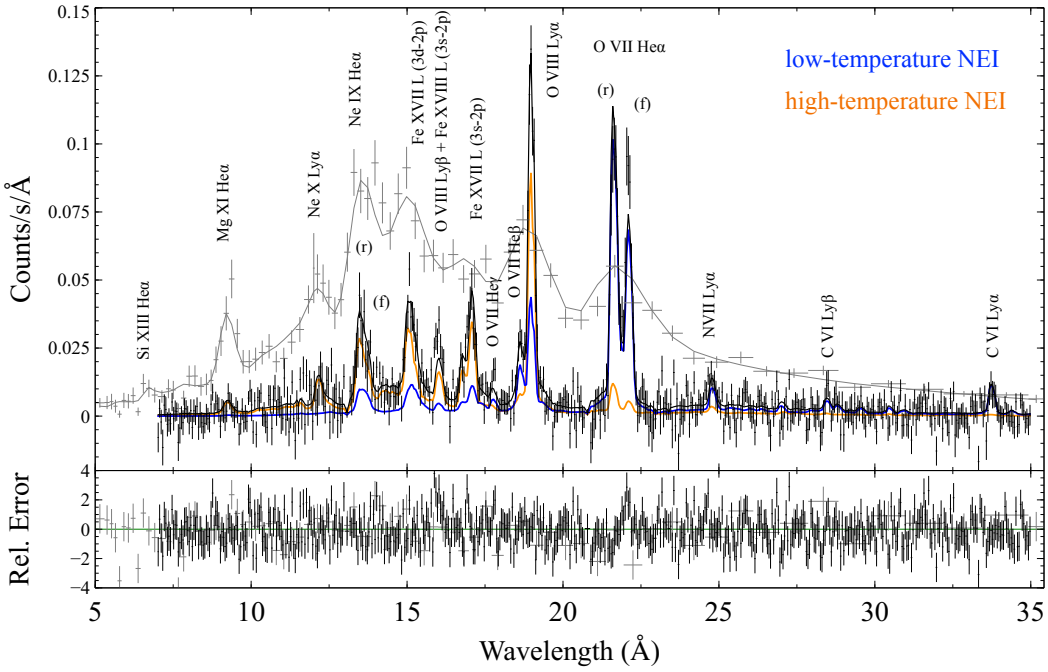

FIGURE 5.15: RGS1+2 (black) and MOS1 (gray) spectra of J0453.6−6829. The colored solid curves indicate the contributions of the low-temperature (blue) and high-temperature NEI (orange) components. The bottom panel shows residuals from the best-fit model.

TABLE 5.2: Best fit parameters of J0453.6−6829

Component	Parameters (unit)	2-NEI	2-NEI+CX	2-NEI−Gaus (RS)
Absorption	$N_{\rm H(Galactic)}$ (10^{20} cm^{-2})	6.0 (fixed)	6.0 (fixed)	6.0 (fixed)
	$N_{\rm H(LMC)}$ (10^{20} cm^{-2})	$8.7^{+2.8}_{-2.7}$	$7.2^{+2.3}_{-2.4}$	$6.9^{+5.2}_{-3.5}$
Power law (PWN)	Normalization (10^{44} photons s^{-1} keV^{-1})	0.35 (fixed)	0.35 (fixed)	0.35 (fixed)
	Γ	2.0 (fixed)	2.0 (fixed)	2.0 (fixed)
Low-temperature NEI	Emission Measure (10^{58} cm^{-3})	81^{+28}_{-20}	60^{+13}_{-13}	43^{+55}_{-25}
$kT_{\rm e}$ (keV)	$0.15^{+0.01}_{-0.01}$	$0.18^{+0.01}_{-0.02}$	$0.15^{+0.05}_{-0.03}$	
	$n_{\rm e}t$ (10^{11} cm^{-3} s)	> 10	> 10	> 10
	C	$0.34^{+0.13}_{-0.10}$	$0.40^{+0.15}_{-0.1}$	$0.44^{+0.47}_{-0.17}$
	N	$0.12^{+0.05}_{-0.04}$	$0.15^{+0.07}_{-0.04}$	$0.18^{+0.18}_{-0.06}$
	O	$0.26^{+0.05}_{-0.04}$	$0.23^{+0.05}_{-0.03}$	$0.53^{+0.39}_{-0.10}$
	Ne	$0.34^{+0.07}_{-0.05}$	$0.33^{+0.08}_{-0.06}$	$0.38^{+0.31}_{-0.07}$
	Mg	$0.42^{+0.08}_{-0.07}$	$0.41^{+0.13}_{-0.08}$	$0.51^{+0.27}_{-0.09}$
	Si	$0.22^{+0.09}_{-0.08}$	$0.19^{+0.11}_{-0.07}$	$0.32^{+0.20}_{-0.11}$
	Fe	$0.25^{+0.04}_{-0.03}$	$0.22^{+0.06}_{-0.03}$	$0.25^{+0.06}_{-0.04}$
High-temperature NEI	Emission Measure (10^{58} cm^{-3})	12^{+5}_{-4}	$7.9^{+7.9}_{-3.5}$	17^{+10}_{-16}
	$kT_{\rm e}$ (keV)	$0.42^{+0.05}_{-0.03}$	$0.48^{+0.09}_{-0.08}$	$0.35^{+0.33}_{-0.08}$
	$n_{\rm e}t$ (10^{11} cm^{-3} s)	$1.6^{+0.5}_{-0.3}$	$1.4^{+0.5}_{-0.3}$	> 2.2
CX	Emission Measure (10^{58} cm^{-3})	...	18^{+100}_{-9}	...
	$v_{\rm col}$ (km s^{-1})	...	< 286	...
	W-statistic/d.o.f.	4124/3627	4107/3625	4085/3622

Plasma Diagnostic Using O VII Heα Line Ratio

We first focus on the O VII Heα line. In the case of J0453.6−6829, contrary to N49, intercombination lines of O VII Heα could not be clearly separated. Therefore we focus on the f/r ratio. We quantified the f/r intensity ratio of O VII by adding four Gaussians instead of multiplet line components of OVII Heα, (i.e., resonance, forbidden and intercombination lines) implemented in the neij code: in this method, the other lines and continua were not changed and were the same as those of the best-fit model. We compared the obtained value with that expected from the NEI model as indicated in Figure 5.16 (a). The resultant f/r ratio, $1.06^{+0.09}_{-0.10}$ requires kT$_{\rm e}$ $<$ 0.025 keV. On the other hand, few O^{6+} (He-like) ions, which emit OVII, are present in such a low-temperature plasma (panel (b) of Figure 5.16), being inconsistent with our result. We thus conclude that any single or multiple NEI component(s) cannot reproduce the observed RGS spectrum. Another possible scenario to account for both f/r ratio and OVIII Lyβ line is an over-ionized plasma. This scenario, however, would make a significant excess of radiative recombination continua, and thus contradicts the observed spectrum.

Spectral Analysis with 2-NEI+CX Model

We next added a CX component to the 2-NEI model (hereafter, 2-NEI+CX model) to enhance the forbidden line intensity of OVII. The free parameters of the CX model are normalization ($n_{\rm H}n_{nh}V$, where n_{nh} is the density of the neutral materials) and shock velocity ($z_{\rm v}$). The ionization temperature was tied to the $kT_{\rm e}$ of the low-temperature NEI component. The best-fit result

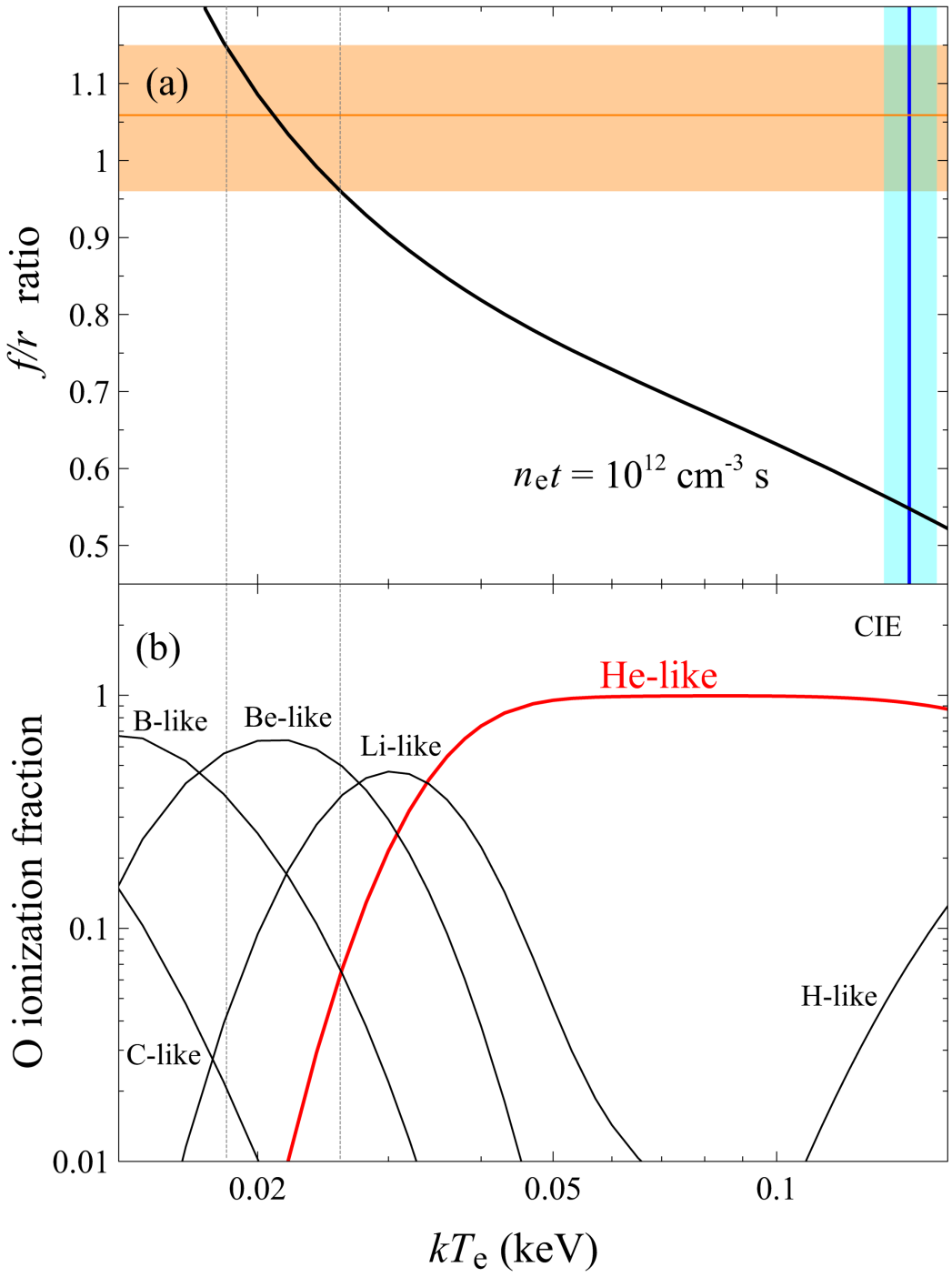

FIGURE 5.16: (a) f/r ratio of OVII Heα as a function of electron temperature kT_e in the case of the best-fit value of $n_e t$ of the low-temperature NEI component. The horizontal orange and vertical blue hatched areas indicate the observed line ratio and kT_e of the low-temperature NEI component, respectively. The curve represents theoretically expected values calculated from the `neij` model in SPEX. (b) Oxygen ionization fraction as a function of kT_e.

and parameters are shown in Figure 5.17 and Table 5.2, respectively. As a result, we successfully fitted the RGS spectrum with the 2-NEI+CX model, except that the discrepancy between the data and model is still seen at the OVIII Lyβ line.

Spectral Analysis with 2-NEI−Gaus Model (RS Model)

We next applied negative Gaussians in addition to the 2-NEI model (hereafter, 2-NEI−Gaus model). The Gaussians were fixed at the centroid wavelengths of the lines whose oscillator strengths are relatively large: resonance lines of Ne IX and O VII, Fe XVII Lα (3d–2p), Fe XVII Lα (3s–2p), and O VIII Lyα. Normalizations (photons s^{-1}) of these five Gaussians were set free and the other parameters are the same as the 2-NEI model. As shown in Figure 5.17, the 2-NEI−Gaus model globally reduces the residuals. The best-fit parameters (Table 5.2) are consistent with those expected for a typical middle-aged SNR. We therefore claim that a presence of RS cannot be ruled out in terms of the spectral fitting.

5.3.4 Discussion

As indicated in the previous section, the high-resolution X-ray spectrum of J0453.6−6829 suggests the presence of CX or RS in the remnant. Similar cases have often been discussed in the literature (e.g., Uchida et al., 2019; Amano et al., 2020; Suzuki et al., 2020). Although it is in general difficult to distinguish between these two possibilities with the available spectroscopies, the SNR morphology and surrounding environment may provide a clue to the true origin of the high f/r ratio. In Table 5.3, we summarize LMC/SMC SNRs for which the f/r (or G) ratios were measured so far using the RGS to compare our results with those from other SNRs in the discussion below.

TABLE 5.3: f/r ratios or G-ratios for OVII Heα

Name	Type of SNe	Ref. Type*	Age (yr)	Ref. Age*	f/r or G ratios	Ref. Ratios*	Surrounding environments	Ref. Surrounding environments*
1E0102−7219	Ib/c or IIL/b	1, 2	1000	3	$0.55^{\ddagger}\pm0.03$	4	no data	
N132D	Ib	1	2500	5	$0.68^{\dagger}\pm0.02$	6	CO and HI clouds	7, 8, 9
DEM L71	Ia	10	4400	11	$0.65^{\dagger}$	12	no data	
N23 (0506−68.0)	II	13	4600	13	$0.99^{\ddagger}\pm0.06$	14	star-forming region	15
N49	II	16	6600	17	$1.23^{\ddagger}\pm0.12$	18	CO and HI clouds	7, 8, 19
J0453	II	20	13000	21	$1.06^{\dagger+0.09}_{-0.10}$	22	HI clouds	22

* References. (1) Blair et al. (2000); (2) Chevalier (2005); (3) Hughes et al. (2000); (4) This work. (5) Vogt and Dopita (2011); (6) Suzuki et al. (2020); (7) Banas et al. (1997); (8) Sano et al. (2017); (9) Sano et al. (2020); (10) Hughes et al. (1998); (11) Ghavamian et al. (2003); (12) van der Heyden et al. (2003); (13) Hughes et al. (2006); (14) Broersen et al. (2011); (15) Chu et al. (1988); (16) Park et al. (2012); (17) Park et al. (2003); (18) This work. (19) Yamane et al. (2018); (20) Lopez et al. (2009); (21) Gaensler et al. (2003); (22) This work.
† f/r ratio ‡ G-ratio $(f+i)/r$

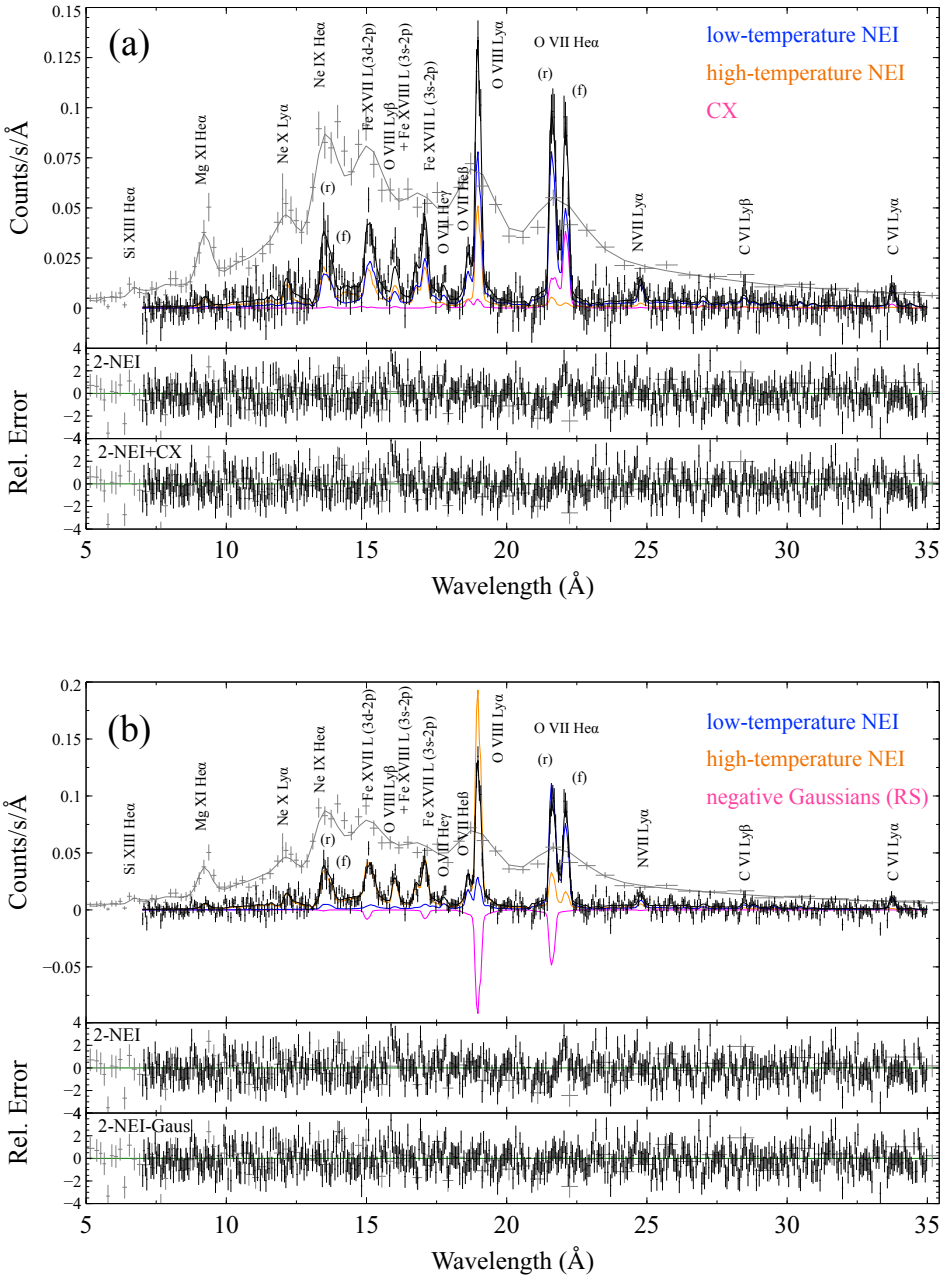

FIGURE 5.17: (a)Same as Figure 5.15 but with the 2-NEI+CX model. The magenta curve represents the CX component. The middle and lower panels show residuals from the 2-NEI and 2-NEI+CX models, respectively. (b)Same as Figure 5.15 but with the 2-NEI−Gaus model. The magenta curve indicates scattered line intensities. The middle and lower panels show residuals from the 2-NEI and 2-NEI−Gaus models, respectively.

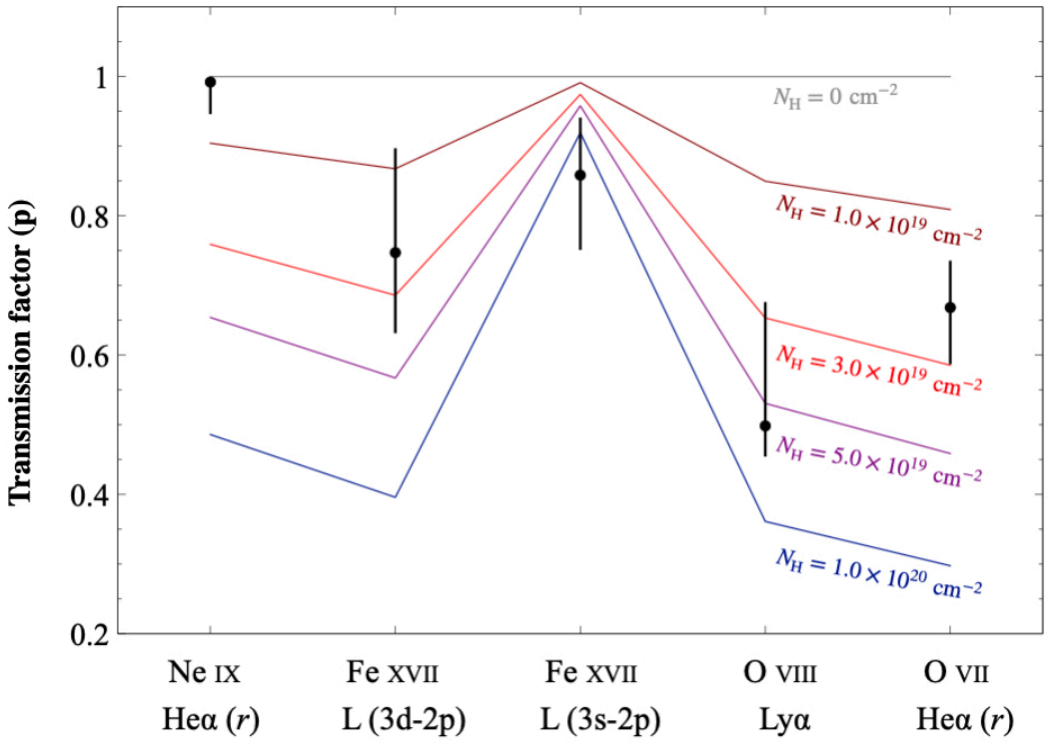

FIGURE 5.18: Transmission factors p for each line. The black points are those estimated from the observed line intensities and normalizations of the negative Gaussians. The colored curves represent expected transmission factors as a function of $N_{\rm H}$.

X-ray Morphology of J0453.6−6829

For quantitative evaluation of the effect of RS, we calculated a transmission factor p by applying the same method as N49. We compared theoretical values of p for several optical depths according to Equqtion (3.40) with those estimated from the best-fit normalizations of the negative Gaussians. Figure 5.18 shows the result. Although the model fails to explain the observed resonance line of Ne IX, the estimated p for J0453.6−6829 are roughly consistent with those at $N_{\rm H} = 1.0$–5.0×10^{19} cm^{-2}, which corresponds to a plasma depth of 3–18 pc under an assumption of the plasma density $n_{\rm H} = 1.1$ cm^{-3} (Williams et al., 2006). Since the diameter of J0453.6−6829 is estimated to be ~ 36 pc from the apparent angular size of the shell ($\sim 2.5'$), the line-of-sight plasma depth that contributes to RS should be 10–50 % of the diameter. If this is really the case, the shell-type SNR would be required to have a highly asymmetric morphology; for instance, a bright shell is prominent only on one side of the remnant (see Figure 5.19).

If J0453.6−6829 has an ideal spherical symmetric structure, the RS effect will be cancelled out and an enhancement of f/r will not occur. Note that the RGS spectrum of J0453.6−6829 was obtained from the entire region. We can thus postulate that asymmetry of an SNR is a key parameter to evaluate the effect of RS. From a soft-band imaging analysis by Lopez et al. (2011),

FIGURE 5.19: Example schematic view of an X-ray emitting plasma that accounts for the result of the calculation of RS.

we found that J0453.6−6829 has a less asymmetric morphology among the six SNRs listed in Table 5.3. Other core-collapse remnants are more "elliptical" (N23) or "non-uniform" (N132D), which are parametrized as P_2/P_0 and P_3/P_0 in their calculation. Although N49 was not analyzed by Lopez et al. (2011), it would also be categorized as a highly elliptical remnant due to its morphology similar to that of N23. It is reasonable that N23, N49, and N132D show relatively high f/r ratios due to RS, as claimed by previous studies (Broersen et al., 2011; Amano et al., 2020; Suzuki et al., 2020). On the other hand, in the case of J0453.6−6829, the effect of RS might be unlikely or insufficient to satisfactorily explain the observed high f/r ratio.

Surrounding Environment of J0453.6−6829

CX is another possibility that causes the enhancement of f/r. An interaction with a dense ambient medium is expected in this case, as in previous studies of Galactic SNRs with the RGS: Puppis A (Katsuda et al., 2012) and the Cygnus Loop (Uchida et al., 2019). While McEntaffer et al. (2012) implied a presence of dense gas in the vicinity of J0453.6−6829 because of a spatial correlation between the X-ray and infrared morphologies, the surrounding environment of this remnant has still been unclear (Williams et al., 2006; Lakićević et al., 2015). As shown in Figure 5.20, we compared the ATCA & Parkes (Kim et al., 2003) HI velocity channel map around J0453.6−6829 with the X-ray morphology and found HI clouds located along with the southwestern half of J0453.6−6829. Figure 5.21 shows the integrated intensity maps of HI. We also found the southwestern part of the remnant is increasingly covered with an HI cloud. The position-velocity diagram suggests that the SNR shell is expanding into the dense gas (panel (b) of Figure 5.21).

If the SNR shell interacts with the HI cloud in the southwestern region, relatively strong forbidden line emission would be detected there. We thus divided the data into two in the cross-dispersion direction (namely, northeast; NE and southwest; SW) as indicated in Figure 5.14. As displayed in Figure 5.22, the forbidden line intensity of OVII in SW is stronger than that in NE. Applying the same method as the entire region, we obtained f/r ratios of $0.97^{+0.18}_{-0.14}$ and $1.41^{+0.40}_{-0.29}$ for NE and SW, respectively. Although statistically

they are equal within the errors, the trend is consistent with the above expectation and thus strongly supports the presence of CX. The best-fit models of 2-NEI+CX for these regions are displayed in Figure 5.23. While the CX component is required both in NE and SW, its contribution is relatively dominant in SW. We thus confirmed that the anomalous f/r ratios is due to the CX emission, mainly caused by an interaction with the southwestern HI cloud.

According to the discussion above, we presume that the emitting region of CX is the southwestern edge of J0453.6−6829, which is in contact with the HI cloud. To quantitatively examine the possibility of CX, we estimate the emitting volume $V_{\rm CX}$ using the volume emission measure of the CX component $\mathrm{EM_{CX}} = n_{\rm H} n_{\rm nh} V_{\rm CX}$, where $n_{\rm nh}$ is the neutral material density of the surrounding gas. Given that the HI gas has a typical density of $n_{\rm nh} = 10\,\mathrm{cm}^{-3}$, we obtain the emitting volume $V_{\rm CX}$ to be 2×10^{58} cm^3. Since the total volume of J0453.6−6829 is estimated to be $V_{\rm SNR} \sim 10^{60}$ cm^3 assuming a diameter of $\sim$ 36 pc, we conclude that the CX occurs in $\sim$ 0.4 % of the SNR radius. The result fits well with the calculation by Lallement (2004) (see Chapter 3) and thus supports the possibility that the observed anomalous f/r ratio is due to CX. Note that the significant residuals seen at $\sim$ 16 Å (Section 5.3.3.3) is still an open question; such discrepancies around the OVIII Lyβ line are often pointed out by many RGS observations (e.g., N49: Amano et al., 2020), and might be due to uncertainties in the atomic data (see also, Plaa et al., 2012).

5.3.5 Conclusion for J0453.6−6829

We performed a high-resolution spectroscopy of J0453.6−6829 with the RGS onboard XMM-Newton and found that the intensity of the forbidden line of OVII is significantly stronger than expected from a simple CIP (2-NEI) model. To account for the obtained high f/r ratio ($1.06^{+0.09}_{-0.10}$), we examined two possibilities: CX and RS. Both models are statistically acceptable, although small residuals remain at $\sim$ 16 Å (around the OVIII Lyβ line) between the data and the 2-NEI+CX model. Such discrepancies are often pointed out by many RGS observations (e.g., Amano et al., 2020; Plaa et al., 2012) and are likely due to uncertainties in the atomic data. From the best-fit result with the RS model, we estimated a transmission factor τ; the result requires a significantly asymmetric shape along the line of sight. This may be inconsistent with the apparent morphology of J0453.6−6829, since a previous systematic X-ray study indicates that this remnant is one of the "least asymmetric" core-collapse SNRs (Lopez et al., 2011). On the other hand, our estimate of the emitting volume for the CX component ($\sim$ 0.4 % of the SNR radius) agrees well with a theoretical expectation (Lallement, 2004). We also found evidence of an interaction between J0453.6−6829 and the dense ambient gas in the ATCA & Parkes HI map, which supports the picture that the observed f/r ratio is due to the CX emission at SNR shock fronts. In conclusion, the presence of CX in J0453.6−6829 is favored in our study, while a slight or significant contribution of the RS effect also cannot be ruled out. Future spatially resolved spectroscopies with high angular resolution missions like Athena will clarify this point.

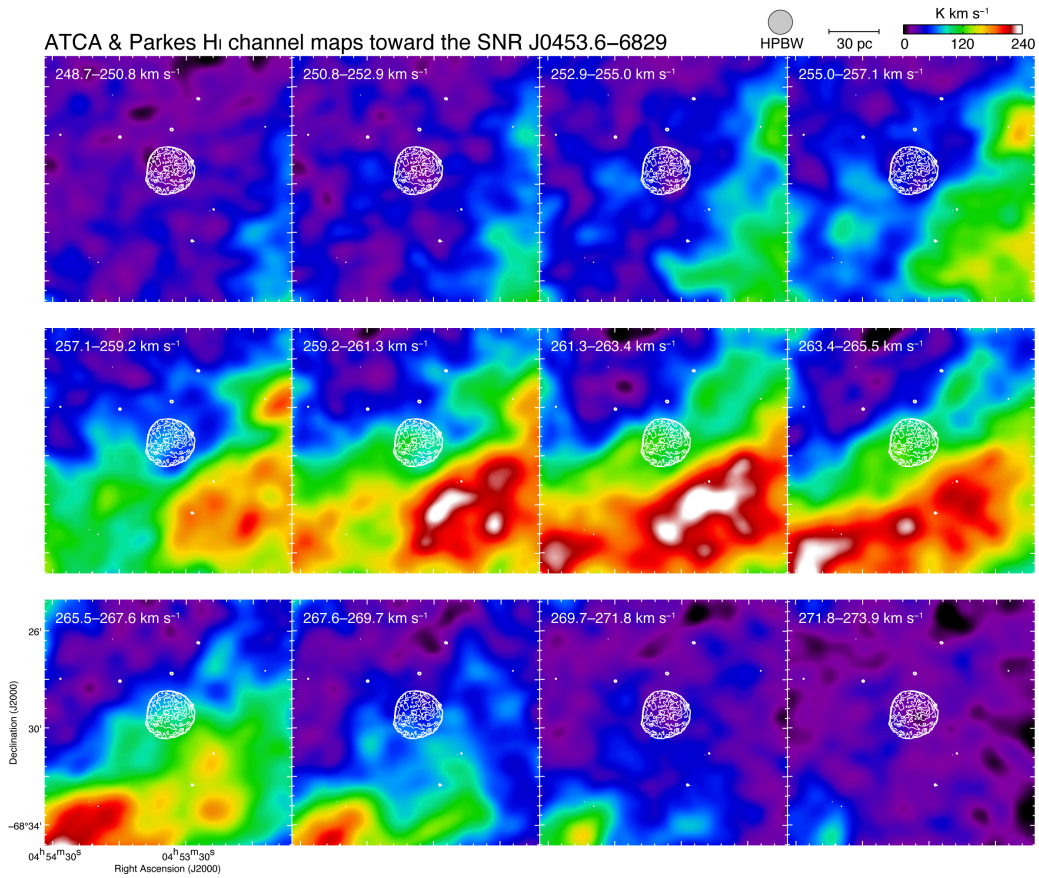

FIGURE 5.20: ATCA & Parkes HI channel maps overlaid with the Chandra X-ray intensity of J0453.6−6829 (white contours). Each panel shows the HI intensity map integrated over the 2.1 km s^{-1} width evenly spaced in the 248.7 − 273.9 km s^{-1} range.

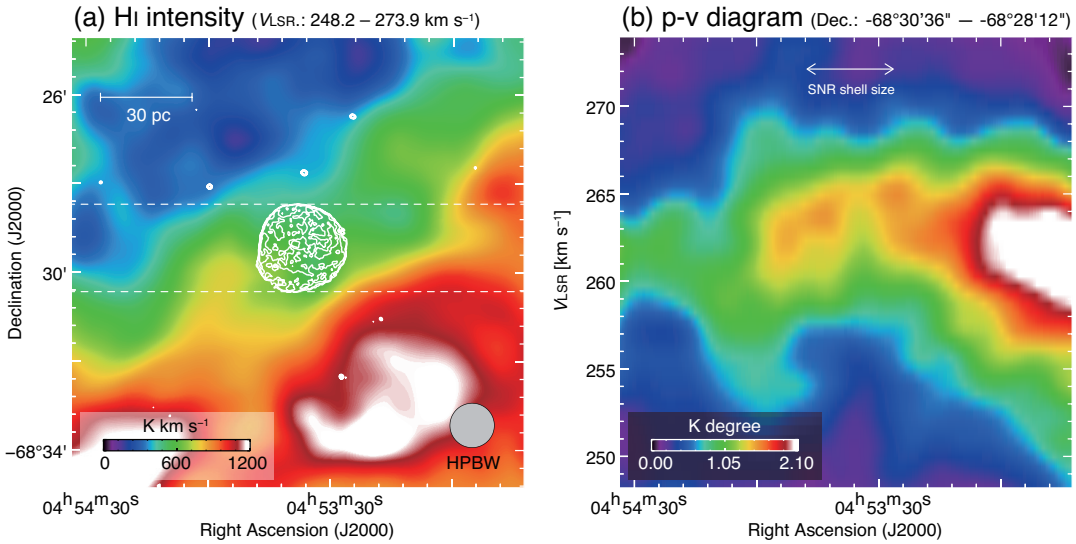

FIGURE 5.21: (a) Integrated intensity map of the ATCA & Parkes HI in VLSR of 248.7 − 273.9 km s^{-1}. (b) Position-velocity diagram of H I image. The integration range in Dec. is from −68°30′36" to −68°28′12" (J2000.0). The white arrow indicates the position of J0453.6−6829.

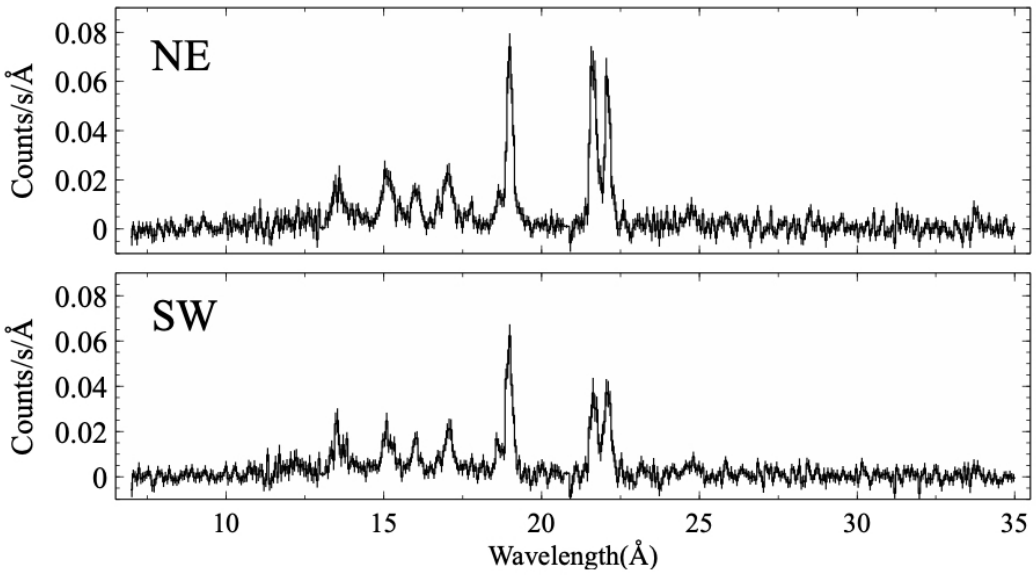

FIGURE 5.22: RGS1+2 spectra of the NE (top) and SW (bottom) regions of J0453.6−6829.

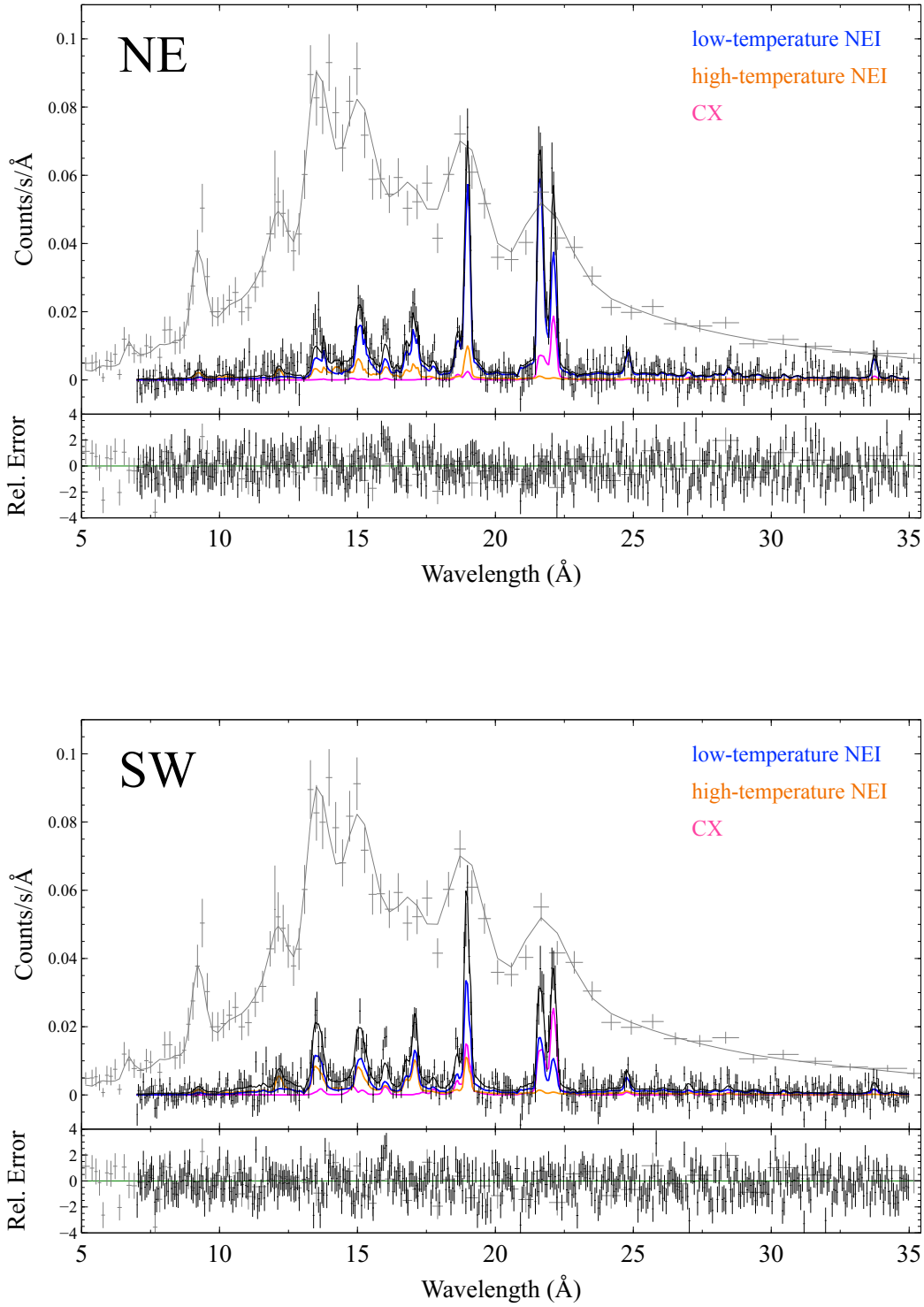

FIGURE 5.23: Same as the panel (a) of Figure 5.15 but for the NE (top) and SW (bottom) regions.

5.4 Summary

We analyzed the RGS spectra of N49 and J0453.6−6829, which are surrounded by dense neutral gas. As a result, we obtained observational evidence for CX and RS.

The RGS spectrum of N49 shows a high G-ratio of O VII Heα as well as O VIII Lyβ/α and Fe XVII (3s–2p)/(3d–2p) ratios, which cannot be explained by the emission from an optically thin CIP. We thus considered the possibility of CX and RS. Although an additional CX emission well reproduces the G-ratio of the O VII Heα lines, the O VIII Lyβ/α and Fe XVII (3s–2p)/(3d–2p) ratios cannot be explained. The effect of RS can well explain the G-ratio of the OVII Heα and FeXVII Lα lines. We estimated the optical depth for the RS from the intensities of the scattered lines and found that the depth is roughly consistent with the size of N49. Therefore, we conclude that RS occurs in the rim of N49.

In the case of the J0453.6−6829, we found a high f/r ratio of OVII Heα lines and OVIII Lyβ/α ratio. Both 2-NEI+CX and NEI−Gaussians (RS) models well explain the f/r ratio of OVII Heα lines although small residuals remain at $\sim$ 16 Å (around the OVIII Lyβ line) between the data and the 2-NEI+CX model. This discrepancy are also observed in the RGS spectrum of N49 and are likely due to uncertainties in the atomic data (Plaa et al., 2012). We focused on the SNR morphology and surrounding environment, since it is difficult to distinguish between the possibilities of CX and RS from the spectral features. Estimated transmission factors τ require a significantly asymmetric shape along the line of sight. This may be inconsistent with the apparent morphology of J0453.6−6829 (Lopez et al., 2011). On the other hand, our estimate of the emitting volume for the CX component ($\sim$ 0.4 % of the SNR radius) agrees well with a previous calculation (Lallement, 2004). We also found evidence of an interaction between J0453.6−6829 and the dense ambient gas in the ATCA & Parkes HI map. Furthermore, relatively strong forbidden line emission was detected in the southwestern region of J0453.6−6829 where the SNR shell interacts with the HI cloud. In conclusion, our results strongly support the presence of CX in J0453.6−6829. Our results help us understand the physical conditions in which CX and/or RS occur. A detailed discussion of the physical conditions is given in Chapter 7.

Chapter 6

Constraint on 3D Structure of SNRs from X-ray Resonance Scattering

In Chapter 5, we showed that CX and RS can be observed in SNRs. These processes are promising means of constraining several important parameters. In this section, we propose a method to constrain the 3D structure of SNRs from the effect of RS. This method would provide us many insight into progenitors and their explosion mechanism. Additionally, we report the result of employing this methodology to one of the brightest extra-Galactic SNRs, 1E 0102−72.9 (hereafter E0102), whose 3D structure is currently a controversial and still open question.

6.1 Method

In our method, the 3D structure of SNRs is constrained by measurement of its line-of-sight length. The column density ($n_{\rm e}L$) can be estimated by the transmission factors of RS, as we performed in Chapter 5. On the other hand, the emission measure ($\propto n_{\rm e}^2 L$) can be derived from the X-ray brightness of the plasma. We can thus constrain $n_{\rm e}$ and L independently from these two observation values.

We describe the detailed method to measure the transmission factor and the emission measure. For simplicity, we assume that the SNR has a cylindrical structure as displayed in Figure 6.1. For nearly optically thin emission from an isothermal plasma with a uniform density, an observed flux (F) of a line emission can be expressed as:

$$F\ (/{\rm cm}^2/{\rm s}) = p\ J(kT_{\rm e}, n_{\rm e}t)\frac{n_{\rm Z}}{n_{\rm H}}EM, \tag{6.1}$$

where p is the transmission factor, $J(kT_{\rm e}, n_{\rm e}t)$ is the emissivity introduced in Subsection 3.1.2, $n_{\rm Z}/n_{\rm H}$ is the elemental abundance. EM is the emission measure described as:

$$EM \ = \ \frac{n_{\rm e}n_{\rm H}}{4\pi d^2}SL \tag{6.2}$$

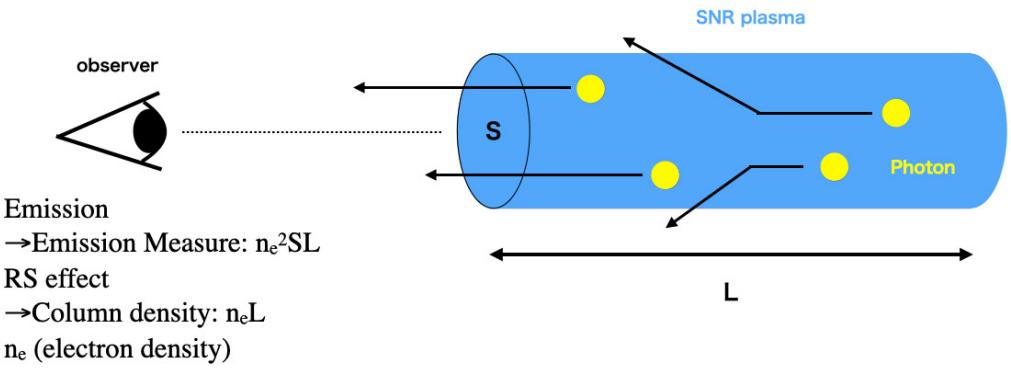

FIGURE 6.1: Sketch of an SNR. For simplicity, we assume that the structure of the SNR is cylindrical column.

$$\sim \frac{0.8\, n_{\rm e}^2}{4\pi d^2} SL, \tag{6.3}$$

where $n_{\rm e}$ is the number density of the electron, and $n_{\rm H}$ is the number density of the hydrogen, d is the distance to the object and SL is the volume of the object (see Figure 6.1). Here, we used a relation $n_{\rm e} \sim 1.2 n_{\rm H}$, which approximately describes a plasma with a solar abundance.

Below, as an example, we describe the procedure to constrain the transmission factors of the O VII Heα (r) line from the observed fluxes of the O VII Heα (r) ($F_{{\rm He}\alpha\ (r)}$) and O VII Heα (f) ($F_{{\rm He}\alpha\ (f)}$) lines. From Equation (6.1), the observed fluxes are described as:

$$F_{{\rm He}\alpha\ (r)} = p_{{\rm He}\alpha\ (r)}\, J_{{\rm He}\alpha\ (r)}(kT_{\rm e}, n_{\rm e}t) \frac{n_{\rm O}}{n_{\rm H}} EM \tag{6.4}$$

$$F_{{\rm He}\alpha\ (f)} = J_{{\rm He}\alpha\ (f)}(kT_{\rm e}, n_{\rm e}t) \frac{n_{\rm O}}{n_{\rm H}} EM, \tag{6.5}$$

where we assume the transmission factor of O VII Heα (f) to be unity, since the oscillator strengths of the O VII Heα (f) line is much smaller than that of O VII Heα (r). We can determine the emissivity of each line by constraining the electron temperature ($kT_{\rm e}$) and ionization timescale ($n_{\rm e}t$) as we described in Chapter 3. Therefore, when $kT_{\rm e}$ and $n_{\rm e}t$, and abundance ($\frac{n_{\rm Z}}{n_{\rm H}}$) are determined, the EM and p can be calculated as:

$$p_{{\rm He}\alpha\ (r)} = \frac{F_{{\rm He}\alpha\ (r)} / F_{{\rm He}\alpha\ (f)}}{J_{{\rm He}\alpha\ (f)} / J_{{\rm He}\alpha\ (r)}} \tag{6.6}$$

$$EM = \frac{n_{\rm H}}{n_{\rm O}} \frac{F_{{\rm He}\alpha\ (f)}}{J_{{\rm He}\alpha\ (f)}}. \tag{6.7}$$

From the transmission factor p, we can estimate $n_{\rm e}L$ as we performed in Chapter 5.

6.2 Overview of E0102

1E 0102−72.9 (hereafter E0102) is a young ($\sim$ 2000 yr; e.g., Banovetz et al., 2021) SNR located in the Small Magellanic Cloud (SMC). Its thermal X-ray emission is mainly explained by metal-rich ejecta in which the X-ray emission is dominated by emission lines from highly ionized O, Ne, and Mg (e.g., Gaetz et al., 2000, Rasmussen et al., 2001). The progenitor of E0102 is still unclear. E0102 is classified to be a Type IIb SNR due to its interaction with the dense wind of the progenitor (e.g., Chevalier, 2005; Seitenzahl et al., 2018). Therefore, its progenitor is considered to be a single WR star or a binary star. However, the progenitor mass is not well constrained, such as $M < 15\ M_{\odot}$ (Katsuda et al., 2018), 25-40 $M_{\odot}$ (Blair et al., 2000), or $M > 50\ M_{\odot}$ (Finkelstein et al., 2006), and there is no firm evidence that it was binary.

Figure 6.2 presents an X-ray image of E0102 obtained with Chandra. Although the X-ray morphology of E0102 appears to be explained by a shell-like symmetry structure at first glance, there are various suggestions about its 3D structure. Based on the X-ray radial profile of E0102, Hughes (1994) suggested that it has a barrel-like partial spherical shell structure rather than a projected spherical shell (Figure 6.3). Flanagan et al. (2004) found that the spectrum of E0102 can be explained by a superposition of red and blue shifting rings from Chandra HETG observations (the left panel of Figure 6.4). Based on this observational result, they proposed that E0102 has a cylindrical structure expanding at a velocity of approximately $\pm$900 km/s along the line of sight (the right panel of Figure 6.4).

We analyze RGS data, aiming to constrain the 3D structure of E0102 and provide implications about its progenitor. E0102 is a relatively compact ($\sim 1'$ in diameter) SNR, which makes it possible to perform high-resolution X-ray spectroscopy with the RGS. Furthermore, we can obtain high statistical data since E0102 has been observed more than 50 times for the on-board calibration of XMM-Newton. These high-quality data enable us to perform robust plasma diagnostics and measurements of the effect of RS.

6.3 Observations and Data Reduction

As a calibration source for XMM-Newton, E0102 has been observed several times each year from 1999 to 2021. We use most of the RGS observations except several data sets whose effective exposures are extremely short. The basic information on the data we use are listed in Table 6.1. The following reduction tasks were done with the Science Analysis System version 16.1.0. The RGS data were processed with the pipeline tool `rgsproc`.

In this study, we analyze a spectrum in which all observations are stacked. We used the publicly available script `rgscombine` in the Science Analysis System to combine all source and background spectra respectively. The total effective exposure time is $\sim$ 3 Ms for both the first- and second-order spectra. To account for the spatial broadening of E0102, we convolved the response files for point-like sources with the profiles of the surface brightness along the dispersion direction using the ftools, `ftrgsrmfsmooth`. This process was

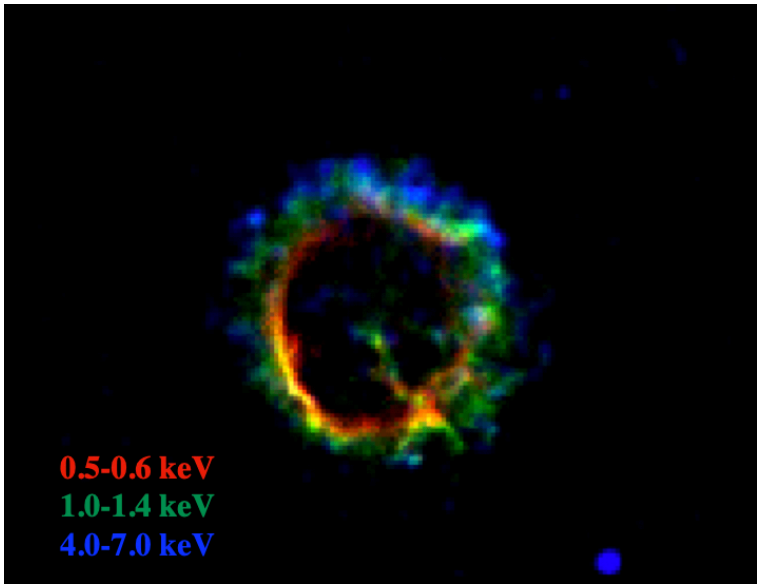

FIGURE 6.2: RGB image of E0102 obtained with Chandra. Red, green and blue colors correspond to the energies 0.5–0.6, 1.0–1.4 and 4.0—7.0 keV.

performed for each observation respectively. To obtain the profiles of E0102, we generated Chandra images in the six energy bands of 0.32–0.6 keV, 0.6–0.7 keV, 0.7–0.85 keV, 0.85–0.95 keV, 0.95–1.2 keV, 1.2–2.0 keV. After this convolution, we constructed the response matrix for the stacked grating spectrum by averaging the response matrices of each observation weighted by the exposure time. We use version 12.10.0c of the XSPEC software for the following spectral analysis. We fit the first- and second- order spectrum of RGS data simultaneously.

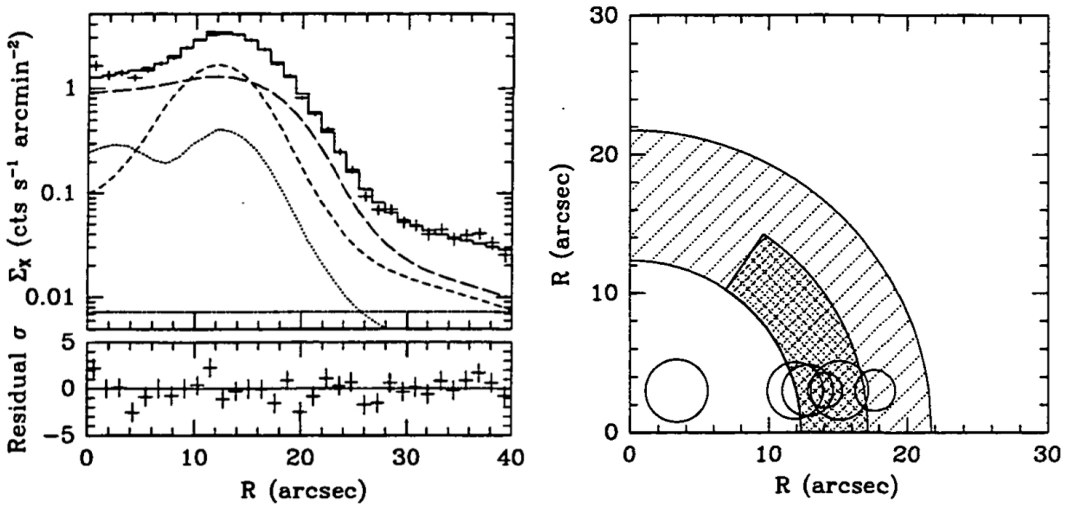

FIGURE 6.3: (left) Radially-averaged X-ray surface brightness of E0102 obtained with ROSAT high resolution imager and the best-fit spatial model (Hughes, 1994). The short-dash curve is the barrel-like component, the long-dash curve is the spherical shell component, the dotted curve is the clumped component, and the background is the straight line. The bottom panel shows the difference between the observed data and the best-fit model. (Right) Cross-sectional view of the geometric model. The observer is in the direction of the vertical axis. The barrel-like component is shown as the doubly hatched region, and the spherical shell component is shown singly hatched region. Circles near the bottom of the figure correspond to the clumped components.

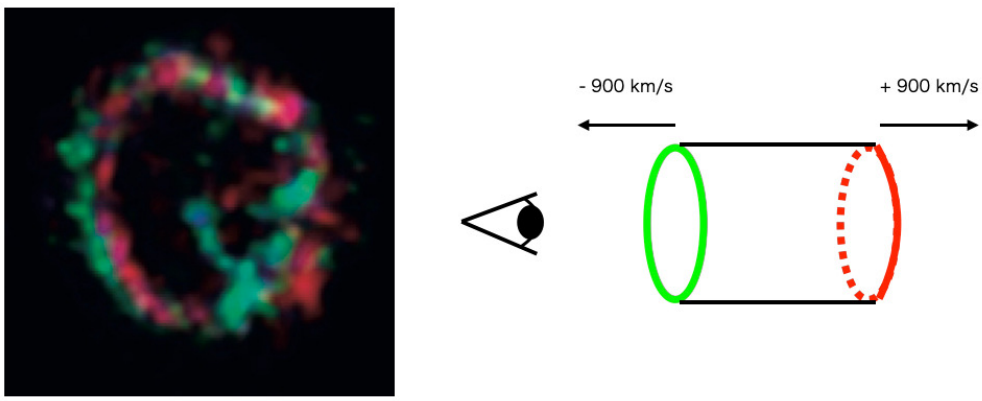

FIGURE 6.4: (Left) Ne X Lyα image of E0102 obtained by Chandra HETG (Flanagan et al., 2004). The red area corresponds to the line-of-sight velocity of +900 km/s, and the green area corresponds to -900 km/s. (Right) 3D structure of E0102 proposed by Flanagan et al. (2004).

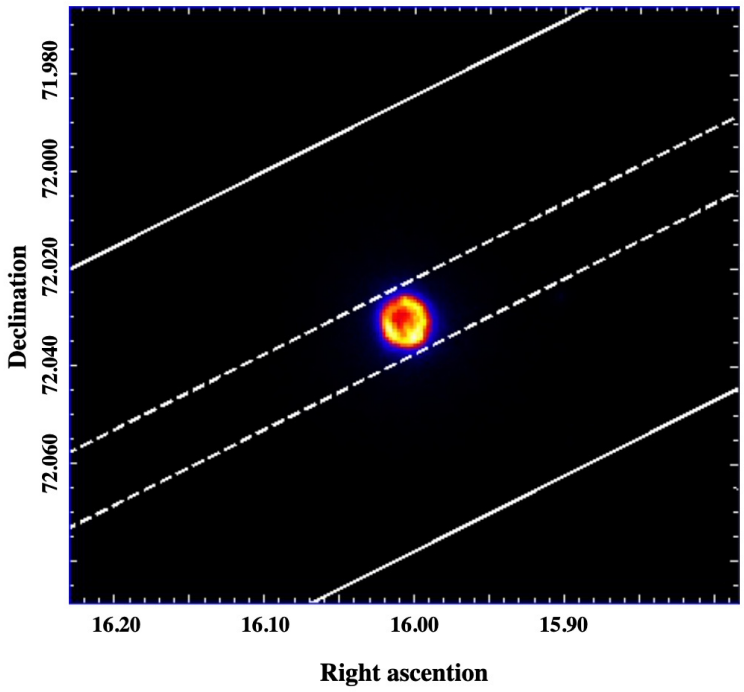

FIGURE 6.5: EPIC-MOS image (0.4–2.0 keV) of E0102. The cross-dispersion width of the RGS (5 arcmin) is in between the white solid line. The spectral extraction region is enclosed by the white dashed line.

TABLE 6.1: Information on the XMM-Newton observations of E0102 used in the analysis.

Obs. ID	Obs. Start Date (yyyy-mm-dd)	Exposure Time (ks)
0123110201	2000-04-16	33.6
0123110301	2000-04-17	18.7
0135720601	2001-04-14	16.6
0135720801	2001-12-25	50.4
0135720901	2002-04-20	8.3
0135721001	2002-05-18	17.6
0135721101	2002-10-13	29.9
0135721301	2002-12-14	54.2
0135721401	2003-04-20	50.9
0135721501	2003-10-27	33.9
0135721701	2003-11-16	42.3
0135721901	2004-04-28	55.0
0135722001	2004-10-26	59.8
0135722101	2004-11-07	45.0
0135722201	2004-11-07	11.6
0135722301	2004-11-07	27.4
0135722501	2005-04-17	41.9
0135722701	2006-04-20	58.3
0412980201	2007-04-25	35.2
0412980301	2007-10-26	60.9
0412980701	2008-11-14	53.1
0412980801	2009-04-13	19.7
0412980901	2009-10-21	55.0
0412981001	2010-04-21	54.1
0412981301	2010-10-19	33.0
0412981401	2011-04-20	26.8
0412981501	2011-11-04	57.6
0412981701	2012-12-06	17.1
0412981701	2012-12-06	32.8
0412981701	2012-12-07	34.3
0412982101	2013-11-07	56.7
0412982201	2014-10-20	59.9
0412982401	2015-10-30	60.1
0412982501	2015-10-28	63.5
0412983201	2016-10-26	54.3
0412983301	2016-12-03	56.0
0412983401	2017-11-02	78.4
0412983501	2017-11-04	61.7
0791580701	2016-04-26	57.6
0791580801	2016-04-26	23.1
0791580901	2016-04-26	20.8
0791581001	2016-04-26	57.3
0791581101	2016-04-27	26.3
0791581201	2016-04-27	13.8
0810880201	2018-10-28	49.2
0810880301	2019-11-18	58.0
0810880501	2019-11-04	37.6

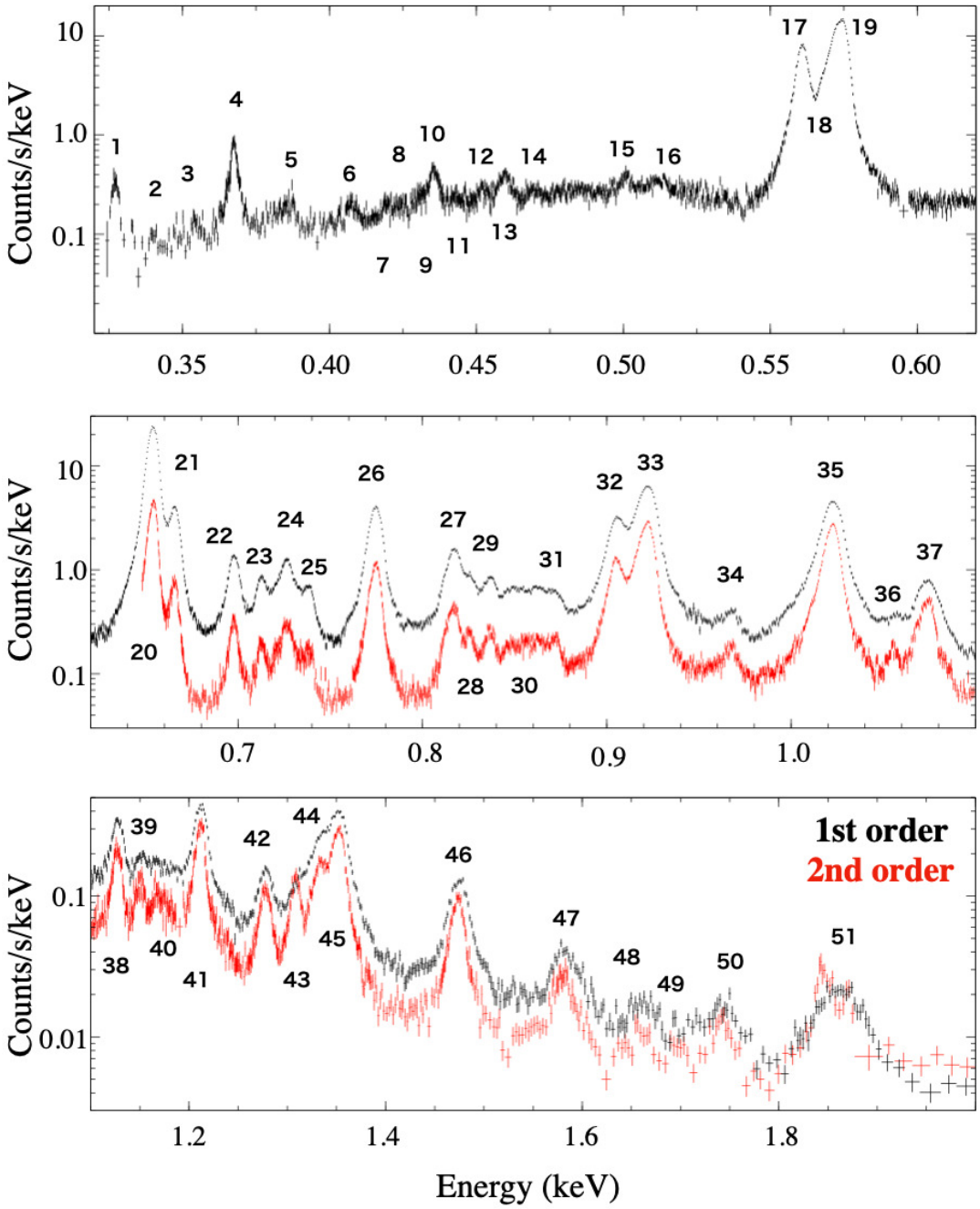

FIGURE 6.6: RGS spectra of E0102. Black and red are the first-order and of second-order spectra of the RGS, respectively. The detected lines are labeled and listed in Table 6.2 with their identification.

TABLE 6.2: Detected Emission Lines and their Identification

Label	Energy (keV)	Ion	Transition	Label	Energy (keV)	Ion	Transition
1	0.329	S XIII	3s → 2p	27	0.817	O VIII	4p → 1s
2	0.341	S XII	3d → 2p	28	0.826	Fe XVII	3d → 2p
3	0.347	Ca XI	3s → 2p	29	0.837	O VIII	5p → 1s
4	0.368	C VI	2p → 1s	30	0.847	O VIII	6p → 1s
5	0.381	S XIV	3d → 2p	31	0.873	Fe XVIII	3d → 2p
6	0.407	S XIV	3p → 2s	32	0.905	Ne IX	2s → 1s (f)
7	0.420	N VI	2s → 1s (f)	33	0.922	Ne IX	2p → 1s (r)
8	0.426	N VI	2p → 1s (i)	34	0.964	Fe XX	3d → 2p
9	0.431	N VI	2p → 1s (r)	35	1.022	Ne X	2p → 1s
10	0.436	C VI	3p → 1s	36	1.056	Fe XXIII	3d → 2p
11	0.443	Ca XII	3d → 2p	37	1.076	Ne IX	3p → 1s
12	0.451	Ar XIV	3d → 2p	38	1.127	Ne IX	4p → 1s
13	0.459	C VI	4p → 1s	39	1.152	Ne IX	5p → 1s
14	0.470	C VI	5p → 1s	40	1.168	Fe XXIV	3p → 2s
15	0.500	N VII	2p → 1s	41	1.211	Ne X	3p → 1s
16	0.511	S XIV	4d → 2p	42	1.277	Ne X	4p → 1s
17	0.561	O VII	2s → 1s (f)	43	1.314	Fe XXI	4d → 2p
18	0.569	O VII	2p → 1s (i)	44	1.343	Mg XI	2s → 1s (f)
19	0.574	O VII	2p → 1s (r)	45	1.352	Mg XI	2p → 1s (r)
20	0.654	O VIII	2p → 1s	46	1.473	Mg XII	2p → 1s
21	0.666	O VII	3p → 1s	47	1.579	Mg XI	3p → 1s
22	0.698	O VII	4p → 1s	48	1.659	Mg XI	4p → 1s
23	0.713	O VII	5p → 1s	49	1.696	Mg XI	5p → 1s
24	0.725	Fe XVII	3s → 2p	50	1.745	Mg XII	3p → 1s
25	0.739	Fe XVII	3s → 2p	51	1.865	Si XIII	2p → 1s (r)
26	0.775	O VIII	3p → 1s				

6.4 Analysis

The purpose of our analysis is to measure the transmission factors, according to the method described in Section 6.1. The analysis is carried out in the following procedure. First, we measure the flux of several emission lines accurately by using the "modified NEI" model described later. Next, we constrain the kT_e and $n_e t$ by plasma diagnostics introduced in Subsection 3.4.1. Finally, we measure the transmission factors of He α (r) and Lyα lines of O and Ne based on the He α (r) / He α (f) and Ly α / Ly β ratios.

6.4.1 Spectral Modeling

Figure 6.6 shows the background-subtracted RGS spectra. K-shell emission lines of He-like and H-like ions are clearly detected. In addition to these lines, we detect a dozen L-shell emissions from Fe and the intermediate-mass elements (S, Ar, Ca) and K-shell emissions from highly excited states of O and Ne. To measure the fluxes of individual lines accurately, contributions of continuum emission and other weak lines cannot be ignored. Therefore, we first tried to roughly reproduce the RGS spectrum using NEI models to estimate the contributions of these emission components. As indicated by previous studies (e.g., Alan et al., 2019), the spectra of E0102 consist of emission from multiple-temperature plasmas. We thus applied two components of velocity-broadened, collisionally ionized plasma models, `bvrnei` in the XSPEC that can reproduce both CIE and NEI plasmas. The free parameters are the electron temperature (kT_e), ionization parameter ($n_e t$), abundances of C, N, O, Ne, Mg, Si, S, Ar, Ca, Fe (= Ni), velocity dispersion (σ), the redshift (or blueshift), and the emission measure. Our foreground absorption models consist of two `tbnew` models: one for the Milky Way and the other for the SMC. The column density of the former was fixed to 5.36×10^{20} cm^{-2} (Dickey and Lockman, 1990) whereas that of the latter is left free. The elemental abundances for the SMC absorption were fixed to values found in the literature (~ 0.2 solar; Russell and Dopita, 1992). The best-fit model is shown in Figure 6.7, the best-fit parameters are listed in Table 6.3. We assume that N abundances of both NEI models are 0 because that became small values ($\sim 10^{-3}$) in our analysis. Although this model is not statistically acceptable, the RGS spectra are roughly reproduced by this model.

6.4.2 Plasma Diagnostics and Transmission Factor Measurement

We measure the fluxes of several lines to constrain the transmission factors by using the NEI model obtained above. The fluxes of the He α resonance, forbidden, and Heβ of O VII and Ne IX, and Lyα and Lyβ lines of the O VIII and Ne X are directly measured with the following procedure. A similar procedure was performed by Suzuki et al. (2020). We remove all the above emission lines from the NEI models by modifying one of the model data files named `apec_v3.0.9_nei_line.fits` in the XSPEC package (hereafter

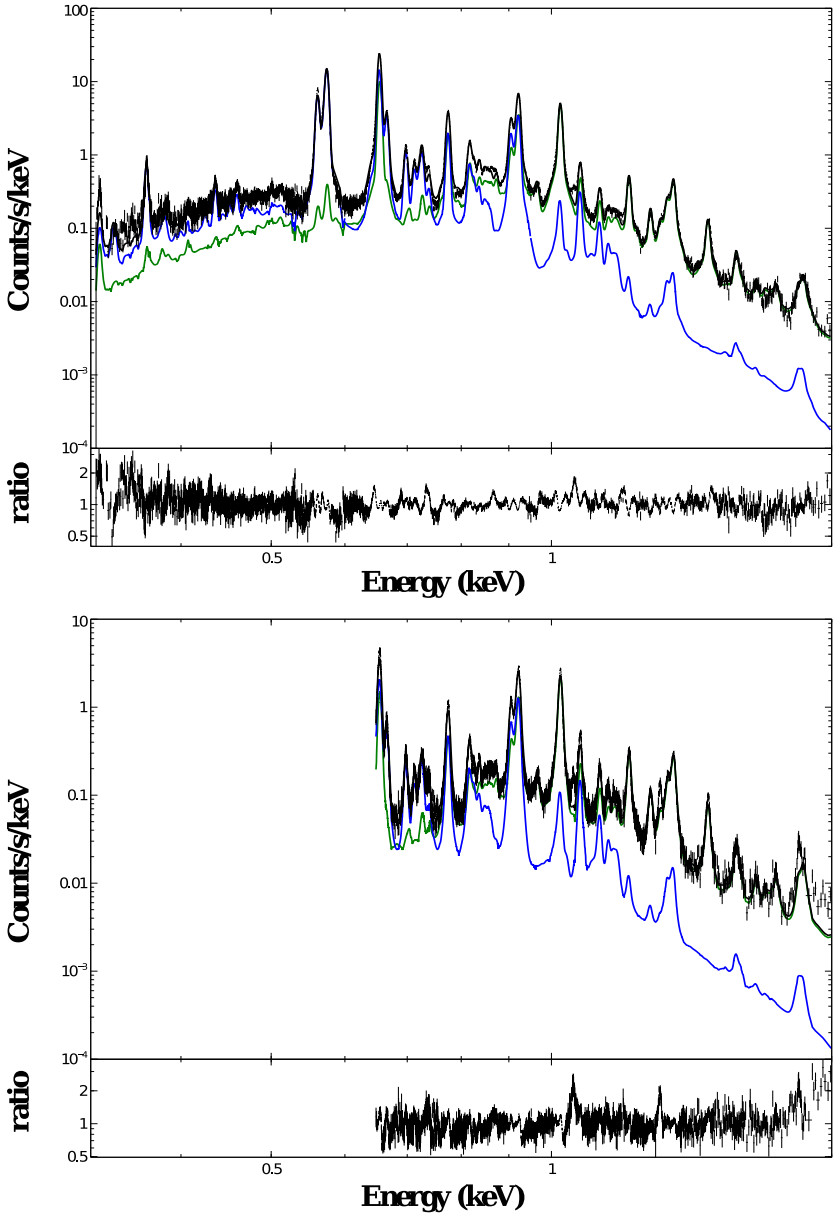

FIGURE 6.7: RGS 1+2 spectra of E0102. Overlaid is the best-fit NEI model. The colored solid curves indicate the contribution of the individual components, low-kT_e (blue) and high-kT_e (green) plasmas.

"modified NEI" model). The best-fit two-temperature NEI model obtained in Subsection 6.4.1 is replaced with a model consisting of the modified NEI plus ten Gaussians for the Heα resonance, forbidden, and Heβ and Lyα and Lyβ lines of O and Ne. All the parameters (e.g., electron temperatures, elemental abundances) of the modified NEI model components are fixed to the best-fit values of the original NEI model. Then we fit the Gaussian components, and obtaining the line fluxes are listed in Table 6.4.

We estimate the kT_e and n_et based on the line fluxes obtained above. We utilize the fluxes of He α forbidden, Heβ, and Lyβ lines. Since these lines have relatively small oscillator strengths, we can derive kT_e and n_et without considering the effects of RS. Figure 6.8 (a-1) shows O VII Heβ/α (f) flux ratio map calculated with AtonDB database and the observed flux ratio. The observed O VII Heβ/α (f) ratio indicates that these lines are emitted by the plasma with an electron temperature of 0.38–0.6 keV. Figure 6.8 (a-2) shows O Lyβ/Heα (f) ratio map. The solid and dashed lines indicate the observed Lyβ/Heα (f) and Heβ/α (f) flux ratios, respectively. The overlap of the contours indicates that oxygen lines are emitted by the plasma with an electron temperature of 0.40 ± 0.01 keV and an ionization time scale of $(7.1 \pm 0.2) \times 10^{10}$ cm^{-3}s. We applied the same procedure to Neon (Figure (b-1), (b-2)). The obtained kT_e and n_et are summarized in Table 6.5.

Since the emissivity of each line has been constrained, we can derive the transmission factors from the line flux ratios as described in Section 6.1. The emissivity ratios calculated using the kT_e and n_et obtained above are summarized in Table 6.5. From Equation (6.8), the transmission factor of Heα (r) and Lyα can be expressed as:

$$p_{\mathrm{He}\alpha\ (r)} = \frac{F_{\mathrm{He}\alpha\ (r)}/F_{\mathrm{He}\alpha\ (f)}}{J_{\mathrm{He}\alpha\ (f)}/J_{\mathrm{He}\alpha\ (r)}} \tag{6.8}$$

$$p_{\mathrm{Ly}\alpha} = \frac{F_{\mathrm{Ly}\alpha}/F_{\mathrm{Ly}\beta}}{J_{\mathrm{Ly}\beta}/J_{\mathrm{Ly}\alpha}}. \tag{6.9}$$

By applying the emissivity ratios in Table 6.5 and the line fluxes in Table 6.4, the transmission factors are calculated as summarized in Table 6.6.

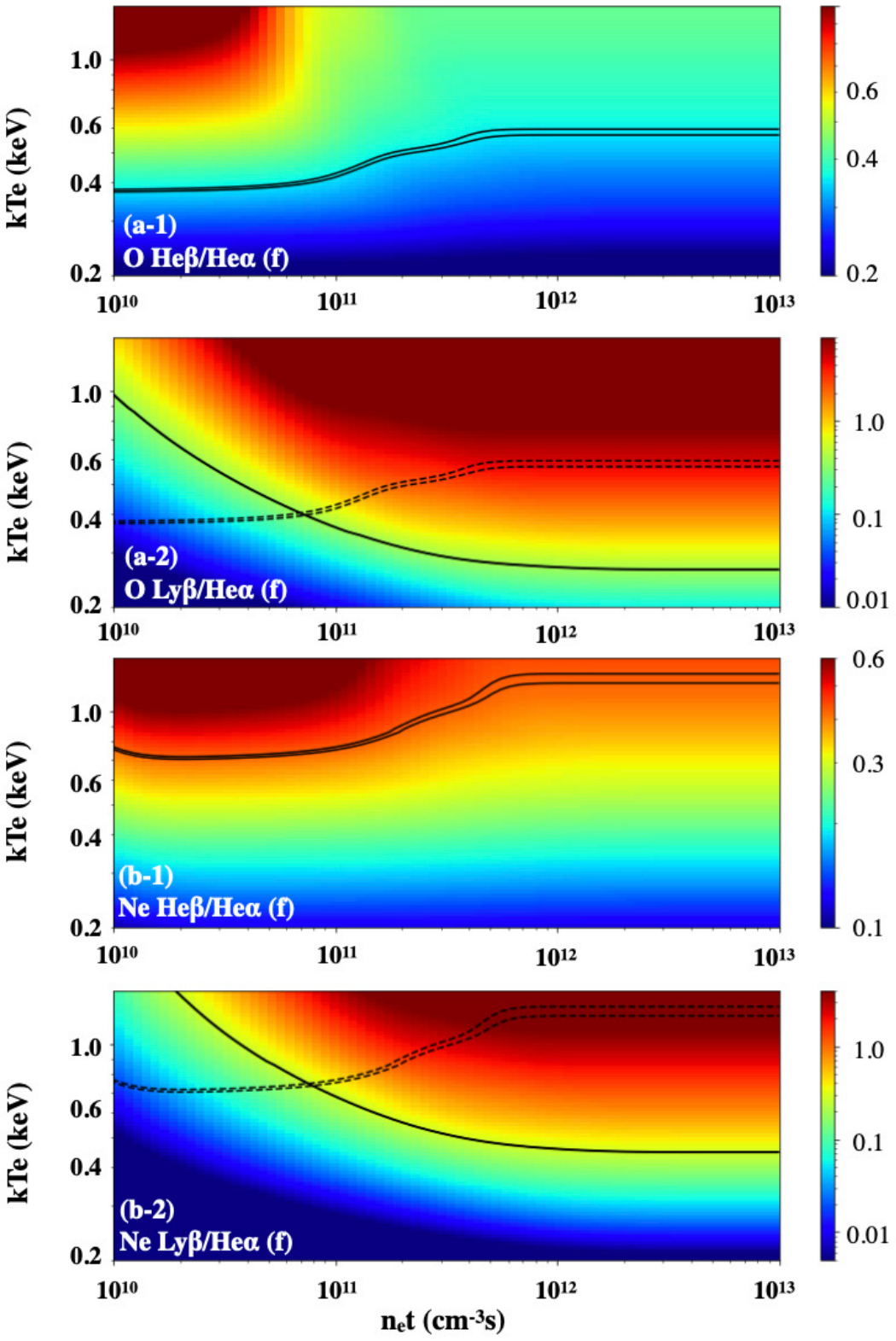

FIGURE 6.8: Theoretical predictions for line ratios of (a-1) Heβ/Heα (f) of O, (a-2) Lyβ/Heα (f) of O, (b-1) Heβ/Heα (f) of Ne, (a-2) Lyβ/Heα (f) of Ne, as a function of ionization time scale ($n_e t$: horizontal axis) and electron temperature (kT_e: vertical axis). The black solid lines indicate the regions constrained by observed line ratios. The black dashed lines indicate the regions constrained by observed Heβ/Heα (f). We constrain the electron temperature and ionization time scale of O and Ne by the overlap of the contours.

TABLE 6.3: Best fit parameters of E0102

Component	Parameters (unit)	Value
Absorption	$N_{\rm H}(MW)$ (10^{20} cm^{-2})	5.36 (fixed)
	$N_{\rm H}(SMC)$ (10^{20} cm^{-2})	$6.95^{+0.010}_{-0.004}$
NEI (low-kT$_{\rm e}$)	$kT_{\rm e}$ (keV)	0.375 ± 0.001
	$kT_{\rm init}$ (keV)	0.01 (fixed)
	$n_{\rm e}t$ (10^{11} cm^{-3})	5.27 ± 0.01
	C	0.62 ± -0.01
	N	0 (fixed)
	O	$1.66^{+0.04}_{-0.01}$
	Ne	$2.78^{+0.09}_{-0.07}$
	Mg	0.75 ± 0.07
	Si	$0.679^{+0.035}_{-0.036}$
	S	$0.724^{+0.028}_{-0.029}$
	Ar	$0.805^{+0.039}_{-0.041}$
	Ca	$0.260^{+0.040}_{-0.041}$
	Fe	0.201 ± 0.020
	σ (10^3 km/s)	1.21 ± 0.01
	$v_{\rm redshift}$	1210 ± 10
	EM (10^{-3} cm^{-3})	$4.30^{+0.02}_{-0.06}$
NEI (high-kT$_{\rm e}$)	$kT_{\rm e}$ (keV)	1.15 ± 0.01
	$kT_{\rm init}$ (keV)	0.01 (fixed)
	$n_{\rm e}t$ (10^{11} cm^{-3})	$7.01^{+0.02}_{-0.05}$
	C	$0.71^{+0.16}_{-0.06}$
	N	0 (fixed)
	O	1.27 ± 0.01
	Ne	$2.67^{+0.09}_{-0.07}$
	Mg	1.60 ± 0.01
	Si	0.401 ± 0.013
	S	1.2 ± 0.1
	Ar	1.8 ± 0.5
	Ca	1.8 ± 0.5
	Fe	$0.294^{+0.001}_{-0.002}$
	σ (10^3 km/s)	1.17 ± 0.01
	$v_{\rm redshift}$	-997^{+7}_{-10}
	EM (10^{56} cm^{-3})	$4.30^{+0.04}_{-0.02}$
	C-statistic/d.o.f.	36047/5772

TABLE 6.4: Observed line fluxes of E0102

	Heα (r) (cm^2/s)	Heα (f) (cm^2/s)	Heβ (cm^2/s)	Lyα (cm^2/s)	Lyβ (cm^2/s)
O	$(4.15 \pm 0.01)\ 10^{-3}$	$(1.96 \pm 0.01)\ 10^{-3}$	$(6.94 \pm 0.04)\ 10^{-4}$	$(5.62 \pm 0.01)\ 10^{-3}$	$(7.96 \pm 0.03)\ 10^{-4}$
Ne	$(1.39 \pm 0.01)\ 10^{-3}$	$(6.23 \pm 0.04\ 10^{-4}$	$(2.66 \pm 0.02)\ 10^{-4}$	$(1.33 \pm 0.01)\ 10^{-3}$	$(1.82 \pm 0.01)\ 10^{-4}$

TABLE 6.5: Obtained kT_e and $n_e t$, and line emissivity ratios

	kT_e (keV)	$n_e t$ (10^{10} cm^{-3}s)	Heα (f)/Heα (r)	Lyβ/Lyα
O	0.40 ± 0.01	7.1 ± 0.2	$0.446^{+0.037}_{-0.020}$	0.130 ± 0.008
Ne	0.74 ± 0.01	7.8 ± 0.2	0.361 ± 0.006	0.134 ± 0.003

TABLE 6.6: Transmission factors

Line ID	Transmission Factor
O VII Heα (resonance)	$0.943^{+0.077}_{-0.043}$
O VIII Lyα	$0.915^{+0.054}_{-0.058}$
Ne IX Heα (resonance)	0.806 ± 0.014
Ne X Lyα	0.982 ± 0.018

6.5 Discussion

In this section, we examine the validity of 3D structures proposed in previous studies by comparison between the transmission factors expected from the proposed structure and those obtained from our analysis.

6.5.1 Cylindrical Model

We examine the possibility of a cylindrical structure proposed by Flanagan et al. (2004). Based on their observations, the 3D structure of E0102 is determined as follows. Flanagan et al. (2004) claims that E0102 has the cylindrical structure expanding at $\pm$900 km/s along the line of sight. Since the age of E0102 is estimated to be 1738 ± 175 yr (Banovetz et al., 2021), we assume that E0102 is in free expansion at $\pm$900 km/s for 1738 years. Therefore, the line-of-sight length of E0102 is about 3.2 pc (Figure 6.9). The inner and outer diameter of E0102 are calculated as 4.2 pc and 5.4 pc from the X-ray image, assuming the distance to E0102 is 62 kpc (Graczyk et al., 2020). Since the 3D structure of E0102 has been determined, we can estimate the electron column density and the transmission factor from the observed line flux.

We describe the procedure to estimate the transmission factor of the O VII Heα (r) line. First, the electron column density is calculated from the volume of E0102 and the observed line flux of the O VII Heα (f). By substituting the values of $F_{\mathrm{He}\alpha\ (f)}$ in Table 6.4 and $J_{\mathrm{He}\alpha\ (f)}$ constrained in subsection 6.4.2 into Equation (6.5), the emission measure $((0.8\ n_{\mathrm{e}}^2)/(4\pi d^2)V)$ is $(3.32 \pm 0.01) \times 10^{11}$ (cm^{-5}), where we assume the oxygen abundance $(n_{\mathrm{O}}/n_{\mathrm{H}})$ to be 2.7 based on the result of our spectral modeling obtained in Subsection 6.4.1. The volume of E0102 is 3.40×10^{57} (cm^3) from Figure 6.9, so the electron density is 7.30 ± 0.02 (cm^{-3}), from the emission measure obtained above. Finally, we obtain the electron column density to be 7.29 ± 0.01 (cm^{-2}) from the electron density and the line-of-sight length of E0102.

Next, we estimate the transmission factor of O VII Heα (r) in a similar way as we did in Chapter 5. We adopt the same assumption as Kaastra and Mewe (1995). Then, the transmission factor is written as Equation (5.5). The optical depth τ at the line centroid is given as Equation (3.55) in Chapter 3. We neglect the micro-turbulence velocity and assume a thermal equilibrium between all ions and electrons, thus the ion temperature (T_{keV}) is equal to the electron temperature obtained in Subsection 6.4.2 (0.4 keV). The oscillator strengths and ion fractions for each element are taken from Atomdb. In the case of E0102 the electron column density is $(7.29 \pm 0.01) \times 10^{20}$ (cm^{-2}).

We also estimate the transmission factors of the Lyα line in a similar way to that of the O VII Heα (r) line. Figure 6.10 and 6.11 show the transmission factors of O and Ne lines as a function of the electron column density. The range of column densities correspond to the blue shaded area, and the transmission factors corresponding to these column densities are shown in the cyan shaded area. The orange shaded areas indicate the transmission factors obtained from our analysis summarized in Table 6.6. As can be seen from Figure 6.10 and 6.11, the cylindrical structure proposed by Flanagan

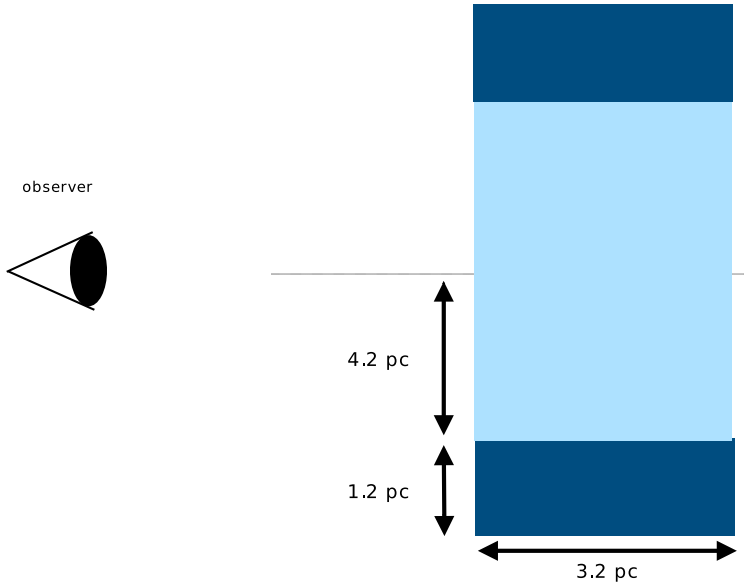

FIGURE 6.9: Cross sectional view of E0102. Here E0102 has the cylindrical structure proposed by Flanagan et al. (2004).

et al. (2004) requires lower transmission factors for each line than those obtained in our analysis. Therefore, we conclude that the structure proposed by Flanagan et al. (2004) is inconsistent with our observational results.

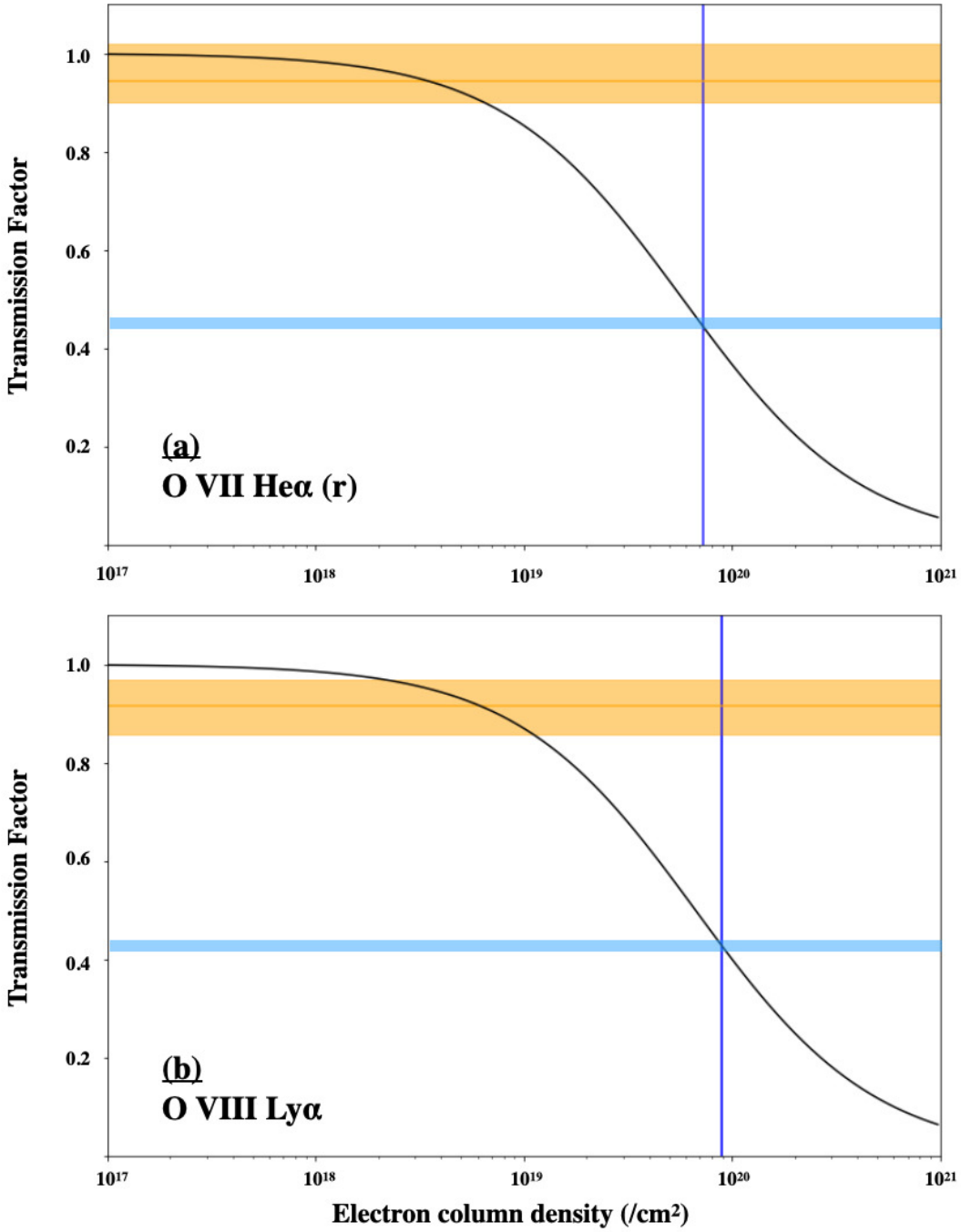

FIGURE 6.10: Relation between the transmission factor and the electron column density of (a) O VII Heα (r), and (b) O VIII Lyα. The black solid curves represent the transmission factor calculated from Equation (5.5).

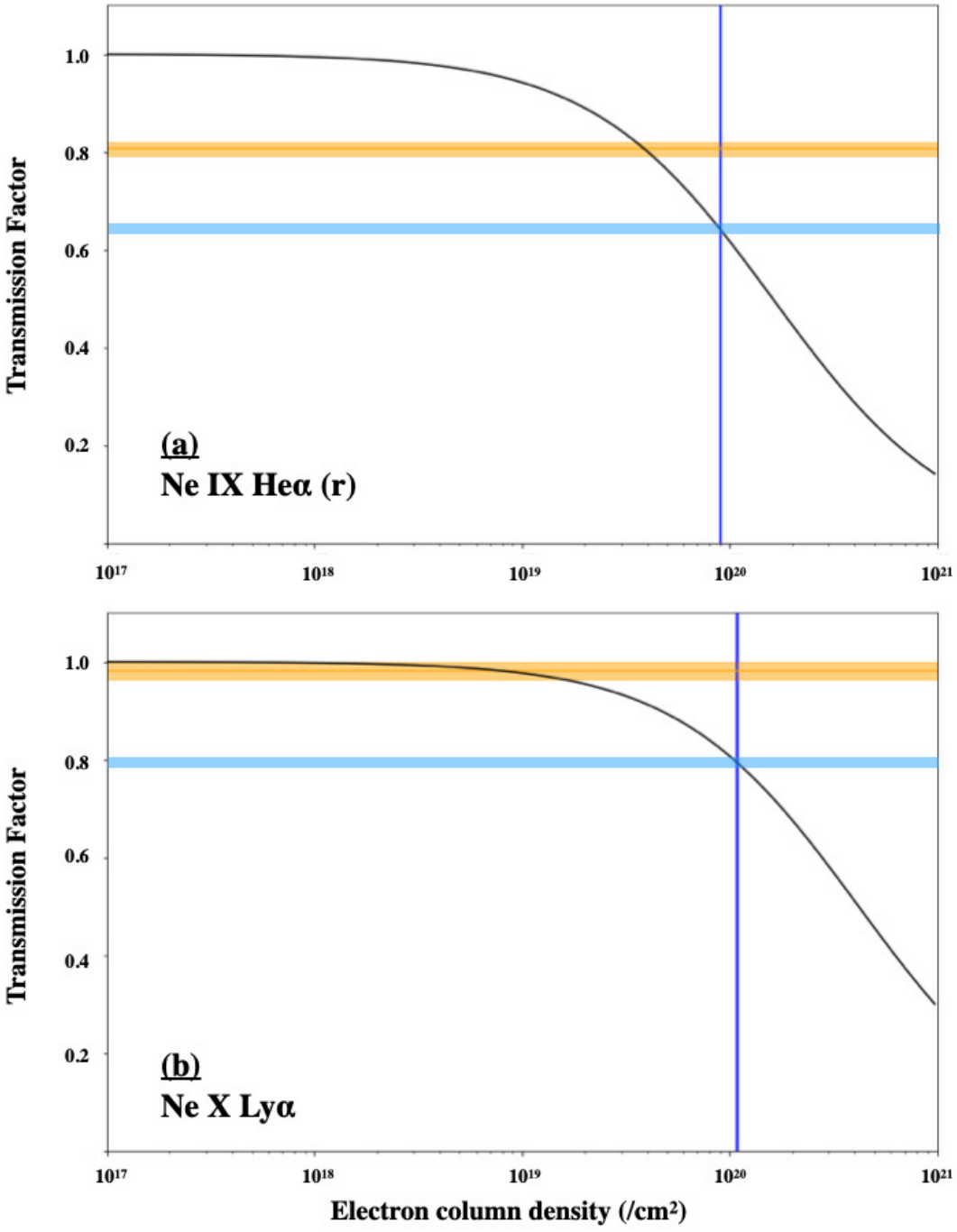

FIGURE 6.11: Same as Figure 6.10 but for Ne lines.

6.5.2 Barrel-Like Structure

Another possible structure of E0102 is a partial spherical shell with a barrel-like shape (Figure 6.12 (a)), which was suggested by Hughes (1994). Assuming the distance to E0102 is 62 kpc (Graczyk et al., 2020), their proposed structure has an inner diameter of 3.7 pc (1.14×10^{19} cm) and an outer diameter of 5.2 pc (1.60×10^{19} cm), as shown in Figure 6.12 (a). In this case, the volume of E0102 is 5.5×10^{57} cm^3. As in Subsection 6.5.1, the electron density can be calculated using the volume of E0102 and the line fluxes.

To estimate the electron column density, we calculate the mean line-of-sight length ($L_{\rm mean}$) of E0102. Figure 6.12 (b) shows the area enclosed by the red dashed line in Figure 6.12 (a). We define $x_{\rm i}$ every 0.01 pc between $x_{\rm min}$ and $x_{\rm max}$, and calculate the line-of-sight length of E0102 ($2 \times l_{\rm i}$) for each $x_{\rm i}$. Using $l_{\rm i}$, the mean line-of-sight length ($L_{\rm mean}$) of E0102 is expressed as:

$$L_{\rm mean} = \frac{1}{n}\sum_{i=1}^{n} l_{\rm i}. \tag{6.10}$$

The mean line-of-sight length ($L_{\rm mean}$) is 4.1 pc, which requires a higher electron column density than that of the cylindrical model calculated in Subsection 6.5.1. The results of calculating the transmission factors from the electron column density obtained above are shown in Figures 6.13 and 6.14. Similar to the cylindrical model, the barrel-like structure requires lower transmission factors than those of our observations for all emission lines. Therefore, we conclude that the barrel-like structure proposed by Hughes (1994) is also inconsistent with our observations.

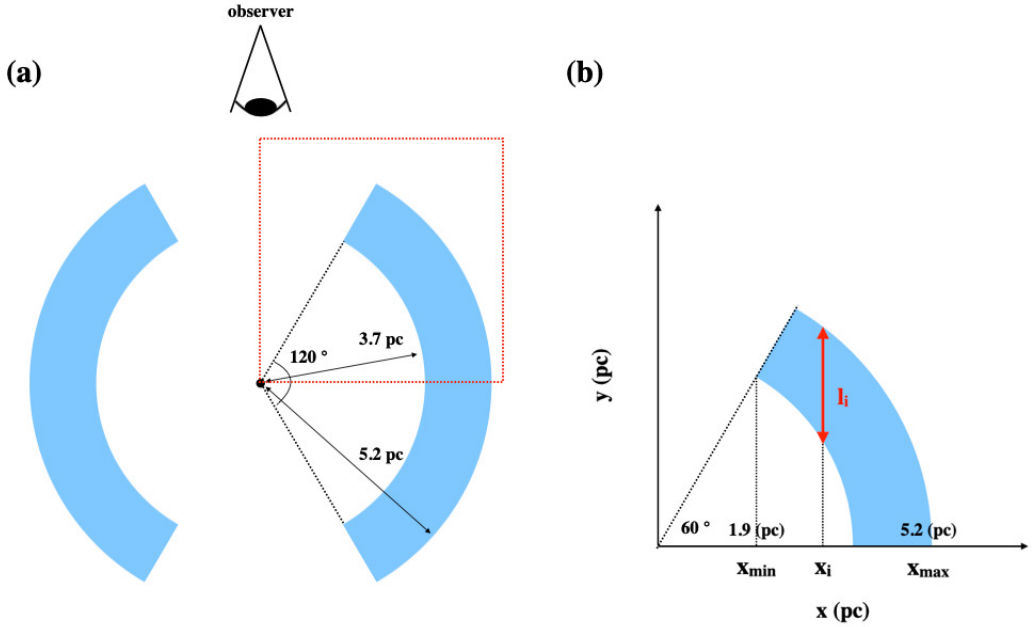

FIGURE 6.12: (a) Cross sectional view of E0102. Here E0102 has the barrel-like structure proposed by Hughes (1994). The area enclosed by the red dashed line corresponds to the area shown in the right panel of Figure 6.3. (b) Area enclosed by the red dashed line in (a). We calculate the length l_i of E0102 along the line-of-sight direction for each x_i, and then determine the average value L_{mean} to obtain the electron column density.

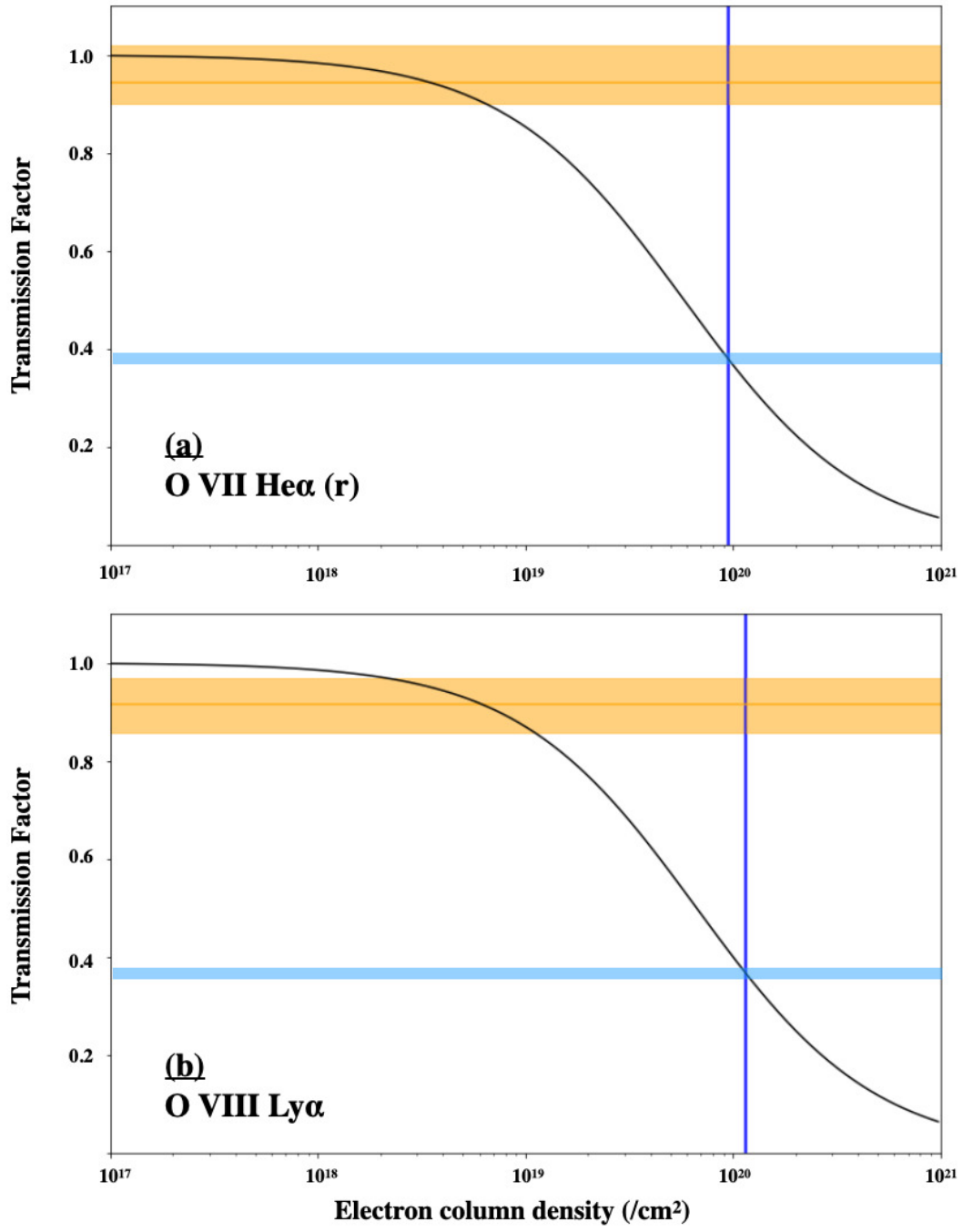

FIGURE 6.13: Same as Figure 6.10, but for the barrel-like structure.

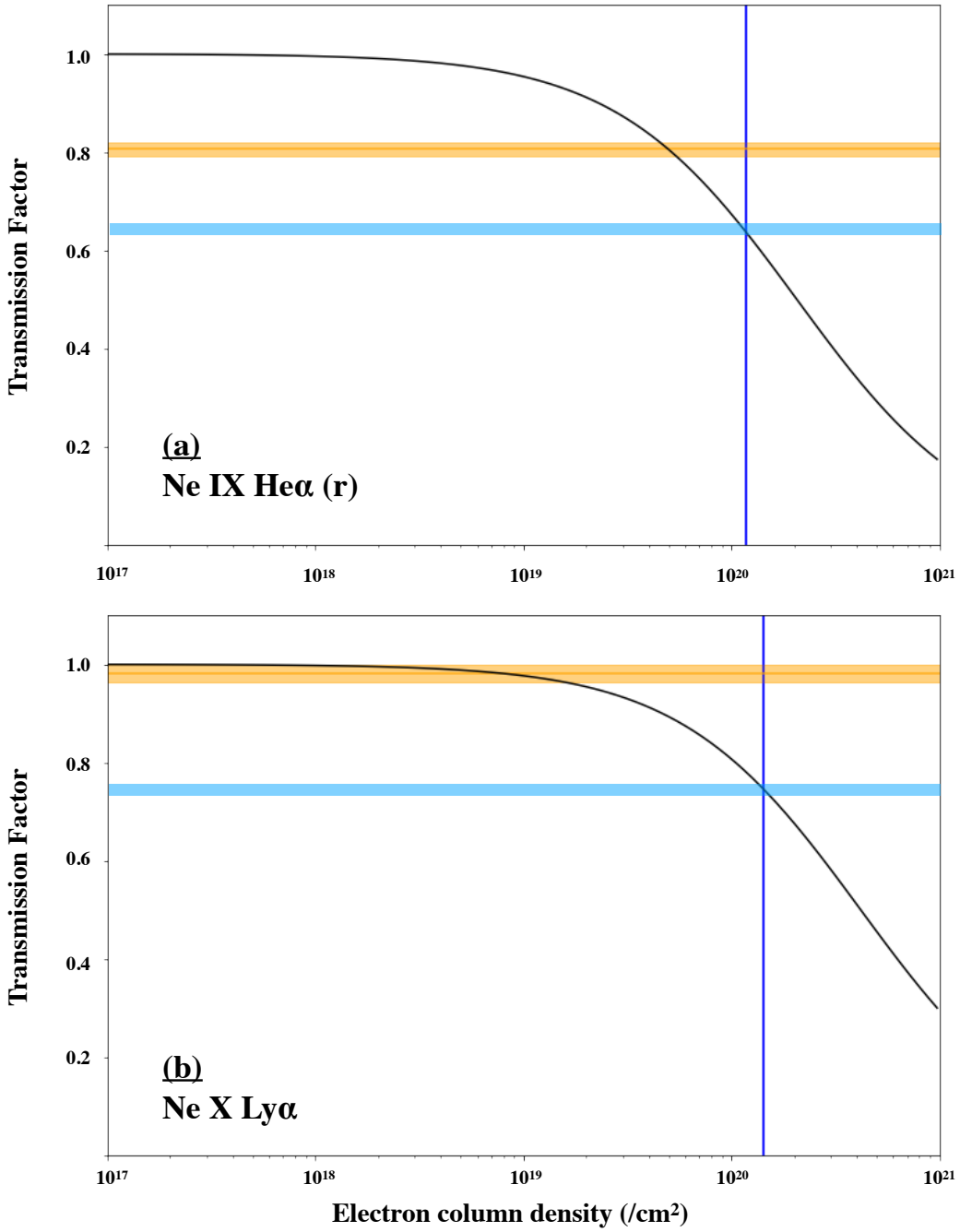

FIGURE 6.14: Same as Figure 6.11, but for the barrel-like structure.

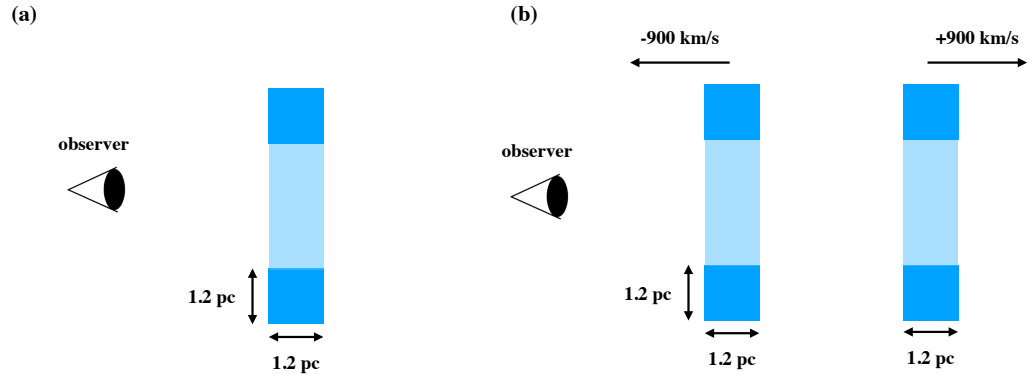

FIGURE 6.15: (a) Cross sectional view of single ring structure. (b) Cross sectional view of double ring structure.

6.5.3 Structures That Explain Our Observation

In this subsection, we propose possible structures that explain our observations. The structures proposed by previous studies require lower transmission factors, which is inconsistent with our observations. For the two structures described below, relatively high transmission factors is expected. We consider that one of these structures is the plausible 3D structure for E0102.

Double-Ring Structure

According to the results in Subsection 6.5.1, a cylindrical structure with a large line-of-sight length ($\sim$ 3.2 pc) requires a stronger scattering effect than that we have observed in Subsection 6.4.2. In the case of a ring-like structure, as shown in Figure 6.15 (a), the thickness of E0102 in the line-of-sight direction is equal to the thickness in the direction perpendicular to the line-of-sight direction. For such symmetrical structures, the RS effect is canceled out, which could explain our observations. However, such a single ring-like structure is inconsistent with the observation by Flanagan et al. (2004). We have estimated that the line-of-sight length of E0102 is 3.2 pc in Subsection 6.5.1, assuming it is in free expansion at the current observed expansion velocity by Flanagan et al. (2004). Since it is unlikely that E0102 is in accelerating expansion, this value can be considered a lower limit for the line-of-sight length of E0102. Therefore, we propose a double ring structure as shown in Figure 6.15 (b) as a structure to explain both Flanagan et al. (2004) and our results. If E0102 had such a structure, the observed scattering effect would be slight and could explain the Doppler velocity ($\pm$900 km/s) observed by Flanagan et al. (2004).

Cylindrical Model Considering Velocity Structure

The kinetic motion of ions can reduce the cross section and optical depth of RS. In Subsection 6.5.1, we considered only thermal motion as the kinetic motion. However, we found that the cylindrical structure proposed by Flanagan

et al. (2004) could also account for our observations by taking into account the bulk motion of ions due to the cylinder's expansion in the line-of-sight direction.

We estimate the effect of the line-of-sight expansion velocity on the optical depth of each emission line. Assuming a uniform density, the line-of-sight velocity is proportional to the line-of-sight distance, as shown in Figure 6.16. We use Figure 6.17 to consider the optical depth for photons emitted at arbitrary point A in E0102. For example, the cross section at point B, which is 0.3 pc away from point A, can be estimated as follows. In the point A stationary system, the photon energy distribution of the O VII Heα emitted at A is represented by the solid black line in Figure 6.17 (b). Since the Doppler broadening due to the thermal motion of ions is significantly larger than the natural width of O VII Heα (r), the energy distribution of photons is expressed by a Gaussian distribution characterized by the variance:

$$\Delta h\nu = \left(\frac{2kT_i}{m_i c^2}\right)^{1/2} h\nu_0, \tag{6.11}$$

where $h\nu_0$ is the rest frame photon energy, m_i is the ion mass, and T_i is the ion temperature. In this case, the cross section of the ion present at point B is represented by the solid red line in Figure 6.17 (b). Of the photons emitted at point A, those scattered at point B are included in σ_2 in Figure 6.17 (b). We thus define σ_2 as the effective cross section at point B.

Figure 6.18 shows the relationship between the distance from where the photon is emitted and the effective cross section at that location. At a distance of more than 0.6 pc away from where the photon is emitted (point A), the effective cross section (σ_2) is less than 0.01 times $\sigma_1 + \sigma_2$. Since the optical depths of E0102 obtained in Subsection 6.5.1 are approximately 3 at most (see the middle column of Table 6.7), RS in the area where the cross section becomes 0.01 times is negligible. Therefore, we adopt 0.6 pc as the upper limit of effective line-of-sight length for E0102. The right column of Table 6.7 summarizes the optical depth τ of each emission line when the line-of-sight length is 0.6 pc. The reduction in cross section due to the expansion significantly decreases the optical depth of each line, making all lines optically thin. Therefore, such an effect may explain our observations.

TABLE 6.7: Optical depth

Line ID	w/o velocity	w velocity
O VII Heα (resonance)	2.92	0.548
O VIII Lyα	3.01	0.579
Ne IX Heα (resonance)	1.01	0.189
Ne X Lyα	0.603	0.113

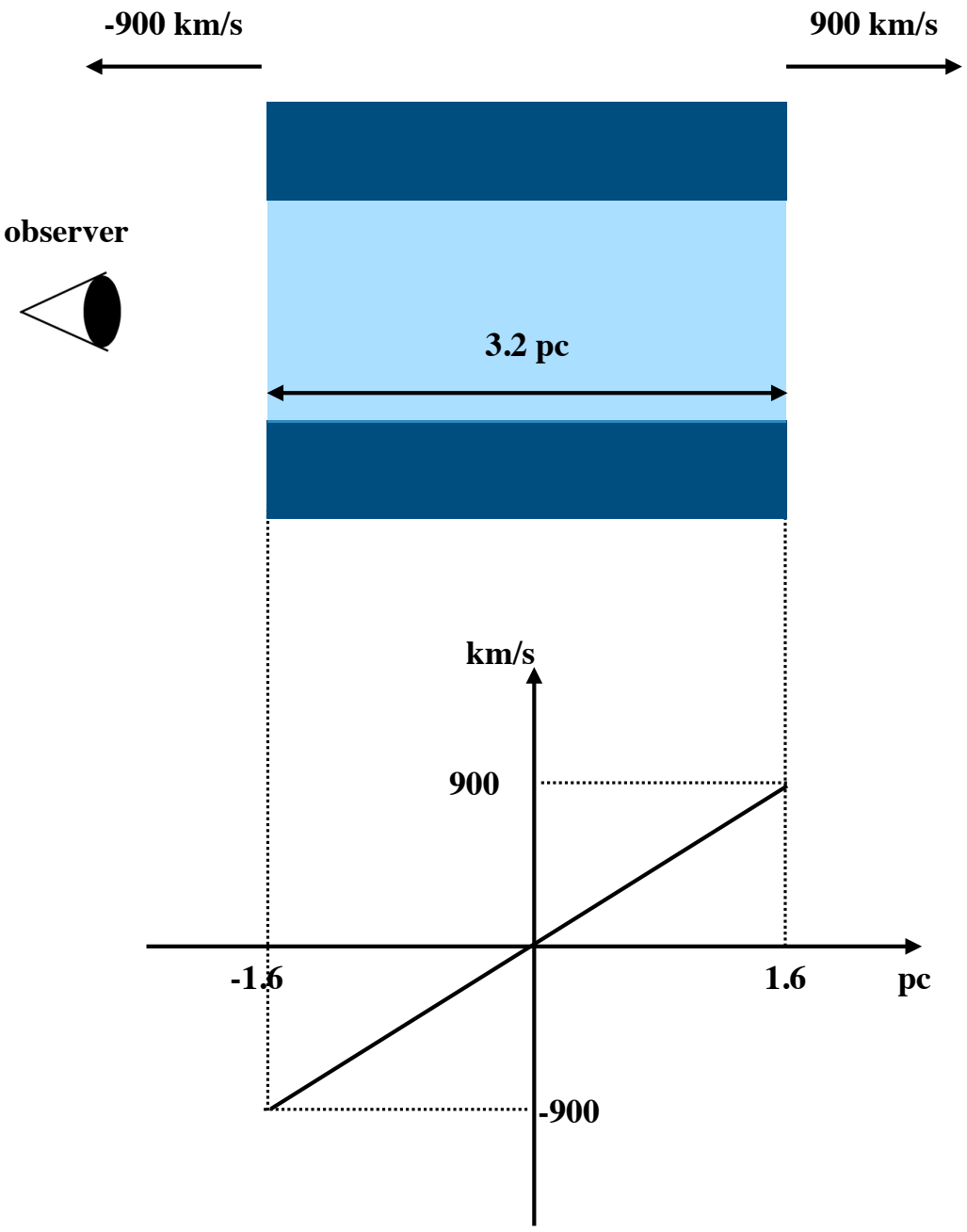

FIGURE 6.16: Cross sectional view of a cylindrical structure and the velocity structure. The upper panel shows the cylindrical structure proposed by Flanagan et al. (2004). The lower panel shows the relationship between line-of-sight distance and velocity. The horizontal and vertical axis corresponds to the distance from the observer and the expansion velocity of E0102 in the line-of-sight direction, respectively.

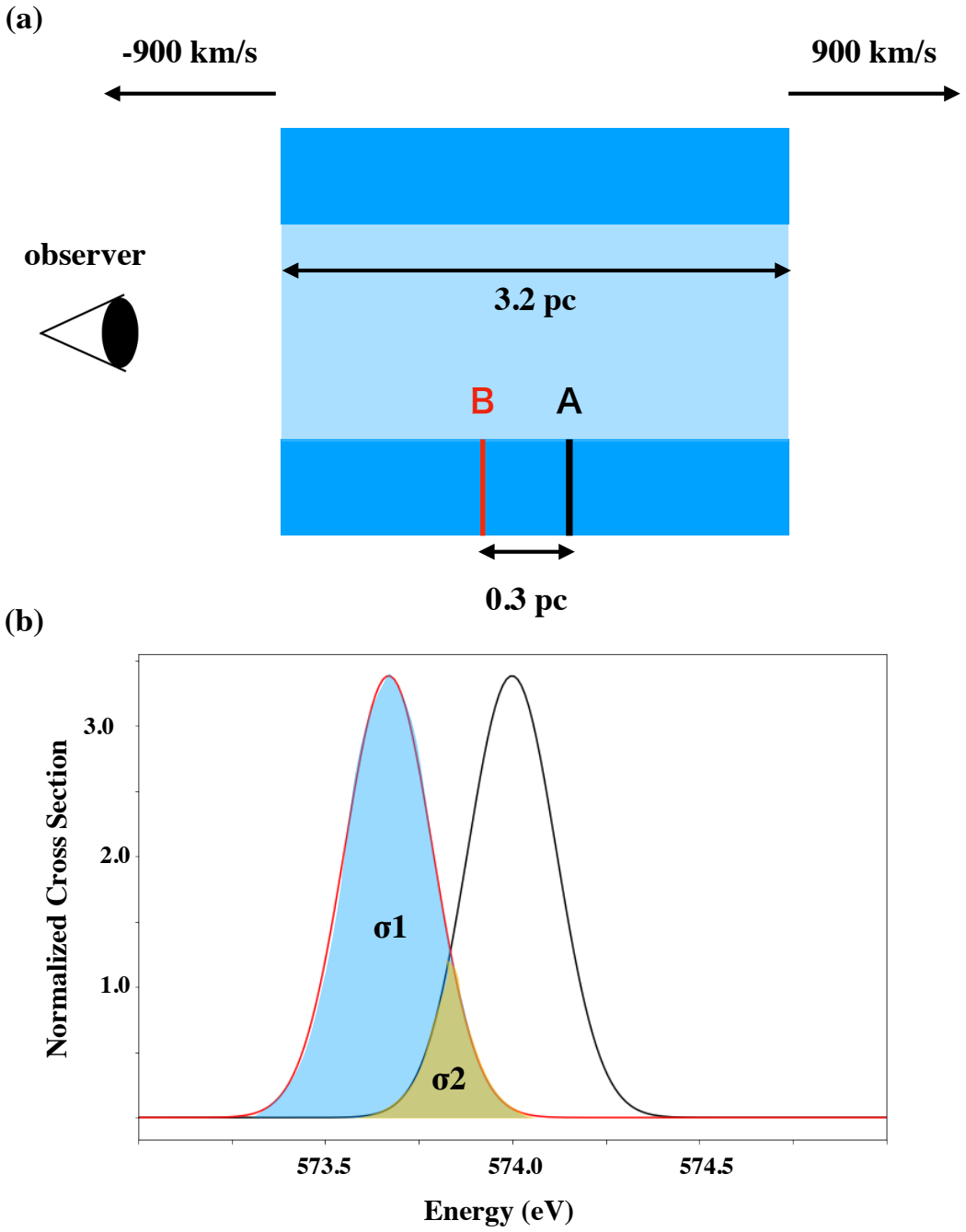

FIGURE 6.17: Line-of-sight distance dependence of RS cross section. (a) Same as the upper panel of Figure 6.16. We consider the cross section at point B of a photon emitted at point A. (b) Photon energy distribution ans RS cross section of the O VII He$\alpha(r)$. The solid black line represents the photon energy distribution of the O VII Heα emitted at A, in the point A stationary system. The solid red line represents the RS cross section at point B. $\sigma_1 + \sigma_2$ corresponds to the cross section without considering the Doppler shift due to expansion. Of the photons emitted at point A, the photons contained in σ_2 are scattered.

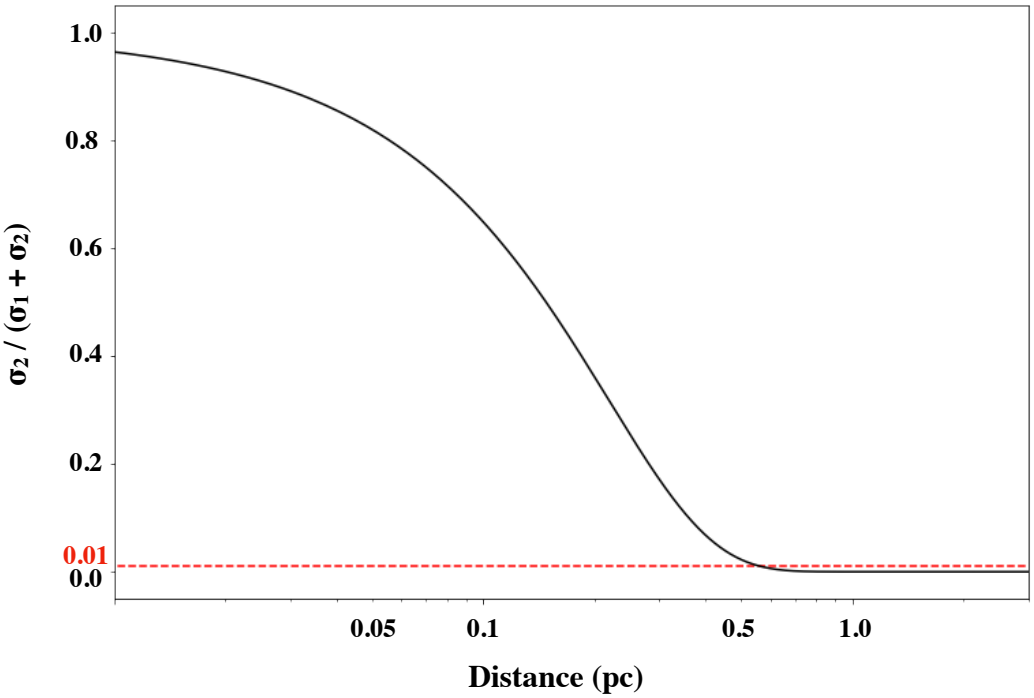

FIGURE 6.18: Relationship between cross section and line-of-sight distance. The horizontal axis corresponds to the distance between two points in E0102. The vertical axis corresponds to the ratio of the cross section without considering the Doppler shift due to expansion to the effective cross section.

6.5.4 Progenitor of E0102

We discuss the implications of the structures proposed in Subsection 6.5.3 for the progenitor of E0102. We proposed a double-ring structure or a cylindrical structure with the expansion velocity, both of which are aspherically symmetric but have an axisymmetric structure. The key to the formation of such structures of SNRs is binary interactions, which create disk-like CSMs and bipolar cavities around SNRs as explained in Chapter 2. When an SN explodes in such a CSM structure, SNR can be elongated along the polar axis, as demonstrated by Blondin et al. (1996). This may explain the cylindrical structure of E0102. Multi-ring structures have been observed in other SNRs such as N103B and SN1987A (e.g., Yamaguchi et al., 2021), whose progenitors are also considered to be binary stars, and their ring-like structures are thought to have been formed by CSMs structure resulted from binary interactions. Therefore, our results and previous studies suggest that the progenitor of E0102 may also be a binary star.

6.6 Summary

We presented a method to constrain the 3D structure of SNRs using the effects of RS and applied this method to the SNR E0102. The transmission factors of the O and Ne lines were estimated to be larger than 0.79. The structures proposed by previous studies require lower transmission factors, which is inconsistent with our results. Therefore, we have proposed a double-ring structure or a cylindrical structure with the expansion velocity as structures that are consistent with both our observations and previous studies. These axisymmetric structures imply that the progenitor of E0102 could be a binary star. As we will explain in Chapter 7, this method can be applied to many celestial objects using the future satellite XRISM.

Chapter 7

Discussion

7.1 Summary of Our Results and Previous Studies

In this section, based on our results and previous studies, we discuss the physical conditions in which CX and/or RS efficiently take place, and the key spectral signature to distinguish between the CX and RS. This information is useful for precise spectroscopy that properly takes into account the contribution of the CX and RS.

7.1.1 Physical Conditions in which RS and/or CX Efficiently Occur

TABLE 7.1: Summary of previous and our RGS stidies

Object name	SN type	Ref.	age	Ref.	Environment	Ref.	RS or CX	Ref.
E0102	Ib/c or IIL/b	1,2	1000–1600	3, 4	no data		RS	5
N132D	Ib	1	2500	6	CO and H I clouds	7, 8, 9	RS?	10
Puppis A	IIL/b	2	3700	11	H I clouds	12	CX	13
DEM L71	Ia	14	4400	15	no data		RS?	16
N23	II	17	4600	17	Star-forming region	18	RS?	19
N49	II	20	5000	20	CO and HI clouds	7, 8, 21	RS	22
J0453.6−6829	II	23	13000	24	HI clouds	24	CX	25
Cygnus Loop	II	26	14000	27	near by clouds interaction region	28	CX and RS?	29
G296.1−0.5	Ib/c	30	20000	31	HI clouds	32	CX	32

References. (1) Blair et al. (2000); (2) Chevalier (2005); (3) Hughes et al. (2000); (4) Banovetz et al. (2021); (5) This work (Chapter 6). (6) Vogt and Dopita (2011); (7) Banas et al. (1997); (8) Sano et al. (2017); (9) Sano et al. (2020); (10) Suzuki et al. (2020); (11) Winkler et al. (1988); (12) Reynoso et al. (1995); (13) Katsuda et al. (2012); (14) Hughes et al. (1998); (15) Ghavamian et al. (2003); (16) van der Heyden et al. (2003); (17) Hughes et al. (2006); (18) Chu et al. (1988); (19) Broersen et al. (2011); (20) Park et al. (2012); (21) Yamane et al. (2018); (22) This work (Chapter 5). (23) Lopez et al. (2009); (24) Gaensler et al. (2003); (25) This work (Chapter 5). (26) Miyata et al. (1998); (27) Levenson et al. (1998); (28) Patnaude and Fesen (2005); (29) Uchida et al. (2019); (30) Castro et al. (2011); (31) Hwang et al. (1994); (32) Tanaka et al. (2022);

In Table 7.1, we summarize SNRs observed with the RGS to date to compare our results with other SNRs. Based on the result of N49, RS tends to be observed in an asymmetric structure of SNRs with a large column density. Therefore, for example, at the rim of SNRs, the effect of RS is expected to be observed.

Our spatially-resolved spectral analysis of J0453.6−6829 has revealed a significant enhancement of CX X-ray emission in the southwest region where

the SNR interact with the dense H I gas. Furthermore, we estimate the volume of the CX-emitting region to be roughly 0.4 % of the entire SNR volume. CX X-ray emission is thus expected to be observed in the outer edge of the shock front in contact with dense clouds. In addition to J0453.6−6829, CX emissions have been observed in other SNRs, such as Puppis A (Katsuda et al., 2012), Cygnus Loop (Uchida et al., 2019), and G296.1−0.5 (Tanaka et al., 2022). All of these studies are based on observations of partially bright structures in the galactic SNRs. These bright structures are considered to be formed as a result of collisions between SNRs and the surrounding dense neutral gases (e.g., Hwang et al., 2005). Hence, our result is in line with the results of these previous studies.

It is worth noting that most of the SNRs in which CX has been observed are older than 10000 years. This tendency can be attributed to the dependence of the cross section of CX on the collision velocity between ions and neutral hydrogen. According to Equation (2.31) in Chapter 2, the shock wave velocity of the young SNR is relatively high, and consequently, the collision velocity between ions and neutral atoms at the shock front is expected to be large. Figure 7.1 shows the relationship between the collision velocity and the total cross section of CX. The cross sections of CX are relatively large in a collision velocity below 2000 km/s and decrease sharply above 2000 km/s. Therefore, it is important to consider the effect of CX in the spectroscopy of evolved SNRs.

7.1.2 Spectral Feature to Distinguish between CX and RS

Both CX and RS have similar observational signatures such as a high f/r ratio, making it difficult to distinguish between these two processes spectroscopically. However, we found that the (3s–2p)/(3d–2p) ratio of Fe XVII Lα lines is a useful spectral feature for distinguishing between the two processes. Because of the following reasons, in typical SNR plasmas, the (3s–2p)/(3d–2p) ratio is sensitive to RS but rarely affected by CX. In the electron temperature range (0.1–0.5 keV) of typical SNR plasmas, most Fe atoms are in the Ne-like ionization state and rarely in the Na-like ionization states (see Figure 3.3). The Fe XVII ($n = 3 \rightarrow 2$) lines are emitted via CX described as:

$$\mathrm{Fe}^{17+} + \mathrm{H} \rightarrow \mathrm{Fe}^{*16+} + \mathrm{H}^{+} \rightarrow \mathrm{Fe}^{16+} + h\nu + \mathrm{H}^{+}. \tag{7.1}$$

Therefore, in typical SNR plasmas where most Fe elements are in a Ne-like ionization state (Fe^{16+}), Fe XVII Lα lines are scarcely emitted by CX. On the other hand, since the Fe XVII Lα lines are scattered by Ne-like Fe, typical SNR plasmas have large optical depths of RS for Fe XVII Lα lines. Since the (3d–2p) line has a larger oscillator strength than the (3s–2p) line (see Table 7.2), the (3s–2p)/(3d–2p) ratio of Fe XVII Lα lines is enhanced by RS. Therefore, a high (3s–2p)/(3d–2p) ratio of Fe XVII Lα lines is an exclusive spectral feature of RS. In fact, a high (3s–2p)/(3d–2p) ratio was observed in the RGS spectrum of N49, but not in the spectrum of J0453.6−6829, which provided an important clue to distinguish between CX and RS.

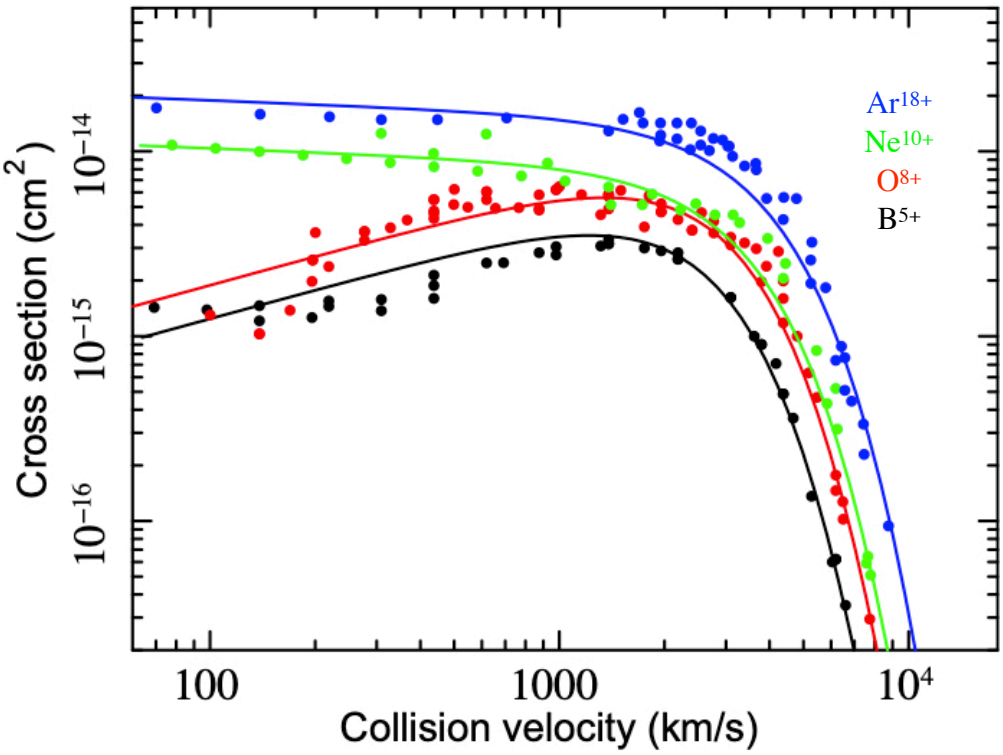

FIGURE 7.1: Total cross sections of CX, as functions of collision velocity, for B^{5+} (black), O^{8+} (red), Ne^{10+} (green), and Ar^{18+} (blue) interacting with a hydrogen atom (Gu et al., 2016).

TABLE 7.2: Oscillator Strength of Fe XVII Lα lines (taken from Atomdb)

Transition	Centroid Energy (Wavelength)	Oscillator Strength
$2s^2 2p^5 3d\ (^1D_1) \rightarrow 2s^2 2p^6\ (^1S_0)$; (3d–2p)	0.826 keV (15.02 Å)	2.49
$2s^2 2p^5 3s\ (^1P_1) \rightarrow 2s^2 2p^6\ (^1S_0)$; (3s–2p)	0.725 keV (17.05 Å)	0.126

7.2 Effect on Elemental Abundances Measurement and Progenitor Estimation

Several previous studies pointed out that ignoring the effects of CX and RS can lead to bias in parameter measurements (e.g., Kaastra and Mewe, 1995). Based on the results of N49 and J0453.6−6829, we evaluate the impact of CX and RS on parameter measurements and the progenitor estimation based on these parameters. In our results, we found that the impact on the measurement of oxygen abundance is particularly large. By comparing the best-fit parameters of the NEI and NEI-Gaussians models in Table 5.1, we find that the oxygen abundance of N49 is underestimated by a factor of ∼1.8, if we do not take into account the RS effect. Katsuda et al. (2018) point out that the Fe/O ratio is sensitive to the progenitor mass. We thus use the Fe/O ratio shown in Katsuda et al. (2018) to evaluate the impact on progenitor mass estimation based on these parameters.

From the best-fit parameters of the NEI model in Table 5.1, without considering RS, the Fe/O ratio of N49 is measured to be about 0.45. On the other hand, a model that takes into account the RS effect (NEI-Gaussians model) measures the Fe/O ratio at 0.25. These Fe/O ratios correspond to CO core masses ($M_{\rm COcore}$) of about 3.2 and 4.5, respectively (Figure 7.2 (a)). As argued by Katsuda et al. (2018), there is a good linear relation between $M_{\rm COcore}$ and progenitor mass ($M_{\rm ZAMS}$: zero age main sequence mass) at a mass range of $M_{\rm ZAMS} < 40\ M_\odot$ (Figure 7.2 (b)). Therefore, the progenitor mass can be estimated using the CO core mass obtained above. As shown in Figure 7.2 (b), without considering RS, the progenitor mass of N49 is estimated to be about 16 $M_\odot$, and with RS, it is estimated to be about 20 $M_\odot$.

It is worth noting that N49 contains the magnetar candidate SGR 0526˘66 (Cline et al., 1981). Although the origin of magnetars is still unclear, they may have been created by very massive progenitors. For example, SGR 1806−20 and CXO J164710.2−455216 are considered to be produced by progenitors with masses of $M > 40\ M_\odot$ (Muno et al., 2005; Figer et al., 2005). The progenitor mass of the AXP 1E 1841−045 and SGR 1900+14 are estimated to be $\sim 20\ M_\odot$ (Kumar et al., 2014) and $\sim 17\ M_\odot$ (Davies et al., 2009), respectively. The progenitor mass of $\sim 20\ M_\odot$ obtained with the model considering RS is in line with the observational studies of progenitors of magnetars.

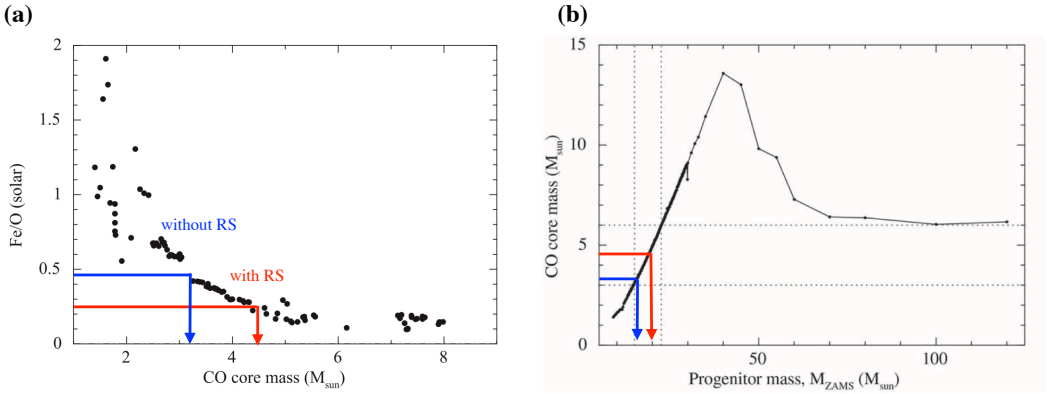

FIGURE 7.2: (a) Fe/O abundance ratios as a function of the CO core mass (Katsuda et al., 2018), based on the nucleosynthesis models by Sukhbold et al. (2016). The abundances are relative to the solar values Anders and Grevesse (1989). The Fe/O ratio obtained by the NEI model (without considering RS) and the corresponding CO core mass are shown in blue. The red arrow indicates those obtained by the NEI-Gaussinas model. (b) CO core mass as a function of a progenitor mass, $M_{\rm ZAMS}$ (Sukhbold et al., 2016). The red and blue arrows are the same as in (a).

7.3 Constraint on 3D Structure of SNRs Using XRISM

In Chapter 6, we proposed a method to constrain the 3D structure of SNR plasmas using the effect of RS. This method can be applied to only compact SNR with RGS. However, using this method with the XRISM satellite, we can determine the detailed 3D structure of many objects including diffuse SNR in the Milky Way. In this section, using the observation of W49B as an example, we explain how to apply this method to galactic SNRs by XRISM.

The XRISM satellite is the 7th Japanese X-ray astronomical satellite, which is to be launched in 2023. The XRISM satellite carries two types of X-ray detectors, an X-ray microcalorimeter array (Resolve) and an X-ray CCD camera (Xtend). The Resolve achieves high-resolution spectroscopy (FWHM: 5–7 eV) in the 0.3–12 keV bandpass. Since Resolve is a non-dispersive spectrometer, it is possible to perform spatially resolved high-resolution spectroscopy of the diffuse SNR in the Milky Way.

Our target W49B is a core-collapse SNR located in the Milky Way. The X-ray spectrum of W49B has strong emission lines from He-like and H-like ions, which indicate that the X-ray emission originates from the metal-rich ejecta. The morphology of W49B is elongated from east to west and is characterized by a bar-like distribution of iron surrounded by a relatively broad distribution of silicon (Figure 7.3). Although the physical origin of the X-ray morphology of W49B is still uncertain, two scenarios have been proposed: a jet-driven core-collapse supernova (hereafter "jet scenario"; Keohane et al., 2007; Lopez et al., 2013) or a spherically symmetric SN that expanded into an inhomogeneous ISM (hereafter "shell scenario"; Zhou et al., 2011). If W49B is the remnant of a jet-like explosion, it is a valuable sample of the remnants of

explosions associated with hypernovae and gamma-ray bursts.

To distinguish between the above two scenarios, we suggest a XRISM observation of the eastern edge of W49B. If the morphology of W49B is a result of interaction with the inhomogeneous ISM, the eastern edge would correspond to the rim of the shell with a relatively long line-of-sight length as shown in the right panel of Figure 7.5. On the other hand, in the case of jet scenarios, this eastern edge region may correspond to the jet-induced ring-like structures, which has been demonstrated by González-Casanova et al. (2014). In the case of a simple structure shown in Figure 7.5, it is possible to distinguish the two scenarios based on the RS effect. Figure 7.6 (a) represents the simulated spectrum of W49B where the spectral extraction region is shown by the red square in Figure 7.5. The thermal emission was modeled according to the spatially resolved spectral analysis performed by Holland-Ashford et al. (2020). We investigate the effect of RS on the Si and Fe Kα lines of the simulated spectrum in both scenarios. Assuming the abundances of heavy elements and ion temperatures (equal to electron temperature) as determined by Holland-Ashford et al. (2020), we calculate the optical depth of Si Heα (r), Si Lyα, and Fe Heα (r) lines according to Equation (3.55). The line-of-sight length of the eastern edge of W49B is assumed to be 10 pc from the X-ray image in the shell scenario and 1 pc from simulation results obtained by González-Casanova et al. (2014) in the jet scenario. Table 7.3 summarizes the optical depths of each emission line, assuming a typical electron density of 10 cm^{-3}. In the jet scenario, the optical depths are roughly 0.1, whereas, in the shell scenario, the depths are approximately 1, which implies that the RS effect can be observed only in the shell scenario. Figure 7.6 (b) and (c) represent the spectra expected to be observed in the two scenarios. We utilize the same assumptions as Kaastra and Mewe (1995) to calculate the transmission factors. Significant scattering effects are expected to be observed from both Si and Fe lines in the shell scenario. Especially, since Fe is the abundant element, the intensity of Fe XXV Heα (r) is expected to be strongly reduced by RS. Therefore, the Fe Heα line is particularly useful in separating these two scenarios.

TABLE 7.3: Optical depths of resonance lines of Si and Fe

Line ID	jet scenario	shell scenario
Si XIII Heα (resonance)	0.0773	0.773
Si XIV Lyα	0.0625	0.625
Fe XXV Heα (resonance)	0.143	1.43

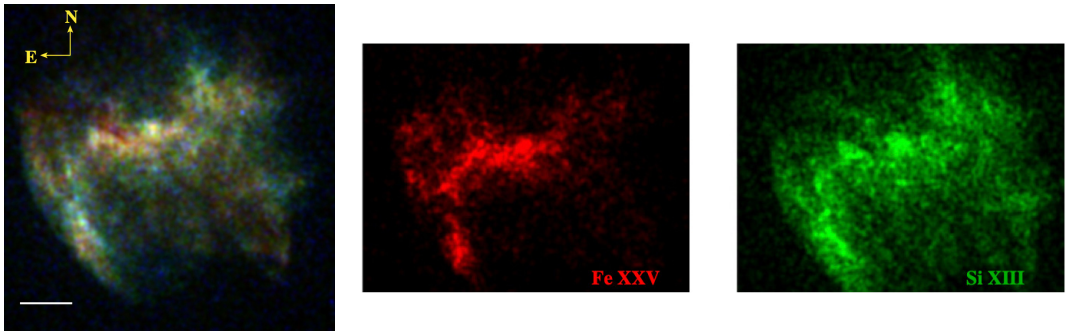

FIGURE 7.3: X-ray image of W49B observed with Chandra ACIS (Lopez et al., 2009). The left panel shows three color image in the soft band (0.3–1.50 keV; blue), medium band (1.5–2.5 keV; green), and hard band (2.5–8.0 keV; red). The middle and right panels represent X-ray images of Fe XXV and Si XIII, respectively.

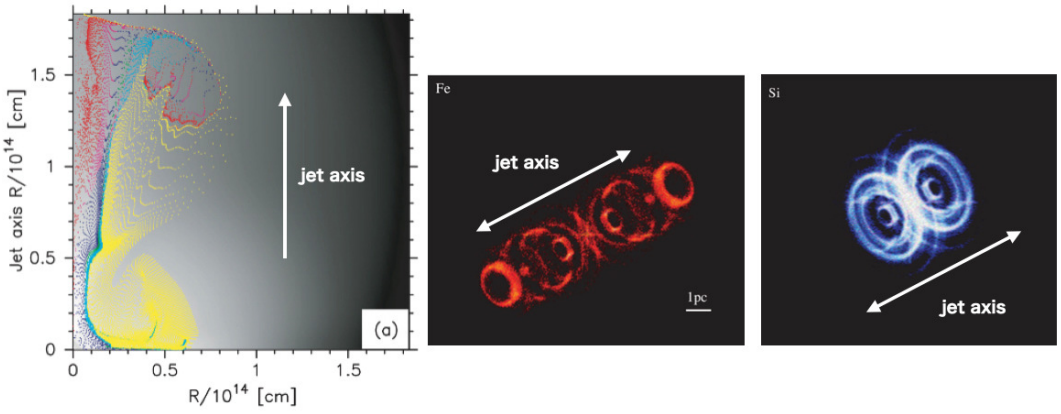

FIGURE 7.4: (left) Density structure of SN simulated by Tominaga (2008). Color of the marks represents the abundance of the mass element (H: yellow, He: cyan, O+C: green, O+Mg: blue, Si: magenta, and Fe: red). A large amount of iron is synthesized in the region along the jet axis. (middle) Fe XXV X-ray emission maps of W49B simulated by González-Casanova et al. (2014). (right) Same as the middle panel but Si XIV map.

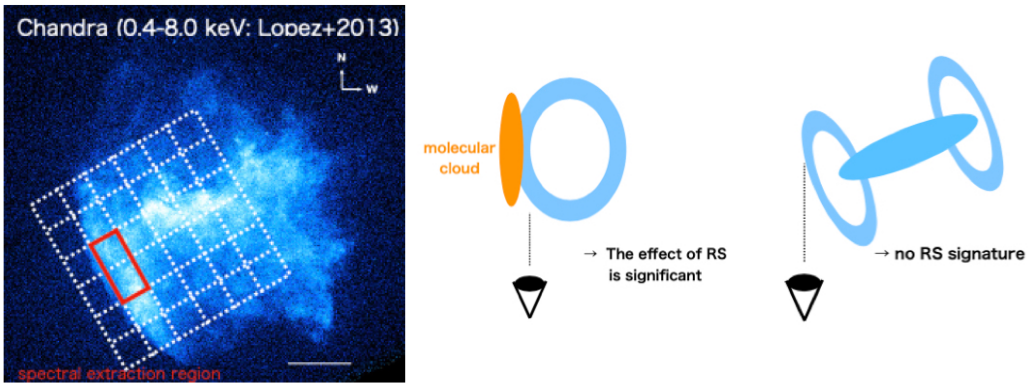

FIGURE 7.5: (right) X-ray full-band (0.5–8.0 keV) exposure-corrected image of W49B as observed for 220 ks by Chandra ACIS (Lopez et al., 2013). The white dashed line corresponds to the field of view of Resolve, and each pixel corresponds to one pixel of Resolve. The spectral extraction region is shown by the red square. (middle) Schematic image of W49B in the shell scenario. In this case, the spectral extraction region (the eastern edge) corresponds to the rim of the SNR. (right) Schematic image of W49B in the jet scenario. The spectral extraction region corresponds to the ring-like structure of the SNR.

7.4 Origin of Excess around 16 Å (0.78 keV)

The RGS spectra of N49 and J0453.6−6829 show the excess around 16 Å(see (a-1) and (a-2) panels in Figure 7.7), which cannot be explained by the effect of CX and RS. Similar discrepancies have been reported for other objects (Figure 7.7 (b-1) to (b-4)), and we attribute these discrepancies to uncertainties in the atomic data related to Fe-L emission lines, such as oscillator strength and rate coefficients of each atomic process (introduced in Chapter 3). The Fe-L emission from Fe XVI to Fe XXIV is observed in the wavelength range of 14-18 Å, which is emitted through a series of atomic processes, such as collisional excitation, radiative recombination, dielectron recombination, and inner-shell ionization. Therefore, comprehensive atomic data covering these processes are required to calculate the emissivities of Fe-L lines. Most of these atomic data have been obtained in theoretical calculations with only a few benchmarks established with laboratory measurements (e.g., Gu et al., 2022). It has been pointed out that there is a discrepancy between the atomic data obtained by theoretical calculations and the data obtained by experiments, which lead to uncertainty of emissivities of Fe-L lines (e.g., Kühn et al., 2022). Since there are Lα lines of Fe XVIII around 16 Å, the discrepancy may be due to uncertainties in the Fe XVIII lines. Significant excess around 16 Å is not observed in the spectrum of E0102, which contains few Fe L-lines in its spectrum. This confirms our suggestion. To solve these problems, it is necessary to experimentally measure atomic data. Ground experiments, such as EBIT are indispensable for the future development of X-ray astronomy.

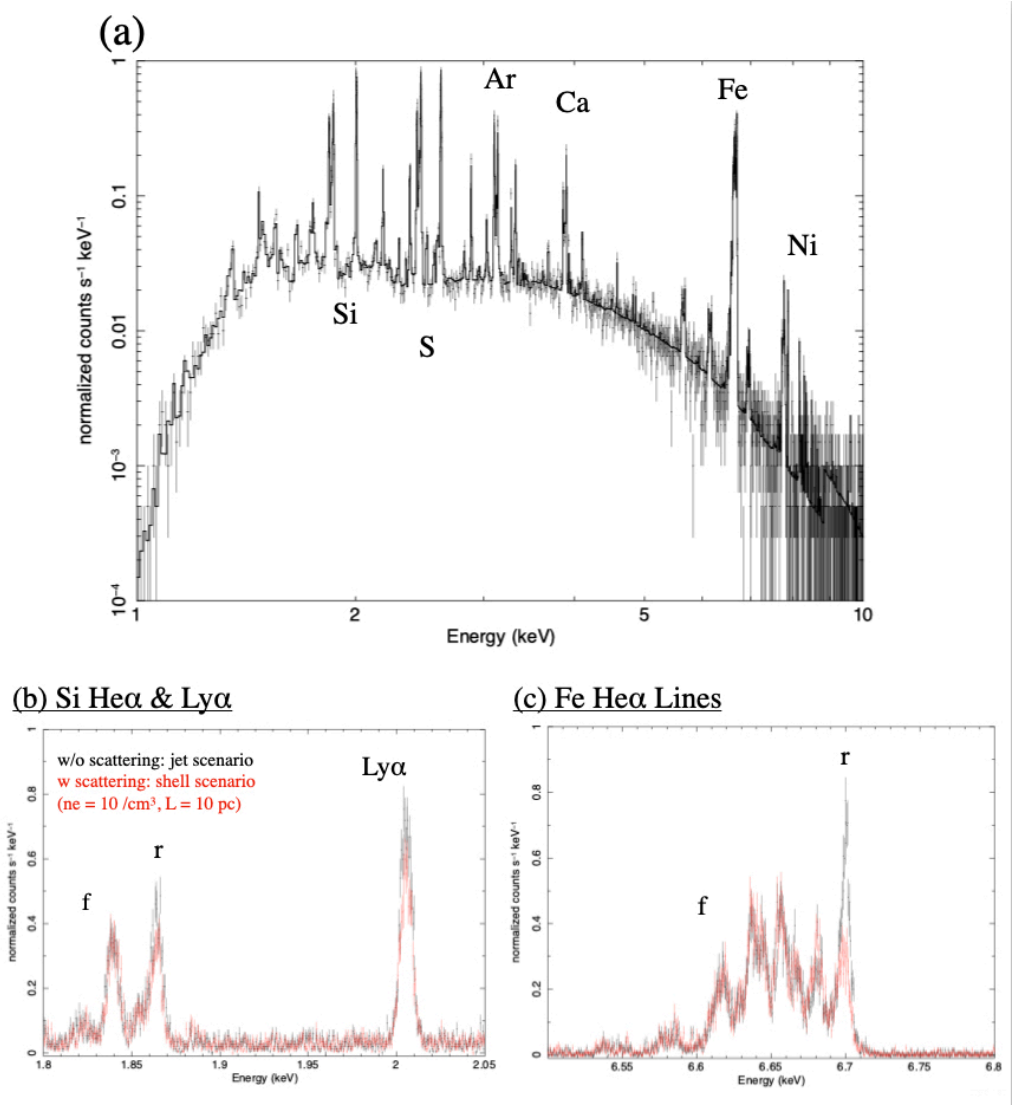

FIGURE 7.6: (a) Simulated Resolve spectrum of W49B. The exposure time is assumed to be 300 ks. (b) Close-up view of the simulated Resolve spectrum around the Si Kα lines expected to be observed in the two scenarios. Jet and shell scenarios are shown in black and red, respectively. The effect of RS reduces the intensity of He$\alpha(r)$ and Lyα in the shell scenario. (c) Same as (b) but Fe Heα lines.

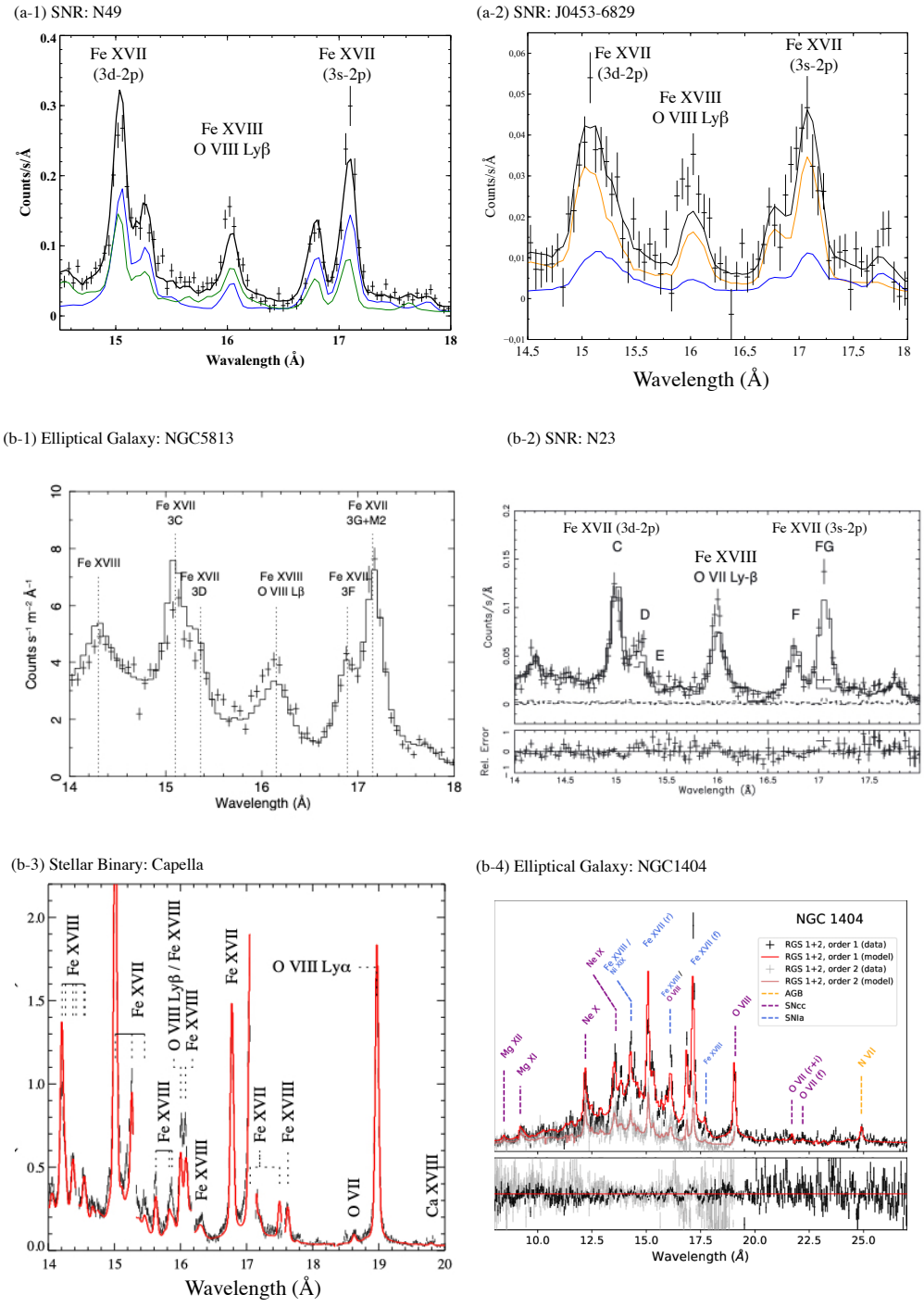

FIGURE 7.7: (a): Close-up views of the RGS spectrum around Fe XVII Lα and O VIII Lyβ obtained by our studies. There are discrepancies between the data and the NEI model around the OVIII Lyβ line ($\sim$ 16 Å). (a-1) RGS spectrum of N49. The overlaid black solid line is the best-fit "NEI" model. The solid blue and green lines correspond to the ISM and ejecta components, respectively. (a-2) RGS spectrum of J0453.6−6829. The colored solid curves indicate the contributions of the low-temperature (blue) and high-temperature NEI (orange) components. (b): Same as (a), but obtained by previous studies. Each panel shows the RGS spectrum of (b-1) elliptical galaxy NGC5813 (Plaa et al., 2012), (b-2) SNR N23 (Broersen et al., 2011), (b-3) stellar binary Capella (Audard et al., 2001), elliptical galaxy NGC1404 (Mernier et al., 2022), respectively.

Chapter 8

Conclusions

We performed a high-resolution X-ray spectroscopy of N49, J0453.6−6829 and E0102 with the RGS onboard XMM-Newton. The important results are summarized as follows:

- We obtained observational evidence for CX and RS from N49 and J0453.6−6829, based on the quantitative evaluation of their effects.
- Based on our results and previous studies, RS seems to be observed in an asymmetric structure of SNRs with a large column density, such as rim of SNRs.
- On the other hand, CX X-ray emission is particularly enhanced at the outer edge of the shock front (a few percent of the shock radius) in contact with dense clouds. Moreover, most of the SNRs in which CX has been observed are older than 10000 years. This tendency may be attributed to the dependence of the cross section of CX on the collision velocity between ions and neutral hydrogen. Therefore, evolved SNRs are suitable targets to search for CX X-ray emissions.
- We underestimate the O abundance by about a factor of 1.8 if we do not take into account the RS effect, which leads to an underestimation of the progenitor mass by about 75 % . This demonstrates the importance of RS in measuring elemental abundances.
- We have presented a method to constrain the 3D structure of SNRs by measuring their line-of-sight length through the effects of RS. We have applied this method to the SNR E0102 located in the SMC. The structures proposed by previous studies require strong scattering, which is inconsistent with our results. Therefore, we have proposed a double-ring structure and a cylindrical structure with the expansion velocity as structures that are consistent with both our observations and previous studies. This method can be applied to many celestial objects using the future satellite XRISM.
- The RGS spectra of N49 and J0453.6−6829 show the excess around 16 Å, which cannot be explained by the effect of CX and RS. We attribute these discrepancies to uncertainties in the atomic data related to Fe-L emission lines. To solve these problems, it is necessary to experimentally measure atomic data. Ground experiments, such as EBIT are indispensable for the future development of X-ray astronomy.

Bibliography

Alan et al. (2019). "A Detailed Archival CHANDRA Study of the Young Core-collapse Supernova Remnant 1E 0102.2-7219 in the Small Magellanic Cloud". In: *The Astrophysical Journal* 873.1, p. 53.

Aldrovandi et al. (1973). "Radiative and dielectronic recombination coefficients for complex ions". In: *Astronomy and Astrophysics* 25, p. 137.

Amano et al. (2020). "Evidence for Resonance Scattering in the X-Ray Grating Spectrum of the Supernova Remnant N49". In: *The Astrophysical Journal* 897.1, p. 12.

Anders and Grevesse (1989). "Abundances of the elements: Meteoritic and solar". In: *Geochimica et Cosmochimica acta* 53.1, pp. 197–214.

Audard et al. (2001). "The XMM-Newton view of stellar coronae: High-resolution X-ray spectroscopy of Capella". In: *Astronomy & Astrophysics* 365.1, pp. L329–L335.

Banas et al. (1997). "Supernova remnants associated with molecular clouds in the large magellanic cloud". In: *The Astrophysical Journal* 480.2, p. 607.

Banovetz et al. (2021). "The Center of Expansion and Age of the Oxygen-rich Supernova Remnant 1E 0102.2-7219". In: *The Astrophysical Journal* 912.1, p. 33.

Blair et al. (2000). "Hubble Space Telescope observations of oxygen-rich supernova remnants in the magellanic clouds. II. Elemental abundances in N132D and 1E 0102.2–7219". In: *The Astrophysical Journal* 537.2, p. 667.

Blondin et al. (1996). "Axisymmetric circumstellar interaction in supernovae". In: *The Astrophysical Journal* 472.1, p. 257.

Broersen et al. (2011). "The high resolution X-ray spectrum of SNR 0506-68 using XMM-Newton". In: *Astronomy & Astrophysics* 535, A11.

Burrows and Vartanyan (2021). "Core-collapse supernova explosion theory". In: *Nature* 589.7840, pp. 29–39.

Burrows et al. (2012). "An investigation into the character of pre-explosion core-collapse supernova shock motion". In: *The Astrophysical Journal* 759.1, p. 5.

Cash (1979). "Parameter estimation in astronomy through application of the likelihood ratio". In: *The Astrophysical Journal* 228, pp. 939–947.

Castro et al. (2011). "AN XMM-NEWTON STUDY OF THE BRIGHT, NEARBY SUPERNOVA REMNANT G296. 1–0.5". In: *The Astrophysical Journal* 734.2, p. 86.

Chevalier (1974). "The evolution of supernova remnants. Spherically symmetric models". In: *The Astrophysical Journal* 188, pp. 501–516.

— (2005). "Young core-collapse supernova remnants and their supernovae". In: *The Astrophysical Journal* 619.2, p. 839.

Chieffi and Limongi (2004). "Explosive Yields of Massive Stars from Z= 0 to Z= $Z_{\odot}$". In: *The Astrophysical Journal* 608.1, p. 405.

Chu et al. (1988). "Environments and populations of supernova remnants in the Large Magellanic Cloud". In: *The Astronomical Journal* 96, pp. 1874–1883.

Cline et al. (1981). "Precise source location of the anomalous 1979 March 5 gamma ray transient". In.

Collaboration, Hitomi (2017). "Solar abundance ratios of the iron-peak elements in the Perseus cluster". In: *Nature* 551.7681, pp. 478–480.

Conselice et al. (2001). "On the nature of the NGC 1275 system". In: *The Astronomical Journal* 122.5, p. 2281.

Cravens (2002). "X-ray emission from comets". In: *Science* 296.5570, pp. 1042–1045.

Davies et al. (2009). "The progenitor mass of the magnetar SGR1900+ 14". In: *The Astrophysical Journal* 707.1, p. 844.

Dickey and Lockman (1990). "HI in the Galaxy". In: *Annual review of astronomy and astrophysics* 28, pp. 215–261.

Dwarkadas et al. (2007). "The evolution of supernovae in circumstellar wind bubbles. II. Case of a Wolf-Rayet star". In: *The Astrophysical Journal* 667.1, p. 226.

Ezoe et al. (2021). "High-resolution X-ray spectroscopy of astrophysical plasmas with X-ray microcalorimeters". In: *Reviews of Modern Plasma Physics* 5, pp. 1–43.

Figer et al. (2005). "Massive stars in the SGR 1806–20 cluster". In: *The Astrophysical Journal* 622.1, p. L49.

Filippenko (1997). "Optical spectra of supernovae". In: *Annual Review of Astronomy and Astrophysics* 35.1, pp. 309–355.

Finkelstein et al. (2006). "Optical structure and proper-motion age of the oxygen-rich supernova remnant 1E 0102–7219 in the Small Magellanic Cloud". In: *The Astrophysical Journal* 641.2, p. 919.

Flanagan et al. (2004). "Chandra High-Resolution X-Ray Spectrum of Supernova Remnant 1E 0102.2–7219". In: *The Astrophysical Journal* 605.1, p. 230.

Gaensler et al. (2003). "Discovery of a New Pulsar Wind Nebula in the Large Magellanic Cloud". In: *The Astrophysical Journal* 594.2, p. L111.

Gaetz et al. (2000). "Chandra X-Ray Observatory Arcsecond Imaging of the Young, Oxygen-rich Supernova Remnant 1E 0102.2–7219". In: *The Astrophysical Journal* 534.1, p. L47.

Ghavamian et al. (2003). "The physics of supernova blast waves. I. kinematics of DEM L71 in the large Magellanic cloud". In: *The Astrophysical Journal* 590.2, p. 833.

Gillaspy (2001). "Highly charged ions". In: *Journal of Physics B: Atomic, Molecular and Optical Physics* 34.19, R93.

González-Casanova et al. (2014). "The morphology and dynamics of jet-driven supernova remnants: the case of W49B". In: *The Astrophysical Journal Letters* 781.2, p. L26.

Graczyk et al. (2020). "A Distance determination to the Small Magellanic Cloud with an accuracy of better than two percent based on late-type eclipsing binary stars". In: *The Astrophysical Journal* 904.1, p. 13.

Gu et al. (2016). "Plasma code for astrophysical charge exchange emission at X-ray wavelengths". In: *Astronomy & Astrophysics* 588, A52.

— (2019). "X-ray spectra of the Fe-L complex". In: *Astronomy & Astrophysics* 627, A51.

— (2022). "X-ray spectra of the Fe-L complex-III. Systematic uncertainties in atomic data". In: *Astronomy & Astrophysics* 664, A62.

Haberl et al. (2012). "Multi-frequency observations of SNR J0453–6829 in the LMC-A composite supernova remnant with a pulsar wind nebula". In: *Astronomy & Astrophysics* 543, A154.

Hanke et al. (2013). "SASI activity in three-dimensional neutrino-hydrodynamics simulations of supernova cores". In: *The Astrophysical Journal* 770.1, p. 66.

Herder, Den et al. (2001). "The reflection grating spectrometer on board XMM-Newton". In: *Astronomy & Astrophysics* 365.1, pp. L7–L17.

Hitomi Collaboration (2018). "Measurements of resonant scattering in the Perseus Cluster core with Hitomi SXS". In: *Publications of the Astronomical Society of Japan* 70.2, p. 10.

Holland-Ashford et al. (2020). "Spatially Resolved Study of Recombining Plasma in W49B Using XMM-Newton". In: *The Astrophysical Journal* 903.2, p. 108.

Hughes (Jan. 1994). "ROSAT HRI Observations of Magellanic Cloud Supernova Remnants (I)". In: *The Soft X-ray Cosmos*. Ed. by Eric M. Schlegel and Robert Petre. Vol. 313. American Institute of Physics Conference Series, p. 144. DOI: 10.1063/1.46727.

Hughes et al. (1998). "ASCA X-ray spectroscopy of large magellanic cloud supernova remnants and the metal abundances of the large magellanic cloud". In: *The Astrophysical Journal* 505.2, p. 732.

— (2000). "Electron Heating and Cosmic Rays at a Supernova Shock from Chandra X-Ray Observations of 1E 0102.2–7219". In: *The Astrophysical Journal* 543.1, p. L61.

— (2006). "The Chandra View of the Supernova Remnant 0506–68.0 in the Large Magellanic Cloud". In: *The Astrophysical Journal* 645.2, p. L117.

Hwang et al. (1994). "An X-ray study of five supernova remnants in the Carina spiral arm". In: *The Astrophysical Journal* 431, pp. 819–825.

— (2005). "CHANDRA X-ray observation of a mature cloud-shock interaction in the bright eastern knot region of Puppis A". In: *The Astrophysical Journal* 635.1, p. 355.

Itoh and Masai (1989). "The effect of a circumstellar medium on the X-ray emission of young remnants of Type II supernovae". In: *Monthly Notices of the Royal Astronomical Society* 236.4, pp. 885–899.

Janev and Winter (1985). "State-selective electron capture in atom-highly charged ion collisions". In: *Physics Reports* 117.5-6, pp. 265–387.

Jansen et al. (2001). "XMM-Newton observatory-I. The spacecraft and operations". In: *Astronomy & Astrophysics* 365.1, pp. L1–L6.

Kaastra (2017). "On the use of C-stat in testing models for X-ray spectra". In: *Astronomy & Astrophysics* 605, A51.

Kaastra and Jansen (1993). "A spectral code for X-ray spectra of supernova remnants". In: *Astronomy and Astrophysics Supplement Series* 97, pp. 873–885.

Kaastra and Mewe (1995). "Optical depth effects in the X-ray emission from supernova remnants". In: *Astronomy and Astrophysics* 302, p. L13.

Kaastra et al. (Jan. 1996). "SPEX: a new code for spectral analysis of X & UV spectra." In: *UV and X-ray Spectroscopy of Astrophysical and Laboratory Plasmas*, pp. 411–414.

— (2008). "Thermal radiation processes". In: *Space Science Reviews* 134, pp. 155–190.

Kastner and Kastner (1990). "Opacity ratios for Doppler-broadened lines from common upper levels". In: *Journal of Quantitative Spectroscopy and Radiative Transfer* 44.2, pp. 275–288.

Katsuda et al. (2008). "Asymmetric ejecta distribution of the Cygnus Loop revealed with Suzaku". In: *Publications of the Astronomical Society of Japan* 60.sp1, S107–S114.

— (2011). "Possible charge-exchange X-ray emission in the Cygnus Loop detected with Suzaku". In: *The Astrophysical Journal* 730.1, p. 24.

— (2012). "High-resolution X-Ray Spectroscopy of the Galactic Supernova Remnant Puppis A with XMM-Newton/RGS". In: *The Astrophysical Journal* 756.1, p. 49.

— (2018). "Progenitor Mass Distribution of Core-collapse Supernova Remnants in Our Galaxy and Magellanic Clouds Based on Elemental Abundances". In: *The Astrophysical Journal* 863.2, p. 127.

Kawasaki et al. (2002). "ASCA observations of the supernova remnant IC 443: thermal structure and detection of overionized plasma". In: *The Astrophysical Journal* 572.2, p. 897.

Kelley et al. (2016). "The Astro-H high resolution soft x-ray spectrometer". In: *Space Telescopes and Instrumentation 2016: Ultraviolet to Gamma Ray*. Vol. 9905. SPIE, pp. 229–245.

Keohane et al. (2007). "A near-infrared and X-ray study of W49 B: a wind cavity explosion". In: *The Astrophysical Journal* 654.2, p. 938.

Khokhlov et al. (1999). "Jet-induced explosions of core collapse supernovae". In: *The Astrophysical Journal* 524.2, p. L107.

Kifonidis et al. (2003). "Non-spherical core collapse supernovae-I. Neutrino-driven convection, Rayleigh-Taylor instabilities, and the formation and propagation of metal clumps". In: *Astronomy & Astrophysics* 408.2, pp. 621–649.

Kim et al. (2003). "A neutral hydrogen survey of the Large Magellanic Cloud: aperture synthesis and multibeam data combined". In: *The Astrophysical Journal Supplement Series* 148.2, p. 473.

Kühn, Steffen et al. (2022). "New measurement resolves key astrophysical Fe XVII oscillator strength problem". In: *Physical Review Letters* 129.24, p. 245001.

Kumar et al. (2014). "CHANDRA AND XMM-NEWTON STUDY OF THE SUPERNOVA REMNANT KES 73 HOSTING THE MAGNETAR 1E 1841–045". In: *The Astrophysical Journal* 781.1, p. 41.

Lakićević et al. (2015). "The influence of supernova remnants on the interstellar medium in the Large Magellanic Cloud seen at 20–600 μm wavelengths". In: *The Astrophysical Journal* 799.1, p. 50.

Lallement (2004). "On the contribution of charge-exchange induced X-ray emission in the ISM and ICM". In: *Astronomy & Astrophysics* 422.2, pp. 391–400.

Levenson et al. (1998). "Panoramic views of the Cygnus Loop". In: *The Astrophysical Journal Supplement Series* 118.2, p. 541.

Lisse et al. (1996). "Discovery of X-ray and extreme ultraviolet emission from comet C/Hyakutake 1996 B2". In: *Science* 274.5285, pp. 205–209.

Liu et al. (2012). "Charge-exchange X-ray emission of nearby star-forming galaxies". In: *Monthly Notices of the Royal Astronomical Society* 420.4, pp. 3389–3395.

Lopez et al. (2009). "Typing supernova remnants using X-ray line emission morphologies". In: *The Astrophysical Journal* 706.1, p. L106.

— (2011). "Using the X-ray morphology of young supernova remnants to constrain explosion type, ejecta distribution, and chemical mixing". In: *The Astrophysical Journal* 732.2, p. 114.

— (2013). "The galactic supernova remnant W49B likely originates from a jet-driven, core-collapse explosion". In: *The Astrophysical Journal* 764.1, p. 50.

Lotz (1968). "Electron-impact ionization cross-sections and ionization rate coefficients for atoms and ions from hydrogen to calcium". In: *Zeitschrift für Physik* 216.3, pp. 241–247.

Masai (1994). "Nonequilibria in thermal emission from supernova remnants". In: *The Astrophysical Journal* 437, pp. 770–780.

McEntaffer et al. (2012). "SNR 0453-68.5: An Asymmetric Remnant and its Plerion in the Large Magellanic Cloud". In: *The Astrophysical Journal* 756.1, p. 17.

Mernier et al. (2022). "The cycle of metals in the infalling elliptical galaxy NGC 1404". In: *Monthly Notices of the Royal Astronomical Society* 511.3, pp. 3159–3178.

Mewe et al. (1978). "Heliumlike ion line intensities. I-Stationary plasmas. II-Non-stationary plasmas". In: *Astronomy and Astrophysics* 65, pp. 99–121.

— (1981). "Calculated X-radiation from optically thin plasmas. IV-Atomic data and rate coefficients for spectra in the range 1-270 A". In: *Astronomy and Astrophysics Supplement Series* 45, pp. 11–52.

Millette, Pierre A (2021). "Stellar Evolution of High Mass-Loss Stars". In: *Progress in Physics* 17.

Mitsuda et al. (2010). "The high-resolution x-ray microcalorimeter spectrometer system for the SXS on ASTRO-H". In: *Space Telescopes and Instrumentation 2010: Ultraviolet to Gamma Ray*. Vol. 7732. SPIE, pp. 280–289.

Miyata et al. (1998). "Metal-rich plasma at the center portion of the Cygnus Loop". In: *Publications of the Astronomical Society of Japan* 50.2, pp. 257–269.

Miyata et al. (2008). "Evidence for resonance line scattering in the Suzaku X-ray spectrum of the Cygnus Loop". In: *Publications of the Astronomical Society of Japan* 60.3, pp. 521–526.

Muno et al. (2005). "A neutron star with a massive progenitor in Westerlund 1". In: *The Astrophysical Journal* 636.1, p. L41.

Nakashima et al. (2018). "Spatial distribution of the milky way hot gaseous halo constrained by Suzaku X-ray observations". In: *The Astrophysical Journal* 862.1, p. 34.

Nomoto (1982). "Accreting white dwarf models for type I supernovae. I-Presupernova evolution and triggering mechanisms". In: *Astrophysical Journal, Part 1, vol. 253, Feb. 15, 1982, p. 798-810.* 253, pp. 798–810.

Okon et al. (2020). "Deep XMM-Newton Observations Reveal the Origin of Recombining Plasma in the Supernova Remnant W44". In: *The Astrophysical Journal* 890.1, p. 62.

Park et al. (2003). "X-ray emission from multiphase shock in the large magellanic cloud supernova remnant N49". In: *The Astrophysical Journal* 586.1, p. 210.

— (2012). "An X-Ray Study of Supernova Remnant N49 and Soft Gamma-Ray Repeater 0526–66 in the Large Magellanic Cloud". In: *The Astrophysical Journal* 748.2, p. 117.

Patnaude and Fesen (2005). "Model simulations of a shock-cloud interaction in the Cygnus Loop". In: *The Astrophysical Journal* 633.1, p. 240.

Plaa, de et al. (2004). "X-ray spectroscopy on Abell 478 with XMM-Newton". In: *Astronomy & Astrophysics* 423.1, pp. 49–56.

— (2012). "Estimating turbulent velocities in the elliptical galaxies NGC 5044 and NGC 5813". In: *Astronomy & Astrophysics* 539, A34.

Podsiadlowski (2017). "Binary Evolution and the Progenitor of SN 1987A". In: *arXiv preprint arXiv:1702.03973*.

Pollock (2012). "Ion-ion charge exchange and X-rays from the winds of hot stars". In: *Astronomische Nachrichten* 333.4, pp. 351–354.

Porquet et al. (2001). "Line ratios for helium-like ions: Applications to collision-dominated plasmas". In: *Astronomy & Astrophysics* 376.3, pp. 1113–1122.

Ramachandran et al. (2019). "Testing massive star evolution, star formation history, and feedback at low metallicity-Spectroscopic analysis of OB stars in the SMC Wing". In: *Astronomy & Astrophysics* 625, A104.

Rasmussen et al. (2001). "The X-ray spectrum of the supernova remnant 1E 0102.2-7219". In: *Astronomy & Astrophysics* 365.1, pp. L231–L236.

Reynoso et al. (1995). "VLA observations of neutral hydrogen in the direction of Puppis A". In: *The Astronomical Journal* 110, p. 318.

Russell and Dopita (1992). "Abundances of the heavy elements in the Magellanic Clouds. III-Interpretation of results". In: *The Astrophysical Journal* 384, pp. 508–522.

Sana et al. (2014). "Southern massive stars at high angular resolution: observational campaign and companion detection". In: *The Astrophysical Journal Supplement Series* 215.1, p. 15.

Sano et al. (2017). "Interstellar gas toward the Magellanic supernova remnants". In: *AIP Conference Proceedings*. Vol. 1792. 1. AIP Publishing LLC, p. 040038.

— (2020). "ALMA CO Observations of Gamma-Ray Supernova Remnant N132D in the Large Magellanic Cloud: Possible Evidence for Shocked Molecular Clouds Illuminated by Cosmic-Ray Protons". In: *The Astrophysical Journal* 902.1, p. 53.

Sato et al. (2016). "Suzaku spectra of a Type-II supernova remnant, Kes 79". In: *Publications of the Astronomical Society of Japan* 68.SP1.

— (2021). "High-entropy ejecta plumes in Cassiopeia A from neutrino-driven convection". In: *Nature* 592.7855, pp. 537–540.

Schenck et al. (2016). "A Chandra Study of the Interstellar Metallicity in the Large Magellanic Cloud Using Supernova Remnants". In: *The Astronomical Journal* 151.6, p. 161.

Seitenzahl et al. (2018). "Integral Field Spectroscopy of Supernova Remnant 1E0102–7219 Reveals Fast-moving Hydrogen and Sulfur-rich Ejecta". In: *The Astrophysical Journal Letters* 853.2, p. L32.

Smith et al. (2014). "ASTRO-H White Paper-New Spectral Features". In: *arXiv preprint arXiv:1412.1172*.

Steenbrugge et al. (2005). "Simultaneous X-ray and UV spectroscopy of the Seyfert galaxy NGC 5548-II. Physical conditions in the X-ray absorber". In: *Astronomy & Astrophysics* 434.2, pp. 569–584.

Strüder et al. (2001). "The European photon imaging camera on XMM-Newton: the pn-CCD camera". In: *Astronomy & Astrophysics* 365.1, pp. L18–L26.

Sukhbold, Tuguldur et al. (2016). "Core-collapse supernovae from 9 to 120 solar masses based on neutrino-powered explosions". In: *The Astrophysical Journal* 821.1, p. 38.

Sumiyoshi et al. (2005). "Postbounce evolution of core-collapse supernovae: long-term effects of the equation of state". In: *The Astrophysical Journal* 629.2, p. 922.

Suzuki et al. (2020). "Plasma Diagnostics of the Supernova Remnant N132D using Deep XMM–Newton Observations with the Reflection Grating Spectrometer". In: *The Astrophysical Journal* 900.1, p. 39.

Takiwaki and Kotake (2011). "Gravitational wave signatures of magnetohydrodynamically driven core-collapse supernova explosions". In: *The Astrophysical Journal* 743.1, p. 30.

Tanaka et al. (2022). "Charge Exchange X-Ray Emission Detected in Multiple Shells of Supernova Remnant G296. 1–0.5". In: *The Astrophysical Journal* 933.1, p. 101.

Thielemann et al. (1996). "Core-collapse supernovae and their ejecta". In: *The Astrophysical Journal* 460, p. 408.

Tominaga (2008). "Aspherical properties of hydrodynamics and nucleosynthesis in jet-induced supernovae". In: *The Astrophysical Journal* 690.1, p. 526.

Tsunemi et al. (1986). "X-ray spectra of the Cassiopeia A and TYCHO supernova remnants and their element abundances". In: *The Astrophysical Journal* 306, pp. 248–254.

Turner et al. (2001). "The European photon imaging camera on XMM-Newton: the MOS cameras". In: *Astronomy & Astrophysics* 365.1, pp. L27–L35.

Uchida et al. (2015). "N49: THE FIRST ROBUST DISCOVERY OF RECOMBINING PLASMA IN AN EXTRA GALACTIC SUPERNOVA REMNANT". In: *The Astrophysical Journal* 808.1, p. 77.

— (2019). "High Forbidden-to-resonance Line Ratio of O VII Discovered from the Cygnus Loop". In: *The Astrophysical Journal* 871.2, p. 234.

van der Heyden et al. (2003). "High resolution spectroscopy and emission line imaging of DEM L 71 with XMM-Newton". In: *Astronomy & Astrophysics* 406.1, pp. 141–148.

Vink (2012). "Supernova remnants: the X-ray perspective". In: *The Astronomy and Astrophysics Review* 20, pp. 1–120.

Vogt and Dopita (2011). "The 3D structure of N132D in the LMC: a late-stage young supernova remnant". In: *Astrophysics and Space Science* 331, pp. 521–535.

Wachter et al. (1979). "Parameter estimation in X-ray astronomy using maximum likelihood". In: *The Astrophysical Journal* 230, pp. 274–287.

Wargelin et al. (Jan. 2008). "EBIT charge-exchange measurements and astrophysical applications". In: *Canadian Journal of Physics* 86.1, pp. 151–169. DOI: 10.1139/P07-125. arXiv: 0708.0233 [astro-ph].

White and Malin (1987). "Possible binary star progenitor for SN1987A". In: *Nature* 327.6117, pp. 36–38.

Williams et al. (2006). "Dust destruction in fast shocks of core-collapse supernova remnants in the large magellanic cloud". In: *The Astrophysical Journal* 652.1, p. L33.

Winkler et al. (1988). *Supernova Remnants and the Interstellar Medium*. Cambridge University Press Cambridge.

Woosley and Weaver (1995). *The evolution and explosion of massive Stars II: Explosive hydrodynamics and nucleosynthesis*. Tech. rep. Lawrence Livermore National Lab.(LLNL), Livermore, CA (United States).

Xu et al. (2002). "High-resolution observations of the elliptical galaxy NGC 4636 with the reflection grating spectrometer on board XMM-Newton". In: *The Astrophysical Journal* 579.2, p. 600.

Yamaguchi et al. (2014). "Discriminating the progenitor type of supernova remnants with iron K-shell emission". In: *The Astrophysical Journal Letters* 785.2, p. L27.

— (2018). "Evidence for Rapid Adiabatic Cooling as an Origin of the Recombining Plasma in the Supernova Remnant W49B Revealed by NuSTAR Observations". In: *The Astrophysical Journal Letters* 868.2, p. L35.

— (2021). "Discovery of Double-ring Structure in the Supernova Remnant N103B: Evidence for Bipolar Winds from a Type Ia Supernova Progenitor". In: *The Astrophysical Journal Letters* 910.2, p. L24.

Yamane et al. (2018). "ALMA Observations of Supernova Remnant N49 in the LMC. I. Discovery of CO Clumps Associated with X-Ray and Radio Continuum Shells". In: *The Astrophysical Journal* 863.1, p. 55.

Zhou et al. (2011). "Unveiling the spatial structure of the overionized plasma in the supernova remnant W49B". In: *Monthly Notices of the Royal Astronomical Society* 415.1, pp. 244–250.